CMOS-MEMS Scanning Microwave Microscopy

by

Mostafa Azizi

A thesis
presented to the University of Waterloo
in fulfillment of the
thesis requirement for the degree of
Doctor of Philosophy
in
Electrical and Computer Engineering

Waterloo, Ontario, Canada, 2016

© Mostafa Azizi 2017

AUTHOR'S DECLARATION

I hereby declare that I am the sole author of this thesis. This is a true copy of the thesis, including any required final revisions, as accepted by my examiners.

I understand that my thesis may be made electronically available to the public.

Abstract

This thesis presents the design, fabrication and experimental validation of an integrated dual-mode scanning microwave microscopy (SMM)/Atomic Force Microscopy (AFM) system that does not require the use of a conventional laser-based AFM or external scanners. Microfabricated SMM probes are collocated with strain-based piezoresistive AFM probes in a CMOS-MEMS process, and are actuated by integrated electrothermal scanners. Integration of AFM enables dual-mode imaging (topography and electrical properties); it also enables control over tip-sample distance, which is crucial for accurate SMM imaging. The SMM (also known as Scanning Near-field Microwave Microscope and Scanning Evanescent Microwave Microscope) is the most well-known type of Scanning Probe Microscopes (SPM) that can quantify local dielectric and conductivity of materials. It has emerged as the most promising means for the fast, non-contact, and non-destructive study of materials and semiconductor devices.

The CMOS-MEMS SMM devices are fabricated by using a standard foundry CMOS process, followed by an in-house mask-less post-processing technique to release them. Single-chip SMM/AFM devices with integrated 1-D and 3-D actuation are introduced. The CMOS-MEMS fabrication process allows external bulky scanners to be replaced with integrated MEMS actuators that are small and immune to vibration and drift. In this work, electrothermal MEMS actuators are utilized to scan the tip over the sample in 3 degrees of freedom, over a 13 µm x 13 µm x 10 µm scan range in the x, y, and z directions, respectively. Furthermore, the availability of polysilicon layers on the CMOS processes allows for on-chip integrated piezoresistive position sensing that obviates the need for the laser system. Vertical tip-sample distance control of a few nanometers is achieved with the integrated piezoresistive position sensors. These devices are used to modulate the tip-sample separation to underlying samples with a periodic signal, improving immunity to long-term system drifts.

To improve the sensitivity of the CMOS-MEMS SMM, different types of matching networks for SMMs are thoroughly analyzed and closed form formulas are presented for each

type. Based on the analyses, the stub matching method is selected to match the high tip-to-sample impedance to the 50 ohm characteristic impedance of the system. After that, with the help of lumped models and EM simulations, different sections of the CMOS-MEMS SMM system are analyzed and suggestions for selecting the best micro-transmission line and bonding-pad transmission lines are given. A measurement circuit for SMM is then presented and explained, showing how this measurement system can improve the output-signal-to-noise ratio and hence the sensitivity of microwave imaging. Calculations for the entire SMM system indicate that sub-attofarad tip-sample impedance can be measured. It is noteworthy that most of the analyses and suggestions given in this thesis can be applied to any Scanning Microwave Microscopes or, even more generally, to any microwave system that needs to sense a small signal.

Finally, the measurement results for the fabricated CMOS-MEMS SMM are presented to verify the proposed methods. Several samples with sub-micron and nanometer feature sizes are imaged. A special test sample with no topography but with buried dielectric materials in grid and stripes is also designed and measured.

Acknowledgements

I would like to thank my advisor, Professor Raafat Mansour, for his support and guidance throughout my PhD; I learned a lot from him and his manners. My sincere thanks to Professor Zoya Popovic, my PhD external examiner, for reading my thesis and her thoughtful feedbacks. I also like to thank my committee members, Professor Dayan Ban, Professor James Martin, and Professor Omar Ramahi for reading my thesis and providing feedback, and Dr. Irene Goldthorpe for attending my defense as a delegate of Professor Ban.

My special thank goes to Dr. Neil Sarkar for his thoughtful discussions and support from the first day until my graduation. I thank all my colleagues at CIRFE lab especially Geoff Lee and Duncan Strathearn for their help in the MEMS design and fabrication process.

I would like to thank all my friends especially Saleh, Desireh, Saman, Hossein, Ali, and Ghasem who created many memorable happy moments during my PhD studies.

Finally and most importantly, I would like to thank two very special women in my life whom I will stay forever indebted to. My wife, Limo, who has been selfless, loving and supportive; I couldn’t have done my PhD without her. And my mother, who has always put my success and education ahead of her dreams and goals. I cannot thank you enough.

Dedication

To my wife,

Limo

Table of Contents

AUTHOR'S DECLARATION ii
Abstract iii
Acknowledgements v
Dedication vi
Table of Contents vii
List of Figures ix
List of Tables xviii
List of Acronyms xix
Chapter 1 Introduction 1
1.1 Motivations 2
1.1.1 CMOS-MEMS Fabrication Process 3
1.2 Objectives 4
1.2.1 Integration of a fully 3D scanner on the probe 5
1.2.2 Systematic analysis for improving the sensitivity of CMOS-MEMS SMM 5
1.2.3 Integrating SMM with AFM 5
1.2.4 Designing novel probes to improve resolution in quantitative imaging. 6
1.3 Thesis Outline 6
Chapter 2 Literature Survey 8
2.1 History 8
2.1.1 STM and AFM 9
2.2 Various SMMs 10
2.3 Tip-Sample Distance Control 17
2.4 Theoretical Analysis 19
2.4.1 Lumped element model for tip-sample interaction [3], [23] 19
2.4.2 Transmission line model of the probe 23
2.4.3 Resonant transmission line 24
2.4.4 Charge image method [1], [24]–[26] 26
2.4.5 Simulation results of the conventional SMMs 31
Chapter 3 Fabrication of CMOS-MEMS SMMs 35
3.1 MEMS SPM's 35

3.2 CMOS-MEMS Fabrication Process 36
3.3 CMOS-MEMS SMM Device Description 39
3.4 Tip-sample Distance Control 43
3.5 SMM/AFM Probe 45
3.6 Thermal Coupling Reduction 49
Chapter 4 Analysis and Design of CMOS-MEMS Scanning Microwave Microscopes 53
4.1 Overall SMM Description 54
4.2 Device Description 55
4.3 Quality Factor Analysis 55
4.3.1 Lumped RLC resonator matching 57
4.3.2 Stub matching 58
4.3.3 Half lambda plus shunt 50 ohm ($\lambda/2+50\Omega$) 63
4.4 Circuit Model Analysis 64
4.4.1 Tip-sample interaction 66
4.4.2 Micro-transmission line 67
4.4.3 Bond pads transmission line 82
4.5 Description of the Matching Network Circuit 94
4.5.1 Discussion 98
4.5.2 Comparison with Keysight method 100
4.6 Measurement Circuit 101
4.6.1 Calculations for minimum detectable signal 105
Chapter 5 Measurement Results 108
5.1 Preliminary Measurement Results 108
5.2 Imaging Results 111
5.2.1 Sample with Subsurface Features 118
Chapter 6 Conclusion and Future work 124
6.1 Conclusion 124
6.2 Future Work 125
Bibliography 127
Appendix A SiO_2 and Silicon etching recipes in the RIE 135
Appendix B Quality factor of high loss transmission lines 136
Appendix C Components used in the SMM measurement system 139

List of Figures

Fig. 1-1. (a) Conventional commercialized AFM and 3-D scanner with laser alignment system. (b) A single chip AFM with piezoresistive position sensing and on-chip MEMS actuators for scanning [10]. 4

Fig. 2-1. Ash and Nichole's proposed SMM: A 10GHz oscillator excites a hemispherical resonator which is loaded by a subwavelength aperture of diameter 1.5 mm [16]. 9

Fig. 2-2. Frequency spectrum for different scanning probe microscopy techniques. SMM bridges the frequency gap between the existing local probe microscopy systems [17]. 11

Fig. 2-3. Schematic of the scanning near-field microwave microscope. The insets show a close view of the coaxial probe, sample, as well as a lumped element circuit model for the tip-sample interaction [3]. 12

Fig. 2-4. System Configuration for the SMM system proposed in [28] (details in the text). 13

Fig. 2-5. Apparatus schematic showing the probe, electronics, and shear-force setup. Note that in reality the laser beam is oriented perpendicular to the direction of enclosure dithering. Insets: intensity contour plots of the fringe E field in the xz lane for bulk samples with εr=300; the tip-sample distance is 100 nm, D=4 μm [23]. 14

Fig. 2-6. (a) Microstrip-line resonator and probe assembly. Evanescent waves extend out of the tapered tip. (b) Schematic of the probe-sample interaction area. Lumped-circuit model of the waveguide, tip, and sample. A dielectric sample is modeled in (c) and a metallic sample is modeled in (d) [32],[17]. 15

Fig. 2-7. Coaxial probe has two main sections, as shown in (a), consisting of a waveguide section over the "handle" and a cantilever beam followed by the tip section. The tip section consists of a protruding tip apex surrounded by a dielectric layer and a metallic shield layer. The cross-section of the probe is shown in (b) [17]. 15

Fig. 2-8. (Left) Tip-sample capacitance as a function of the spacing. As the tip oscillates above the sample surface, the tip impedance is also modulated at the same frequency. The inset shows the schematic of the tapping mode AFM and the microwave electronics (D—directional coupler, A—amplifier, M—mixer), as well as the cantilever structure and the SEM of the Pt tip. The scale bar is 500 nm [31]. (Right) (a) Layer structure of the Al_2O_3–SiO_2 / Si sample. (b) AFM image of the polished sample surface. (c) Contact and (d) tapping mode MIM-C images taken by the same tip at the same area. The darker regions are buried SiO_2. Electronic drift can be observed in (c) but not in (d). Line cuts are shown in both (c) and (d) for comparisons of the signal strength and the spatial resolution [31]. 16

Fig. 2-9. (a) A standard conductive AFM is connected to a performance network analyzer (PNA). A half lambda coaxial transmission line terminated with a 50-ohm shunt resistor is used for matching. (b) Sketch showing the arrangement of gold caps on the four steps of the dielectric staircase structure. (c) Topographical image of the 50 nm stepped calibration sample and profile along the white line [33]. 17

Fig. 2-10. (a) Comparison of images obtained in DF, HMDF and HMDF, with tapping modes from a locally B-doped Si sample. The first two images were taken simultaneously. (b) Line cuts along the dashed lines in the images above [39]. 18

Fig. 2-11. Lumped element circuit model for the tip-sample interaction. 20

Fig. 2-12. (a) Parallel strip transmission line probe. (b) Comparison of analytical lumped element model and finite element numerical data at 4 GHz for the real and imaginary parts of reflection coefficient [3]. 21

Fig. 2-13. (a) Shielded λ/4 coaxial resonator probe proposed in [25] (b) Equivalent lumped series resonant circuit for SMM [1]. 26

Fig. 2-14. (a) Image charge distribution for a thick sample in contact with the tip. The q_n series represents the charge redistribution on the tip, the q'_n series represents the effect of polarization of the dielectric sample, and the q''_n is the effective value of q_n inside the sample. (b) The iterative image charges in tip-bulk sample system in non-contact mode [26]. 29

Fig. 2-15. Measured and fitted resonant frequency as a function of tip-sample distance for a MgO single crystal [26]. 31

Fig. 2-16. Simulated structure in HFSS (a) side view (b) top view (c) zoomed tip area. (d,e) HFSS simulation results compared to theoretical results in [26]. 33

Fig. 2-17. Simulation in HFSS (a) side view (b) zoomed area near the tip. (c,d,f) HFSS simulation results compared to theoretical results in (e) top view and electric fields on the excitation sheet [3]. 34

Fig. 3-1. Cross-section view showing the thickness of each metal and IMD layers of 2 Polly 4 Metal (2P4M) 0.35µm CMOS process from TSMC [52]. 37

Fig. 3-2. Maskless release process for CMOS-MEMS. (a) Foundry CMOS process cross-section. (b) Anisotropic etch of SiO_2 intermetal dielectric layers. (c) Isotropic Si substrate etch, releases the devices. [53] and [54]. 38

Fig. 3-3. (a) Grooves in the backside of the wafer to suspend cantilevers over the edge of the

chip. (b) After oxide and Silicon etch on top. 38

Fig. 3-4. Single degree of freedom shielded SMM probe. A CPW to flexible transmission line transition is included in the signal path from the PNA to the tip. Internal metal layers are used for conduction while the top and bottom layers are used to shield the microwave signal. DC pads are used for vertical actuation using the thermal bimorph effect. 40

Fig. 3-5. CMOS-MEMS lateral electrothermal actuator. Inset is a cross-section of an individual beam, showing the offset internal mechanical layers used to generate a thermal moment. 42

Fig. 3-6. Chevron actuator used for lateral actuation: Layout and SEM image. 42

Fig. 3-7. CMOS-MEMS 3 DOF integrated AFM-SMM device. A CPW to flexible transmission line transition connects the microwave signal to the tip. Actuators are used to bend the transmission line and scan the tips. 43

Fig. 3-8. (a) Close-up of the balanced cantilever design used for AFM operation. The temperature in the piezoresistors is balanced, whereas the strain from tip-sample forces is only recorded on one of the piezoresistors. (b) A schematic circuit showing the Wheatstone bridge and applied voltages for the bridge and the vertical actuator. 44

Fig. 3-9. FEM simulation of the SMM tip in (a) 100 nm, and (b) 1 nm tip-sample distance of a bulk dielectric sample with a dielectric constant of 15. 45

Fig. 3-10. Effect of tip-sample distance on SMM sensitivity in (a) 100 nm, and (b) 1 nm tip-sample distance of a bulk dielectric sample (Red: without sample; Blue: with sample). ..45

Fig. 3-11. Close-up of SMM/AFM tip. The tip radius obtained in the release process is ~150nm. Metal-1 and metal-3 shielding layers are shown here. 46

Fig. 3-12. The process of getting sharp via tips through RIE oxide etching. 47

Fig. 3-13. SEM images of two larger via tips, survived (left), and not survived (right) after the oxide and silicon etching. 47

Fig. 3-14. Wedge-type tip: (Right) SEM image, and (left) layout. 48

Fig. 3-15 (a) Standard AFM sample [57] (b) AFM image, obtained by scanning over a range of 7 µm x 0.6 µm. Height control of better than 10 nm is achieved. 48

Fig. 3-16. (Top) The layout of a part of the SMM device that is thermally isolated from the vertical and lateral actuators. (Bottom) SEM showing thermal de-coupling. 50

Fig. 3-17. Layout of an SMM device with isothermal scanner design with 4 chevron actuators. 51

Fig. 3-18. SEM image of an SMM with isothermal scanner design. 52

Fig. 4-1. Block diagram of the SMM system, which includes; tip-sample interaction, SMM device fabricated with CMOS-MEMS technology, the matching network and the measurement system. 54

Fig. 4-2. (Top) SMM device and its components, and (bottom) and SEM image of wire bonded device. 56

Fig. 4-3. Series resonator loaded with a small capacitor ΔC 57

Fig. 4-4. Stub matching connected to a small capacitor ΔC. L_1+L_{stub} (grey TLs) makes a resonator. 59

Fig. 4-5. Comparing equation (4-8) simulated in MATLAB, with circuit simulations using a standard transmission line model in ADS. Solid-line: MATLAB simulation, Asterisks: ADS circuit simulation points. 60

Fig. 4-6. Sensitivity of a system with two transmission lines connected together. 60

Fig. 4-7. Voltage and current distribution along a quarter lambda transmission line resonator. 61

Fig. 4-8. Half lambda plus shunt 50 ohm (λ/2+50Ω) matching method used by Keysight Technologies. 63

Fig. 4-9. HFSS simulation of a stripline micro-TL and the tip-sample interaction, SEM image of the tip and the tip-sample circuit model. 66

Fig. 4-10. Cross-section of some possible micro-transmission lines in teh CMOS-MEMS process. 68

Fig. 4-11. Finding properties of a transmission line from 2-port full-wave simulation. 70

Fig. 4-12. Microstrip micro-TL and its circuit model. 72

Fig. 4-13. Rectangular coax micro-TL. Top left: real and imaginary parts of characteristic impedance. Top right: propagation and attenuation constants. Middle left: inductance and resistance per unit length of the micro-TL model. Middle right: Capacitance and conductance per unit length of the micro-TL model. Bottom left: E-field at the cross-section of the micro-TL (HFSS simulation). Bottom r: H-field at the cross-section of the micro-TL

(HFSS simulation). 74

Fig. 4-14. Microstrip micro-TL. Top left: real and imaginary parts of characteristic impedance. Top right: propagation and attenuation constants. Middle left: inductance and resistance per unit length of the micro-TL model. Middle right: Capacitance and conductance per unit length of the micro-TL model. Bottom left: E-field at the cross-section of the micro-TL (HFSS simulation). Bottom right: H-field at the cross-section of the micro-TL (HFSS simulation). 75

Fig. 4-15. Slotline on M1 layer micro-TL. Top left: real and imaginary parts of characteristic impedance. Top right: propagation and attenuation constants. Middle left: inductance and resistance per unit length of the micro-TL model. Middle right: Capacitance and conductance per unit length of the micro-TL model. Bottom left: E-field at the cross-section of the micro-TL (HFSS simulation). Bottom right: H-field at the cross-section of the micro-TL (HFSS simulation). 76

Fig. 4-16. Real part of the characteristic impedance for some of the micro-TLs. 78

Fig. 4-17. Effective relative permittivity for some of the micro-TLs. 78

Fig. 4-18. Quality factor ($\beta/2\alpha$) for some of the micro-TLs. 79

Fig. 4-19. Sensitivity figure of merit for some of the micro-TLs. 79

Fig. 4-20. Test structure for comparing different micro-TLs. 81

Fig. 4-21. (Top) CPW structure scaled 400% in vertical direction. (Middle) CPW complete model. (Bottom) EM simulation (red dashed line) and Circuit Model (blue solid line). 83

Fig. 4-22. CPW on M4 layer. Top left: real and imaginary parts of characteristic impedance. Top right: propagation and attenuation constants. Middle left: inductance and resistance per unit length of the micro-TL model. Middle right: Capacitance and conductance per unit length of the micro-TL model. Bottom left: E-field at the cross-section of the micro-TL (HFSS simulation). Bottom right: H-field at the cross-section of the micro-TL (HFSS simulation). 84

Fig. 4-23. CPW test structures with Silicon underneath etched for reducing substrate losses. 85

Fig. 4-24. Slow-Wave CPW structure and its circuit model. (The side view is scaled in vertical direction for better visualization). 87

Fig. 4-25. CPW on M4 with floating M1 stripes. Top left: real and imaginary parts of characteristic impedance. Top right: propagation and attenuation constants. Middle left:

inductance and resistance per unit length of the micro-TL model. Middle right: Capacitance and conductance per unit length of the micro-TL model. Bottom left: E-field at the cross-section of the micro-TL (HFSS simulation). Bottom right: H-field at the cross-section of the micro-TL (HFSS simulation). 88

Fig. 4-26. Comparison of attenuation constant (α) between different TLs for bond pads. 89

Fig. 4-27. Comparison of characteristics impedance (Z_0) between different TLs for bond pads. 89

Fig. 4-28. ADS simulation to compare different bond pad transmission lines. 90

Fig. 4-29. CPW transition and its EM simulation. 91

Fig. 4-30. Microwave path from bonding pads to the tip. Side view is scaled in the vertical direction for better visualization. 92

Fig. 4-31. Bond-wires from either CPW or slotline bonding pads to the PCB board, simulated in HFSS. 93

Fig. 4-32. Return loss measurement and circuit simulation comparison for a CMOS SMM. Smith chart, phase and magnitude of S_{11} is shown for two different measurements and corresponding circuit model. 94

Fig. 4-33. (a) Typical impedance of an SMM device over frequency range of 1-20 GHz taken with PNA-X on an RF probe station. (b) SEM of the SMM device; impedance is measured from GSG pads. 95

Fig. 4-34. Left: Stub matching of a typical SMM impedance at 5 GHz on a Smith chart. Right: HFSS simulation of the entire structure including matching network, bond-wires, CPW lines and micro-TL. 96

Fig. 4-35. Simulation and measurements results for the matching network, connected to the device. Simulation in HFSS. 97

Fig. 4-36. PCB layout and picture of some of manufactured PCBs. 98

Fig. 4-37. Matching with transmission line on PCB and parasitic component of an SMD capacitor. 98

Fig. 4-38. Change in S_{11} vs. change in load when the CMOS-MEMS SMM is matched with (a) a single-stub line and (b) when it is matched with $\lambda/2+50\Omega$ method. 101

Fig. 4-39. Thermal noise effect of the device and detection circuit on the output noise. 103

Fig. 4-40. High sensitivity measurement system. The modules of the system are shown in Appendix C. 103

Fig. 4-41. Budget analysis for the SMM measurement system. P_{in}: Microwave Source power, RL: Return loss from the matching network, Δf: tapping frequency, K: constant depending on SMM design, A_{RF}: RF gain, CR_m: Mixer conversion loss, C: Cancellation of common signal. 104

Fig. 4-42. Effect of phase noise at the output of the mixer. 105

Fig. 5-1. (a) SMM probe with CPW pads and electrothermally actuated sample scanner. (b) Unshielded SPM probe design suspended over the edge of the die for scanning of off-chip samples. (c) Close-up of shielded SPM probe design with on-chip sample positioning. (right) The tip-sample approach curve for SMM. Inset figure shows FEA simulation of field distribution in tip-sample region for unshielded geometry. 108

Fig. 5-2. (a) System diagram for SMM measurements. From left to right: 50-ohm termination represents the PNA input impedance. Coax lines are a single-stub matching network. A simplified model of the tip sample interaction is on the right side. (b) Measurement frequency should be close to the matched point (m1). 109

Fig. 5-3. (a) CMOS-MEMS 3 DOF integrated AFM-SMM device. A CPW to flexible rectangular coaxial line transition connects the microwave signal to the tip. Actuators are used to bend the waveguide and scan the tips. (b) Data comparing intermittent contact with copper to parasitic signal from electrothermal actuation in air. 110

Fig. 5-4. (a) Forward and reverse scans of a region of a CMOS chip. Arrays of aluminum vias on the sample were exposed with a SiO2 etch step. (b) Arrays of aluminum via holes on a CMOS chip that was exposed with a SiO_2 etch step and used as a sample for our device. 111

Fig. 5-5. (a) CMOS-MEMS SMM assembled on a daughter-board with stub matching and RF connector. (b) SMM with daughter-board mounted on a stage (stage from [28]). Sample stage moves up and down with a motor. 112

Fig. 5-6. DVD: 740 nm spacing between successive lines and minimum of 400 nm between the pits. 113

Fig. 5-7. Simultaneous AFM/SMM image of DVD pits imaged with an early version of SMM in a scan area of 7 µm x 7 µm taken with an early version of the SMM. 113

Fig. 5-8. Simultaneous AFM/SMM image of DVD pits with the latest SMM device with better sensitivity, less noise and more range of motion: 13µm x 13µm scan area. 114

Fig. 5-9. Simultaneous AFM/SMM image of repeated 22nm Intel Ivy Bridge SRAM cells with exposed contact pads: some areas of doped silicon is visible in the SMM image but not in the AFM image. Features are less than 200 nm in width and approximately 5 to 10 nm tall. 114

Fig. 5-10. Simultaneous AFM/SMM image of two different areas of repeating SRAM unit cells. SMM images show more detailed features of the sample compared to AFM. 115

Fig. 5-11. Simultaneous AFM/SMM image of carbon nanotubes on a glass slide. (a) SMM amplitude, (b) AFM amplitude, (c) SMM phase and (d) AFM phase. 116

Fig. 5-12. Simultaneous AFM/SMM image of graphene nano-flakes. (a) SMM amplitude, (b) AFM amplitude, (c) SMM phase and (d) AFM phase. 117

Fig. 5-13. SMM sample: Grids and stripes of silicon nitride and SU-8, repeated with different pitch in a total area of 500 µm x 500 µm. Two sets were fabricated: with and without a thin layer of HfO_2. 118

Fig. 5-14. Fabricated SMM samples: 0.5, 1, 2 and 5 µm grids and stripes in a 500 µm x 500 µm area.. 119

Fig. 5-15. HFSS simulation structure for the grid sample with a thin layer of oxide on top... 119

Fig. 5-16. Simultaneous SMM and AFM images of the 5 micron grid without HfO_2 on top. SMM reveals images with more contrast between the two regions. Scan area: 17 µm x17 µm. 120

Fig. 5-17. Simultaneous SMM and AFM images of the 5 micron grid with HfO_2 on top. SMM can image buried samples. 120

Fig. 5-18. Simultaneous SMM and AFM images of the 5 micron grid without HfO_2 on top... 121

Fig. 5-19. Simultaneous SMM and AFM images of the 5 micron grid with HfO_2 on top. 121

Fig. 5-20. Simultaneous SMM and AFM images of 5 µm stripes without the HfO_2 layer on top. 122

Fig. 5-21. Simultaneous SMM and AFM images of 2 µm stripes with 20 nm of HfO_2 on top. Flat AFM, but clear stripes in SMM. 122

Fig. 5-22. Simultaneous SMM and AFM images of 2 µm stripes with 20 nm of HfO_2 on top. Flat

AFM, but clear stripes in the SMM image. 123

Fig. 6-1. Block diagram of a feedback oscillator employing a resonator for frequency stabilization. Square open-loop resonator with an active feedback loop for loss compensation [75]. 125

Fig. B-1. Comparing different quality factors for a microstrip micro-TL with 700 µm. 139

Fig. B-2. Actual Q factor for some of the micro-TLs. 139

Fig. C-1. Baseband Amplifier design, and Circuit. Bottom: Layout and fabricated BB amp. 141

Fig. C-2. Baseband Amplifier measurements and simulation results. 142

List of Tables

Table 4-1. Overall quality factor due to individual Q factors when two different transmission lines are connected to make a quarter lambda resonator 62

Table 4-2. Convergence table for HFSS simulation of the entire CMOS-MEMS SMM system, showing large errors despite the large number of tetrahedrons. This error is 300 times larger than the required accuracy to capture tip-sample interactions of two different materials. 65

Table 4-3. Comparing overall sensitivity of SMM with different micro-TLs. 81

Table 4-4. Comparing overall sensitivity of SMM with different bond pad TLs. 91

Table 4-5. Comparing the effect of each section of the CMOS-MEMS SMM on the overall sensitivity. 100

List of Acronyms

AFM	Atomic Force Microscope
SMM	Scanning Microwave Microscope
SPM	Scanning Probe Microscope
STM	Scanning Tunneling Microscope
TL	Transmission Line
Micro-TL	Micro-Transmission Line
CPW	CoPlanar Waveguide
MEMS	Micro-Electro Mechanical Systems
CMOS	Complementary Metal Oxide Semiconductors
RIE	Reactive Ion Etching
SiO_2	Silicon dioxide
HfO_2	Hafnium dioxide
RF	Radio Frequency
LNA	Low Noise Amplifier
TSMC	Taiwan Semiconductor Manufacturing Company
HFSS	High Frequency Structure Simulator
ADS	Advance Design System
TSMC	Taiwan Semiconductor Manufacturing Company

Chapter 1
Introduction

The Scanning Microwave Microscope (SMM), as one of several instruments that offer Scanning Probe Microscopy (SPM) techniques, is used for surface imaging and for providing information about atomic structure and material properties. SPMs are the highest resolution instruments capable of imaging and patterning materials at the sub-micrometer to nanometer-length scale. The fundamental importance of scanning probe techniques is evidenced by the large number of imaging modalities that have been developed to study structural, topographic, electronic, magnetic, and other properties of samples. The SMM (also known as Scanning Near-field or Scanning Evanescent Microwave Microscope) is the most well-known type of SPM that can quantify local dielectric and conductivity of materials. It has emerged as the most promising means for fast, non-contact, and non-destructive study of materials and semiconductor devices.

SMM operation is based on the near-field reactive loading of an electrically small antenna probe by the sample of interest, where both probe dimensions and probe-to-sample spacing are much smaller than the free-space wavelength. The spatial resolution that can be achieved using this technique is dictated by the distance from the antenna to the sample and the size of the antenna probe tip, rather than the wavelength of the microwave signal.

The fundamental physics of microwave microscopy are as follows. In the microwave frequency region, connecting a microwave (or an RF) source to a metal tip with a sharp curvature of radius $R_0 << \lambda$ will generate evanescent waves whose wave vectors can go up to $k_r \sim 1/R_0$, with a spatial resolution power given by $\sim R_0$. These evanescent waves only exist near the metal tip and decay exponentially away from the surface. Interaction between the metal tip and a sample will change the field configuration near the tip [1].

1.1 Motivations

An SMM provides many unique measurement and imaging capabilities that are not afforded by other existing SPMs. For example, an SMM can be used to map variations in the resistivity and permittivity or permeability of materials simultaneously over a wide range of frequencies. Since the microwave scans can be performed at many different frequencies, and both the magnitude and phase of the signal can be used to construct images, multi-frequency and multimodal images can be constructed to obtain additional information regarding embedded structures, material properties, and non-uniformity [2].

As traditional measurements require large, pure, and homogeneous samples, part of the motivation to employ an SMM is prompted by the deficiencies of traditional far-field measurements. In addition, there is an increasing need to examine new physics in nanometer-length scales that are present in highly correlated electron systems and biological systems. Also prompting studies in this field are technologically motivated investigations of semiconductor and other functional materials at the nanometer scale [3]. On the practical side, state-of-the-art microelectronics and telecommunication devices all operate at gigahertz frequencies, creating a huge interest in understanding material properties in the microwave regime [4]. Furthermore, compared to the atomic force microscope (AFM) and scanning tunneling microscope (STM), the long-range electrostatic-like force involved in the SMM relieves the stringent requirement of proximal probes, thus enabling high-speed, noncontact, and non-destructive measurements [1].

Scanning capacitance measurements of semiconductors is one promising application of SMM. Usually, an insulating oxide layer of a few angstroms grows on semiconductors like Si or GaAs due to oxygen exposure; from the conductive AFM tip and the semiconductor, a metal-oxide-semiconductor (MOS) system is formed. For a given tip bias, the width of the space charge region is also a function of the charge carrier density in the semiconductor, which in many cases is approximately the concentration of impurity donor or acceptor atoms, i.e., the dopant concentration. Measuring the capacitance difference ΔC of the tip-sample

interface and its variation with an applied tip-sample bias is an important extension for the electrical characterization of semiconductors (referred to as dC/dV imaging). Calibrated SMM enables two-dimensional mapping of the carrier density across different regions of a semiconductor, with applications in the failure analysis, characterization and performance modeling of semiconductor devices, as well as dopant and carrier profiling [5], [6]. Recent developments in resolution and the extension to other semiconducting materials (SiGe, Ge, InGaAs, InP, etc.) has led to a strong growing interest from the semiconductor community for the characterization of advanced structures [7].

Further motivations for research into SMMs span interdisciplinary fields. For instance, SMMs can find buried defects and determine characteristics of buried materials because of the penetration depth of microwave signals, which is a unique capability of SMMs [8]. As well, [9] has shown an important application of scanning microwave microscopy for the single-grain-boundary characterization of metallic ferromagnetic (FM) thin films, which provides a unique opportunity for integrated radiofrequency (RF)/microwave magnetic devices such as antennas, filters, inductors, etc., at radio and microwave frequency ranges.

Overall, then, SMMs show significant promise for numerous applications across several fields. Moreover, with the advent of new technologies and applications of different materials in the microwave regime, there will be a growing demand for this type of microscopy.

1.1.1 CMOS-MEMS Fabrication Process

Conventional SPMs need bulky piezoelectric scanners that are susceptible to vibration and drift due to their large size (several orders of magnitude) compared to the small steps of the scanners. Moreover, these large piezoelectric scanners can be very expensive. Also conventional AFMs, as the most well-known SPM, use a laser system that requires alignment and very sensitive detection, which is again bulky and expensive. CMOS-MEMS fabrication replaces external bulky scanners with integrated MEMS actuators that are small and immune to vibration and drift. In this work, electrothermal MEMS actuators are utilized to move the

probe in x, y and z directions. Furthermore, the availability of polysilicon layers on CMOS processes allows for piezoresistive position sensing integrated on a chip, negating the need for bulky and expensive laser systems. Fig. 1-1-(a) shows a conventional commercial atomic force microscope with the illustration of the external scanners and laser system compared to an integrated single-chip AFM fabricated with CMOS-MEMS technology in a total area of $\simeq 1mm^2$ [10].

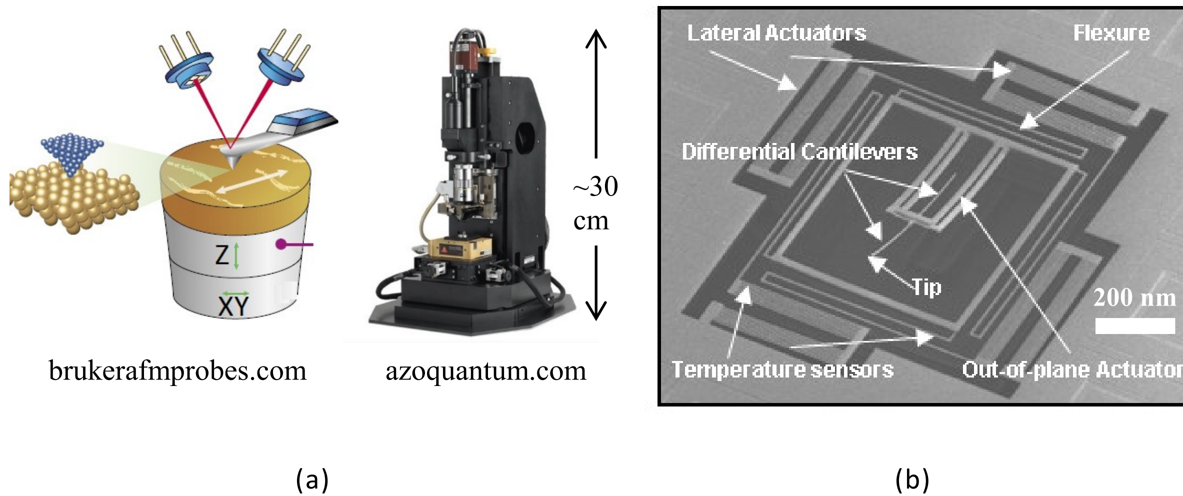

Fig. 1-1. (a) Conventional commercialized AFM and 3-D scanner with laser alignment system. (b) A single chip AFM with piezoresistive position sensing and on-chip MEMS actuators for scanning [10].

1.2 Objectives

The objective of this thesis is to develop a high resolution, high sensitivity chip-scale SMM with on-chip 3 degrees of freedom (DoF) scanners, integrated with AFM, so that the entire system is capable of measuring both topographical and electrical properties of a broad range of samples. Based on this goal, the stages of this research will proceed as explained in the following sections.

1.2.1 Integration of a fully 3D scanner on the probe

Fully 3D scanners using MEMS electrothermal actuators are integrated on the same chip as the SMM using CMOS-MEMS technology. For vertical actuators, bimorphs are used, and for lateral actuators, multi-morphs and chevron actuators are used. These actuators reduce the size of the SMM to the same order of the sample and also significantly reduce the total cost. Moving the microwave probe with electrothermal actuators causes changes in the reflected signal due to device movement and changing temperature; so some decoupling techniques and modes of operation are used to mitigate these effects.

1.2.2 Systematic analysis for improving the sensitivity of CMOS-MEMS SMM

CMOS-MEMS SMM has the benefit of being smaller and cheaper. However, being fabricated on CMOS and integrated with the scanning actuators, it suffers from higher loss both in silicon and conductor material. Therefore, the sensitivity analysis and improvement of the entire SMM system is an essential task. A systematic analysis based on the quality factor of transmission lines is presented for the sensitivity analysis and design of the SMM system. Accurate circuit models are derived for different sections of the SMM and different designs are compared to achieve the best performance. A measurement circuit is also presented and explained to minimize noise and detect small signals from tip-sample interaction. Most of the analysis and suggestions presented can be applied to any Scanning Microwave System or more generally, it can be applied to any microwave sensing system.

1.2.3 Integrating SMM with AFM

The accuracy of any near-field measurement is directly related to the accuracy with which the tip-sample distance can be maintained, and thus it is imperative to keep this distance constant and small. Also, in most applications, it is important to extract both physical

(topographical) and electrical properties of the sample simultaneously. All of this is accomplished in this thesis by combining an SMM (to find the electrical properties of the sample) with an AFM (to find the topographical image of the sample). We show a combined AFM device based on piezoresistive position sensing in the tapping mode (reported in [10], [11]) for closed-loop distance control of our SMM device. Also, a special test sample with no topography but with buried change in materials is designed and tested to highlight the fact that SMM can image buried material not detected by AFM.

1.2.4 Designing novel probes to improve resolution in quantitative imaging.

In order to perform a sensitive high-resolution quantitative measurement, the microwave signal should be confined near the area of the sample to be measured. Therefore, extra care should be taken to design the tip so that the parasitic stray signal between the probe (constructed of a transmission line and a sharp tip) and the medium is minimized. We have designed and tested some shielded transmission lines in the CMOS-MEMS process that shields the microwave path from the surrounding medium up to the probe-tip.

The resolution of any near-field measurement is directly proportional to the curvature of the tip. A tip curvature of around 150 nm is achieved with the standard CMOS-MEMS process without any further processing steps.

1.3 Thesis Outline

Following the motivations and objectives presented in Chapter 1, a comprehensive literature survey on the SMM is provided in Chapter 2, where various types of SMMs as well as current trends and the state-of-the-art of research and practice in this area are described. The theory behind the SMM technique is also discussed in this chapter.

In Chapter 3, after a short review of MEMS SPMs, the fabrication process for CMOS-

MEMS is explained, followed by a description of the SMM device. The importance of tip-sample distance control and integration of AFM is then discussed. Finally, some of the design challenges such as thermal coupling to the microwave path and change of reflected signal due to the movement of the tip are discussed and possible solutions presented.

In Chapter 4, CMOS-MEMS SMM is first described from an overall system point of view. Then, with the help of lumped model and EM simulations, the sensitivity of the SMM system is analyzed. Furthermore, a measurement circuit for improving sensitivity is presented and analyzed. It is worth noting that the analyses and suggestions given in this chapter can be applied to any Scanning Microwave System or, even more generally, to any microwave system that needs to sense a small signal.

Chapter 5 features the measurement results. First, some of the preliminary results achieved without the use of the high sensitivity measurement circuit is presented. Then, the imaging results with the help of the measurement system is explained and several samples are imaged. A test sample designed to image buried structures is also explained and imaged with our SMM system.

In Chapter 6, conclusions and suggestions for future work are presented. Some potential approaches for further improvement in SMM sensitivity are suggested.

Chapter 2
Literature Survey

In this chapter, a short history of SMM is first presented, starting with the seminal paper of Synge that overviews the Scanning Microwave Microscopy. Then, a brief review of AFM and STM is presented. After that, various types of SMM are reviewed, followed by descriptions of some tip-sample distance control methods, which are crucial in SMM operation. At the end, theoretical analyses of conventional SMMs in the literature are summarized and some FEM simulation results for the conventional SMMs are presented.

2.1 History

In 1928, Synge realized that there was a fundamental limit to optical imaging. Predicting that the extreme resolution limit would be 0.05 μm, he suggested a method which is now known as Scanning Near-Field Microscopy [12]. Due to practical limitations at that time, Synge could not show the idea but did surmise that resolutions of 0.01 μm would be possible if these four limits could be overcome:

1. The source of illumination must be high intensity in order for evanescent fields to appreciably interact with the sample.
2. Motion control should be on the order of 10^{-6} cm laterally and 10^{-7} cm vertically.
3. Planarity of the target should be on the order of 10^{-6} cm.
4. Construction of the small probe structure should be on the order of 10^{-6} cm.

In his paper, Synge mentioned that a “distinguished physicist” suggested the idea to him; today, we know that this distinguished physicist was Albert Einstein [13].

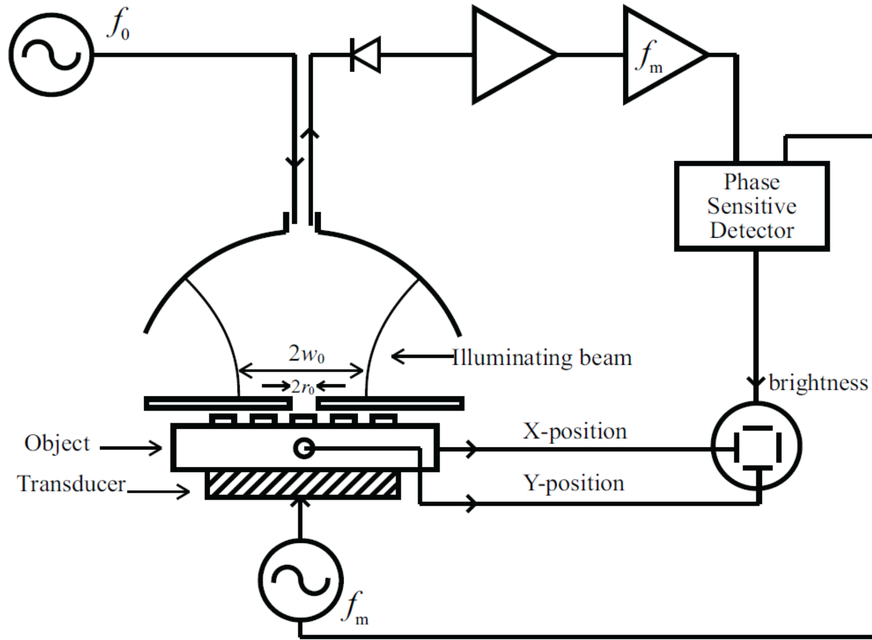

Fig. 2-1. Ash and Nichole's proposed SMM: A 10GHz oscillator excites a hemispherical resonator which is loaded by a subwavelength aperture of diameter 1.5 mm [16].

Building on Synge's earlier research, Frait [14] in 1959 and Soohoo [15] in 1962 showed the first near-field microwave microscopy for measuring magnetic properties of material around 10 GHz by opening a 500-µm hole in a resonator as an aperture and bringing the sample almost in touch with the hole. Despite these achievements, the first *scanning* near-field microwave microscopy was not developed until 1972, by Ash and Nicholls [16]. They showed that the Abbe barrier for resolution ($\lambda_0/2$), which was previously thought to be the resolution limit, could be broken in near-field, and that the resolution in near-field is determined by the size and geometry of the probe rather than wavelength. They demonstrated 0.5 mm spatial resolution with a sub-wavelength aperture in a 10 GHz (λ_0=3 cm) resonator (Fig. 2-1); this λ/60 resolution was achieved for metallic features. They also resolved an edge between two different dielectric materials with their system.

2.1.1 STM and AFM

In 1981, Scanning Tunneling Microscope (STM) for measuring nano-scale metal surfaces

was invented by Gerd Binning and Heinrich Rohrer at IBM. The STM mode of operation is straightforward: an extremely sharp tip (ideally atomically sharp) is placed into close proximity with a conductive substrate and a voltage is applied between the probe tip and substrate. Then, the gap between the two is decreased until electrons are passed from one to the other. A current magnitude is exponentially dependent on the distance between the tip and the sample. Once the tunneling of electrons occurs, the tip is then scanned across the sample and current levels are recorded as a function of location, resulting in a topographical map of the surface. There are two main modes for STM: constant current and constant height. The inventors of STM received the Nobel Prize for in 1986. That same year, the Atomic force Microscopy (AFM) was invented by Gerd Binning, Calvin Quate, and Christopher Gerber to expand the types of surfaces on which atomic scale information can be obtained (it also works for non-metal surfaces). These two techniques gave birth to a family of related techniques called Scanning probe microscopy (SPM) that provide information about atomic scale structure and processes. SPM's are widely regarded as the workhorse instruments of nanotechnology.

2.2 Various SMMs

SPM techniques such as the STM, AFM, scanning capacitance microscope (SCM), magnetic force microscope (MFM), and scanning thermal microscope (SThM) operate with sensing signals far below 1 GHz. Other probes, such as near-field scanning optical microscope (NSOM), operate with sensing signals in the optical regime (300–750 THz: 400–800 nm). However, between NSOM and AFM/STM techniques, there is a very large frequency gap (Fig. 2-2). Scanning microwave microscope (SMM) with possible sensing signals from 0.1 to 140 GHz bridges this gap between the existing local probe microscopy systems [17].

All earlier versions of SMM were aperture-based probes. Waveguide or aperture-based SMMs suffer from attenuation when they work below cut-off frequency; in these types of SMM, a linear improvement in resolution results in an exponential reduction in sensitivity.

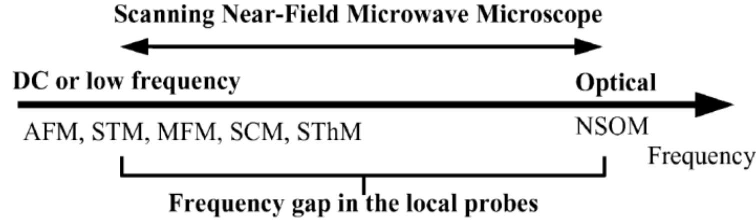

Fig. 2-2. Frequency spectrum for different scanning probe microscopy techniques. SMM bridges the frequency gap between the existing local probe microscopy systems [17].

As there is no cut-off frequency in a transmission line, coaxial transmission line probes have much better performance than aperture or waveguide probes [1]. An open-ended coaxial probe was first proposed by Fee et al. [18], who achieved a resolution of λ/4000.

Coaxial probes became one of the most famous types of SMM. Anlage's group at the University of Maryland used a λ/2 coaxial transmission line with a sharp tapered tip protruding from the open end, while the other side was capacitively coupled to a microwave source (Fig. 2-3)[19]–[21]. Frequency shift and changes in quality factors of the coaxial resonator were used to find electrical properties (dielectric constant and loss tangent or resistivity) of material. This type of SMM was also used to find topography images of metallic surfaces [22]. For the tip- circuit interaction, they used a feedback loop, and FM modulated the microwave source at a low frequency to disentangle frequency shift and quality factor parameters. A $2f_{FM}$ lock-in measures the curvature of the $V_{diode}(f)$ curve, and gives an output that can be related to the quality factor of the resonator, Q.

Although using a sharp tip concentrates the evanescent field close to the end of the tip, but because of far-field interaction between the propagating field and sample (non-tip-end interaction with sample), the characteristic dimension (and consequently the quantitative resolution) is set by the separation between the tip and the outer coaxial conductor, which is typically a few hundred microns [23]. Therefore, several shielding methods have been proposed for this type of SMM, which will be described later.

Concurrently, another group at Berkeley used coaxial resonator as the SMM probe, but they closed the open side of the coaxial resonator (here it is λ/4 because one side is short and

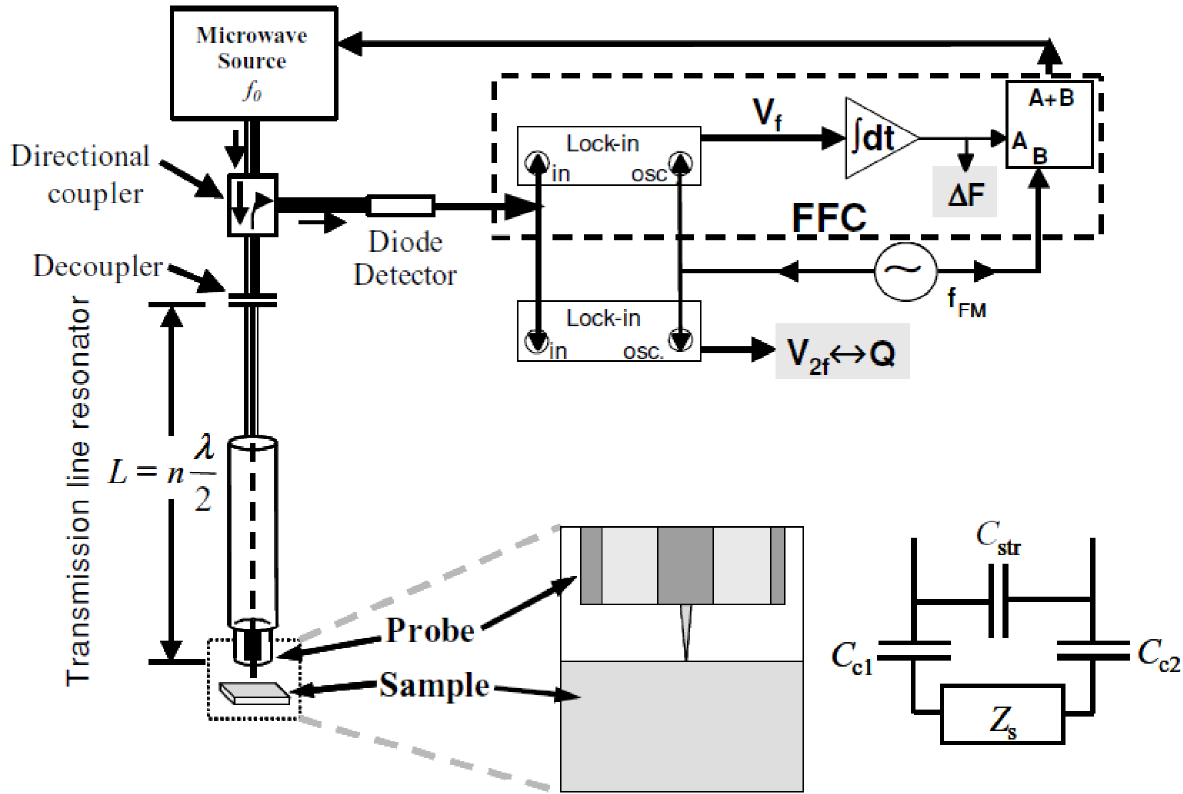

Fig. 2-3. Schematic of the scanning near-field microwave microscope. The insets show a close view of the coaxial probe, sample, as well as a lumped element circuit model for the tip-sample interaction [3].

the other side is open circuit) and opened only a small area for the tip. In this way, the electrical field will be confined near the tip and parasitic capacitance will be reduced, which increases measurement sensitivity[24]–[26]. The researcher used a sapphire disc of 100-200 μm diameter and coated the outer area of the sapphire disc to prevent far-field radiation as shown in Fig. 2-4. In this configuration, the f_r shift and Q are determined by measuring the error signal of the phase-lock-loop and the amplitude of the output signal of the resonator using a diode detector, respectively [25]. A resolution of 10 nm was achieved.

V.V. Talanov et al., rather than attempting to shield the parasitic “stray fields” inherently present in unbalanced geometries with a sharp tip, proposed a microfabricated balanced stripline oriented perpendicular to the sample [23] (Fig. 2-5). With electrode spacing at the tip $D \approx 1$–10 μm the fields are largely confined between the two electrodes and therefore the characteristic probe dimension is on the order of D. The parallel strip resonator tip confines

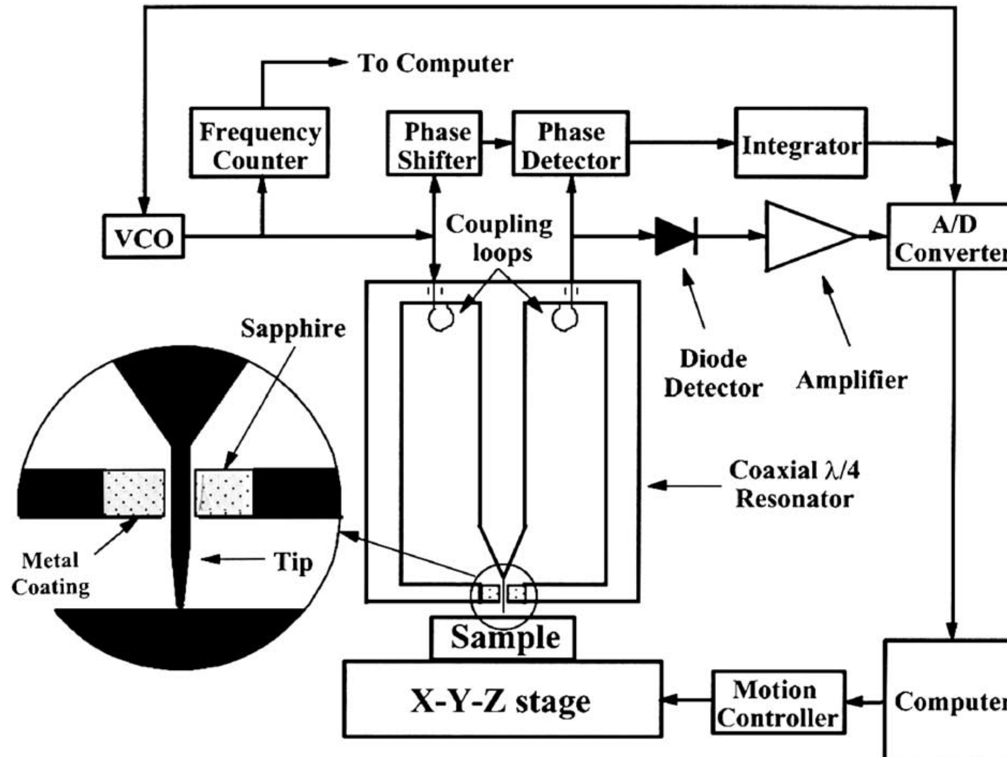

Fig. 2-4. System Configuration for the SMM system proposed in [28] (details in the text).

the evanescent electric field more than 99% locally, which is crucial in some applications such as electrical metrology on semiconductor production wafers or combinatorial materials libraries. For this probe, they also reported a quantitative model and measurement of low permittivity thin film materials on semiconductor wafers [27].

M. Tabib-Azar et al. worked on characterization of different materials using a capacitively coupled microstrip resonator and a tapered sharp tip, with which they formed both magnetic and electric dipoles. An electric dipole is shown inFig. 2-6.(a),(b); for a magnetic dipole, they connected the signal to the ground using a thin piece of wire [29]. In their first paper, the researchers reported 100-150 μm resolution. Later, by using a stripline resonator for better shielding and a chemically etched sharp tip and tip-sample distance modulation, they achieved 0.4 μm resolution [2]. They also used a lumped element model for the transmission line and for the tip-sample interaction (for dielectric and metallic samples), as shown in Fig. 2-6.(c), (d). In their next paper, they integrated a conventional AFM with their SMM and

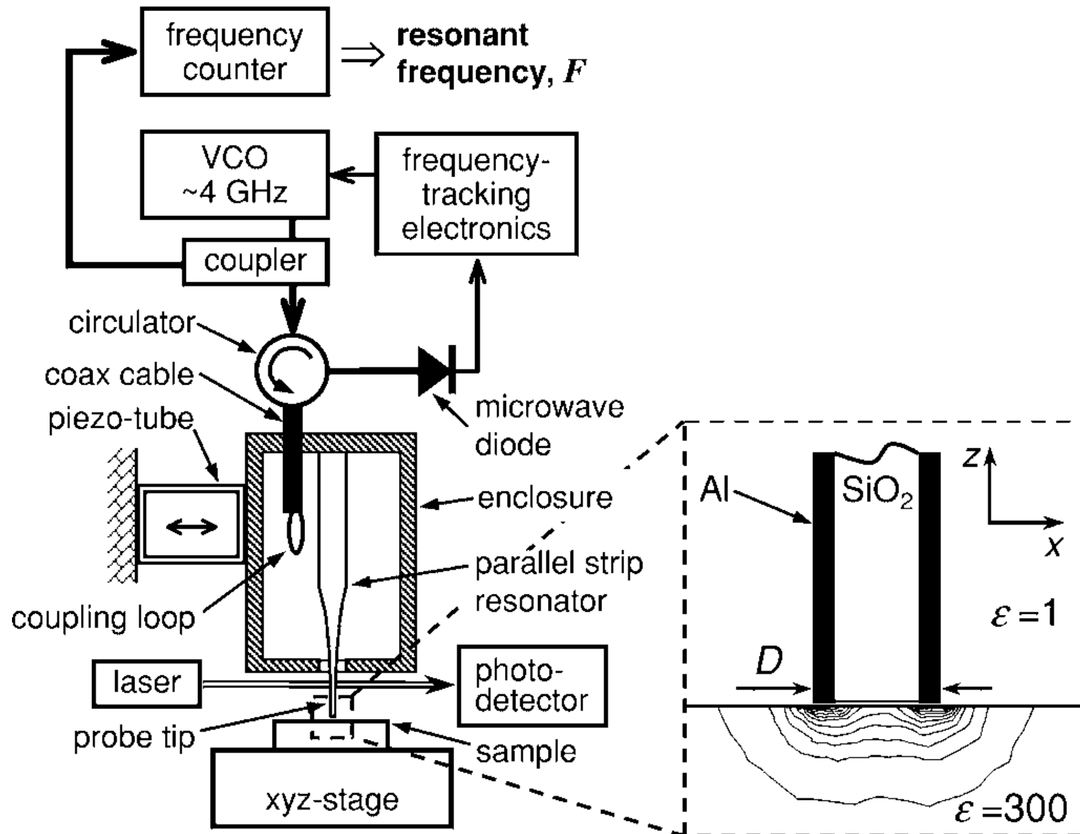

Fig. 2-5. Apparatus schematic showing the probe, electronics, and shear-force setup. Note that in reality the laser beam is oriented perpendicular to the direction of enclosure dithering. Insets: intensity contour plots of the fringe E field in the xz lane for bulk samples with εr=300; the tip-sample distance is 100 nm, D=4 μm [23].

also used a micro-machined coaxial transmission line [17].

At Stanford, Lai et al. introduced a type of SMM that is combined with AFM. In their first paper, they used a coplanar waveguide (CPW) cantilever and two probes for excitation and sensing [4]. Later, they used only one probe in reflection mode and shielded the microwave signal using a stripline transmission line. Shielding the transmission line increases sensitivity by decreasing the non-localized tip to sample interaction [30]. In another paper, they described how operating in tapping mode would eliminate thermal and other long time drifts [31]. Here, they used a Lock in Amplifier (LIA) in this mode for better sensitivity. Fig. 2-8 shows the tapping mode operation compared to contact mode for a topography-free sample as well as a schematic of combined AFM/SMM electronics.

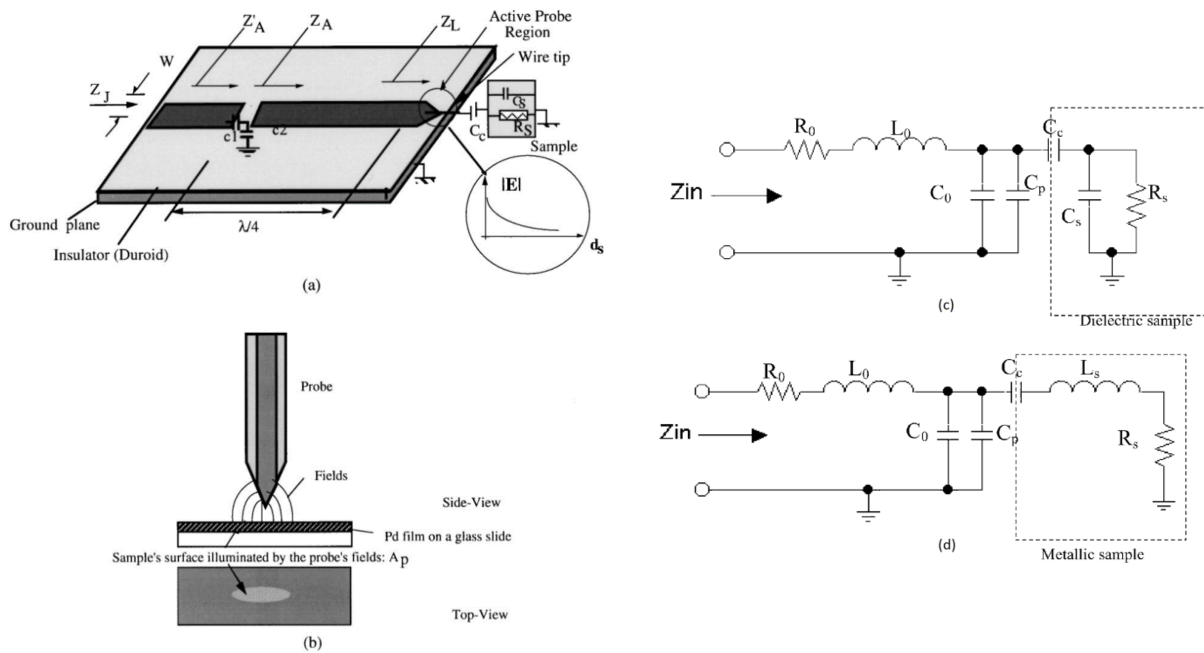

Fig. 2-6. (a) Microstrip-line resonator and probe assembly. Evanescent waves extend out of the tapered tip. (b) Schematic of the probe-sample interaction area. Lumped-circuit model of the waveguide, tip, and sample. A dielectric sample is modeled in (c) and a metallic sample is modeled in (d) [32],[17].

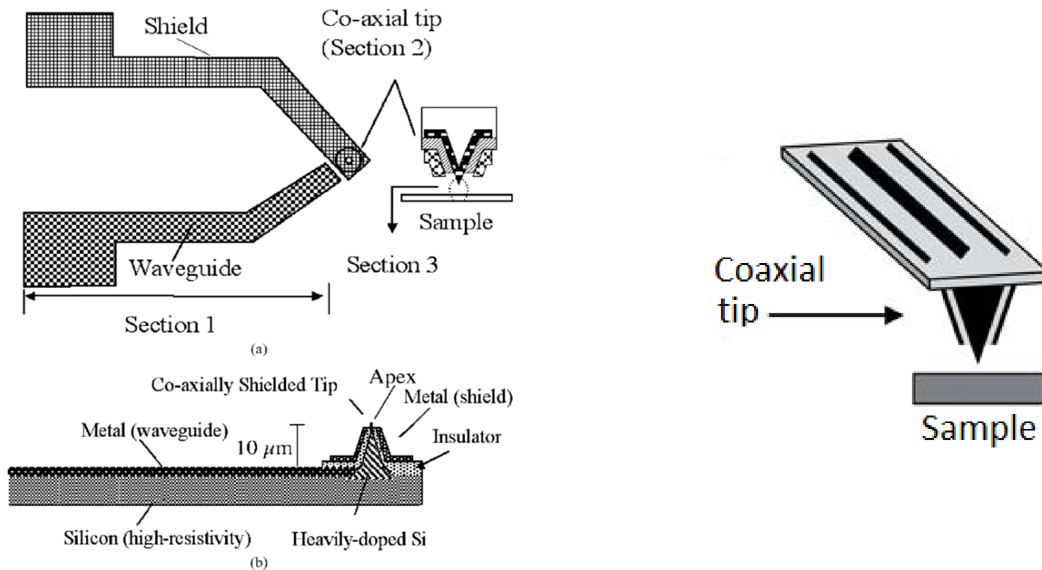

Fig. 2-7. Coaxial probe has two main sections, as shown in (a), consisting of a waveguide section over the “handle” and a cantilever beam followed by the tip section. The tip section consists of a protruding tip apex surrounded by a dielectric layer and a metallic shield layer. The cross-section of the probe is shown in (b) [17].

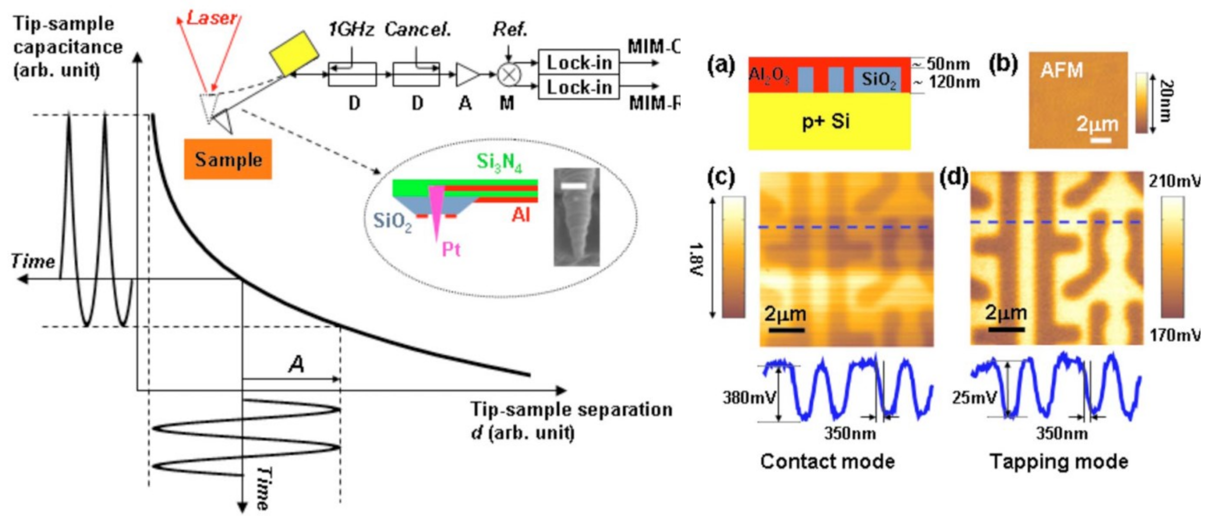

Fig. 2-8. (Left) Tip-sample capacitance as a function of the spacing. As the tip oscillates above the sample surface, the tip impedance is also modulated at the same frequency. The inset shows the schematic of the tapping mode AFM and the microwave electronics (D—directional coupler, A—amplifier, M—mixer), as well as the cantilever structure and the SEM of the Pt tip. The scale bar is 500 nm [31]. (Right) (a) Layer structure of the Al_2O_3–SiO_2 / Si sample. (b) AFM image of the polished sample surface. (c) Contact and (d) tapping mode MIM-C images taken by the same tip at the same area. The darker regions are buried SiO_2. Electronic drift can be observed in (c) but not in (d). Line cuts are shown in both (c) and (d) for comparisons of the signal strength and the spatial resolution [31].

Huber et al. introduced a calibrated SMM integrated with standard AFM based on standard calibration samples for both capacitance and dopant profiling measurements [5], [33], [34]. They used a conductive AFM tip in contact mode, shielded it for decreasing stray capacitance, and combined it with a Performance Network analyzer (PNA). A half lambda coaxial transmission line terminated with a 50-ohm shunt resistor is used to bring the high tip-sample impedance close to that of a PNA. To determine absolute capacitance values from PNA reflection amplitudes, a calibration sample of conductive gold pads of various sizes on a SiO_2 staircase structure was used. The thickness of the dielectric SiO_2 staircase ranged from 10 to 200 nm. The quantitative capacitance values determined from the PNA reflection amplitude were compared to control measurements using an external capacitance bridge. Depending on the area of the gold top electrode and the SiO_2 step heights, the corresponding

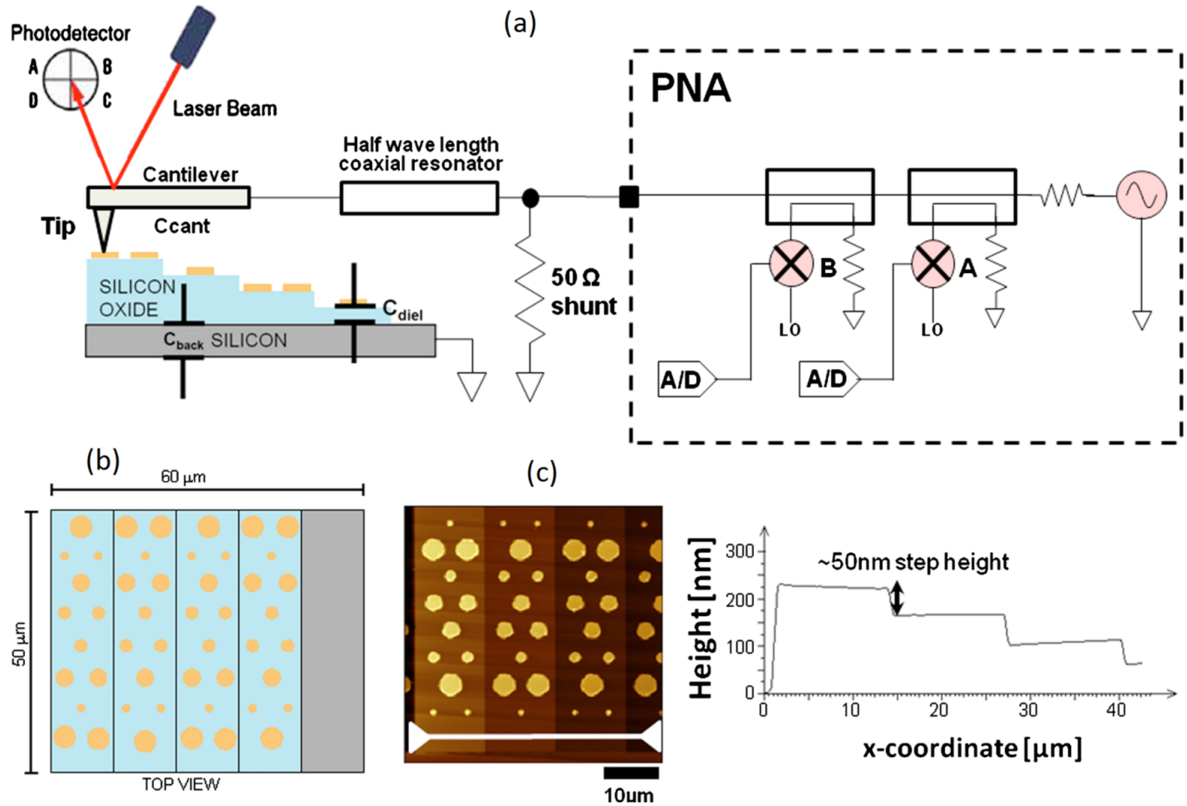

Fig. 2-9. (a) A standard conductive AFM is connected to a performance network analyzer (PNA). A half lambda coaxial transmission line terminated with a 50-ohm shunt resistor is used for matching. (b) Sketch showing the arrangement of gold caps on the four steps of the dielectric staircase structure. (c) Topographical image of the 50 nm stepped calibration sample and profile along the white line [33].

capacitance values, as measured with the SMM (Fig. 2-9).

More recent research on SMM: researchers at IEMN in France reported an interferometric SMM for characterization of capacitors and tunnel junctions [35] Recently, More recent SMMs are reported in. Farina et al. reported a time-domain reflectometry method for SMM [36]. Tselev et al. reported an application of SMM for non-invasive nanoscale imaging in liquid environment [37].

2.3 Tip-Sample Distance Control

One of the strengths of near-field microscopy of any kind is that measurements can be made

without any physical contact between the near-field tip and the sample or device being tested. The precision of any near-field measurement is directly related to the precision with which the tip-sample distance can be maintained, and a good rule of thumb is that the tip should be held reliably at a distance above the sample that is less than one-tenth of the tip size D. The challenge is integration of each technique with a suitable near-field microwave microscopy probe [3]. Imtiaz et al. uses an STM for distance control over metallic samples [38]. The shear-force distance control method, originally applied for NSOM, is used in [23] for SMM.

Several authors have addressed this issue by combining SMM with AFM [31],[17],[40]. Authors in [39] utilized a height modulation distance following technique combined with tapping mode and showed an improvement in both spatial resolution and material property

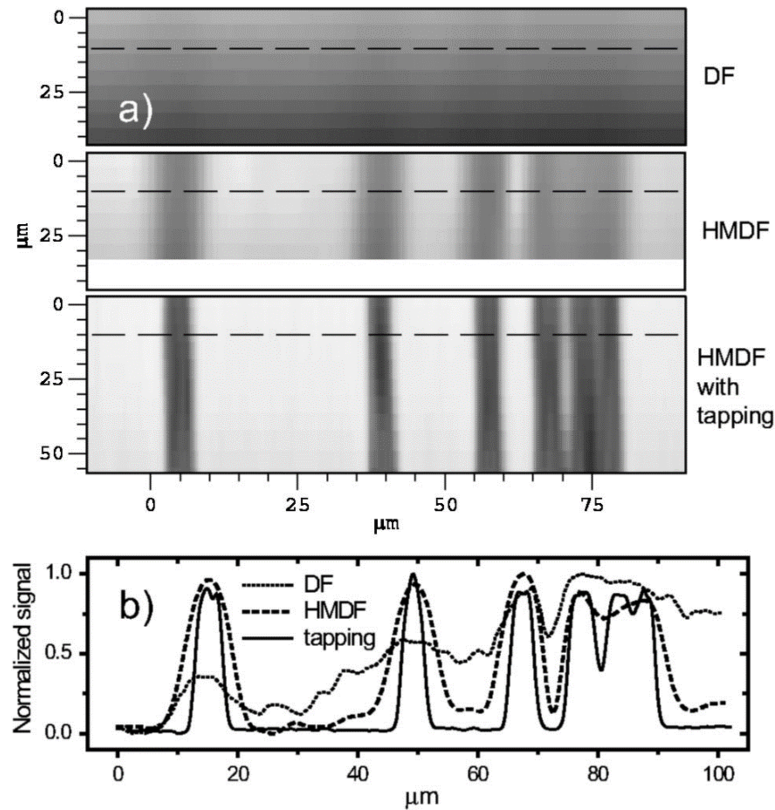

Fig. 2-10. (a) Comparison of images obtained in DF, HMDF and HMDF, with tapping modes from a locally B-doped Si sample. The first two images were taken simultaneously. (b) Line cuts along the dashed lines in the images above [39].

sensitivity (Fig. 2-10). The best result is achieved when the tip is in tapping mode.

2.4 Theoretical Analysis

In this section, two well-known theoretical analyses for SMMs are first discussed. Next, FEM simulation results of these SMMs are given and the proposed SMM probes simulated for comparison purposes.

If electrical properties of the sample such as permittivity and permeability change in near proximity to a near-field probe, detection system parameters such as resonant frequency, quality factor or amplitude and phase of reflection and/or transmission coefficients will likewise change. A theoretical analysis of SMM seeks to find a relationship between measurable system parameters and electrical properties of the sample. Two methods have been described here: The first one is a lumped element model for sample-to-tip interaction, which is very useful and handy for quick system analysis. The second method is a charge image method based on spherical tip and quasi-electrostatic tip-sample interaction assumptions.

2.4.1 Lumped element model for tip-sample interaction [3], [23]

Consider the near-field tip as a two-terminal, linear, passive system (e.g., antenna) connected to the detection apparatus such as a transmission line, LC-oscillator, etc. If the sample is lossless and only the near-zone and/or evanescent field exists beyond the plane of the terminals, then no real power is transmitted into the sample. Such fields store reactive energy, however, and therefore the tip is seen as a reactance by the probe detection circuit. If the sample and/or tip are lossy, then some of this energy dissipates and the impedance gains a resistive part. Thus the interaction between the sample and the probe can be described in terms of the lumped element impedance $Z_t = R_t + iX_t$. Generally, Z_t depends on the tip geometry, the sample electrodynamic properties, and the tip-sample distance. The complex Poynting theorem yields the following expression for the reactance of the near-field tip (i.e.,

electrically small antenna):

$$X_t = \frac{4\omega}{|I_i|^2} \int_V (w_m - w_3) d^3x \tag{2-1}$$

where I_i is the harmonic input current at the tip terminals (such that input voltage $V_i = Z_t I_i$), $W_m = \boldsymbol{B} \cdot \boldsymbol{H}^*/4$ and $W_e = \boldsymbol{E} \cdot \boldsymbol{D}^*/4$ are the magnetic and electric energy densities, respectively, and the integral is taken over the entire volume beyond the plane defined by the terminals (i.e., the probe sampling volume). Depending on the dominant type of reactive energy stored in this field, the tip is considered either *electric* or *magnetic*. The real part of the tip impedance, Rt, can be due to conduction losses (Joule heat) and electric and magnetic absorptive dissipation in the sample and/or the tip:

$$R_t = \frac{\omega}{|I_i|^2} \int_V \left(\frac{\sigma}{\omega} |\boldsymbol{E}|^2 + \epsilon_0 \epsilon'' |\boldsymbol{E}|^2 + \mu_0 \mu'' |\boldsymbol{H}|^2 \right) d^3x \tag{2-2}$$

As well as conventional far-field radiation generated by the tip (i.e., radiation resistance) that can often be neglected for most near-field tips. Note that similar expressions can be derived for the tip complex admittance, as well.

2.4.1.1 Impedance of an electric tip

Generically, the impedance Z_{tE} of an electric tip formed by the open end of a two-conductor transmission line (e.g., flush open, terminated with STM tip, etc.), can be represented as a network of the tip-to-sample coupling capacitance $1/C_c = 1/C_{c1} + 1/C_{c2}$, the sample "near-field" impedance Z_s, and the tip stray capacitance C_{str} .

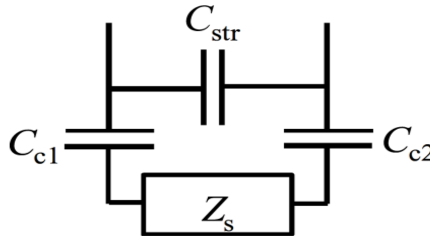

Fig. 2-11. Lumped element circuit model for the tip-sample interaction.

$$(Z_{tE})^{-1} = \left(\frac{1}{i\omega C} + Z_s\right)^{-1} + i\omega C_{str} \tag{2-3}$$

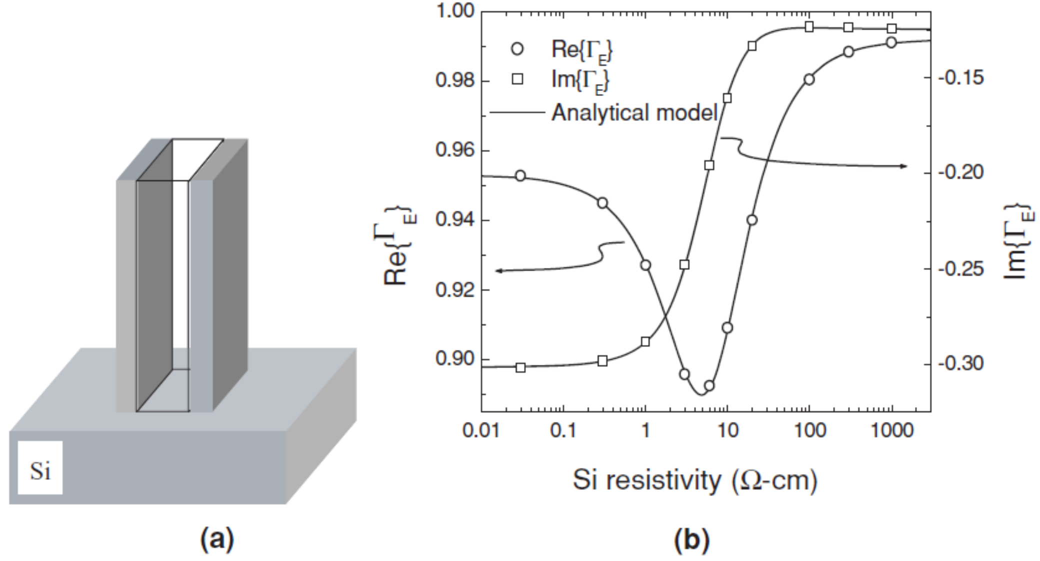

Fig. 2-12. (a) Parallel strip transmission line probe. (b) Comparison of analytical lumped element model and finite element numerical data at 4 GHz for the real and imaginary parts of reflection coefficient [3].

Z_s is due to the energy stored and/or dissipated in the sample under test. Both C_c and C_{str} depend on the tip-sample distance h. To obtain high enough sensitivity to the sample properties (i.e., to make $Z_{tE} \sim Z_s$), it is imperative that both $1/\omega C_c Z_s$ and $\omega C_{str} Z_s$ be much smaller or at least on the order of unity, which can typically be achieved by making $h \ll D$, where D is the characteristic tip size.

Under the above conditions, let us estimate the near-field impedance due to a homogeneous bulk sample, Z_{sb}, while assuming the true near-field situation $|k_s|D \ll 1,\ k_s = \omega(\varepsilon_0\varepsilon_s\mu_0)^{1/2}$. Due to its static nature, the sampling near-field occupies a volume governed by D, and the first integral is on the order of $\varepsilon_0\varepsilon_s|E_0|^2D^3$, where $|E_0| \sim V_i/D$ is an estimate for the average electric field in the sample. Then $Z_{sb} = R_{sb} + \boldsymbol{i}\, X_{sb}$. Therefore, $Z_{sb} = 1 / \boldsymbol{i}\omega\varepsilon_0\varepsilon_s D$, which is basically the impedance of a capacitor with a geometrical capacitance $\varepsilon_0 D$ filled up with material of complex relative permittivity $\varepsilon_s = \varepsilon' - \boldsymbol{i}\varepsilon''$. Let us illustrate this concept for a variety of materials.

Dielectric. If the sample is a low-loss dielectric with $\varepsilon_s = \varepsilon(1 - \boldsymbol{i}\ tan\delta),\ tan\delta \ll 1,$ then the near-field impedance is:

$$Z_{sb} = \frac{tan\,\delta}{\omega\epsilon_0\epsilon' D} - \boldsymbol{i}\frac{1}{\omega\epsilon_0\epsilon' D} \tag{2-4}$$

Its reactive part is capacitive and the probe is sensitive to the sample dielectric constant as well as the loss tangent ($tan\,\delta$).

Semiconductor. At microwave frequencies, semiconductors can exhibit $\varepsilon' \sim \varepsilon'' = 1/\varepsilon_0\omega\rho$, i.e., contributions from the two conduction mechanisms, displacement and physical, are comparable. Then:

$$Z_{sb} = \frac{1}{D/\rho + \boldsymbol{i}\omega\epsilon_0\epsilon' D} \tag{2-5}$$

Therefore, the sample resistance and reactance are of the same order. The sample reactance is again capacitive in this case.

Normal metal. A conductive metal can be characterized by the relative permittivity $\varepsilon_s \approx -\boldsymbol{i}/\varepsilon_0\omega\rho$. Thus, Z_{sb} represents the dc resistance of the tip sampling volume:

$$Z_{sb} = \rho/D \tag{2-6}$$

Unlike the conventional surface impedance of a bulk metal, Z_{sb} has *no* reactive part because the geometrical inductance is negligible in the case of an electric probe. This equation implies that when D is much smaller than the metal skin-depth the probe spatial resolution is governed by the tip size rather than the sample skin-depth. This creates a unique opportunity for near-field microwave microscopy to study just the subsurface portion of the material, unlike conventional far-field techniques that are sensitive to the entire skin-depth layer.

2.4.1.2 Impedance of a magnetic tip

In the case of $|k_s|D \gg 1$, the lumped element impedance of the magnetic tip can be obtained by the method of images:

$$Z_{tM} = \boldsymbol{i}\omega L_0 + \frac{\omega^2 M^2}{Z_s + \boldsymbol{i}\omega L_1} \qquad (2\text{-}7)$$

where L_0 is the loop self-inductance, L_1 is the sample effective inductance, M is the tip-sample mutual inductance (i.e., tip-to-sample coupling), and Z_s is the sample surface impedance. Away from the sample, the tip impedance approaches $i\omega L_0$.

2.4.2 Transmission line model of the probe

When a transmission line terminated with either an electric or magnetic tip forms a near-field microwave probe, the tip-sample system can be treated as a discontinuity in this line. Consider a near-field tip with impedance Z_t terminating the probe transmission line of characteristic impedance Z_0. The impedance of a substantially electric tip should satisfy the condition $|Z_{tE}| \gg Z_0$, while for a substantially magnetic tip $|Z_{tM}| \ll Z_0$. Then the complex reflection coefficient from the electric tip can be found as follows:

$$\Gamma_E = |\Gamma_E| \exp(i\theta_{\mathrm{E}}) = \frac{Z_{tE} - Z_0}{Z_{tE} + Z_0} \cong \exp\left(-\frac{2Z_0 R_{tE}}{R_{tE}^2 + X_{tE}^2}\right) exp\left(\boldsymbol{i}\frac{2Z_0 X_{tE}}{R_{tE}^2 + X_{tE}^2}\right) \qquad (2\text{-}8)$$

and the reflection coefficient from the magnetic tip is:

$$\Gamma_M = |\Gamma_M| \exp(i\theta_{\mathrm{E}}) = \frac{Z_{tM} - Z_0}{Z_{tM} + Z_0} \cong -\exp\left(-\frac{2R_{tM}}{Z_0}\right) exp\left(-\boldsymbol{i}\frac{2X_{tM}}{Z_0}\right) \qquad (2\text{-}9)$$

To obtain the exponential forms in the right-hand side above, the approximation $(1-x) / (1+x) \approx exp(-2x)$ was used, which is better than 1% accurate for $x < 0.25$.

In order to validate the lumped element model, it was compared to results of numerical modeling for the near-field tip geometry and for two types of samples: Si wafers with and without implants. As will be discussed below, both the bulk Si resistivity and the implant sheet resistance were varied. The tip was formed by the open end of a parallel strip transmission line (Fig. 2-12-(a)) that consists of two metallic electrodes supported by a rectangular quartz bar. For the purposes of modeling, the tip size was on the order of 100 μm, and the tip-sample separation was 250 nm. The modeling was performed using HFSS.

To find the reflection coefficient for the case of bulk Si, equation (2-5) was substituted into (2-3) and the result into (2-8), which yields the real and imaginary parts of the complex reflection coefficient as a function of the Si bulk resistivity. These two quantities were also extracted from the FEM. This modeling was performed for a variety of probe sizes, and representative results are shown in Fig. 2-12-(b), where the Si resistivity ranges from 0.01 to 1000 cm.

It is clear that over a wide range of Si resistivities, the analytical lumped element model agrees exceptionally well with the FEM. The two free parameters used to fit the lumped element model to the FEM data are D and C_c, while the characteristic line impedance Z_0 was obtained from 2D modeling of the strip-line cross-section. By fitting data for various tip sizes, they found that the characteristic tip size D was governed by the entire cross-section of the tip. In addition, C_c was found to be in good agreement with the parallel plate capacitor estimate.

2.4.3 Resonant transmission line

To increase measurement sensitivity, many microwave microscopes employ a distributed circuit resonator which reduces the impedance mismatch, $|Z_{tE}| \gg Z_0$ or $|Z_{tM}| \ll Z_0$, between the tip and the probe feed line. Using standard transmission line theory, one can solve for the voltage at any point in the microscope, including an external detector. Such models can include many details of the microscope design and are very successful at reproducing its gross and fine properties. The disadvantage of such models is the lack of clear intuitive analytical expressions for the measured quantities. Here an approach is suggested that provides general analytical expressions relating the sample electrodynamic properties to the probe resonant frequency and Q-factor.The resonant condition of a transmission line resonator can be written as follows:

$$\exp(-\boldsymbol{i}2hL)\,\Gamma\Gamma_0 = exp(-\boldsymbol{i}2\pi n) \qquad (2\text{-}10)$$

where L is the resonator length, $h = h' - \boldsymbol{i}h'' = \omega(\varepsilon_0\varepsilon_{eff}\mu_0)^{1/2} - \boldsymbol{i}h''$ ($h' \gg h$) is the transmission

line complex propagation constant and $\varepsilon_{\mathrm{eff}}$ is the effective dielectric constant of the transmission line, Γ is given by equations (2-8) or (2-9), Γ_0 is the complex reflection coefficient from the resonator opposite end (i.e., short, open, or coupling impedance), and n = 1,2, . . . is the mode number. As an example, consider an electric tip terminating a half-wavelength resonator. Substitution of $\Gamma_0 = 1$ and equation (2-8) into (2-10), using the complex angular frequency $\omega = \omega' + \boldsymbol{i}\omega''$, and separating the real and imaginary parts yields the following expressions for the probe resonant frequency $F = \omega'/2\pi$ and the unloaded Q-factor:

$$F = \frac{\pi n}{2\pi L\sqrt{\epsilon_0 \mu_0 \epsilon_{eff}}}\left[1 + \frac{Z_0 X_{tE}}{\pi n (R_{tE}^2 + X_{tE}^2)}\right] \tag{2-11}$$

$$Q = \frac{\omega'}{2\omega''} = \left(\pi n + \frac{Z_0 X_{tE}}{R_{tE}^2 + X_{tE}^2}\right) \Big/ \left(2h''L + \frac{2 Z_0 R_{tE}}{R_{tE}^2 + X_{tE}^2}\right) \tag{2-12}$$

From equation (2-11), one can find the relative shift in the probe resonant frequency versus change in the tip capacitance C_t for a low-loss sample as follows:

$$\frac{\Delta F}{F} = -\frac{Z_0}{L\sqrt{\epsilon_0 \mu_0 \epsilon_{eff}}}\Delta C_t \tag{2-13}$$

Equation (2-13) provides an estimate for the microscope's sensitivity. For typical probe parameters $L \sim 1$ cm, $Z_0 \sim 50$ *ohm*, $\varepsilon_{eff} \sim 2$ and typical precision in $\Delta F/F$ measurement *~0.1 ppm*, ΔC_t is on the order of 10^{-19} *F = 100 zF*. Capacitance resolution down to a few zepto-Farads has been demonstrated in state-of-the-art experiments.

According to equation (2-12) there is a small change in the quality factor due to change in the probe resonant frequency ω'. However, in practice the losses are not uniform in the transmission line, i.e., h'' depends on z. In this case, there will be an extra change in the quality factor due to redistribution of the resonator currents near the tip, even in the case of a lossless sample.

2.4.4 Charge image method [1], [24]–[26]

Operating below the cut-off frequency, waveguide probes suffer severely from waveguide decay. In these probes, a linear improvement in resolution will cause an exponential reduction in sensitivity. As a result, it is very hard to reconcile the conflict between resolution and sensitivity. As there is no cut-off frequency in a transmission line, coaxial transmission line probes have much better performance than aperture or waveguide probes.

As the resolution is mainly determined by the cross-section of the transmission line at the open end, shrinking the cross-section still causes significant transmission line decay. This is especially true when a long section of a coaxial transmission line is used to form a resonator. If the cross-section is wide, the unshielded propagating waves at the open end of the transmission line tend to increase the difficulty of quantitative analysis, since both near-field and far-field interactions have to be considered in this case. To overcome this problem, the shielded coaxial resonator probe was proposed by Wei and Xiang [24] (Fig. 2-13-(a)).

This design minimizes the far-field background signal and allows submicron spatial resolution even in the quantitative analysis of complex dielectric constant. The coating layer should be as thin as the skin depth to avoid the formation of a micro-transmission line with

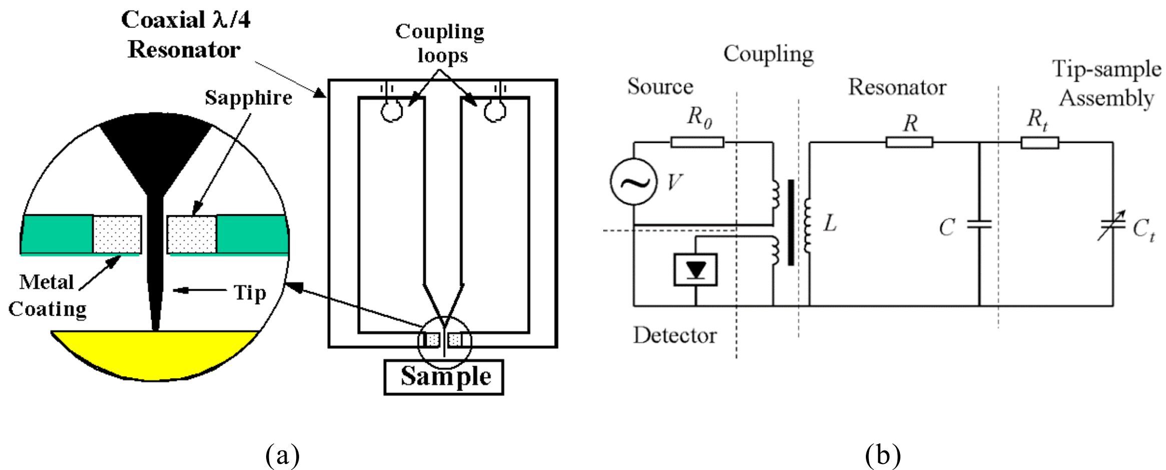

Fig. 2-13. (a) Shielded λ/4 coaxial resonator probe proposed in [25] (b) Equivalent lumped series resonant circuit for SMM [1].

heavy loss near the aperture while still maintaining effective shielding of far-field components. The resonant frequency (*f_r*) and quality factor (*Q*) as functions of the properties (e.g., dielectric constant and loss tangent) of the materials placed in the vicinity of the tip can be detected by the electronics [26].

2.4.4.1 System design and analysis

The resonant system can be analyzed using an equivalent lumped series resonant circuit, as shown in Fig. 2-13-(b), with effective capacitance *C*, inductance *L*, and resistance *R* (for an ideal quarter-wave resonator):

$$C = \frac{2\pi\epsilon_0}{\ln(R_2/R_1)} l \ , \quad L = \frac{\mu_0}{2\pi} l \ln(R_2/R_1) \ , \quad R = \frac{2R_s}{\pi^3}\left(\frac{1}{R_2} + \frac{1}{R_1}\right) l \qquad \text{(2-14)}$$

where $l=\lambda/4$ is the effective cavity length, R_s is the surface resistance of cavity material, R_2 and R_1 are the radii of center and outer conductors, respectively, and ε_0 and μ_0 are the permittivity and permeability of free space, respectively. The uncoupled (Q_u) and coupled (Q_c) quality factors of the resonant system are given by:

$$Q_u = \frac{1}{\omega_r C R} \ , \quad Q_c = \frac{1}{\omega_r C} \frac{1}{R + R_0/p^2} \qquad \text{(2-15)}$$

2.4.4.2 Theory

A recursive algorithm has been developed to calculate the total charges on the tip-sample system and used to derive the dielectric constant. *Two critical approximations* were made in obtaining these analytical solutions: *(1)* spherical tip: because the main part of the probe interacting with the sample is the tip cap, this is a good approximation, especially when the probe is held at a distance from the sample shorter than the probe radius; *(2)* quasi-electrostatic: because the effective region with significant non-zero field distribution is several orders smaller than the relative long wavelength of the microwave, the phase effect can be neglected. Under the above approximations, the problem is simplified to solving the static electric field distribution in the sample under *two boundary conditions*: equipotential

surface of the sphere and continuity at the sample surface. The field can be solved in many ways. A straightforward way is the *charge image method*. The quantitative relations relate the tip radius (R_0), tip-sample distance (g) and real and imaginary dielectric constant [1]. In this report, the discussion is limited to the area of homogeneous and isotropic dielectric materials, i.e., $\varepsilon = \varepsilon' + j\varepsilon'' \gg \varepsilon_0$ *with* $\varepsilon' \gg \varepsilon''$ and $\mu = \mu' + j\mu'' \cong \mu_0$, where ε and μ are complex dielectric constants and magnetic permeability of the samples.

The simplest configuration is considered: the tip scans directly (soft contact) on the surface of a dielectric material with a thickness much larger than the tip radius, as shown in Fig. 2-13. To first order, the tip can be represented as a charged conducting sphere. It can be assumed that the tip has the same potential as the open end of the resonator, since it only extends out a length several orders of magnitude smaller than the wavelength beyond the cavity (the experimental results suggest that this approximation is extremely accurate). The dielectric material under the tip will be polarized by the electric field of the tip and reacts on the tip, causing the redistribution of the charges on the tip to maintain the equal-potential surface of the conducting sphere. The reaction can be represented by an image charge q'_1 located in the sample, and the redistribution can be represented by another image charge q_2 inside the tip sphere. This process is iterative and forms three series of image point charges to meet the boundary conditions at both tip and dielectric sample surfaces, as shown in Fig. 2-13. The field distribution (peak value) inside the sample can be expressed as a superposition of the contributions from the series of point charges q''_n as

$$\vec{E}_1 = \frac{q}{2\pi(\epsilon + \epsilon_0)} \sum_{n=1}^{\infty} \left(\frac{1}{n} b^{n-1} \frac{r\vec{e}_r + (z + R_0/n)\vec{e}_z}{[r^2 + (z + R_0/n)^2]^{3/2}} \right) \qquad (2\text{-}16)$$

where $b = (\varepsilon - \varepsilon_0)/(\varepsilon + \varepsilon_0)$, $q = 4\pi\varepsilon_0 R_0 V_0$, R_0 is the radius of the tip, and $\boldsymbol{e_r}$ and $\boldsymbol{e_z}$ are the unit vectors along the directions of the cylindrical coordinates r and z, respectively. It is straightforward to confirm that this field distribution satisfies Coulomb's law and the boundary conditions on the surfaces of both dielectric and conducting sphere simultaneously, and therefore is the correct and sole solution of this problem. In contrast to the dipole model

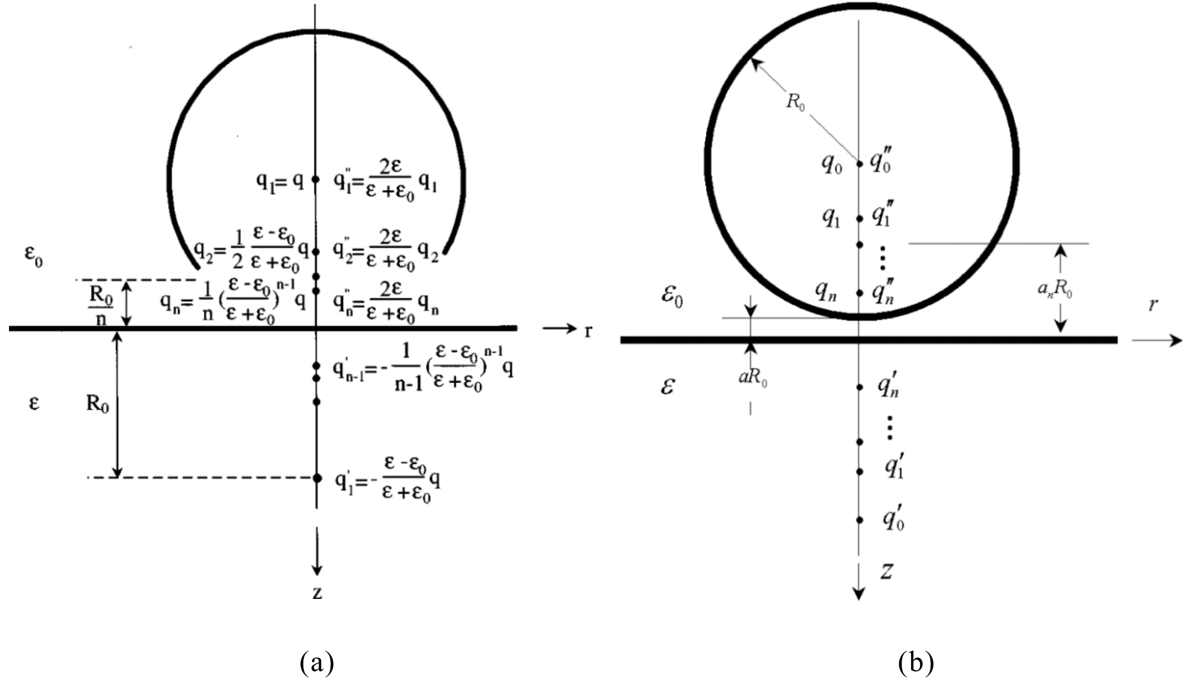

Fig. 2-14. (a) Image charge distribution for a thick sample in contact with the tip. The q_n series represents the charge redistribution on the tip, the q'_n series represents the effect of polarization of the dielectric sample, and the q''_n is the effective value of q_n inside the sample. (b) The iterative image charges in tip-bulk sample system in non-contact mode [26].

of tapered waveguide probes for NSOM, where electric dipoles lie above and parallel to the sample surface, this is a monopole model (appropriate for the tip configuration of SEMM). The electric field here is concentrated in a very small volume under the tip, almost perpendicular to the sample surface.

Since the majority of the microwave energy is concentrated in the cavity and the field distribution inside the cavity will not be disturbed significantly by the tip-(dielectric) sample interaction, the perturbation theory for microwave resonators can be used to calculate the f_r and Q shifts caused by the dielectric material:

$$\frac{\Delta f_r}{f_r} = -\frac{\int_V (\Delta\epsilon' \overrightarrow{E_1}.\overrightarrow{E_0} + \Delta\mu' \overrightarrow{H_1}.\overrightarrow{H_0})dv}{\int_V (\epsilon_0 E_0^2 + \mu_0 H_0^2)dv} = A\left(\frac{\ln(1-b)}{b} + 1\right) \tag{2-17}$$

$$\Delta\left(\frac{1}{Q}\right)_d = \frac{\int_V (\Delta\epsilon''\overrightarrow{E_1}.\overrightarrow{E_0} + \Delta\mu''\overrightarrow{H_1}.\overrightarrow{H_0})dv}{\int_V (\epsilon_0 E_0^2 + \mu_0 H_0^2)dv} = -\frac{\Delta f_r}{f_r}\tan\delta \quad (2\text{-}18)$$

where $\boldsymbol{E_0}$, $\boldsymbol{H_0}$ and $\boldsymbol{E_1}$, $\boldsymbol{H_1}$ refer to the electric and magnetic field before and after the perturbation respectively, l is the wavelength, $A=4\pi\epsilon_0 R_0(V_0^2/E)$ is a constant determined by the geometry of the tip–resonator assembly ($A \approx 16R_0 \ln(R_2/R_1)/\lambda$ for an ideal $\lambda/4$ coaxial resonator), and $\tan\delta = \epsilon''/\epsilon'$. From formulas (2-17) and (2-18), it was found that the microscope signals are proportional to the tip radius R_0. This result can be understood by considering that the electric field near a conducting sphere at a given voltage is inversely proportional to the tip radius and the total contribution to the signal is the integration of the square of field over the volume of the sample. Besides the dielectric loss from the sample, the extra current required to support the charge redistribution induces additional resistivity loss. The corresponding Q shift can be expressed as:

$$\Delta\left(\frac{1}{Q}\right)_c = -B\frac{\Delta f_r}{f_r} \quad (2\text{-}19)$$

And the total Q shift is:

$$\Delta\left(\frac{1}{Q}\right)_t = -(B + tan\,\delta)\frac{\Delta f_r}{f_r} \quad (2\text{-}20)$$

Formulas (2-19) and (2-20) allow quantitative measurements of the local complex dielectric constant for samples of thickness $\gg R_0$. The constants A and B can be properly calibrated by measuring a standard sample such as sapphire with a known dielectric constant and loss tangent.

If there is an air gap between the sample and the tip (Fig. 2-14-b), the expression for the frequency shift is given by

$$\frac{\Delta f_r}{f_r} = -A\sum_{n=1}^{\infty}\frac{bt_n}{a_1 + a_n} \quad (2\text{-}21)$$

where t_n and a_n have the following iterative relationships:

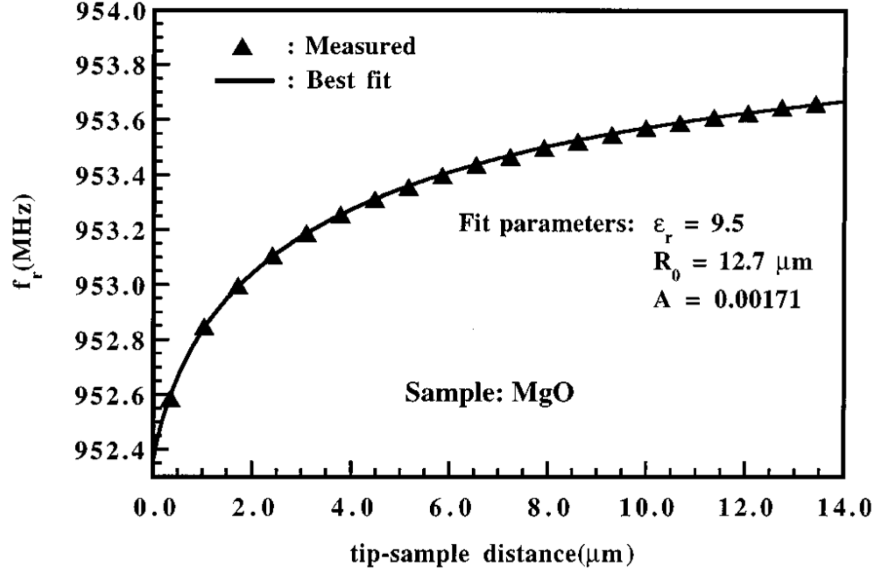

Fig. 2-15. Measured and fitted resonant frequency as a function of tip-sample distance for a MgO single crystal [26].

$$a_n = 1 + r - 1(1 + r + a_{n-1}) \;, \qquad t_n = bt_{n-1}/(1 + r + a_{n-1}) \qquad \text{(2-22)}$$

With the initial conditions of $a_1 = 1{+}r$, $t_1 = 1$ (where r is the gap-to-tip radius ratio). From equation (2-17), f_r is a function of the gap width, which provides a calibration method. Fig. 2-15 shows the measured and fitted f_r as a function of gap width for a MgO single crystal. The fitting parameters are $\varepsilon_r = 9.5$, $R_0 = 12.5\ \mu m$ and $A = 1.71 \times 10^{-3}$.

2.4.5 Simulation results of the conventional SMMs

In this thesis section, I first simulate structures proposed by others for comparison and then show our designed structure simulation results. Two well-known structures have been simulated and compared with the literature. The first structure is a sharp tip with radius of curvature of 10 μm, which is the extension of the inner conductor of a coaxial cavity resonator (shown in Fig. 2-16). The resonator is coupled with a loop to the other side circuitry using wave-port in HFSS.

This structure has the benefit of high sensitivity (stemming from the use of a high quality

factor resonator) and a potential to achieve very fine resolution, which is determined by the tip curvature and tip-to-sample distance. The structure works in TEM coaxial mode. A further benefit is that one can measure the sample properties in multiple frequencies. One problem of this structure is its bulky resonator, which makes it impossible to integrate with IC or MEMS devices.

As described previously, a change in the sample properties (here ε_r) would alter the evanescent field very close to the tip. Therefore, the reflection coefficient would change phase (and/or magnitude), resulting in a frequency (and/or quality factor) change in the resonator. As can be seen in Fig. 2-16, I got almost the same results as [26], with the same curve. However, as I did not know the exact values for the structure, I achieved higher sensitivity, which means that the quality factor of my structure is better (i.e., the radius of my cavity may have been bigger).

The second structure I simulated is shown in Fig. 2-17. In this structure, a parallel aluminum strip with a quartz layer in between has been simulated. This structure has the benefit of a non-contact, non-destructive tip, confining the electromagnetic field inside the strip. Consequently, a quantitative measurement of local properties of the sample is possible. Because it has two conductors, this structure supports TEM mode, which eliminates the loss mechanism due to the cut-off frequency of some waveguide structures. The probe operates in balanced odd mode only, where the two Al strips carry equal and opposite currents, forming an electrically small quadrupole-like antenna outside of the enclosure. The parasitic far-field radiated power is a few orders of magnitude less than that of unbalanced dipole-like geometries, while the near-zone fields are mostly confined in between the Al strips. In practice, this parallel strip is actually a tapered one, which connects to a half-lambda resonator to increase sensitivity.

I have tried to simulate the same structure as the one described in [3] and [23], but again I did not have all of the requisite information to do so. It is clear that the simulation results agree very well with theoretical formulations. Both real and imaginary parts of S_{11} Fig. 2-17

(e,f) are similar to the theoretical results (Fig. 2-17 (f)) .

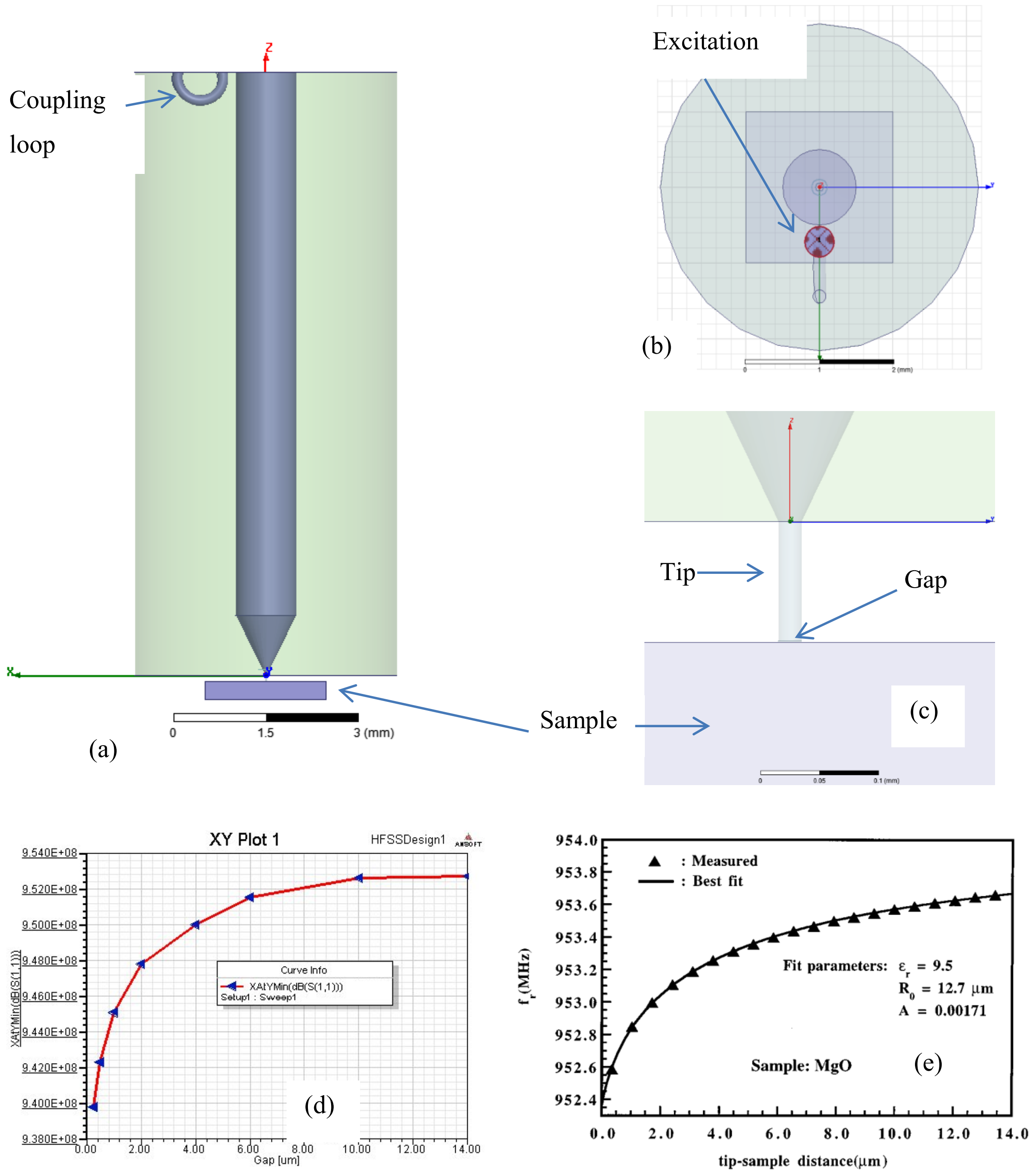

Fig. 2-16. Simulated structure in HFSS (a) side view (b) top view (c) zoomed tip area. (d,e) HFSS simulation results compared to theoretical results in [26].

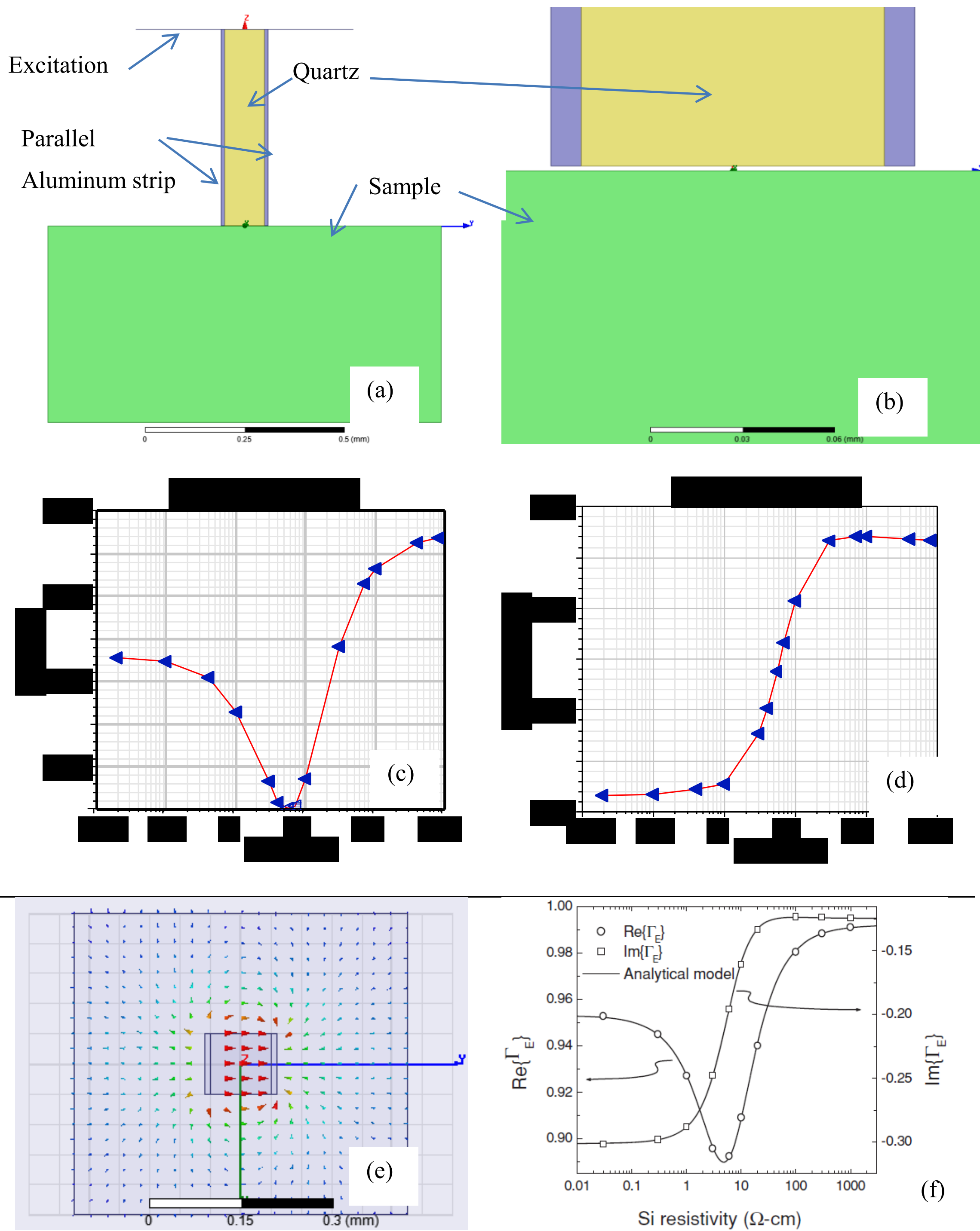

Fig. 2-17. Simulation in HFSS (a) side view (b) zoomed area near the tip. (c,d,f) HFSS simulation results compared to theoretical results in (e) top view and electric fields on the excitation sheet [3].

Chapter 3
Fabrication of CMOS-MEMS SMMs

In this chapter, after a short review of MEMS SPMs, the fabrication process for the CMOS-MEMS is explained. Then a description of the SMM device is presented. The importance of tip-sample distance control and integration of the AFM is then discussed. Finally, some of the design challenges such as thermal coupling to the microwave path and change of reflected signal due to the movement of the tip are discussed and possible solutions are presented.

3.1 MEMS SPM's

The first micro-machined STM consisted of a piezoelectric multimorph with patterned electrodes [41]. Another STM, fabricated in single-crystal silicon is reported in [42]. These works demonstrated open-loop 3-axis positioning with a conductive path to the tip, but without AFM imaging capability. More recently the co-fabrication of control electronics with an array of single-axis cantilevers for AFM was demonstrated [43]. Another example of a single-axis cantilever with integrated position sensing is the Akiyama probe [44]. In [45], a thermal profiler with integrated 1-D actuation was presented. A paper from University of Waterloo [46] was the first to include 3-axis positioning, strain sensors, and position sensors (i.e., all of the mechanical components required for an SPM to acquire an image) in a single device.

In [10], the first imaging results with a CMOS-MEMS contact-mode AFM were presented. The resolution was compromised by thermal coupling from actuation due to the high temperature coefficient of resistivity (TCR) of the polysilicon strain sensors. Frequent thermal calibration and post-processing of the data were required in order to extract the sample topology from the cantilever signal. Thermal coupling issues were first mitigated

using forced oscillation and higher harmonic detection [47], and then further suppressed using a dynamic FM-AFM mode [48]. In [49], we reported the first SMM measurements with a self-actuating probe. These devices were fabricated in the commercially available SOIMUMPs process. A 2-D scanner with integrated electrothermal chevron actuators and an integrated microwave CPW interface was reported there.

3.2 CMOS-MEMS Fabrication Process

CMOS-MEMS processes were introduced in the 1980s and the field has grown significantly over the past two decades [50]. These processes are well-suited to integrated SPM device fabrication because they allow for complex signal routing, various types of actuation and sensing methods, and integrated electronics. Some examples of CMOS cantilever sensor systems that exploit the various material properties available in CMOS-MEMS processes are discussed in [51].

Fig. 3-1 shows the cross-section and thickness of each metal and inter-metal dielectric (IMD) layer for the 0.35μm CMOS process from TSMC[1]. MEMS devices are constructed using composite metal-dielectric layers as the structural layers.

Our fabrication process falls under the category of post CMOS-MEMS processes (Fig. 3-2). We begin with a standard foundry CMOS process with four metal layers and two resistive polysilicon layer options. The topmost exposed metal layer is used as a mask for an anisotropic etch step that removes the dielectric (SiO_2 etch); this layer is also used for routing and structure design. Following the completion of the oxide etch, we perform an isotropic Si etch of the underlying substrate to release the devices. In this step, the device is under etched about 15 μm.

Two other optional maskless process steps may be used. In the first step, grooves may be diced or laser-etched into the backside of the wafer to suspend cantilevers over the die edge

[1] Taiwan Semiconductor Manufacturing Company

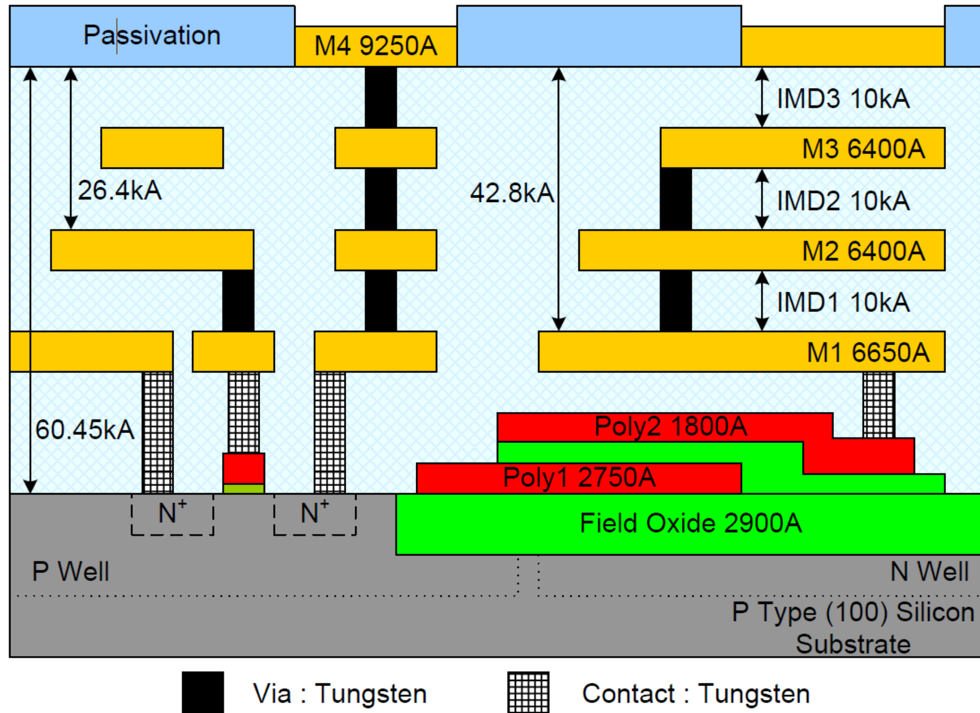

Fig. 3-1. Cross-section view showing the thickness of each metal and IMD layers of 2 Polly 4 Metal (2P4M) 0.35µm CMOS process from TSMC [52].

upon release, as shown in Fig. 3-3-(a). This helps to look at the tip-sample area under optical microscopes and find the area of interest for imaging. After oxide and Silicon etching on the top side (shown in Fig. 3-3-(b)), it is easier to snap the device from the diced lines on the backside by applying a controlled lateral force from both sides. In the second step, we may remove the polymer buildup that occurs during the SiO_2 etch using EKC.

There are several process features that are advantageous in the design of CMOS-MEMS SPMs; in the electrical domain, the designer can choose between conductive (Al), insulating (SiO_2), and semiconducting (polysilicon) materials. This allows for complex routing of signals in a monolithic beam. It also allows for the placement of resistive heat sources and temperature sensors. Also, the temperature coefficient of resistivity of polysilicon materials can be exploited to measure local temperatures. We use these process features to design MEMS actuators and position sensors for our CMOS-MEMS SMM.

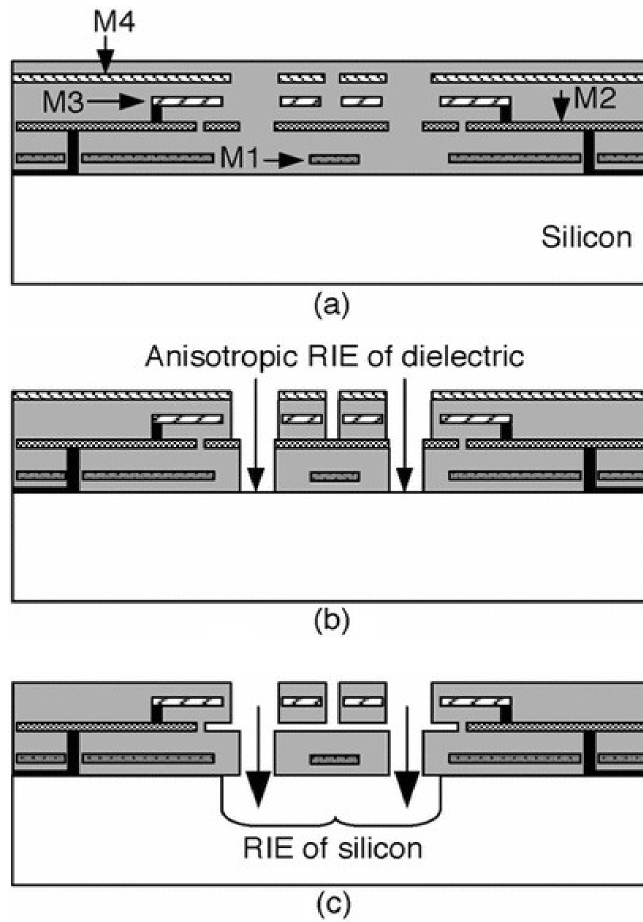

Fig. 3-2. Maskless release process for CMOS-MEMS. (a) Foundry CMOS process cross-section. (b) Anisotropic etch of SiO_2 intermetal dielectric layers. (c) Isotropic Si substrate etch, releases the devices. [53] and [54].

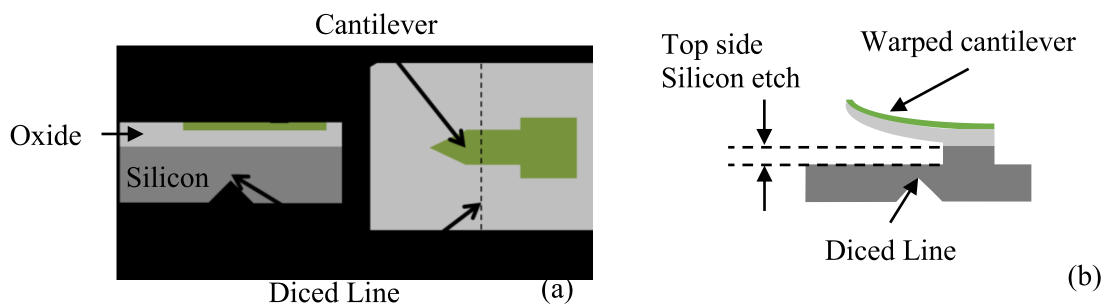

Fig. 3-3. (a) Grooves in the backside of the wafer to suspend cantilevers over the edge of the chip. (b) After oxide and Silicon etch on top.

The thermal conductivity of Al is 191 $Wm^{-1}K^{-1}$, while that of SiO_2 is 1.4 $Wm^{-1}K^{-1}$. This enables the design of thermally isolating members that can be used to separate heat sources from nearby regions that are mechanically and electrically interconnected. Another feature is that the polysilicon-metal contacts in CMOS-MEMS processes are thermocouples that can be used as local temperature sensors.

In the mechanical domain, the thermal coefficients of expansion (TCE) of Al and SiO2 are disparate as well. The TCE of Al is around $14.6 \pm 3.0 \times 10^{-6}$ K^{-1} and the TCE of SiO_2 is 0.4-1.0×10^{-6} K^{-1}. This feature is desirable in the design of lateral and vertical electrothermal bimorph actuators. Further discussion of the mechanical material properties and how they relate to electrothermal actuator design can be found in [55].

Although a wide variety of material properties are available to the designer, they are seldom optimized to improve SPM performance. For instance, the performance of CMOS electronics improves with low TCR whereas the design of temperature-based position sensors improves with high TCR. Another example is that piezoresistive cantilevers benefit from a high gauge factor, while it is desirable to suppress strain effects in CMOS. Thus, our CMOS-MEMS SMM design has to adopt to existing commercial CMOS 0.35 µm that is designed for CMOS electronics rather than for MEMS.

3.3 CMOS-MEMS SMM Device Description

A CMOS-MEMS 1-DOF SMM probe is presented in Fig. 3-4. This device incorporates a CPW to a shielded transmission line (here a rectangular coaxial line) transition. The flexible transmission line is displaced in the tip-sample approach direction using a vertical electrothermal bimorph actuator. Internal metal layers are used for conduction while the top and bottom layers are used to shield the microwave signal. DC pads are utilized for vertical actuation using the thermal bimorph effect. This device was used to obtain characteristic tip-sample approach curves and to validate our simulations.

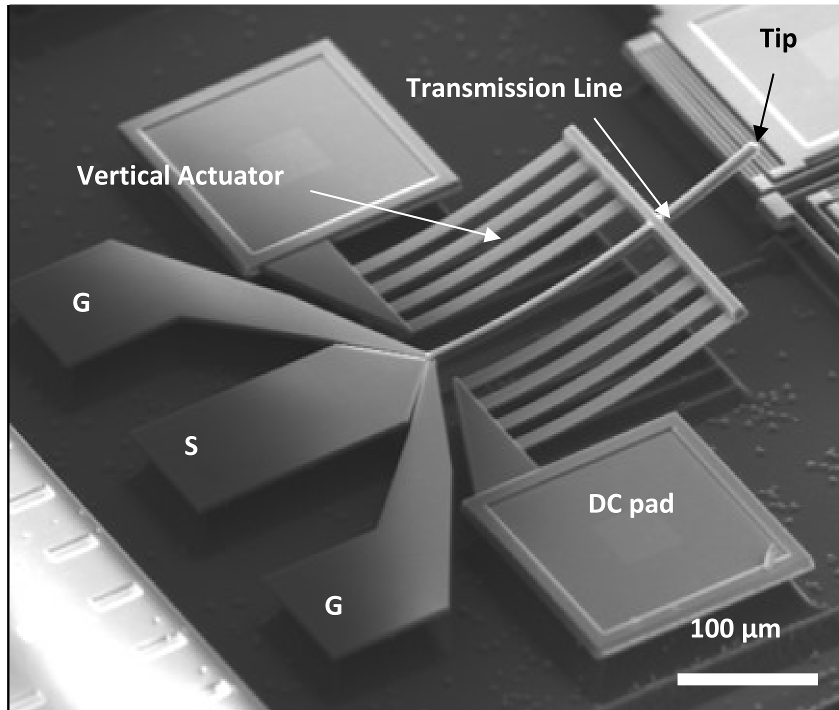

Fig. 3-4. Single degree of freedom shielded SMM probe. A CPW to flexible transmission line transition is included in the signal path from the PNA to the tip. Internal metal layers are used for conduction while the top and bottom layers are used to shield the microwave signal. DC pads are used for vertical actuation using the thermal bimorph effect.

Maximum vertical features of a sample that can be imaged are set by the vertical range of motion of the actuator. Since the vertical range scales with the square of length (L^2), while the stiffness scales with $1/L^3$, there is a tradeoff between range and stiffness. We can combine several vertical actuators in parallel to increase stiffness while maintaining the same range of motion. The position resolution of the actuator is inversely related to its range of motion. This has profound consequences on the operation of the instrument. A high speed, high resolution instrument requires a stiff actuator with limited vertical scan range [56].

To add three degrees of freedom to the device, lateral MEMS actuators are needed. One of the lateral actuator geometries used, is shown in Fig. 3-5 and discussed in [55]. In-plane actuation is achieved using the electrothermal bimorph effect. A lateral moment is generated by offsetting the internal metal layers in the actuator beams with respect to the top metal layer (mask layer). Rectilinear motion is achieved by mirroring a bimorph in order to cancel

the arcuate component of the motion, while parasitic out-of-plane motion is mitigated using a folded design pattern.

Electrothermal actuators are a suitable choice for both static and dynamic actuation in single-chip SPMs. Moderate static forces (≃50 nN) and large displacements (≃20 μm) can be produced by lateral electrothermal actuators, at the expense of increased power consumption (1 to 5 mW). The thermal time constants of the lateral actuators used in this work are in the range of 1-4 ms, which translates to scan speeds above 100 Hz. Although the efficiency of the actuators rolls off at high frequencies, a resonance with moderate Q (≃50) can be clearly observed by piezoresistive detectors that are integrated in vertical bimorph beams. In the device reported here, the vertical resonance occurs at 225 kHz, and can be excited electrothermally with a 100 mV input. A useful figure of merit when comparing actuators is the work-per-unit-volume, which is the product of the blocked force and output displacement. When comparing actuators implemented in CMOS-MEMS processes, the work-per-unit-volume of electrothermal actuators is 2 to 3 orders of magnitude greater than that of comb-drive electrostatic actuators. Although parallel plate actuators may achieve high forces near the pull-in instability, their small range of motion (<1 μm) precludes their use as the vertical actuators in single-chip SPMs. One type of actuator that has been used in this work as a lateral actuator is a multimorph actuator that is based on the bimorph effect (shown in Fig. 3-5).

Another type of electrothermal actuator that we use for the lateral actuator design is chevron actuators (shown in Fig. 3-6). The work-per-unit-volume of the chevron actuators is 2500% higher than that of the lateral multimorphs. The out-of-plane stiffness of the new actuators is also improved by a factor of roughly 350% [56].

A CMOS-MEMS 3-DOF SMM/AFM device is presented in Fig. 3-7. The following features of the device are desirable in the SMM context. After the CMOS-MEMS release process, the substrate is singulated in order to obtain cantilevers and tips that are suspended over the edge of the chip. This device geometry permits observation of the tip-sample region while

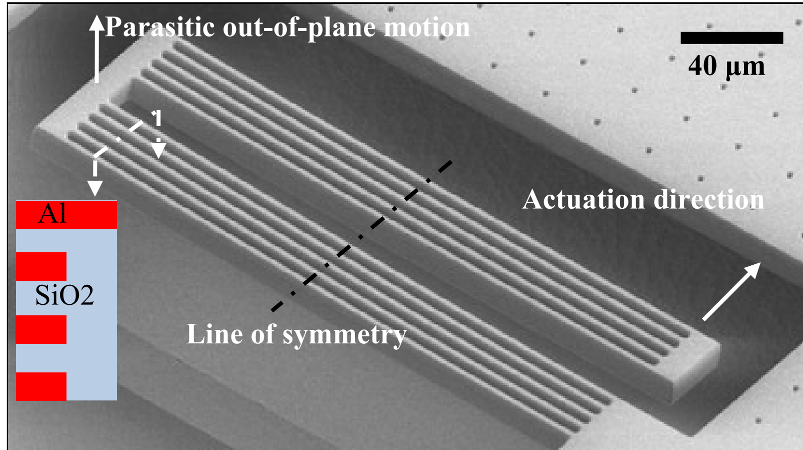

Fig. 3-5. CMOS-MEMS lateral electrothermal actuator. Inset is a cross-section of an individual beam, showing the offset internal mechanical layers used to generate a thermal moment.

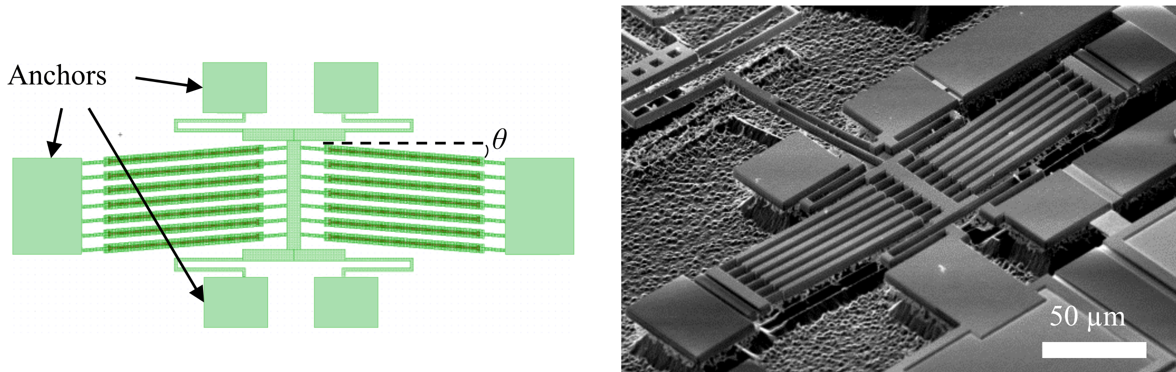

Fig. 3-6. Chevron actuator used for lateral actuation: Layout and SEM image.

imaging. To carry the microwave signal to the tip, a flexible transmission line is required to be able to move the tip. Lateral scanning is achieved by applying a DC bias and a differential AC signal to the left and right lateral actuators. The result is a spherical coordinate scan (r,φ,θ) in which the angle φ is related to the difference between the left and right actuator deflections, the radius r is proportional to the average of the left and right actuator deflections, and the elevation θ is provided by the out-of-plane bimorph (vertical actuator). The SMM device is capable of scanning its tip in 3 degrees of freedom over a sample, with an approximate scan range of 13 µm x 13 µm x 15 µm in the x, y and z directions.

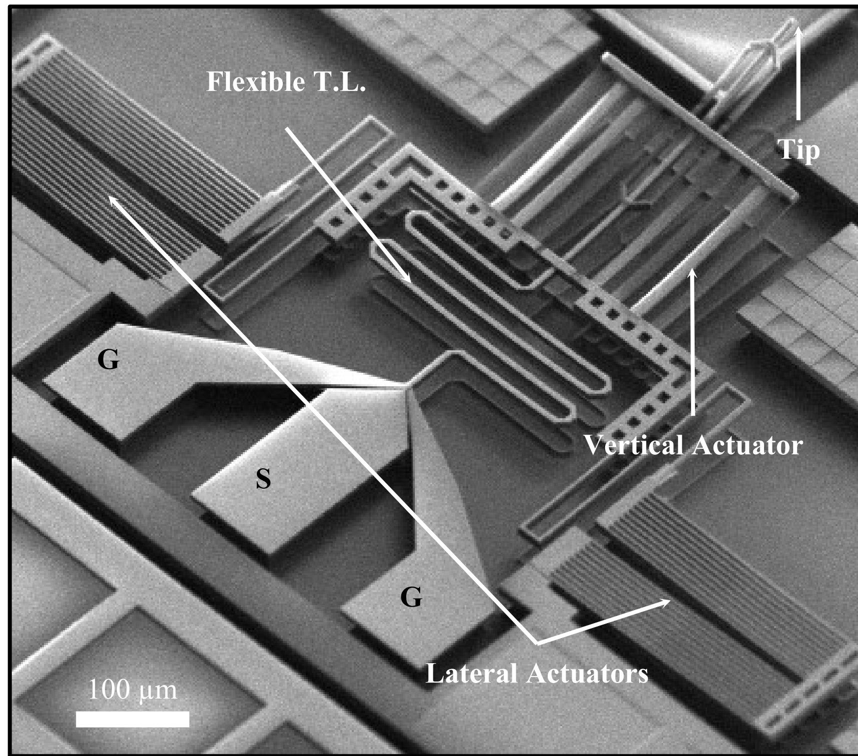

Fig. 3-7. CMOS-MEMS 3 DOF integrated AFM-SMM device. A CPW to flexible transmission line transition connects the microwave signal to the tip. Actuators are used to bend the transmission line and scan the tips.

3.4 Tip-sample Distance Control

The precision of any near-field measurement is directly related to the precision with which the tip-sample distance can be maintained [3]. The challenge is in the integration of a tip-sample distance control technique with the SMM device. Imtiaz et al. uses STM for precise distance control over metallic samples [38]. Lai et al. addressed this issue by combining SMM with a commercial AFM; they also showed that operating it in tapping mode would eliminate thermal and other long-term drifts [31].

If tip-sample distance is not kept constant, the air gap capacitance between the tip and sample (and consequently tip impedance) will change and become indistinguishable from

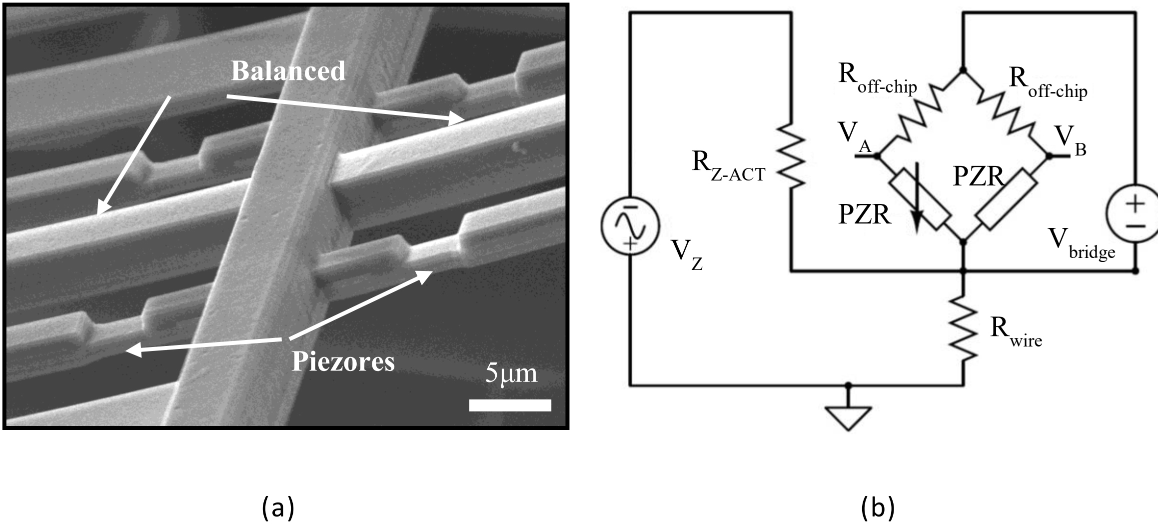

Fig. 3-8. (a) Close-up of the balanced cantilever design used for AFM operation. The temperature in the piezoresistors is balanced, whereas the strain from tip-sample forces is only recorded on one of the piezoresistors. (b) A schematic circuit showing the Wheatstone bridge and applied voltages for the bridge and the vertical actuator.

changes of sample properties. In our work, we have integrated an AFM with the SMM in order to control the tip-sample gap. An integrated balanced pair of piezoresistive strain sensors for AFM operation is included in order to maintain a constant tip-sample separation (Fig. 3-8). The piezoresistors on the balanced cantilevers are connected to two other resistors to form a Wheatstone bridge. The output voltage of the bridge is used for tip-sample distance control.

Keeping a constant and low tip-sample distance during SMM imaging is of great importance because the intensity of the evanescent field decreases exponentially with a spatial constant of R_0 (probe characteristic size). To confirm this, HFSS simulations of a 200 nm diameter coaxial probe with tip-sample distances of 1 nm and 100 nm from a bulk dielectric sample with a dielectric constant of 15 were performed (Fig. 3-9). The results were then exported to ADS and, after matching the tip-sample impedance with ideal transmission lines, the frequency shifts were measured. As shown in Fig. 3-10, the smaller the tip-sample distance, the higher the sensitivity of the SMM. One should note that these simulations are only meant to show the effect of tip-sample distance, and that the values shown are not for

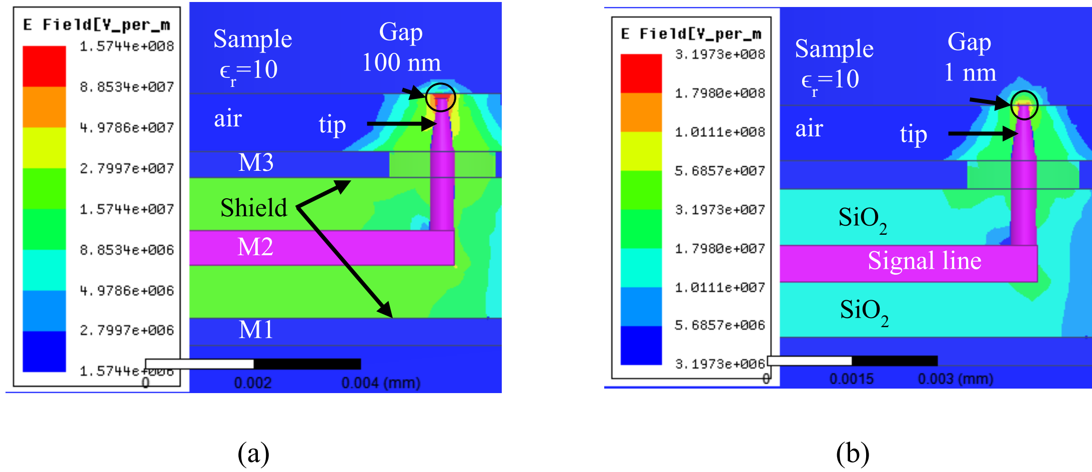

Fig. 3-9. FEM simulation of the SMM tip in (a) 100 nm, and (b) 1 nm tip-sample distance of a bulk dielectric sample with a dielectric constant of 15.

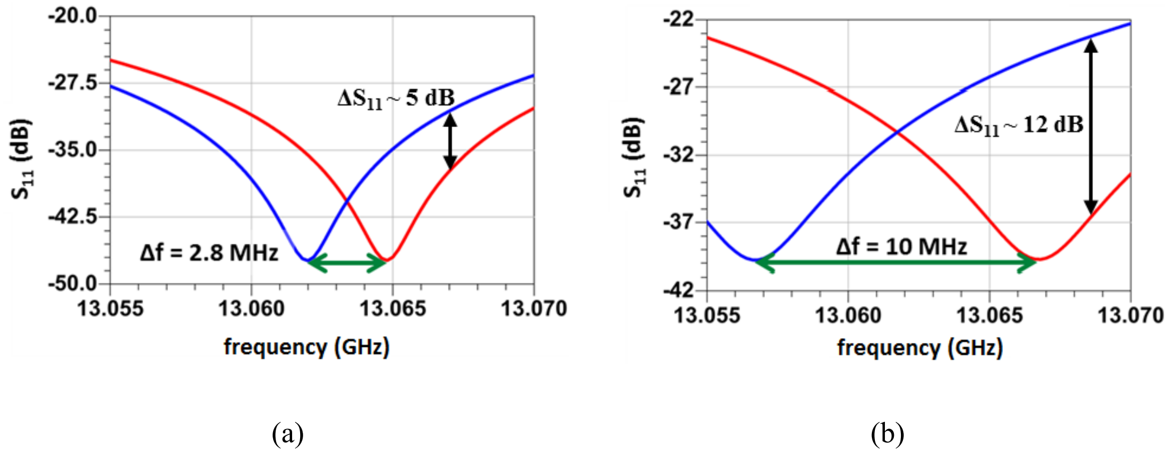

Fig. 3-10. Effect of tip-sample distance on SMM sensitivity in (a) 100 nm, and (b) 1 nm tip-sample distance of a bulk dielectric sample (Red: without sample; Blue: with sample).

the entire SMM system. A detailed analysis of the entire SMM is discussed in Chapter 4.

3.5 SMM/AFM Probe

Shielding the microwave signal path up to the tip is necessary to obtain quantitative electrical imaging and sensitivity improvement. Therefore, in all of the presented CMOS-MEMS geometries, the microwave signal path is shielded in order to eliminate parasitic capacitive

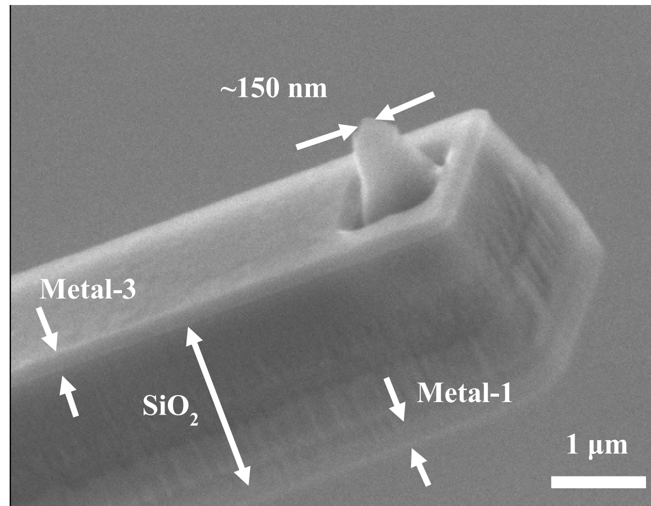

Fig. 3-11. Close-up of SMM/AFM tip. The tip radius obtained in the release process is ~150nm. Metal-1 and metal-3 shielding layers are shown here.

coupling to the sample. This is done by fabricating rectangular coaxial, stripline and microstrip transmission lines. In rectangular coax and stripline, metal layer 2 is used for signal line, while metal layers 1 and 3 and the 'via' holes between them are used for shielding. In microstrip, M3 or M4 are used for ground and M1 is used for signal.

The device in Fig. 3-7 includes a sharp tip with a ~150nm radius for SMM/AFM operation. The tip was designed with minimum feature squares from the signal layer (metal 2) to the topmost metal layer (metal 4), connected with tungsten via holes. Tip sharpness was obtained by milling during the RIE steps in the release process, without any additional post-processing. AFM can be used in non-contact mode to maintain a constant tip-sample gap for SMM, or in intermittent contact mode for noise and long-term drift reduction, as discussed in [47] and [31]. Fig. 3-11 shows an SMM/AFM tip and metal shielding layers.

In general, two different types of tips have been investigated for CMOS-MEMS SMMs. The first one is called the "via type", which is illustrated in details in Fig. 3-11. It is made by connecting several tungsten vias from the signal line to the topmost metal layer on M4 (via12, via23 and via34 connect M1 to M3). Then, during oxide etching in the RIE, it is sharpened without any extra processing steps. This process is illustrated in detail in Fig. 3-12 for a stripline micro-transmission line.

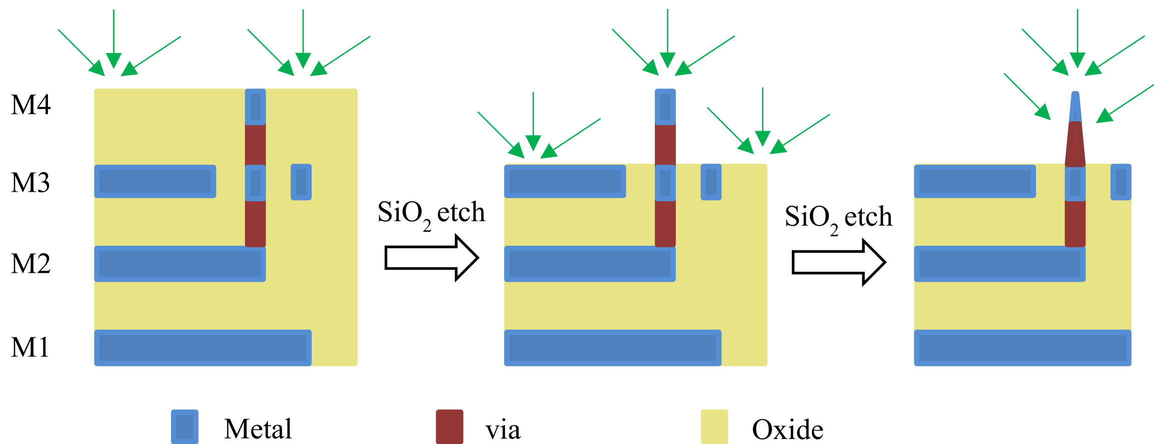

Fig. 3-12. The process of getting sharp via tips through RIE oxide etching.

With this method, tips with a curvature of ~150 nm are achievable. However, one issue with this type of tip is reliability. The problem is that during oxide etching, the vias might be attacked and the tip (and thus the entire device) will be lost.

Fig. 3-13 shows a version of a larger via tip that survived in one instance but not in another. The larger tips are intended to protect the vias at the topmost metal layer (M4). If very sharp tips are needed, a focused ion beam instrument (FIB) can be used to remove the native oxide on the Aluminum, sharpen it to a smaller radius (~75nm), and deposit a Platinum coating.

The second type of tip that was designed and tested is called a wedge-type tip. Similar to

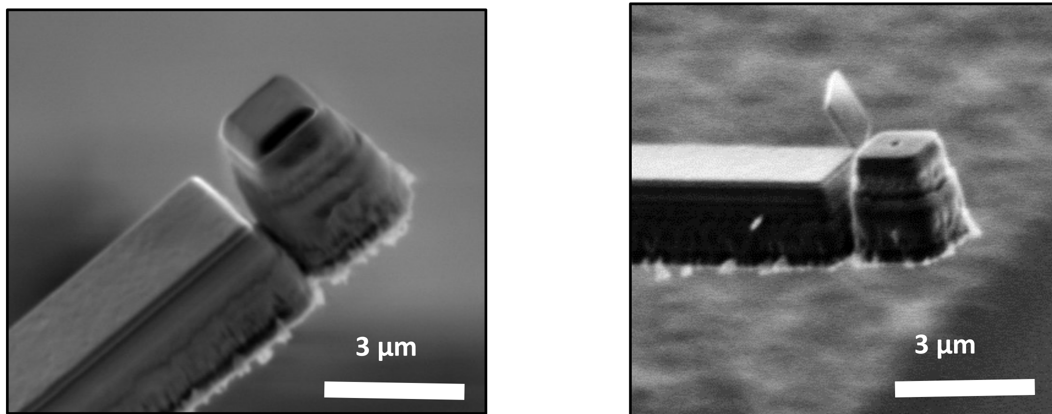

Fig. 3-13. SEM images of two larger via tips, survived (left), and not survived (right) after the oxide and silicon etching.

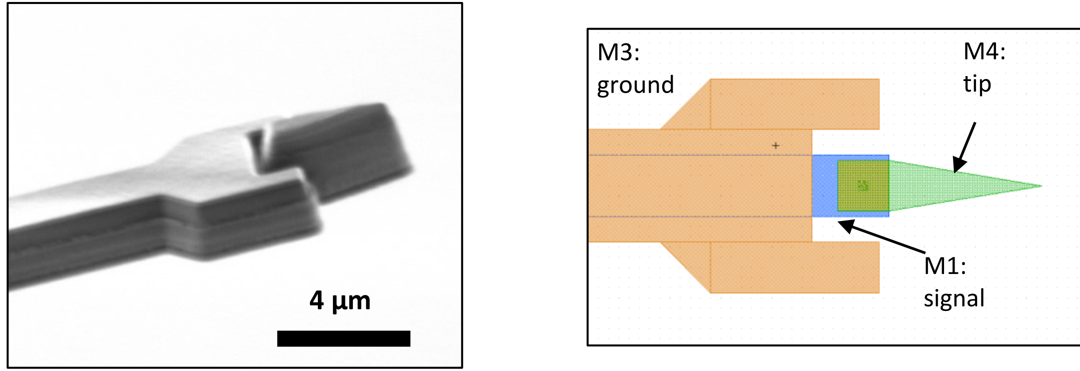

Fig. 3-14. Wedge-type tip: (Right) SEM image, and (left) layout.

via tips, the signal in wedge-type tips is connected to the topmost metal with vias, but a larger metal pad at M4 protects the vias. M4 is then extended a few microns in a triangular shape, as shown in Fig. 3-14. The problem with this type of tip, however, is that it might reduce the resolution in quantitative imaging because most of the tip is not electrically shielded and thus can interact both with the sample and the medium around the sample.

A standard AFM calibration grating with a 3 μm pitch and 90 nm height was used to demonstrate the imaging functionality of the SMM device in AM-AFM mode (refer to [56] for an explanation of AM-AFM mode). The scan speed is limited by the dynamics of the PID controller that was used in these imaging experiments. A 7 μm line scan consisting of 200

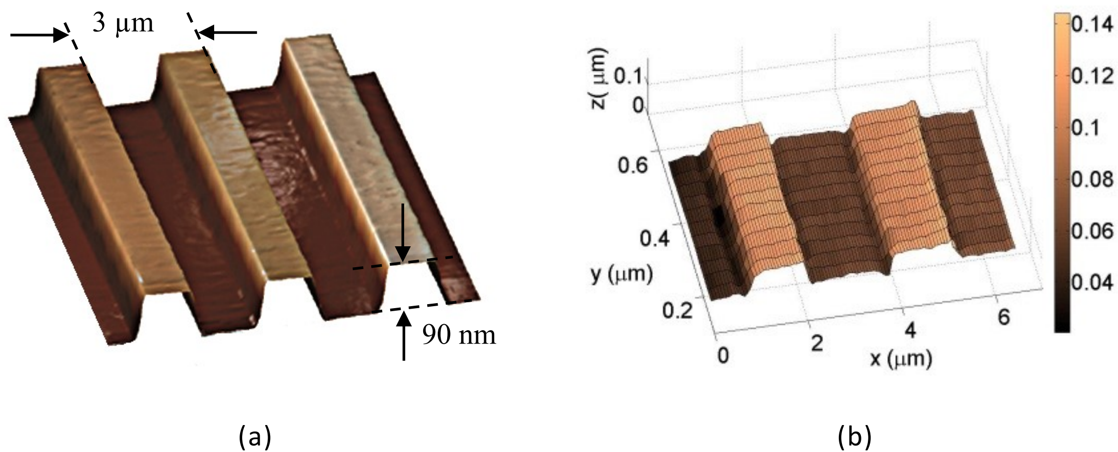

Fig. 3-15 (a) Standard AFM sample [57] (b) AFM image, obtained by scanning over a range of 7 μm x 0.6 μm. Height control of better than 10 nm is achieved.

points takes approximately 5 seconds, and the image consists of 16 lines. The vertical resolution of this measurement is a function of the noise in the piezoresistive bridge measurement, which may be reduced by limiting the bandwidth (and thus reducing the scan speed). We anticipate 1-10nm control of the tip-sample distance using this approach. FM-AFM methods reported in [48] may improve the resolution further. Fig. 3-15 demonstrates the capability of our device to scan over a 3D object, which is also a verification of its tip-sample distance control capability.

Further imaging results for different samples is presented in chapter 5.

3.6 Thermal Coupling Reduction

One of the challenges of electrothermal actuators is that the temperature of the actuators changes when they move the tip. Moreover, because the microwave path is not fully isolated from the actuators, it also gets heated up and cooled down with the actuators. This causes a change in properties of the material and thus slightly changes the characteristics of the transmission lines enough to change the reflected signal, which is convoluted with the change in S_{11} due to sample properties. The thermal coupling to the microwave path can be mitigated by placing thermal isolators between the path and the actuators. Fig. 3-16 shows the layout and SEM image of a part of the SMM device that is thermally isolated from the vertical and lateral actuators.

The temperature of the vertical actuators changes with the same frequency as that of tapping the tip to the sample. Therefore, it is not possible to filter out this signal in the receiver. For the lateral actuators, the scan rate is on the order of 1 hertz or slower, so it can be extracted from the final image by processing the background slow-varying signal. Also, isothermal lateral actuators can help reduce thermal coupling to the tip, as explained in [56]. In this type of lateral scanner, two actuators are excited differently, so the temperature in the middle does not change while moving the tip. The thermal cross-talk from the lateral actuators is considerably reduced with the help of isothermal actuators, as shown in Fig. 3-17

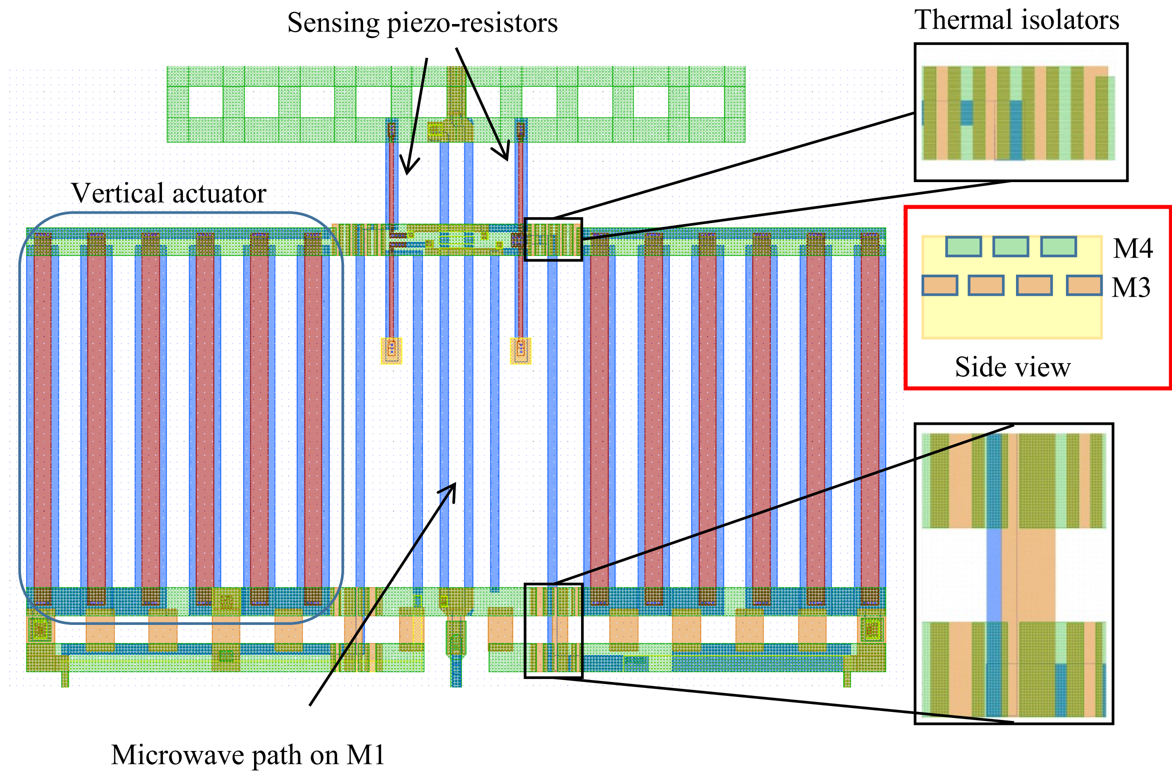

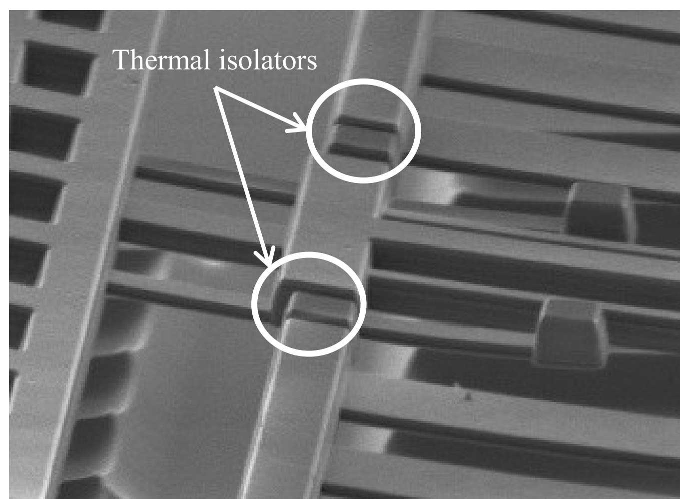

Fig. 3-16. (Top) The layout of a part of the SMM device that is thermally isolated from the vertical and lateral actuators. (Bottom) SEM showing thermal de-coupling.

and Fig. 3-18.

Another similar challenge in SMMs with integrated scanners is that when the tip is moved, the reflected signal changes. Again, the tip moves in the approach direction with the same

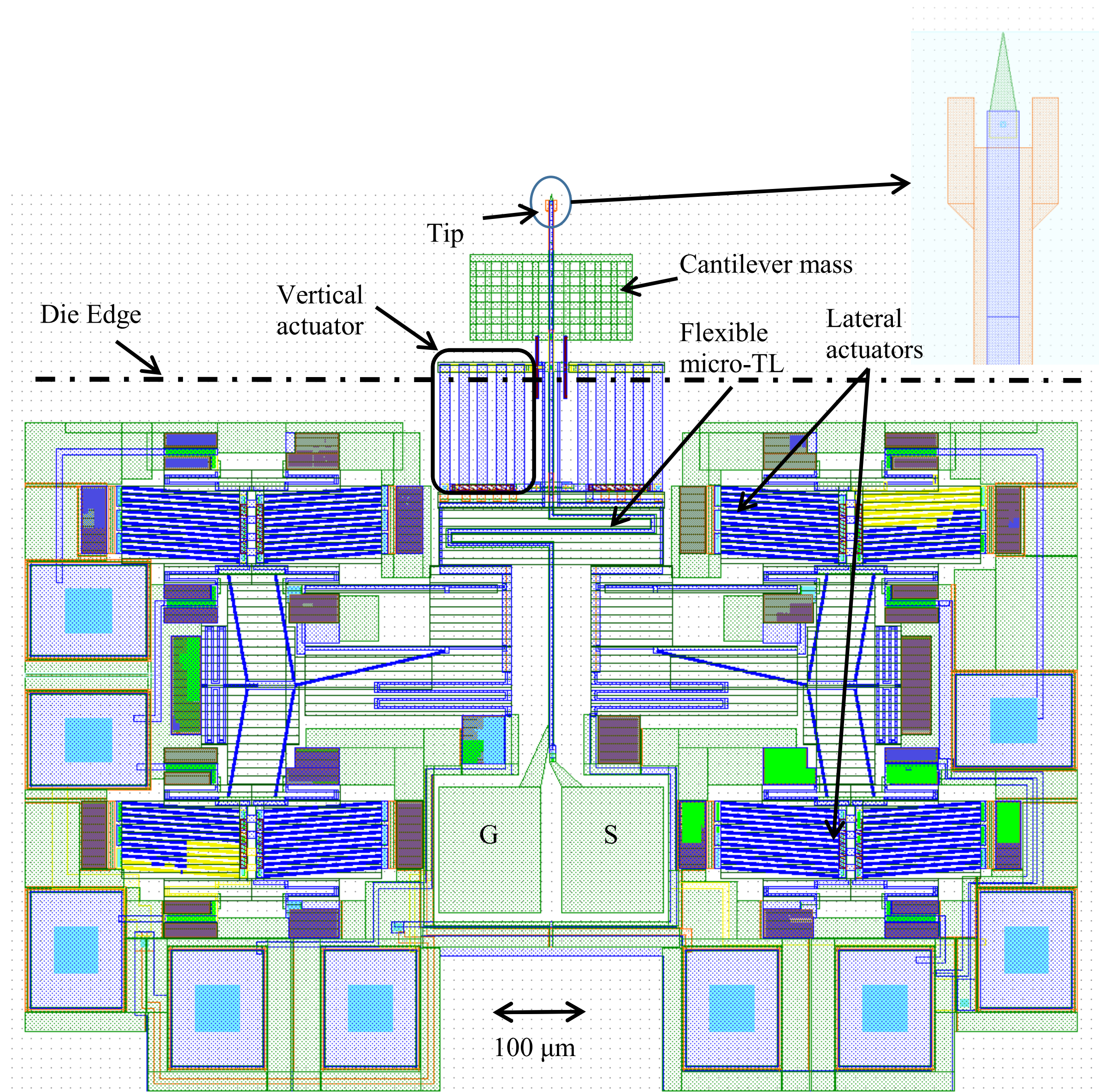

Fig. 3-17. Layout of an SMM device with isothermal scanner design with 4 chevron actuators.

frequency as the tapping, and in the lateral direction with the low frequency scan rate. The main challenge is de-coupling the movement of the microwave path in the approach direction from the tip-sample interaction that is measured at the same frequency. This signal can be calibrated with a known sample with low dielectric constant, so that any change in amplitude of the detected signal will be because of tip-sample interaction.

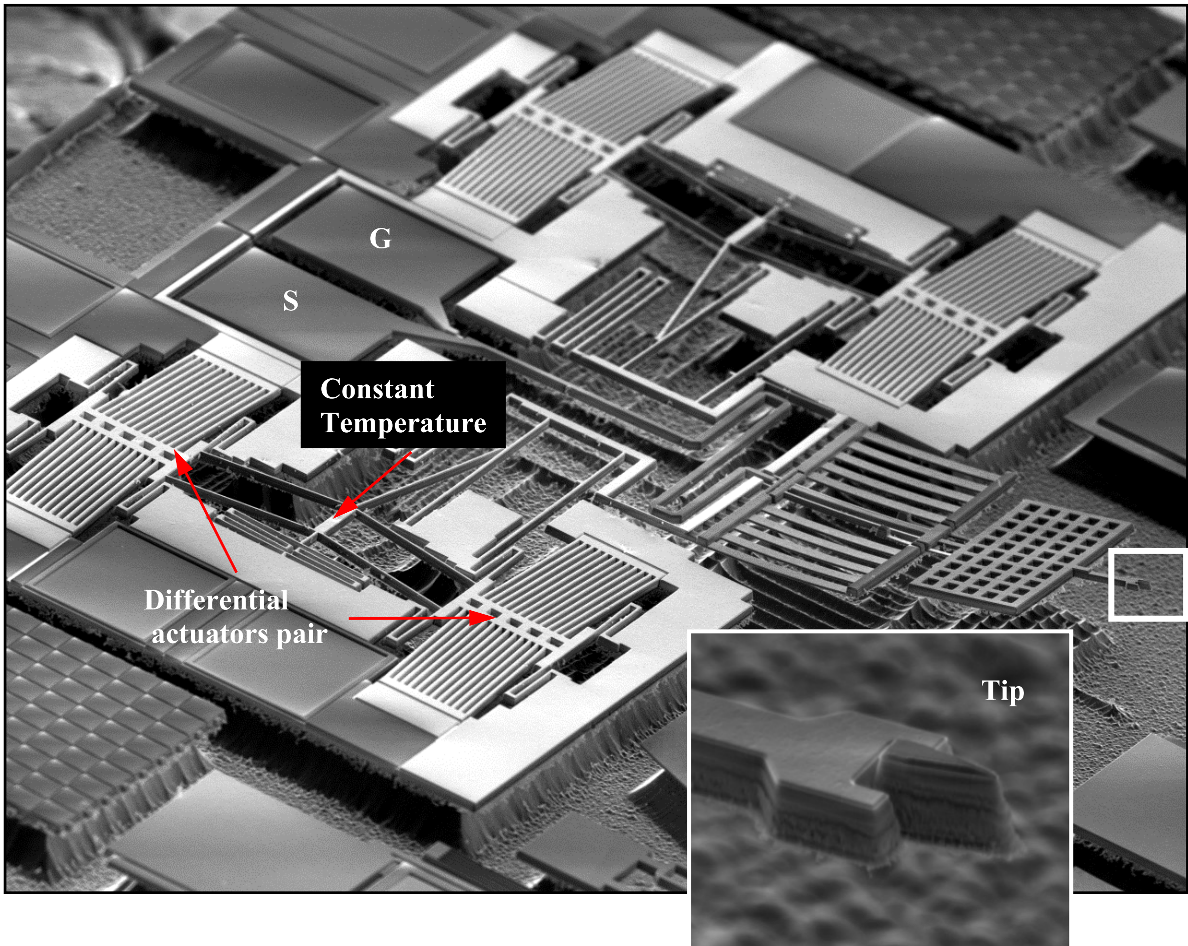

Fig. 3-18. SEM image of an SMM with isothermal scanner design.

Chapter 4

Analysis and Design of CMOS-MEMS Scanning Microwave Microscopes

As discussed in previous chapters, CMOS-MEMS SMM has several advantages over conventional SMMs, such as on-chip scanners and piezoresistive tip-sample distance control that eliminates the need for bulky scanners and cumbersome laser/photodiode detection methods, respectively. Therefore this type of SMM has the benefits of being smaller and cheaper; but, being fabricated on CMOS and integrated with the scanning actuators, it suffers from higher loss in both silicon and the conductor material. CMOS 0.35μm technology from TSMC uses a silicon substrate with approximately 12 S/m of resistivity, and the conductor is an alloy of aluminum with approximately 1.7×10^7 S/m of conductivity (three times less than copper), which is quite lossy. Also the metal thickness is less than 1 μm, which is further reduced after the RIE oxide etching because the exposed metal layers are milled to some extent; if the metal is not protected, thicknesses in the order of 0.5-0.6 μm are observed. Hence, sensitivity analysis and improvements to the entire SMM system are imperative.

In this chapter, CMOS-MEMS SMM is first described from an overall system point of view. Then, a quality factor analysis is presented for sensitivity analyses of different SMMs. After that, with the help of a lumped model and EM simulations, the sensitivity of the CMOS-MEMS SMM system is analyzed. Finally, the measurement circuit for SMM is explained and end calculations for typical values of the CMOS-MEMS SMM are presented to show the smallest detectable capacitor. It is worth noting that the analysis and suggestions presented in this chapter can be applied to any Scanning Microwave System or, even more generally, to any microwave system that needs to sense a small signal.

4.1 Overall SMM Description

This chapter provides the designer with a tool to systematically analyze and improve the sensitivity of the overall SMM system. Here, sensitivity improvement means getting maximum change at the output of the system when the tip-sample impedance changes. A block diagram of the entire SMM system is shown in Fig. 4-1. It consists of a sharp tip in close proximity to the sample under test, an SMM device fabricated with CMOS-MEMS technology, a matching network, and the measurement system.

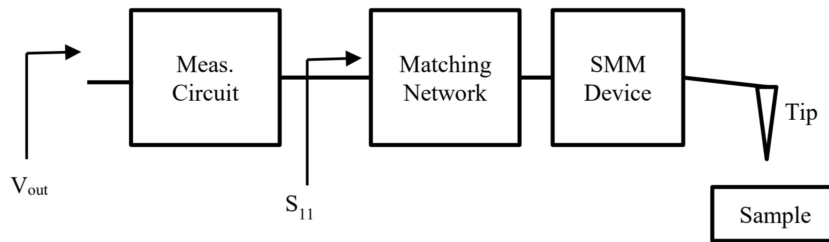

Fig. 4-1. Block diagram of the SMM system, which includes; tip-sample interaction, SMM device fabricated with CMOS-MEMS technology, the matching network and the measurement system.

The objective here is to maximize V_{out} with a known change in the tip-sample impedance. In order to obtain the best sensitivity, it is important to deliver the maximum signal to the tip to create an interaction with the sample. The input impedance of the SMM device is very high, since the end of the transmission line (at the tip) is open circuit and the length of the transmission line to the tip is electrically small (smaller than $\lambda/10$) at frequencies below 20 GHz. Therefore, in the SMM system, a matching network is required to match the high impedance of the SMM device to that of the measurement system (here, it is 50 ohm). In this chapter, different options for the matching network will be investigated and compared.

The overall design and analysis is divided into four main parts: 1) a micro-transmission line that carries the signal to the tip; 2) coplanar waveguide pads and transition to the micro-TL; 3) matching network, and 4) measurement circuit. Each section must be carefully designed for maximum sensitivity. The design and impact of each part will be described in

detail, and guidelines for improved sensitivity will be given. A quality factor analysis is also presented that gives the designer better insight into the impact of each section on overall sensitivity.

The measurement circuit after the matching network is responsible for capturing small changes of the reflected signal as a result of tip-sample interaction. At the end of the chapter, we describe how a microwave interferometry technique can help improve sensitivity.

4.2 Device Description

Detailed fabrication process of the CMOS-MEMS device (shown in Fig. 4-2) is described in Chapter 3. The microwave signal path of the SMM device consists of a Coplanar Waveguide (CPW) or a slot-line pair of pads (used for wire bonding to a PCB) that transition to a flexible micro-transmission line (micro-TL), which in turn guides the signal to the tip, as shown in Fig. 4-2. It is important to use a shielded micro-TL to prevent interaction with the medium and radiation from the micro-TL itself, and to localize the interaction between the tip and the sample. This requires a pair of signal-ground to be routed to the tip. The micro-TL should also be flexible so that it can be moved with electrothermal actuators during scanning. There are two chevron electrothermal actuators at both sides of the device that move the tip (and the micro-TL) in the lateral direction, and a set of oxide-aluminum bimorph beams that can move the tip in the vertical direction.

4.3 Quality Factor Analysis

One can look at the matching network and the SMM device as a resonator, similar to conventional SMMs. From this perspective, the change in input reflection coefficient as a result of change in tip-sample interaction impedance can be studied based on the parameters of the microwave resonator – namely, the quality factor and the resonance frequency. The matching network can either be lumped or distributed. It will be shown that if the resonator

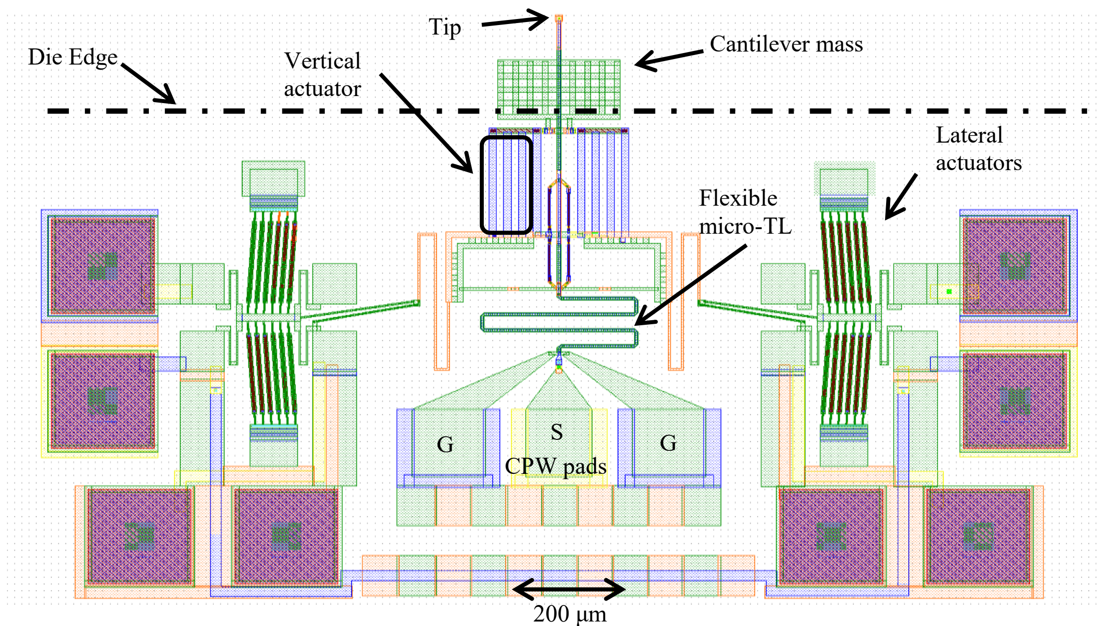

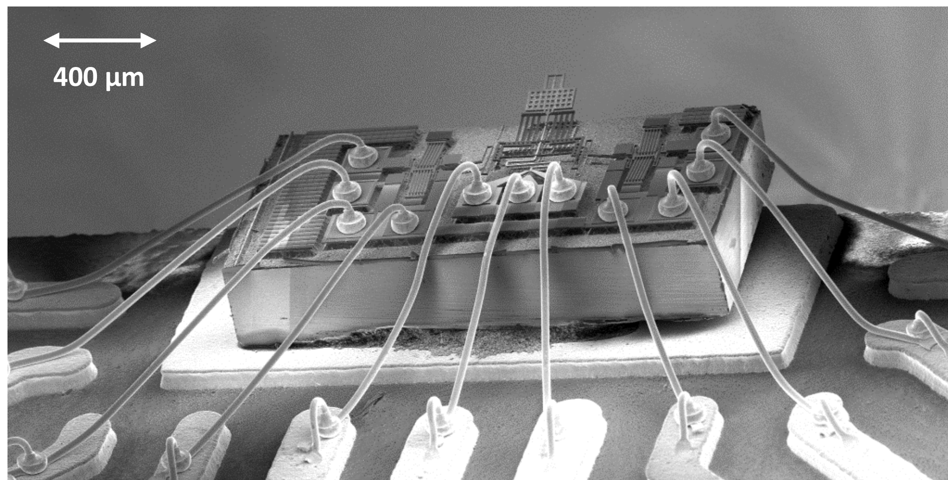

Fig. 4-2. (Top) SMM device and its components, and (bottom) and SEM image of wire bonded device.

is a lumped RLC, $|\Delta S_{11}|$ will be proportional to the square of the quality factor (Q^2) of the lumped resonator, but if it is a distributed resonator (e.g., stub matching circuits), it will approximately be proportional to the Q of the distributed resonator. In either case, an improvement in sensitivity will be achieved by improving the quality factor of the overall SMM system.

4.3.1 Lumped RLC resonator matching

For the case of lumped RLC resonator loaded with a small capacitor as shown in Fig. 4-3, closed form formulas are derived here.

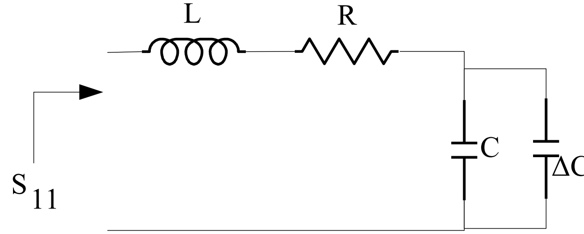

Fig. 4-3. Series resonator loaded with a small capacitor ΔC

In order to get input matching we can choose $R=Z_0$. Thus for a series RLC resonator, we have:

$$Q = {}^{1}/_{\omega CR}\ , \omega = {}^{1}/_{\sqrt{LC}} \tag{4-1}$$

Therefore, we can find L and C as a function of frequency and quality factor:

$$C = {}^{1}/_{R\omega Q}\quad , L = {}^{1}/_{C\omega^2} \tag{4-2}$$

Next, we can find the change in input reflection coefficient $|\Delta S_{11}|$, if the load changes by ΔC

$$|\Delta S_{11}| = \left|\frac{Z_{in}^1 - Z_0}{Z_{in}^1 + Z_0} - \frac{Z_{in}^0 - Z_0}{Z_{in}^0 + Z_0}\right| \tag{4-3}$$

where Z_{in}^1 is the input impedance when there is a load impedance of ΔC and Z_{in}^0 is when there is no load. If we assume that the change in load is very small compared to Z_{in}^0, one can write

$$Z_{in}^0 = Z_{in}^1 = Z_{in} \tag{4-4}$$

$$|\Delta S_{11}| = \left|\frac{Z_{in}^1 - Z_{in}^0}{Z_{in} + Z_0}\right| = \left|\frac{\Delta Z_{in}}{Z_{in} + Z_0}\right| \tag{4-5}$$

$$\Delta Z_{in} = \frac{j\Delta C}{\omega C^2} \tag{4-6}$$

where at resonance ($\omega = \omega_0$), $Z_{in} = Z_0 = R$:

$$|\Delta S_{11}| = \left|\frac{j\Delta C}{2R\omega_0 C^2}\right| = Q^2\, \Delta C \frac{Z_0\omega_0}{2} \tag{4-7}$$

From equation (4-7), one can observe that for a lumped RLC resonator model, change in S_{11} is directly proportional to the square of the quality factor of the resonator and directly proportional to the resonant frequency and characteristic impedance of the measurement system. Except for the quality factor the other two parameters are usually determined by the application, Z_0 is usually 50 ohms, but we may have a choice for ω_0 if it is not strictly defined by a specific application.

4.3.2 Stub matching

For single-stub matching, deriving a closed form expression is not straightforward, but it can be studied with simulation software; using Keysight's ADS we find:

$$|\Delta S_{11}| \cong Q_{TL} \Delta C \frac{Z_l\, \omega_0}{\beta l} \tag{4-8}$$

where Q_{TL}, Z_l and β are the quality factor, characteristics impedance and propagation constant of the transmission line. Description of the simulation method: To find the empirical simulation-based equation of (4-8), the circuit shown in Fig. 4-4 is simulated in Keysight's ADS, using a standard transmission line model, with and without the ΔC load (1aF is used). The two S_{11} are subtracted from each other to get $|\Delta S_{11}|$. Several simulations are carried out for each parameter (Q_{TL}, Z_l, ω_0 , βl) and for both open and short circuit stubs to find their relationship with change in S_{11}. In each ADS circuit simulation point shown in Fig. 4-5, the four parameters (Q_{TL}, Z_l, ω_0 , βl) are first set, and then an optimization is run to get a better than 25 dB return loss for S_{11} by changing L_1 *and* L_{stub}. Fig. 4-5 shows the comparison between equation (4-8) simulated in MATLAB and ADS circuit simulations (similar to Fig. 4-4). The stub matching transmission lines make either quarter lambda or half lambda resonators, depending on whether the stub is short circuit or open circuit. Thus, $l = L_1 + L_{stub}$

$=n\lambda/4$ (n is integer). In equation (4-8), $Q_{TL} = \beta/2\alpha$ and $\beta l = n\pi/2$ (n is integer).

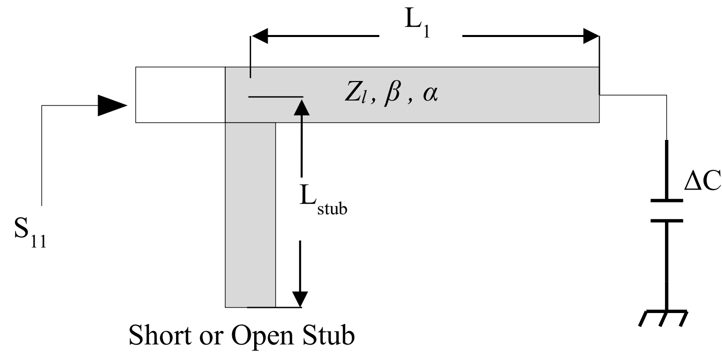

Fig. 4-4. Stub matching connected to a small capacitor ΔC. L_1+L_{stub} (grey TLs) makes a resonator.

Similar to the lumped RLC case, $|\Delta S_{11}|$ is proportional to Z_l and ω_0 for stub matching, but there are two important differences here. Firstly, in stub matching, change in S_{11} is proportional to Q_{TL}, and secondly, it is inversely proportional to βl, which means the shortest possible transmission line resonator at ω_0 gives the best sensitivity. It is interesting to note that the higher order modes of distributed resonators (higher values of βl) show less improvement in $|\Delta S_{11}|$. This can be intuitively described by the fact that at higher order mode resonators, a smaller portion of the resonator gets perturbed by the tip-sample interaction and thus less change is observed in S_{11}. In looking at the impedance of the SMM device (Fig. 4-33), one can see that it has a lossy capacitive load, so the shortest possible matching network is a short-circuited stub matching network that a quarter lambda resonator.

The actual device cannot be easily modeled with one transmission line or a simple lumped model because it has several sections including the micro-TL connected to the tip and the bonding pads transmission line. However, for the case of two transmission lines connected together as shown in Fig. 4-6, one can find a formula for the overall system sensitivity based on the overall Q factor.

In more complicated scenarios, however, simulations or circuit models can be used for accurate analysis. The quality factor analysis presented for a single transmission line can provide some insight towards better design and sensitivity. Let us assume that the quality

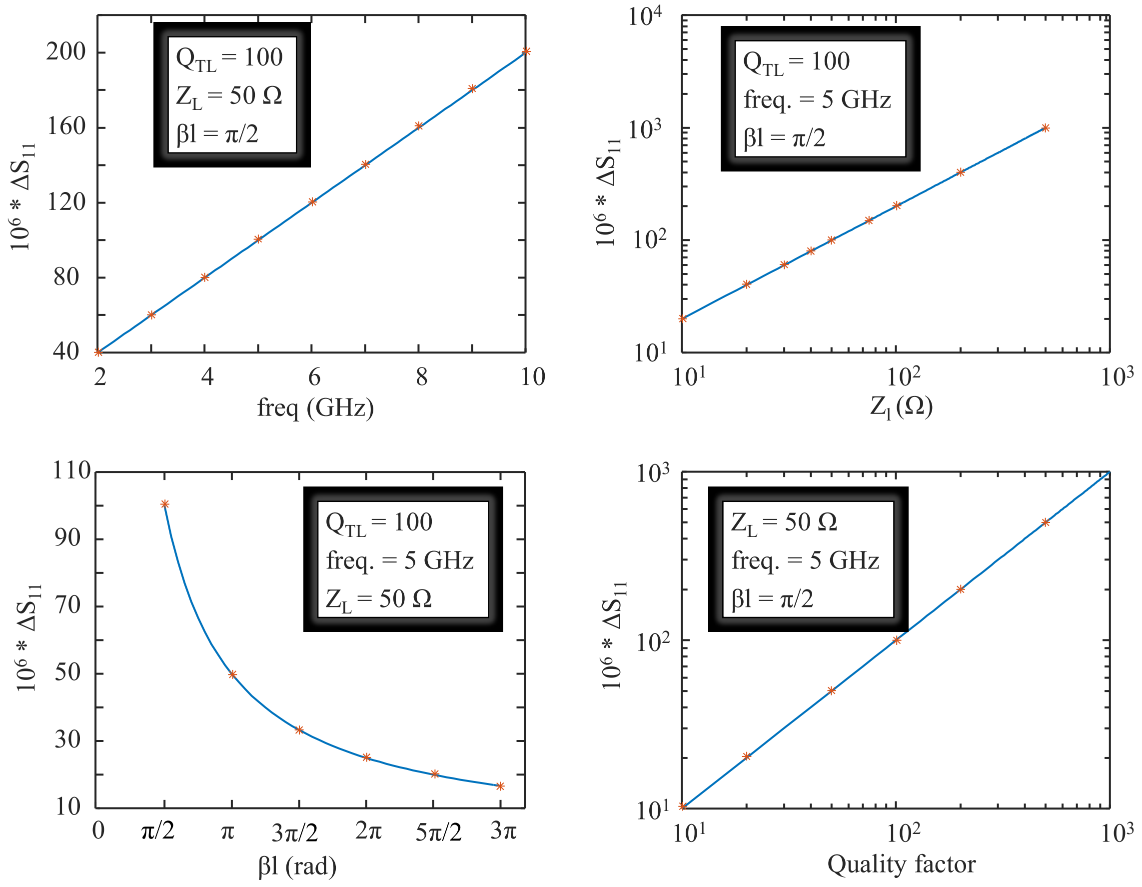

Fig. 4-5. Comparing equation (4-8) simulated in MATLAB, with circuit simulations using a standard transmission line model in ADS. Solid-line: MATLAB simulation, Asterisks: ADS circuit simulation points.

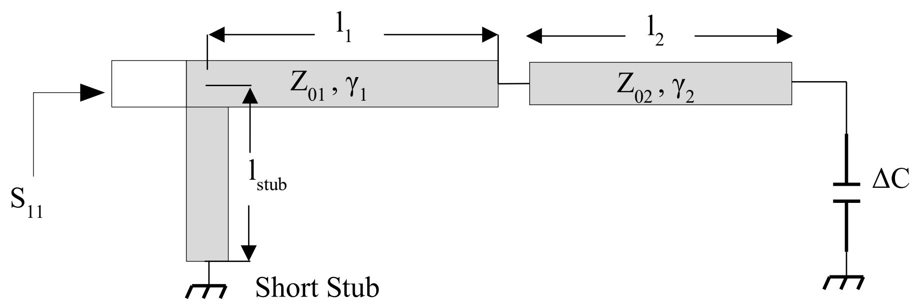

Fig. 4-6. Sensitivity of a system with two transmission lines connected together.

factor of each transmission line is divided in two parts, namely conductive quality factor (Q_c)

and dielectric quality factor (Q_d). Fig. 4-7 shows the voltage and current distribution along a quarter lambda transmission line.

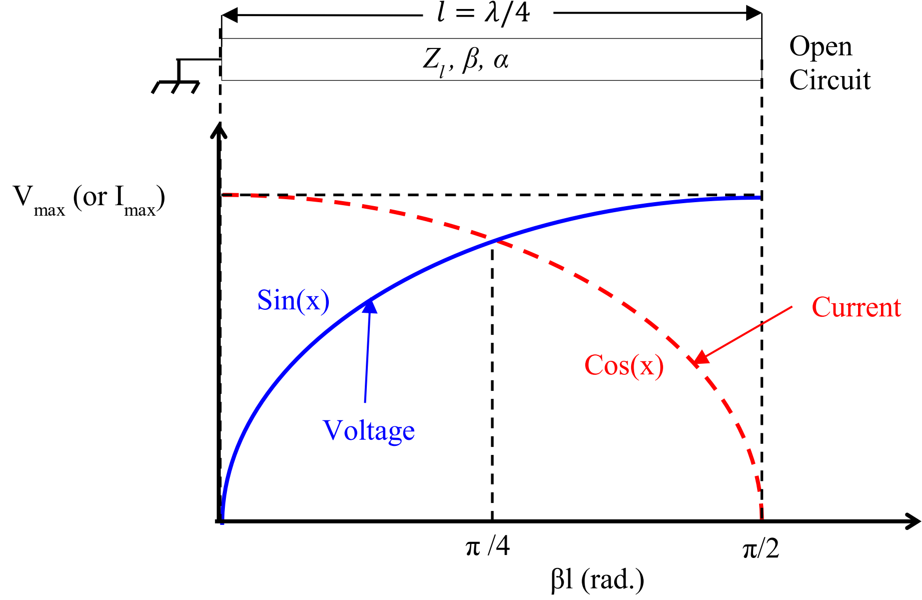

Fig. 4-7. Voltage and current distribution along a quarter lambda transmission line resonator.

Voltage is minimum at the short-circuit side and maximum at the open-circuit side, current is the opposite. Knowing the conductive loss is proportional to i^2 and dielectric loss is proportional to v^2, we can deduce the following equations:

$$Q_c = \omega \frac{max.\ stored\ energy}{conductive\ lost\ power}, \qquad Q_d = \omega \frac{max.\ stored\ energy}{dielectric\ lost\ power} \tag{4-9}$$

$$Q_c^{-1} = \frac{\left(Q_{c1}^{-1} \int_0^{\theta 1} \cos^2(\theta)\, d\theta + Q_{c2}^{-1} \int_{\theta 1}^{\pi/2} \cos^2(\theta)\, d\theta\right)}{\int_0^{\pi/2} \cos^2(\theta)\, d\theta} \tag{4-10}$$

$$Q_d^{-1} = \frac{\left(Q_{d1}^{-1} \int_0^{\theta 1} \sin^2(\theta)\, d\theta + Q_{d2}^{-1} \int_{\theta 1}^{\pi/2} \sin^2(\theta)\, d\theta\right)}{\int_0^{\pi/2} \sin^2(\theta)\, d\theta} \tag{4-11}$$

$$Q_t^{-1} = Q_c^{-1} + Q_d^{-1} \tag{4-12}$$

where $\theta_i = \beta_i l_i$,i=1,2. To get a better sense of these equations let us assume that that the electric lengths of the two transmission lines are equal ($\theta_1 = \theta_2 = \pi/4$) and we want to find the overall

quality factor due to individual Q factors. Then we will have:

Table 4-1. Overall quality factor due to individual Q factors when two different transmission lines are connected to make a quarter lambda resonator

Q_{c1}	Q_{d1}	Q_{c2}	Q_{d2}	Q_t
Q_{c1}	Inf.	Inf.	Inf.	1.22 Q_{c1}
Inf.	Q_{d1}	Inf.	Inf.	5.5 Q_{d1}
Inf.	Inf.	Q_{c2}	Inf.	5.5 Q_{c2}
Inf.	Inf.	Inf.	Q_{d2}	1.22 Q_{d2}

Similarly, from equations (4-10) to (4-12), we can find the total quality factor as a function of the 4 conductive and dielectric quality factors and write:

$$\frac{1}{Q_t}=\frac{1}{1.22\,Q_{c1}}+\frac{1}{5.5\,Q_{d1}}+\frac{1}{5.5\,Q_{c2}}+\frac{1}{1.22\,Q_{d2}} \tag{4-13}$$

This shows that at the short-circuit side, conductive loss is dominant while at the open-circuit side dielectric loss is dominant. In Fig. 4-6 we can assume that the second transmission line is the micro-TL in the SMM device and the first section (l_1 and l_{stub}) is the transmission line on the PCB board.

Based on the presented analysis, we can then arrive at some useful conclusions. First, the PCB transmission line has a lot higher Q than any micro-TL that can be fabricated on CMOS-MEMS, so a smaller l_2 is better. Due to mechanical constraints, the length of the micro-TL line generally cannot be reduced, but it is possible to decrease the electric length, $\beta_2 l_2$, which is in fact what we need. For this, micro-TLs with smaller effective permittivity should be designed.

A second conclusion is that, in a quarter lambda resonator, the overall Q is less affected by the conductive loss ($\propto i^2$) of the micro-TL but degrades more with substrate loss ($\propto v^2$). In most instances of transmission lines on the CMOS-MEMS process, Q is dominated by conductive loss because the lossy silicon is etched except for where the bonding pads are, because they require anchoring to the substrate. For this section, either a CPW or coplanar

stripes are used. A thorough discussion on the effects of bonding-pad loss through substrate and how to decrease this loss is presented in section 4.4.3. An alternative approach for improving sensitivity is to design the micro-TL with very high characteristic impedance, as suggested by equation (4-8) and circuit simulations.

4.3.3 Half lambda plus shunt 50 ohm (*λ/2+50Ω*)

Another method used by some researchers [33] for matching in SMM in collaboration with Keysight, is the half lambda plus shunt 50 ohm (λ/2+50Ω) approach. In this method, a low-loss coaxial cable is connected to the SMM probe, and the shunt 50 ohm resistor is connected to the ground at the end of the cable, as shown in Fig. 4-8. With some simplifying assumptions, we can find changes in S_{11} if the load is changed by ΔC. We assume that the cable loss is small and that ΔC is very small.

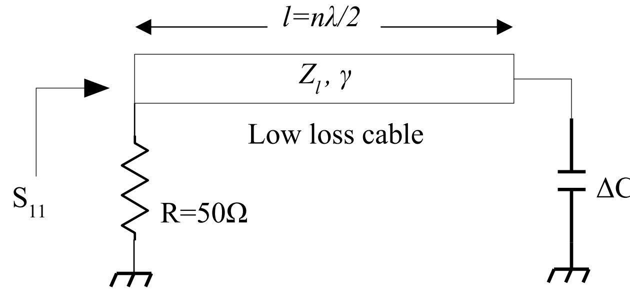

Fig. 4-8. Half lambda plus shunt 50 ohm (λ/2+50Ω) matching method used by Keysight Technologies.

Then, one can write

$$y_{in} = (\frac{1}{R}) + \frac{1}{Z_l}\left(\frac{1 - e^{-2\gamma l}e^{-j2\omega\Delta C Z_l}}{1 + e^{-2\gamma l}e^{-j2\omega\Delta C Z_l}}\right) \qquad (4\text{-}14)$$

where $\gamma = \alpha + j\beta$ is the complex propagation constant. If we substitute $l = n\lambda/2$ (n is an integer) and use the approximation of:

$$\frac{1 - e^{-x}}{1 + e^{-x}} = tanh\left(\frac{x}{2}\right) \cong \frac{x}{2} \quad , \qquad if\ |x| \ll 1$$

where $x = 2\alpha l + j2\omega\Delta C Z_l$. By putting $Y_0 = 1/R$ (=.02, in 50 ohm system) then change in S_{11}

(with and without ΔC) can be found:

$$|\Delta S_{11}| = \frac{Y_0 - y^1{}_{in}}{Y_0 + y^1{}_{in}} - \frac{Y_0 - y^0{}_{in}}{Y_0 + y^0{}_{in}} \cong \left|\frac{\alpha l + j\omega \Delta C Z_l}{2 Z_l Y_0} - \frac{\alpha l}{2 Z_l Y_0}\right| = \frac{Z_0 \omega \Delta C}{2} \tag{4-15}$$

where $y^1{}_{in}$ is input admittance when the load is ΔC and $y^0{}_{in}$ is when there is no load (open circuit). Note that here Z_l is the characteristics impedance of the half lambda transmission line and Z_0 is the characteristics impedance of the system (e.g.; Z_0 of Network Analyzer). Equation (4-15) is valid for a lossless (and low loss) transmission line and for small change in load impedance and shows that sensitivity improves with increased frequency, however it does not depend on the Q or Z_l of the transmission line.

A comparison between these three methods and detailed design for stub-matching is presented in section 4.5.

4.4 Circuit Model Analysis

Full wave simulation of the entire SMM system is very difficult and time consuming due to having very small and very large features at the same time. The area of interaction between the tip and the sample is very small (~100 nm) compared to the PCB area (~ 1 cm) and even to the CPW bonding pads (~ 200 µm). Therefore, the change in the input reflection coefficient $|\Delta S_{11}|$, as a function of change in the impedance of the sample ($|\Delta Z_{sample}|$) is so small that very large meshes are required to capture the difference between two different samples with different electrical properties. Often, the calculation error is larger than the change that needs to be measured. To put this in perspective, an example of typical expected values will be calculated here. Let us assume:

$$\Delta C = 1\ aF, Q_{Stub} = 50, Z_0 = 50, f_0 = 5\ GHz, \beta l = \pi/2 \tag{4-16}$$

If these values are put in equation (4-8), $|\Delta S_{11}|=5\times10^{-5}$, which means that error between consecutive passes in HFSS simulation should be at least 5×10^{-5}. However, this is nearly impossible, even with today's powerful computers and computational servers. Table 4-2

shows a typical convergence of such a system. After 8 passes and more than 100,000 tetrahedrons, the $|\Delta S_{11}|$ error is still larger than 0.01. In other words, this error is about 300 times larger than the required accuracy to capture the tip-sample interaction of two different materials.

Table 4-2. Convergence table for HFSS simulation of the entire CMOS-MEMS SMM system, showing large errors despite the large number of tetrahedrons. This error is 300 times larger than the required accuracy to capture tip-sample interactions of two different materials.

Pass Number	Total Tetrahedra	Max Mag. Delta S
1	36256	N/A
2	45008	0.8047
3	49323	0.18527
4	52665	0.039492
5	63074	0.052281
6	77202	0.032422
7	87804	0.020664
8	108134	0.014643

One possible way to overcome this problem is to divide the simulation into 3 or 4 smaller ones. For example, one way of dividing it is to simulate: 1) tip-sample interaction, 2) micro-transmission line, 3) CPW or coplanar strips pads, and 4) matching network on PCB and bond-wires. The problem of convergence and error for the tip-sample interaction is still relevant here. To deal with this problem, we note that most of the time we are interested in the change in S_{11} between two or more different samples and not the absolute S_{11} value. Therefore, we can simulate the tip-sample interaction with a particular sample and save the final mesh, and then use this same mesh for other samples, changing only the electrical properties of the sample (i.e., no change in geometry).

However, even if we overcome all these hurdles in full-wave simulation, the result will still be only an approximate result, for a few reasons. First, CMOS material properties will change within a few percentage points from run to run and batch to batch, and second, in

CMOS-MEMS SMM, the entire structure is moved by actuators that bend and heat up the structure, etc., which changes the properties of the material and the micro-transmission line. Therefore, any simulation is only going to be only an approximation. Apart from technical difficulties in simulating the entire structure in full-wave simulators (such as HFSS), there are several benefits to building a circuit model to study and design SMMs for sensitivity improvement and investigating different scenarios, as explained in the rest of this chapter. Different parts of SMM (namely, tip-sample interaction, micro-transmission line, tapered transition to bonding pads, CPW bond pads and PCB board, and matching network) are studied in the following sections.

4.4.1 Tip-sample interaction

For the tip-sample interaction impedance, lumped models based on different samples were proposed in [58]. For CMOS-MEMS SMM, the tip-sample interaction is simulated in HFSS and then the parameters of the model are extracted in Keysight's ADS by matching FEM and

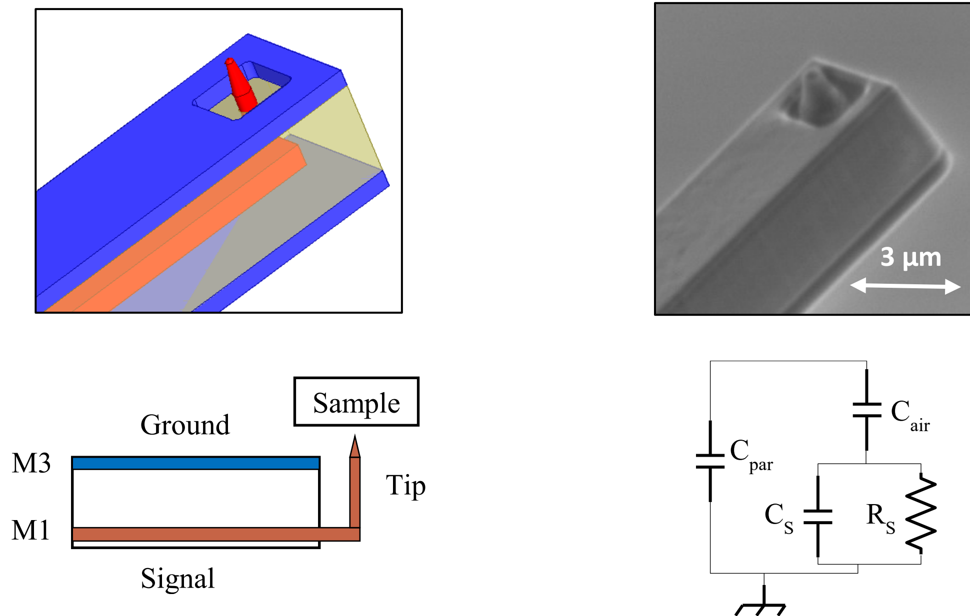

Fig. 4-9. HFSS simulation of a stripline micro-TL and the tip-sample interaction, SEM image of the tip and the tip-sample circuit model.

circuit simulations (Fig. 4-9). In this model, C_{air} is the capacitance between the tip and the sample and depends on the tip dimension and tip-sample distance; C_s and R_s are the capacitance and resistance models for the sample impedance; and C_{par} is the parasitic capacitance between the probe and the surrounding medium. With effective shielding, C_{par} can be neglected or absorbed in the micro-transmission line model. For a dielectric sample close to the tip (tip-sample distance smaller than tip dimension), one can write [3]:

$$C_{air} = \epsilon_0 \frac{D^2}{g}, \qquad C_s = \epsilon_0 \epsilon_r D, \qquad R_s = \frac{1}{\omega \epsilon_0 \epsilon_r \tan\delta \, D} \tag{4-17}$$

where D is the effective length of the tip and g is the gap between the tip and the sample. It is useful here to work out some typical numbers. If we assume a tip-sample distance of 40 nm, an effective tip diameter of 150 nm and a dielectric constant of 3 and 7 for two different materials, we get C_{air} = 5 aF, C_{s1} = 4 aF (ε_r=3), C_{s2} = 9.3 aF (ε_r=7) and R_s=infinity. Therefore, ΔC = 1 aF. For consistency, a 1 aF change in sample's impedance is assumed in the simulations. It is important to note that tip-sample distance has an inverse relationship with sensitivity. For example, with the above model, increasing the tip-sample distance from 40 nm to 100 nm will decrease ΔC by a factor of 3 and consequently, sensitivity will be decreased by the same factor. This shows the importance of having an accurate method for controlling the tip-sample interaction discussed in previous chapters.

4.4.2 Micro-transmission line

SMM works based on microwave interaction between the tip and the sample. Therefore, a transmission line is required to take the microwave signal from the bonding pads to the tip. Micro-transmission line design is important for improving the overall sensitivity of the system, especially in the rather lossy process of 0.35 μm CMOS-MEMS, which is what we use. In a conventional SMM, a regular coaxial line is used to carry the microwave signal to a high quality factor coaxial resonator [3], [28], and the center conductor is usually extended to be used as the tip. In more recent SMMs, the tip is at the end of a cantilever, and either a

single metal trace of around 300 µm [33], a stripline [59], or a CPW [4] is used to carry the microwave signal to the tip. In this thesis, we present a more comprehensive investigation of different micro-transmission lines implemented in a CMOS chip to come up with the best choice. Here, again, even though the analysis is done for CMOS-MEMS SMM, it can be applied to other versions of SMM as well.

The choice of transmission line is highly dependent on the fabrication process and device structure. In this thesis, we use 0.35 µm technology from TSMC (Taiwan Semiconductor Manufacturing Company), which has 4 metal and 2 poly layers that can be used for micro-TL design. Numerous types of transmission lines, including microstrip, stripline, CPW, and rectangular coaxial line, are possible in this process. Also, since scanners and position sensors are integrated in the chip in this type of SMM to move the tip in 3 directions, the micro-TL needs to be flexible and lightweight. One design constraint is that the maximum width of the micro-TL should be less than 6 µm, as otherwise it will be too heavy to move. Thus, very wide micro-TLs such as CPW lines will not result in desirable mechanical properties. Fig. 4-10 shows the cross-section of some possible choices for micro-TL design. Note that the silicon underneath the micro-TL will be etched, leaving about 15 µm of air between the metal1 layer (the lowest metal layer) and the lossy silicon substrate (resistivity ~ 8 ohm.cm), which considerably reduces substrate losses.

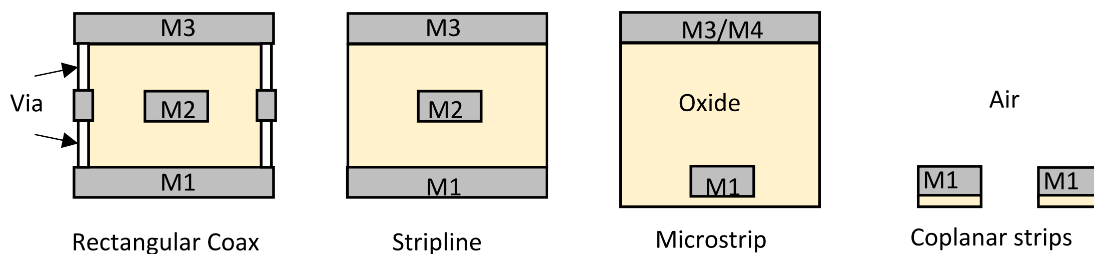

Fig. 4-10. Cross-section of some possible micro-transmission lines in teh CMOS-MEMS process.

At first glance, it is not clear which micro-TL results in the best sensitivity. One way is to simulate the entire system with different micro-TLs (with changing design parameters for each micro-TL) and compare the results. Because of the complications of simulations

explained at the beginning of this section, this method is a very time-consuming process and does not give the designer any intuition. Most transmission line analysis is done for low loss and non-radiating transmission lines. In those cases, one can usually find the properties of the TL from its cross-section. However, when dimensions and thicknesses of the metal layers become less than skin depth[2], a full-wave simulator such as HFSS and ADS is required to find an accurate model for the TL.

Let us first analyze a transmission line. A standard and accurate method to find the properties of a transmission line (such as characteristic impedance and propagation constant) is to simulate a certain length of the TL and find its S-parameters. ABCD parameters can then be found from S-parameters, and from ABCD parameters, the RLGC parameters of a transmission line can be found. This process is shown Fig. 4-11 and the following equations:

$$\gamma = \alpha + j\beta = \frac{acos\,h(A)}{(\Delta l)} \tag{4-18}$$

$$Z_0 = \sqrt{B/C} \tag{4-19}$$

$$Z_{ser} = \gamma \times Z_0 \longrightarrow L = \frac{imag(Z_{ser})}{\omega} \; [H/m], R = real(Z_{ser}) \; [\Omega/m] \tag{4-20}$$

$$Y_{shunt} = \gamma/Z_0 \longrightarrow C = \frac{imag(Y_{shunt})}{\omega} \; [F/m], G = real(Y_{shunt}) \; [S/m] \tag{4-21}$$

where γ is the complex propagation constant, β is the propagation constant and α the is attenuation constant, Δl is the length of transmission line used to find the S-parameters, Z_{ser} is the series impedance, and Y_{shunt} is the shunt admittance of the transmission line in the RLGC model shown in Fig. 4-11.

In the literature, SMMs are designed in a few different ways. Haenssler et al. [60] looks at the entire SMM system as a 2-port network and tries to minimize the insertion loss for this

[2] The Skin Effect is the tendency of an AC current to become distributed within a conductor such that the current density is largest near the surface of the conductor, and decreases with greater depths in the conductor. The electric current flows mainly at the "skin" of the conductor, between the outer surface and a level called the skin depth.

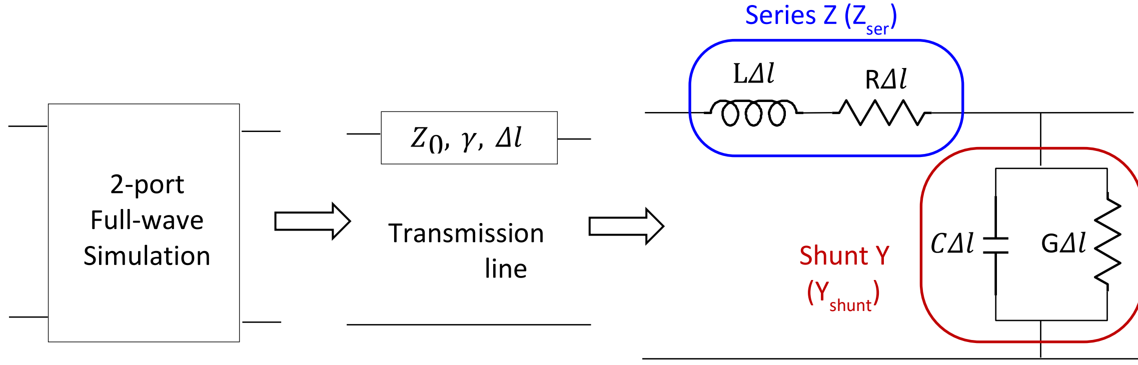

Fig. 4-11. Finding properties of a transmission line from 2-port full-wave simulation.

network. The flaw of this method is that the tip-sample impedance is nowhere near 50-ohm; in fact, it is a very high capacitive impedance. Lai et al. [61] uses a shielded stripline transmission line and argues that for best performance, the series resistance and capacitance model for the short transmission line should be minimized. While this argument may be correct for cases where series resistance is the dominant factor of transmission line loss, it is not correct for a general condition. Huber et al. [33] uses a half-lambda transmission line with a shunt 50-ohm resistor to match a single trace of about 300 µm that is connected to the unshielded part of the tip. In the following, a general method is presented for the micro-TL analysis and design.

Knowing that the entire SMM system, including the SMM device and the matching network, will make a resonator, and based on the quality factor analysis in section 4.3, one can figure out that a micro-TL that has the highest quality factor should give the best sensitivity. Therefore, quality factor analysis for transmission lines can be utilized to analyze and choose the best micro transmission line. For a transmission line at resonance [62]:

$$Q_{res} = \omega \frac{max.\,stored\ Energy}{lost\ power\ in\ one\ cycle} = \frac{\beta}{2\alpha} \tag{4-22}$$

This total Q of the transmission line is a combination of two quality factors for the series and shunt sections of the transmission line, such that:

$$Q_{cap} = \frac{\omega C}{G}\ ,Q_L = \frac{\omega L}{R} \tag{4-23}$$

where Q_{cap} and Q_L are quality factors of series L and shunt C segments of the lumped element model of the transmission line (Fig. 4-11). This method of analyzing transmission lines has two important benefits. First, the transmission line does not need to be at resonance for this analysis to be true. This is an important criterion because most of the transmission lines used for SMM are electrically short. The second benefit is that series and shunt segments of the transmission lines are separated here and can be studied individually. For example, using the standard quality factor definition of $\beta/2\alpha$, it is not easy to tell which section of the micro-TL contributes to more loss without simulations, but if Q_{cap} and Q_L are known, one can find which section should be improved.

Now let us look at the micro-TLs shown in Fig. 4-10. In CMOS, oxide is low loss and metal is lossy, especially at higher frequencies due to the thin metal layers and low conductivity of the aluminum alloy used. From this, we can see that the quality factor of the series segment is dominant. Therefore any design that improves Q_L will improve overall Q.

Now, one can intuitively say that for higher Q_L, the series inductor should be increased (or R should be decreased), which means that the separation between signal and ground metals (forward and return current) should be higher. In this instance, the total magnetic flux and consequently L increases with increased separation. The increased separation does not increase R much and, as a result, Q_L and overall Q would increase. From this simple intuitional analysis, it becomes clear that microstrip realization results in better Q than stripline or rectangular coax. As can be seen from simulation results as well as the quality factor analysis, microstrip is indeed the best choice in terms of sensitivity improvement.

The coplanar strips could also be a good choice with careful design. However, they are not shielded (so this would not be a good option near the tip) and are not suitable for meandering the micro-TL to make it flexible. Moreover, between the meander line and the tip area, a soft micro-TL is required in order to move the structure out of plane with the bimorph electrothermal actuators. In this area, other types of micro-TLs can become too stiff, so the best option is the coplanar stripes. For example, a 3-metal-layer micro-TL such as microstrip

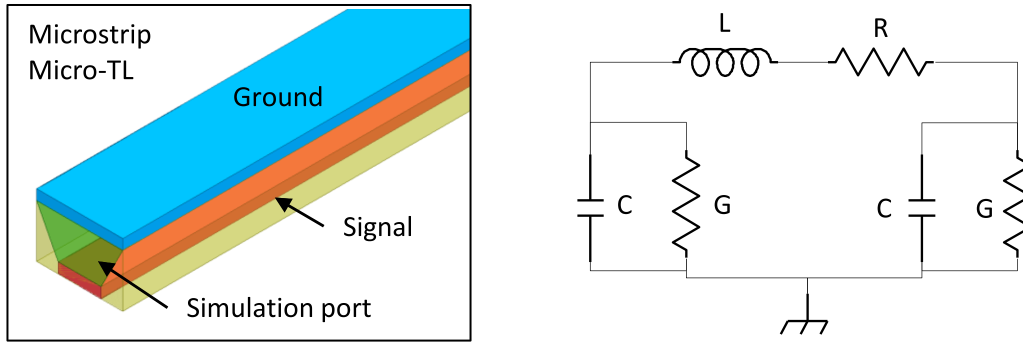

Fig. 4-12. Microstrip micro-TL and its circuit model.

or stripline will have about 200 times more stiffness than when using only the first metal layer as a coplanar stripe. This is because stiffness is proportional to thickness cubed [63], and a stack of 3 metal layers has about 200 times more stiffness than a single metal layer.

A circuit model for the micro-TL is shown in Fig. 4-12. Since the micro-TL is an electrically short transmission line smaller than λ/10, it can be modeled with only one segment of the general transmission line RLGC model. Another shunt segment is added to make a symmetrical pi model.

In this model, the series resistor is not dependent on frequency because the width and thickness are smaller than or comparable to skin depth. For a certain micro-TL (e.g., microstrip), changing the width does not significantly change the quality factor because both the inductance and the resistance of the micro-TL undergo similar changes (i.e., increasing the width decreases both R and L to the same proportion) and Q_l would not change much. However, if we increase the gap between the signal and the ground return path, R might not change much but L certainly does because the area of integration of total flux increases, and thus Q_L and consequently Q_t increases. This describes why a microstrip line promotes better sensitivity than a stripline. In the following section, a detailed analysis and comparison between different micro-TLs is presented.

4.4.2.1 Simulation results micro-TLs

In this section, simulation results for different micro-TLs are presented. First, a certain length

of the micro-TL is simulated in HFSS (200 μm). Both lumped-ports and wave-ports are used and compared in these simulations, but only lumped-port results are presented, since both resulted in similar s-parameters. An HFSS driven-modal solution is used here because the propagation mode along the micro-TLs is quasi-TEM (the other option is a driven-terminal, which is better suited for TEM modes). Next, ABCD parameters are extracted from the 2-port s-parameters, and finally transmission line properties are found using equations (4-16) to (4-21). The results of the rectangular coax (very similar to stripline) microstrip and slotline micro-TLs are presented, followed by a discussion and comparison of different lines. The electric and magnetic fields for each micro-TL are also shown to show that the correct mode is excited in the structure.

It can be noted that for all the micro-TLs, characteristic impedance is highly dependent on frequency. Furthermore, the imaginary part of the micro-TL is comparable to or in some cases even higher than the real part, which shows very high losses in the micro-TLs. Their frequency dependencies make them highly dispersive. The electric and magnetic fields of the rectangular coax micro-TL in Fig. 4-13 show that they are not completely confined and that some of the fields pass through the shield. This occurs because the shield thickness is thinner than skin depth. Another point to notice is that the series resistance does not change with frequency. This might seem surprising, but since the skin depth of this aluminum alloy is between 1.2 and 2.7 microns (which is bigger than the metal thickness and comparable to the width), all the current within a 2-10 GHz frequency range passes through all the cross-sections of the metals. As a result, resistance does not change much with frequency.

Another thing to consider is that by looking at the E- and H-fields of the microstrip and slotline micro-TLs in Fig. 4-14 and Fig. 4-15, we can see that the amplitude of the electric field passing through the silicon substrate is a few orders of magnitude smaller than the maximum electric field of the micro-TLs. Therefore, silicon substrate loss becomes negligible here, and mainly the silicon-oxide loss tangent contributes to conductance (shunt losses). This is the reason why G is almost proportional to frequency ($G \propto \omega\varepsilon''$).

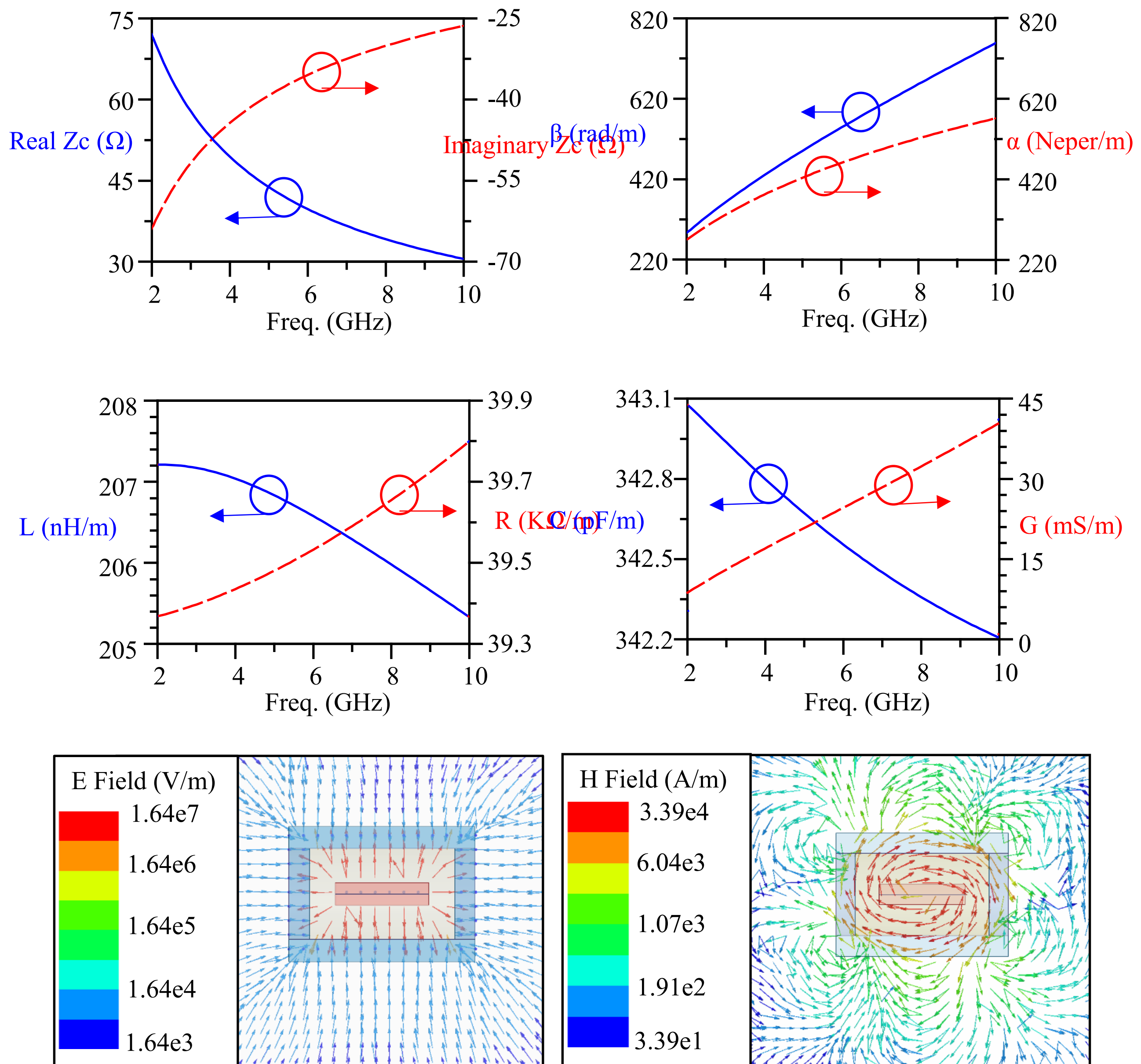

Fig. 4-13. Rectangular coax micro-TL. Top left: real and imaginary parts of characteristic impedance. Top right: propagation and attenuation constants. Middle left: inductance and resistance per unit length of the micro-TL model. Middle right: Capacitance and conductance per unit length of the micro-TL model. Bottom left: E-field at the cross-section of the micro-TL (HFSS simulation). Bottom r: H-field at the cross-section of the micro-TL (HFSS simulation).

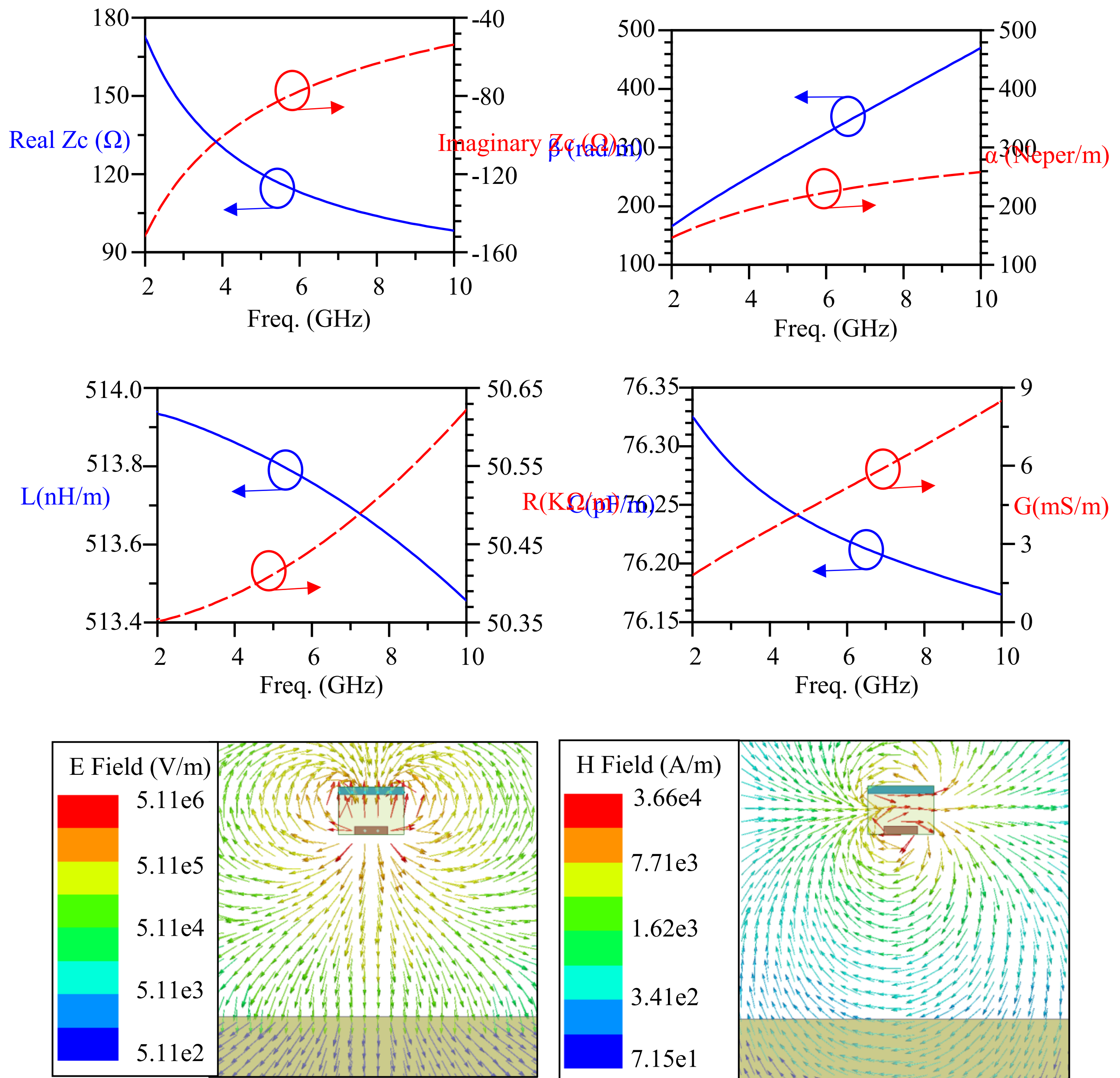

Fig. 4-14. Microstrip micro-TL. Top left: real and imaginary parts of characteristic impedance. Top right: propagation and attenuation constants. Middle left: inductance and resistance per unit length of the micro-TL model. Middle right: Capacitance and conductance per unit length of the micro-TL model. Bottom left: E-field at the cross-section of the micro-TL (HFSS simulation). Bottom right: H-field at the cross-section of the micro-TL (HFSS simulation).

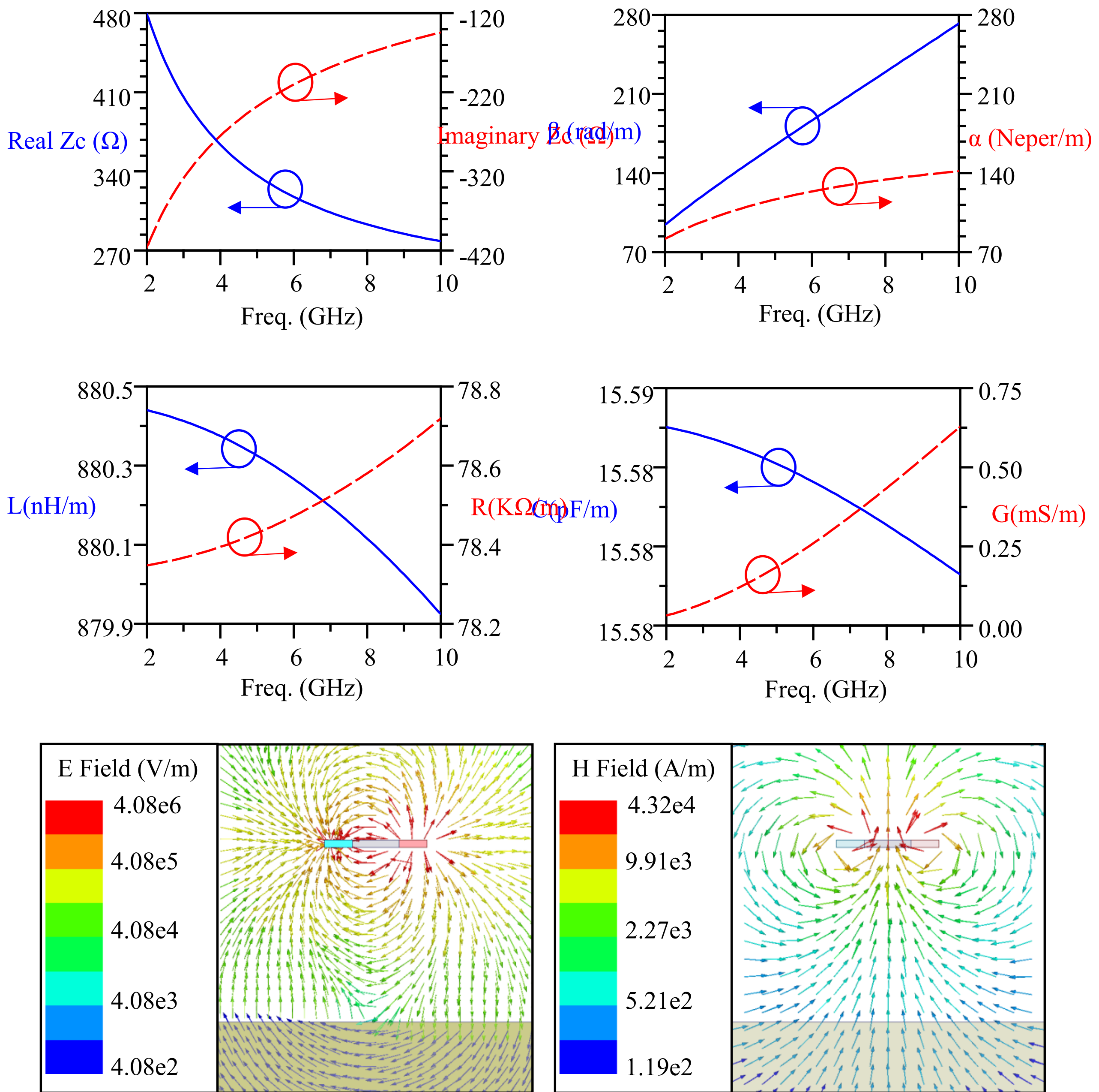

Fig. 4-15. Slotline on M1 layer micro-TL. Top left: real and imaginary parts of characteristic impedance. Top right: propagation and attenuation constants. Middle left: inductance and resistance per unit length of the micro-TL model. Middle right: Capacitance and conductance per unit length of the micro-TL model. Bottom left: E-field at the cross-section of the micro-TL (HFSS simulation). Bottom right: H-field at the cross-section of the micro-TL (HFSS simulation).

4.4.2.2 Figure of merit for the micro-TL

Now that we know the characteristics of micro-TLs, we can compare them to see which one results in better overall sensitivity of the system. To make this comparison, we assume that the lengths of the micro-TLs are the same and that the frequency of operation is also the same. By looking at equations (4-8) to (4-12), one can figure out that a micro-TL with higher Z_0 and quality factor will result in better overall sensitivity. Moreover, in realizing that micro-TLs have a significantly smaller quality factor than the PCB section, a lower electric length or effective epsilon will result in better overall sensitivity. Therefore, we can define a figure of merit based on these parameters:

$$\text{FoM}_{sensitivity} = \frac{Z_0 Q}{\sqrt{\epsilon_{r_eff}}} \tag{4-24}$$

For a discussion on quality factors of lossy transmission lines, please refer to Appendix B.

Let us first compare Z_0, effective relative permittivity and Q (=β/2α) of different micro-TLs. And after that, we can compare the newly defined figure of merit. In this comparison, the ground metal is 5.4 µm for the microstrip, stripline and rectangular coax micro-TLs and the signal line is 2.7 µm. For the slotline both the signal and ground lines are on the metal1 layer with a width of 2.4 µm and spacing of 4 µm.

In Fig. 4-16, the characteristic impedance of the slotline micro-TL is the highest, followed by microstrip. This is because more separation between signal and ground increases L and decreases C and Z_l is proportional to $\sqrt{L/C}$. For effective permittivity (Fig. 4-17), it is the opposite: a rectangular coax line has the highest effective ε_r, while a slotline has the lowest. This is in large part because there is no dielectric for the slotline micro-TL, and so it gets less effective ε_r. However, it is mainly because of the high losses in these types of transmission lines that they are so dispersive.

Quality factors (β/2α) of the micro-TLs are compared in Fig. 4-18, where we can see that slotline and microstrip are a lot better than stripline or rectangular coax. As discussed earlier, conductive loss and quality factor are dominant in these types of micro-TLs, making them

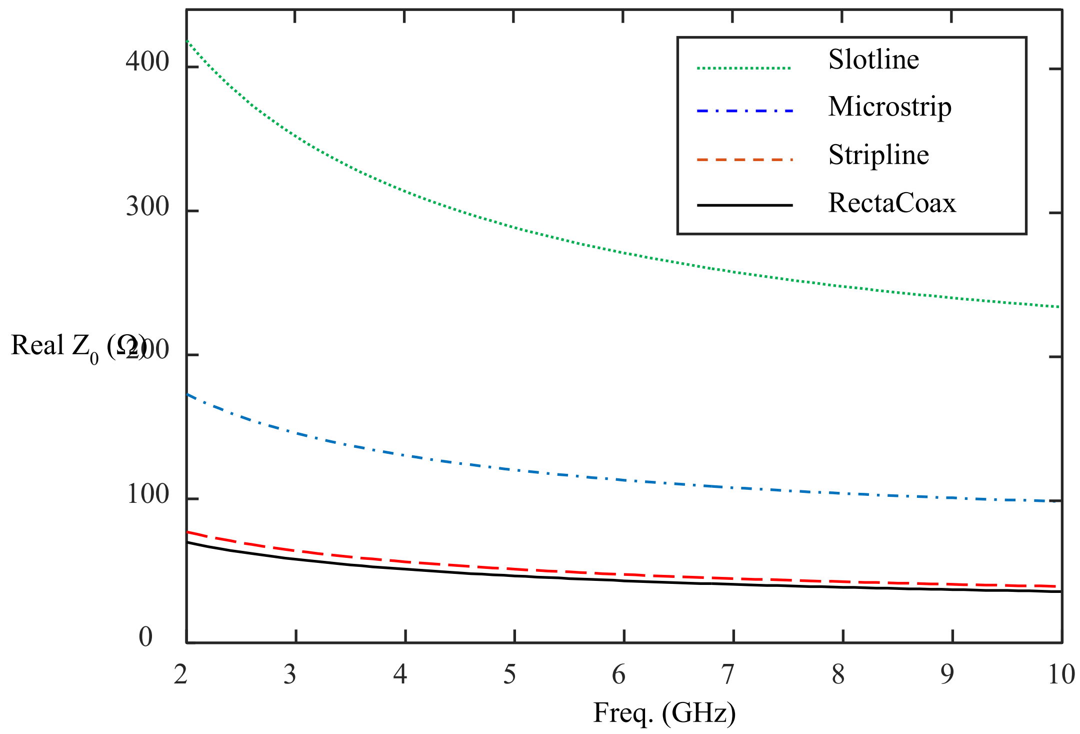

Fig. 4-16. Real part of the characteristic impedance for some of the micro-TLs.

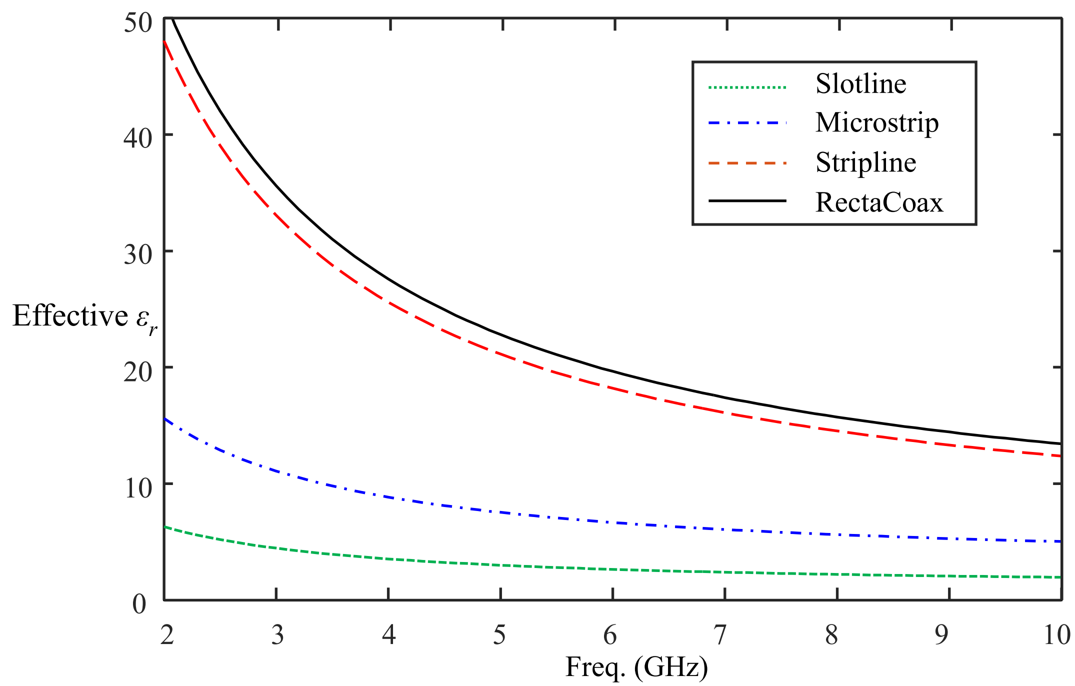

Fig. 4-17. Effective relative permittivity for some of the micro-TLs.

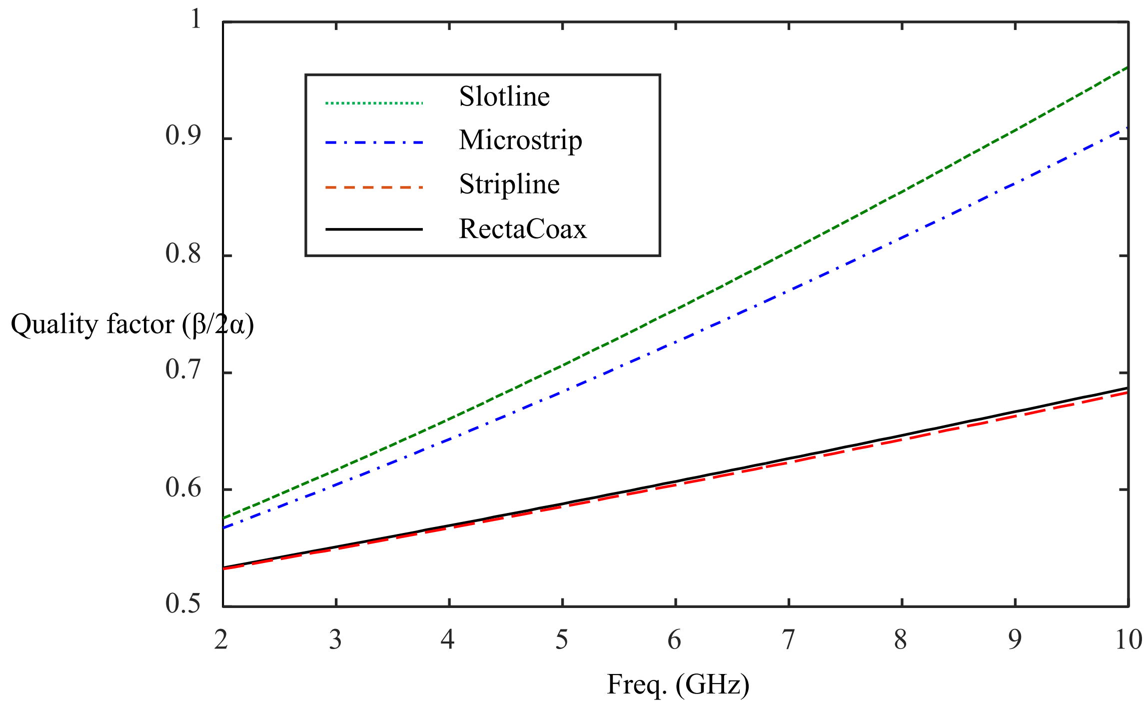

Fig. 4-18. Quality factor (*β/2α*) for some of the micro-TLs.

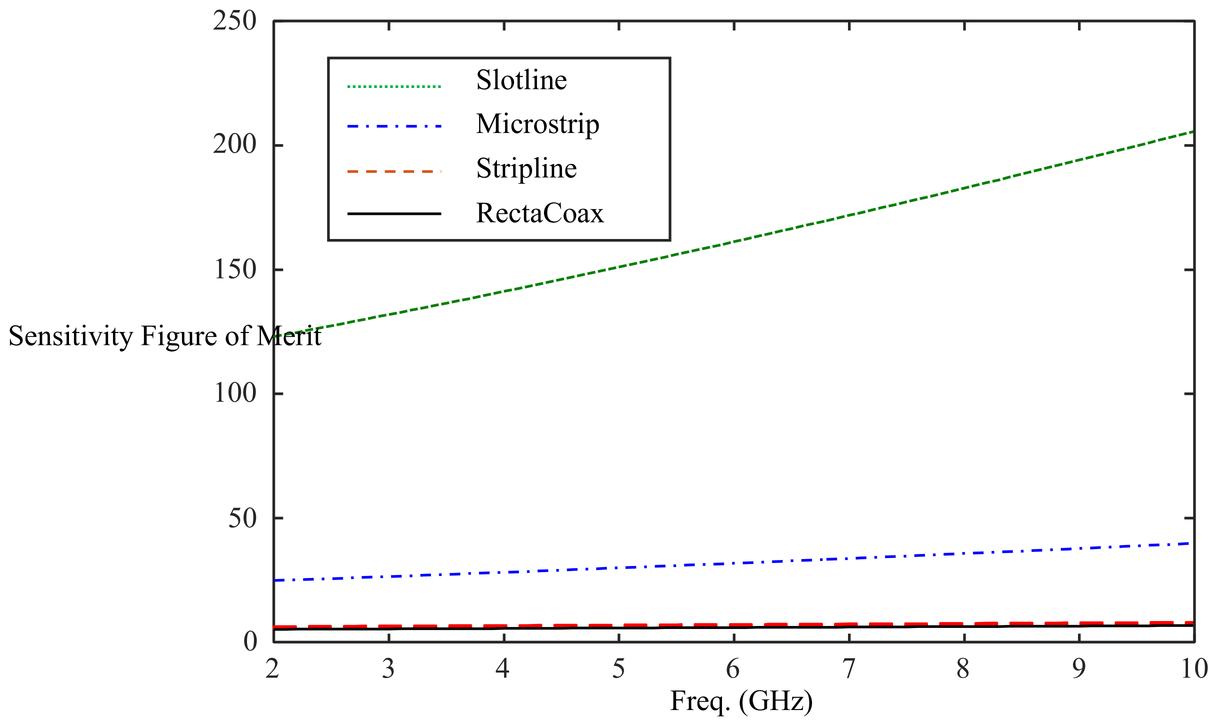

Fig. 4-19. Sensitivity figure of merit for some of the micro-TLs.

proportional to inductance and inversely proportional to series resistance of the line. For most of the micro-TLs, R is approximately the same; so, to improve Q, L should be increased, and this can be achieved by increasing the gap between signal and ground paths.

Now that we have a comparison between the important components of the overall sensitivity of the system, we can combine them with equation (4-24) and compare their sensitivity figures of merit.

As expected, slotline shows the highest FoM, followed by microstrip line. However, slotline is not suitable for the portion of the micro-TL that acts as a soft spring. It is also not the best choice near the tip, since it does not shield the surrounding medium as effectively as microstrip or stripline. Furthermore, microstrip is the preferred structure in the flexible micro-TL area. Near the tip (last 100 µm), stripline or coax micro-TLs provide better overall shielding and minimize the interaction of the micro-TL to the medium. Hence, if quantitative imaging is required, they are a better choice closer to the tip.

To confirm our results, we carry out a simulation in ADS to compare these micro-TLs in the overall system. An 800 µm length of each micro-TL is connected to a matching network made of transmission lines with the characteristics of an RO4003 PCB board and a G-CPW transmission line ($Q_c = 200$ & $Q_d=500$). The load is changed by 1aF, and any changes in S_{11} are compared before and after changing the load. For each micro-TL, an optimization is run to obtain the matching point at 5 GHz, with a return loss of better than 20 dB. The optimization parameters are the two stub lengths of Fig. 4-6. The results shown in Table 4-3 indicate very good agreement with equation (4-8); the slight difference is because overall Z_0 is assumed to be the Z_0 of the PCB transmission line, and the effect of micro-TL on Z_0 is neglected here.

To compare and validate simulation results, two identical test structures are fabricated. The test structures consist of a CPW line connected to a micro-TL, with the only difference being that the micro-TL in one is a microstrip while in the other it is a stripline. An integrated

Table 4-3. Comparing overall sensitivity of SMM with different micro-TLs.

Micro-TL type	Overall Q	$\lvert\Delta S_{11}\rvert$ Circuit Simulation	$\lvert\Delta S_{11}\rvert$ Theory equation (4-8)
Rectangular coax, w = 2.7 μm	18.9	17.4e-6	18.9e-6
Stripline: w = 2.7 μm	22.1	20.8e-6	22.1e-6
Stripline: w = 1.5 μm	23.8	23.4e-6	23.8e-6
Microstrip: w = 1.5 μm	88.4	90.1e-6	88.4e-6
Microstrip: w = 2.7 μm	97.8	100e-6	97.8e-6
Slotline: w = 2.7 μm, gap = 4 μm	139.2	141.7e-6	139.2e-6
No Micro-TL (only PCB TL)	142.3	142.8e-6	142.4e-6

sample close to the tip is actuated periodically in the approach direction with on-chip electrothermal actuators and the output voltage of the measurement circuit (explained in section 4.6) is observed. The microstrip output signal is approximately four times larger than the stripline case, which agrees well with the simulation results presented in Table 4-3. Fig. 4-20 shows an SEM image of the test structured fabricated in the CMOS-MEMS process.

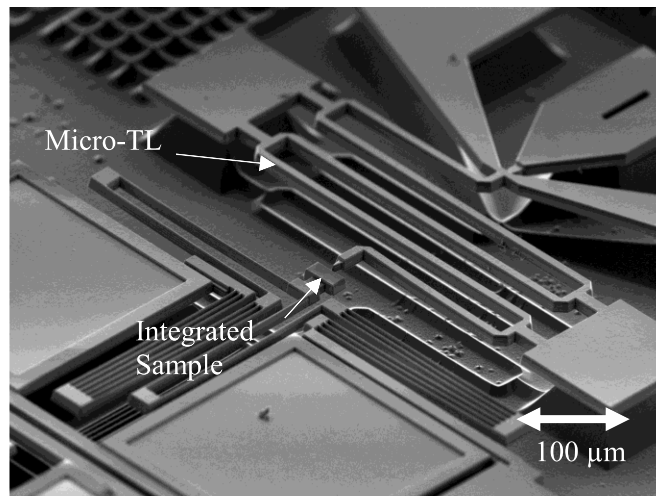

Fig. 4-20. Test structure for comparing different micro-TLs.

4.4.3 Bond pads transmission line

In order to connect the SMM device to the outside world either a CPW line (GSG pads) or a coplanar strip line (2 pads) is used. The pads should be at least 100 µm x 100 µm to be able to wire-bond them to a PCB board.

The signal line on the microstrip micro-TL is on the M1 layer; therefore, for the first design, the CPW bonding pads were put on M1 layer. Since it was only about 100 µm long, however, its effect on the overall system was ignored. After the first measurement, we realized that most of the loss actually comes from the CPW pads. So the next obvious design was to move them to the topmost layer of M4 (and bring the signal line to M1 with via holes where the silicon underneath is etched), which is farther from the lossy substrate and improves sensitivity. After studying the effect of individual parts on the quality factor of the overall system, we noted that having the CPW pads on M4 still had a considerable effect. This is because dielectric losses have a more pronounced impact on overall quality factor, as described in section 4.3, due to higher voltage closer to the tip. One way to decrease substrate losses is to shield the field with lower metal layers, which improves overall system sensitivity. There are several ways to do the shielding, and these will be discussed in greater detail in this section.

A circuit model for the bond-pad TL (CPW line or stripes) is shown in Fig. 4-21. This model is similar to a regular transmission line circuit model except that the substrate section is divided into two parts, oxide and silicon. In the oxide part, conductance is neglected because it is very small compared to the loss of Silicon. Also C_{air} is the capacitor between the signal and ground pads through air which is usually small compared to C_{ox} and neglected unless the gap between signal and ground is smaller than oxide thickness. Fig. 4-21 shows the circuit model and a comparison between EM and circuit model simulations which shows very good agreement between the two simulations in a wide frequency range (1-20 GHz).

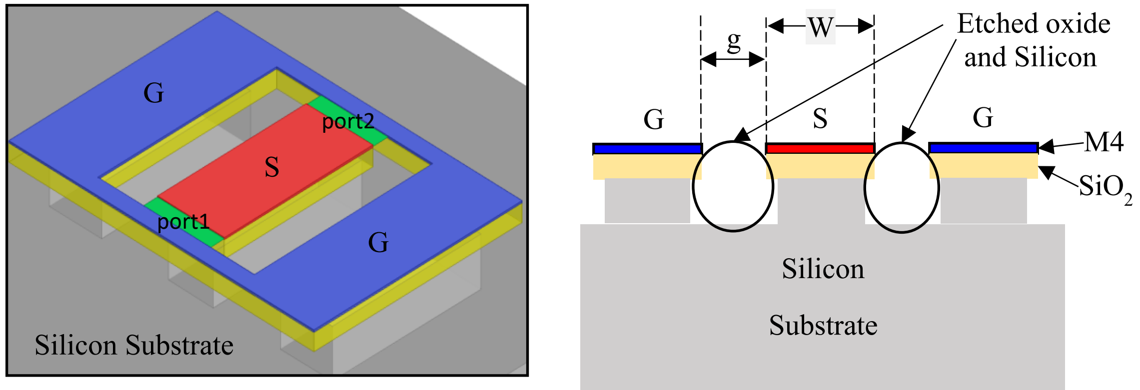

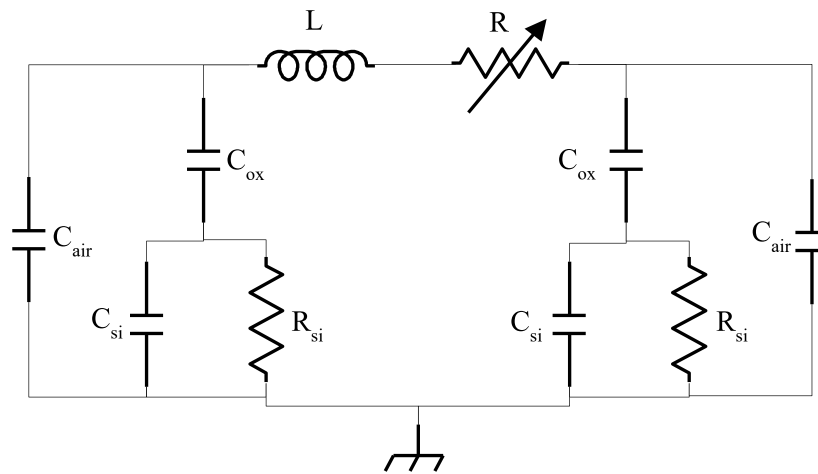

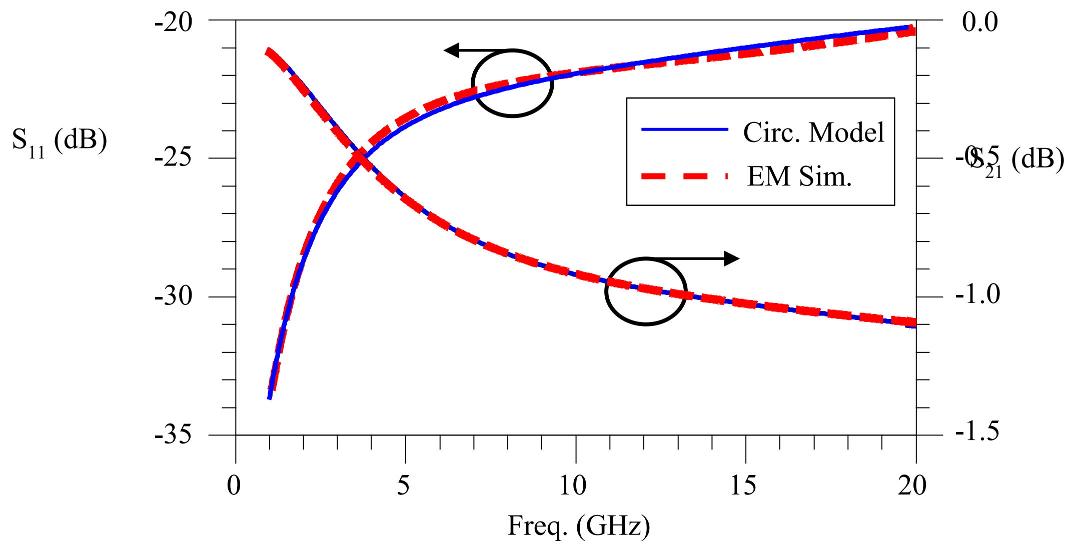

Fig. 4-21. (Top) CPW structure scaled 400% in vertical direction. (Middle) CPW complete model. (Bottom) EM simulation (red dashed line) and Circuit Model (blue solid line).

Based on the model and because of substrate losses, it is best when the pads are on the topmost layer, i.e., on the metal-4 (M4) layer to reduce the effect of silicon resistance (R_{si}).

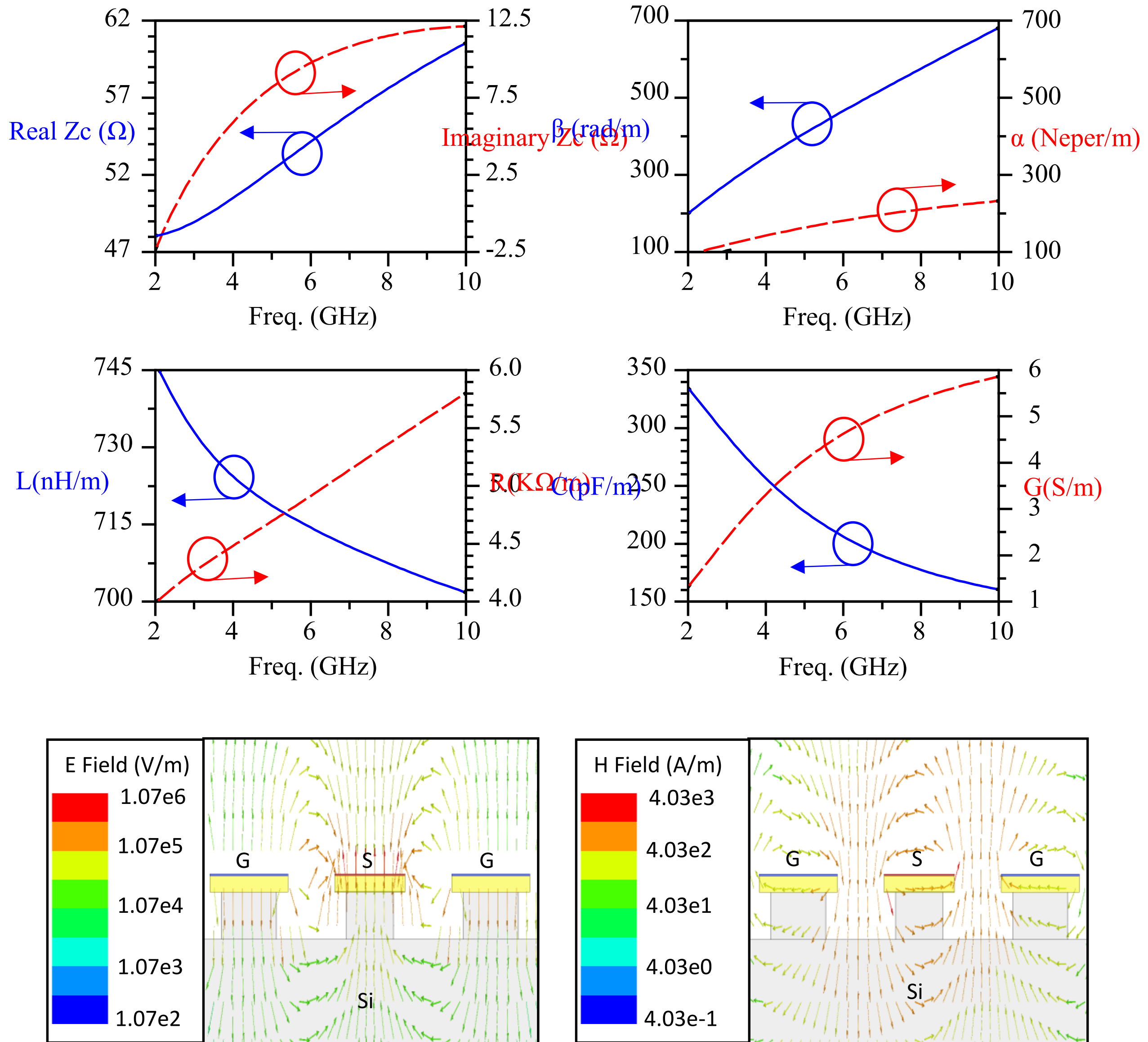

Fig. 4-22. CPW on M4 layer. Top left: real and imaginary parts of characteristic impedance. Top right: propagation and attenuation constants. Middle left: inductance and resistance per unit length of the micro-TL model. Middle right: Capacitance and conductance per unit length of the micro-TL model. Bottom left: E-field at the cross-section of the micro-TL (HFSS simulation). Bottom right: H-field at the cross-section of the micro-TL (HFSS simulation).

However, there are other ways to reduce the substrate effect, which will be discussed in the following section. Fig. 4-22 shows the simulation results for a CPW transmission line on the metal4 layer, with a width of 90 µm and a gap of 20 µm. To compare different transmission lines, we still use the standard RLGC method instead of the model shown in Fig. 4-21.

In order to reduce substrate losses, a few test structures were fabricated where Silicon underneath the CPW were etched. Unfortunately none of them could withstand the high force of the wire bonding machine, and they broke in the process.

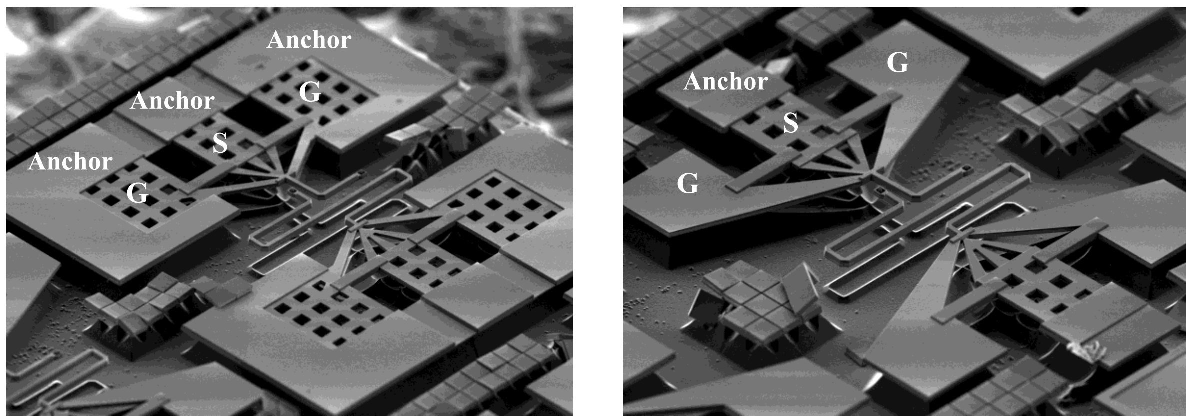

Fig. 4-23. CPW test structures with Silicon underneath etched for reducing substrate losses.

4.4.3.1 Slow-Wave CPW

Recently, a few studies have looked into improving transmission line design [64]–[66] based on slow-wave transmission lines. The idea is to prevent the electric field from penetrating the lossy substrate without affecting the magnetic field, which means eliminating R_{si} and C_{si} in the model shown in Fig. 4-21 without changing L and R. This helps retain the conductive quality factor while increasing the dominant dielectric quality factor (by decreasing or eliminating substrate loss). One way of implementing slow-wave CPWs is by putting a series of floating narrow stripes along the propagation of the transmission line (as shown in Fig. 4-24). Compared to silicon, the floating metal stripes provide a lower resistivity medium for the electric field from signal line to ground. Therefore, the model for this type of CPWs will have a series resistance of the metal stripes (R_{metal}) instead of the parallel combination of C_{si}

and R_{si} shown in Fig. 4-21. Here again, C_{air} can usually be ignored.

Putting narrow floating stripes is better than putting a floating solid metal (on M1 layer) shield because it reduces eddy currents on the floating shield and therefore reduces losses. The narrower these stripes are, the less the loss due to the eddy current.This type of slow-wave CPW can improve the overal sensitivity of SMMs by reducing substrate losses.

In section 4.4.2, we described how a larger relative dielectric constant in micro-TLs can decrease overall Q and sensitivity by keeping the wave in the higher loss CMOS section compared to the PCB section. The same argument is valid here, which means we would like to decrease substrate loss but not "slow" the wave. Therefore, the design should focus on decreasing substrate loss while keeping relative permitivity as low as possible. In [67] and [66], we can see how narrower stripes with smaller pitch can increase effective relative permitivity. Also, the smaller the gap between floating metal shields and the CPW line, the higher the effective relative permitivity will become. Therefore, for SMM applications, it is best when the stripes are on metal1 and rather wide. We have used 10 µm M1 stripes based on the above-mentioned analysis and simulation results.

HFSS simulation results for a slow-wave CPW with 90 µm width, 20 µm gap, 10 µm stripes on metal1 with 1 µm gap between the stripes is shown in Fig. 4-25.

Comparing simulation results of CPW both with and without floating stripes shown in Fig. 4-22 and Fig. 4-25, one can see that conductance per unit length is reduced considerably when the floating stripes are used, which means the quality factor of the shunt element is improved. The capacitance per unit length has also increased because silicon capacitance is no longer in series with oxide capacitance, which improves the quality factor of the shunt element. On the other hand, resistance and inductance per unit length has not changed much, and consequently the series element Q is not affected.

To compare the different transmission lines described for the bonding pads, the figure of merit presented in equation (4-24) can be used. If we replace $Q=\beta/2\alpha$, sensitivity FoM will be proportional to Z_0 and inversely proportional to the attenuation constant (α). Fig. 4-26 and

Fig. 4-27 show a comparison between the characteristic impedance and attenuation constant for several types of transmission lines.

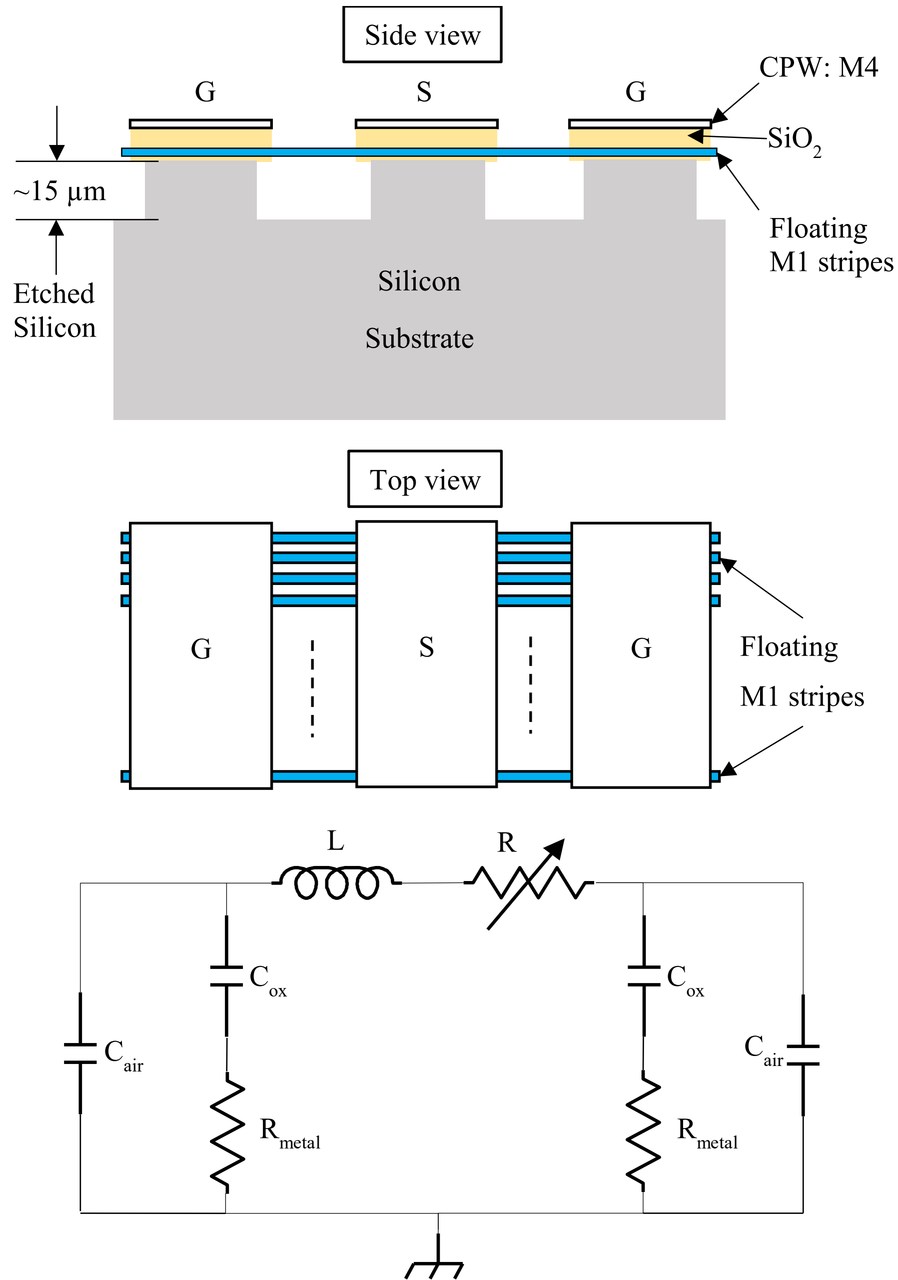

Fig. 4-24. Slow-Wave CPW structure and its circuit model. (The side view is scaled in vertical direction for better visualization).

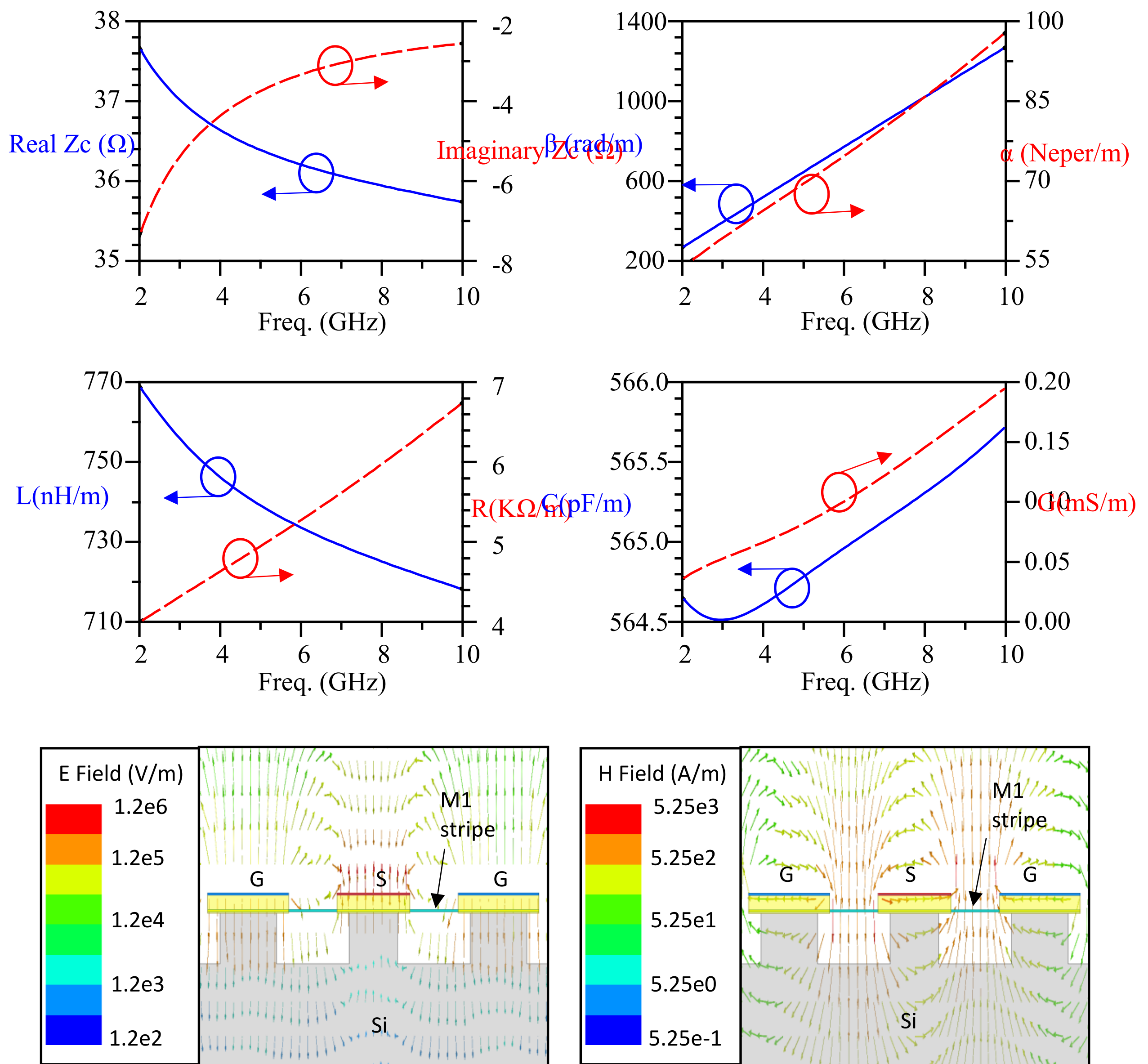

Fig. 4-25. CPW on M4 with floating M1 stripes. Top left: real and imaginary parts of characteristic impedance. Top right: propagation and attenuation constants. Middle left: inductance and resistance per unit length of the micro-TL model. Middle right: Capacitance and conductance per unit length of the micro-TL model. Bottom left: E-field at the cross-section of the micro-TL (HFSS simulation). Bottom right: H-field at the cross-section of the micro-TL (HFSS simulation).

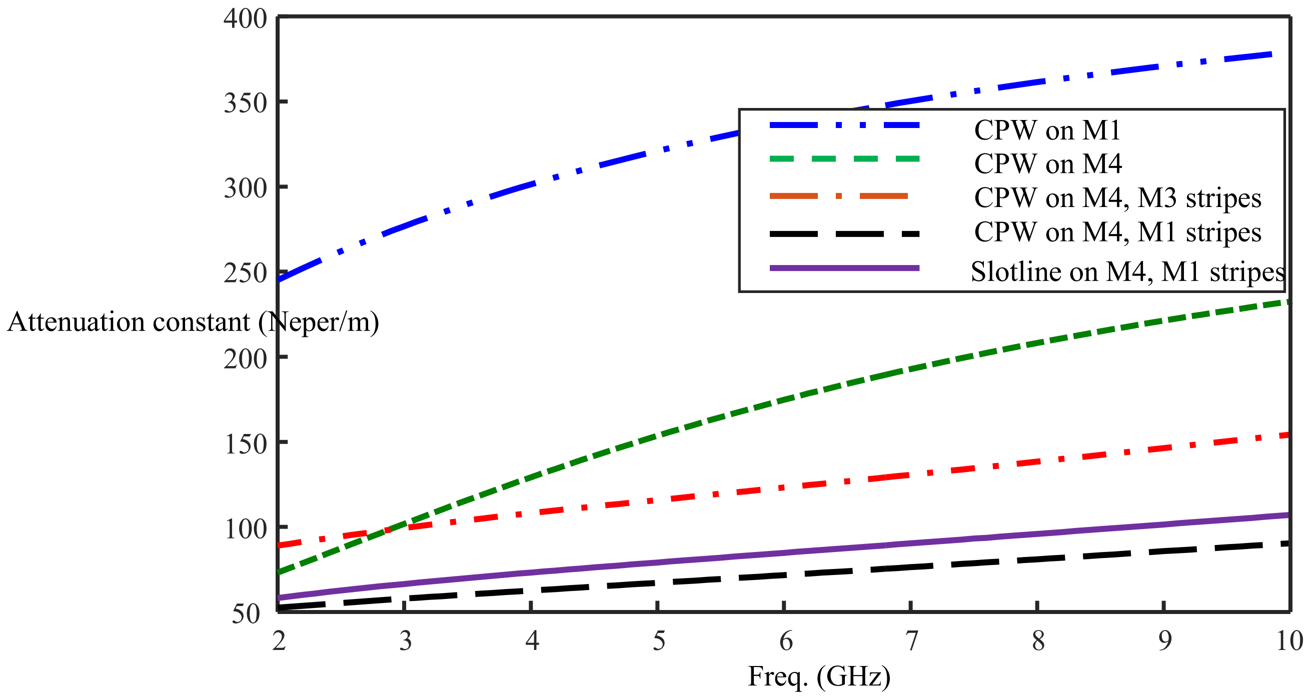

Fig. 4-26. Comparison of attenuation constant (α) between different TLs for bond pads.

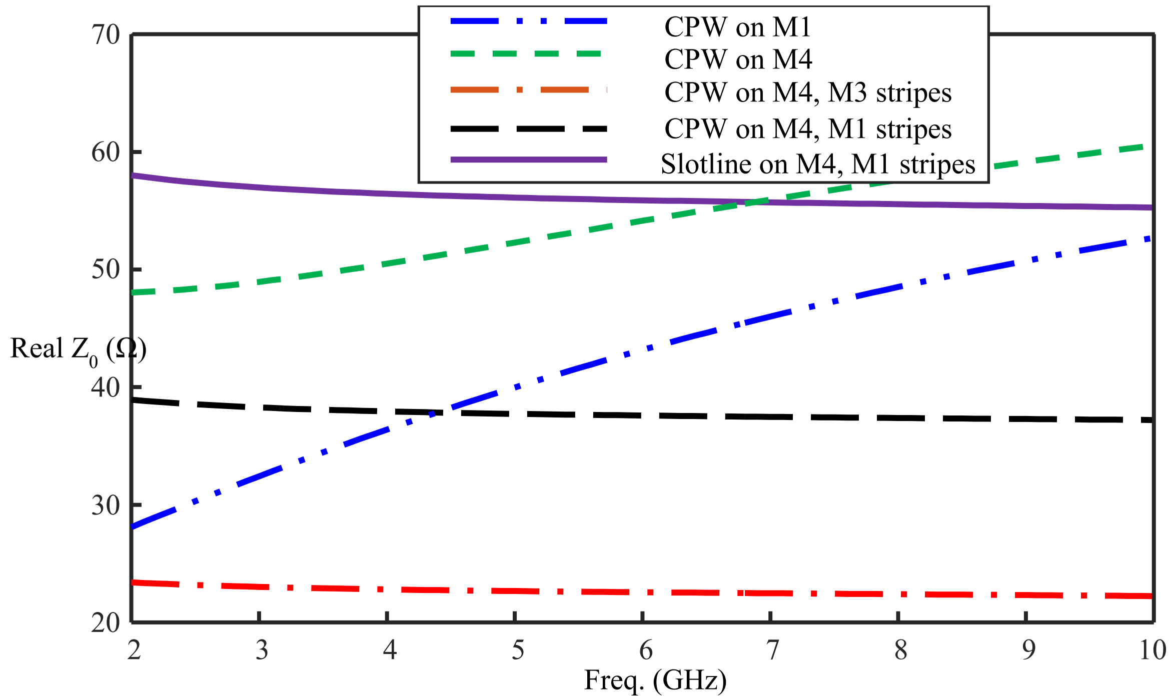

Fig. 4-27. Comparison of characteristics impedance (Z_0) between different TLs for bond pads.

Fig. 4-26 and Fig. 4-27 show that when stripes of M1 layer are floating underneath M4 pads, the attenuation constant is very low compared to the rest of the transmission lines and their Z_0 is also among the highest; hence, using bonding pads with either CPW or slotline on M4 layer and M1 stripes underneath will result in optimal sensitivity.

Additionally, to compare different CPW and slotlines in the overall system, an ADS simulation is carried out. In this simulation, 800 µm of microstrip micro-TL (as described in section 4.4.2) are connected to a CPW with an overall length of 200 µm, which is then connected to a matching network on the PCB (with properties of RO4003 G-CPW PCB lines and Q_c = *200* & Q_d=*500*), as shown in Fig. 4-28. For comparison, a slotline is used instead of the CPW.

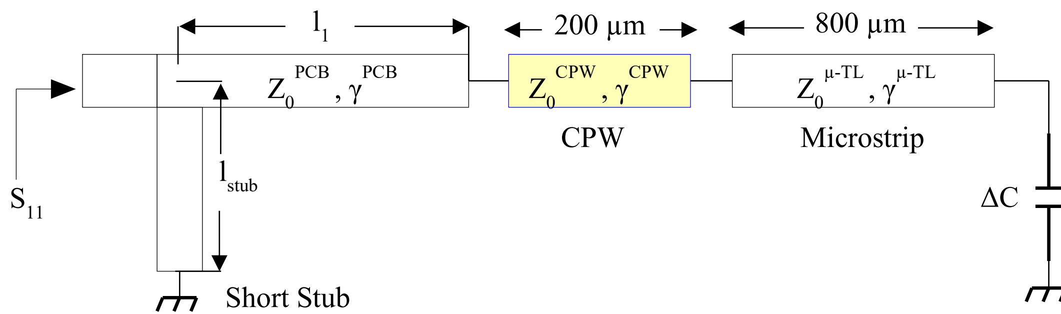

Fig. 4-28. ADS simulation to compare different bond pad transmission lines.

Here, ΔC is change by 1 aF and an optimization is run to get a matching point at 5 GHz (return loss of 20 dB) by changing l_1 and l_{stub} variables. Table 4-4 shows the overall quality factor and change in S_{11} with different types of CPW and slot line options.

These simulations show that putting the stripes under the CPW line significantly improves overall sensitivity. It also confirms that, in SMM applications, improvement comes from shielding the substrate and not "slowing" the wave (i.e., when the stripes are on M3 and hence effective permittivity is the highest among the compared lines, sensitivity is reduced).

It is note-worthy that in the micro-TL design, since the silicon underneath is etched, there is little loss from the substrate. There is thus no benefit to designing slow-wave micro-TLs, as such an approach can actually reduce overall sensitivity due to increasing the effective

relative permittivity.

Table 4-4. Comparing overall sensitivity of SMM with different bond pad TLs.

Bond-pad transmission line	Overall Q	$\|\Delta S_{11}\|$ Circuit Sim.
CPW M1	6.5	7.1e-6
CPW M4	15.6	16.6e-6
CPW M4 - 10µm M1 stripes & spacing	76.6	76.4e-6
CPW M4 - 10µm M1 stripes, 1µm spacing	86.2	**85.9e-6**
CPW M4 - 1µm M1 stripes& spacing	86.3	85.7e-6
CPW M4- 10µm M3 stripes& spacing	50.2	44.1e-6
CPW M4 – floating M1	86.2	84.1e-6
CPW M4 – ground M1 (G-CPW)	86.8	82.9e-6
Slotline M4 - 10µm M1 stripes, 1µm spacing	83.0	**85.2e-6**
only PCB TL and micro-TL	97.1	100e-6

After selecting the transmission line for bonding pads and the micro-TL, we need to design and simulate the proper transition from the pads to the micro-TL. When a CPW is used for the bonding pads, all the pads are tapered and the signal line is brought to the M1 layer with a staircase set of vias to be connected to the microstrip micro-TL.

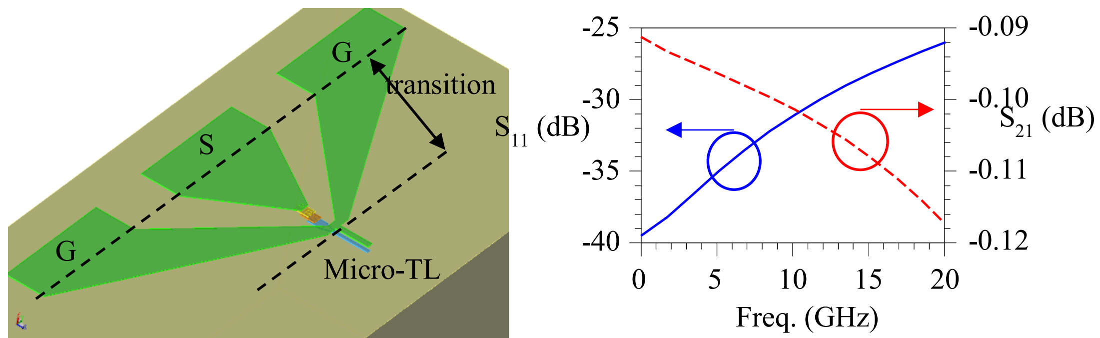

Fig. 4-29. CPW transition and its EM simulation.

The CPW pads take up a lot of space on the chip, so we decided to remove one of the ground pads and use slotline bonding pads on some of the SMMs. The slotline should be excited in odd mode. Placing floating metal stripes underneath to reduce substrate losses can be used for slotlines as well. Fig. 4-30 shows the microwave path on the CMOS SMM chip in one of the latest designs. It starts with a slotline for bonding pads 100µm x 130µm with 10µm M1 stripes underneath separated 1µm, followed by a coplanar stripe 180µm long with a metal stack of M1 to M4 for reduced loss. This is the transition zone between the pads and the micro-TL in this design. After that, the flexible microstrip micro-TL of around 400µm in length is used with signal and ground widths of 2.7µm and 4µm, respectively. Then a soft coplanar stripe on M1 for 150µm (2.4µm width and 4µm gap) and eventually another microstrip of about 150µm long are used up to the tip.

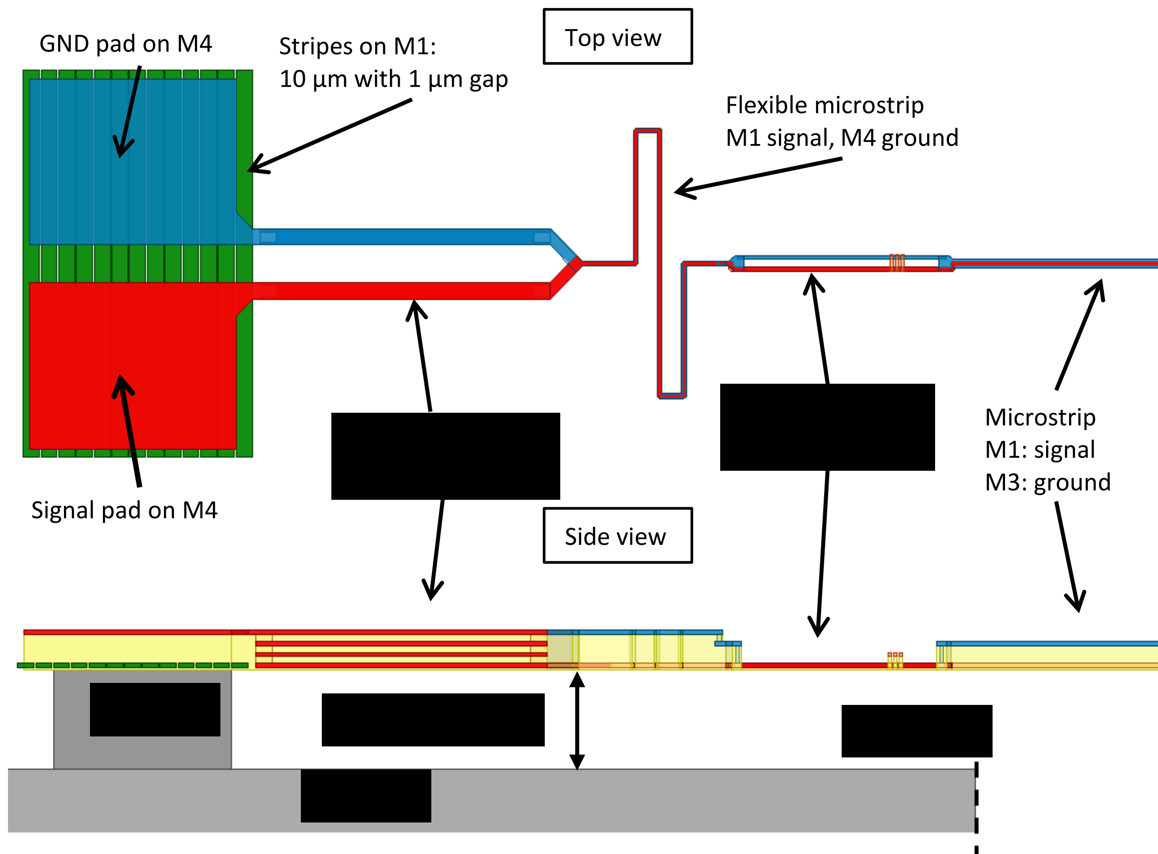

Fig. 4-30. Microwave path from bonding pads to the tip. Side view is scaled in the vertical direction for better visualization.

This microwave path is then wire-bonded to a PCB. The wire-bonding is done in our lab with a gold thread of 40μm in diameter. The total length of wire bond is less than 1 mm, usually close to 700μm. In the overall full wave simulations, bond wires are also considered, as shown in Fig. 4-31. Since the diameter of the bond wires is more than 50 times thicker than the metal thickness on TSMC 0.35μm CMOS, and the conductivity of gold is about 3 times more than the aluminum alloy used in this process, the effect of wire-bond losses on the overall system is usually negligible. Nevertheless, because of their length (which is comparable to micro-TL length), the bond-wires need to be taken into account when designing the matching network. There are some models for bond wires in the literature [68]. Here, for simplicity, the model provided by NXP in ADS is used, as this part is fixed and will not be "designed".

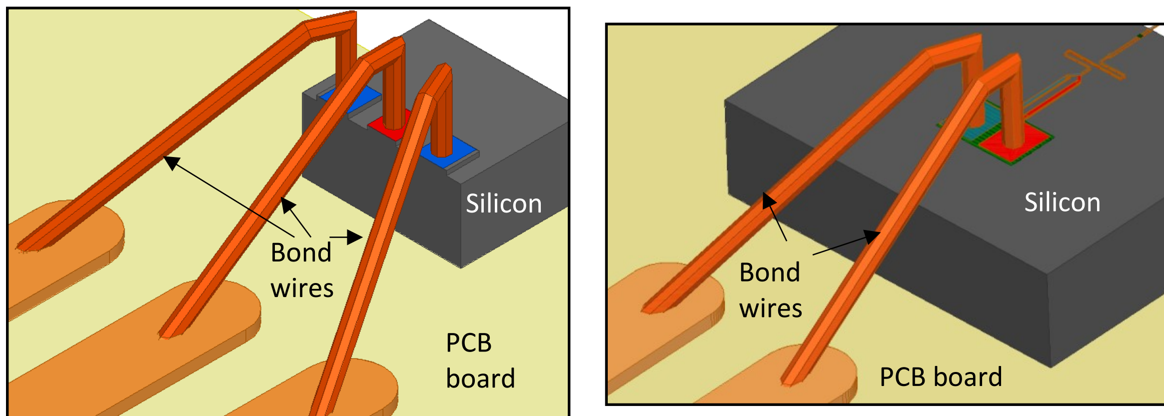

Fig. 4-31. Bond-wires from either CPW or slotline bonding pads to the PCB board, simulated in HFSS.

To ensure the circuit models are accurate, a few measurements with CPW probes from CPW lines are compared with the circuit models presented for micro-TL and bonding pads. In Fig. 4-32, an SMM with 120μm CPW lines on a metal4 layer followed by an 890μm microstrip micro-TL is measured on two different chips, and the results compared with circuit simulations. Circuit models, as shown in Fig. 4-12 and Fig. 4-21, are used for the micro-TL and bonding pads, respectively. For transition between the micro-TL and bonding pads, a similar model based on HFSS simulations is used. The results show that, first, the measurements are repeatable from one chip to another, and that, second, the circuit models

presented in this chapter can represent the CMOS SMM structure with very good accuracy.

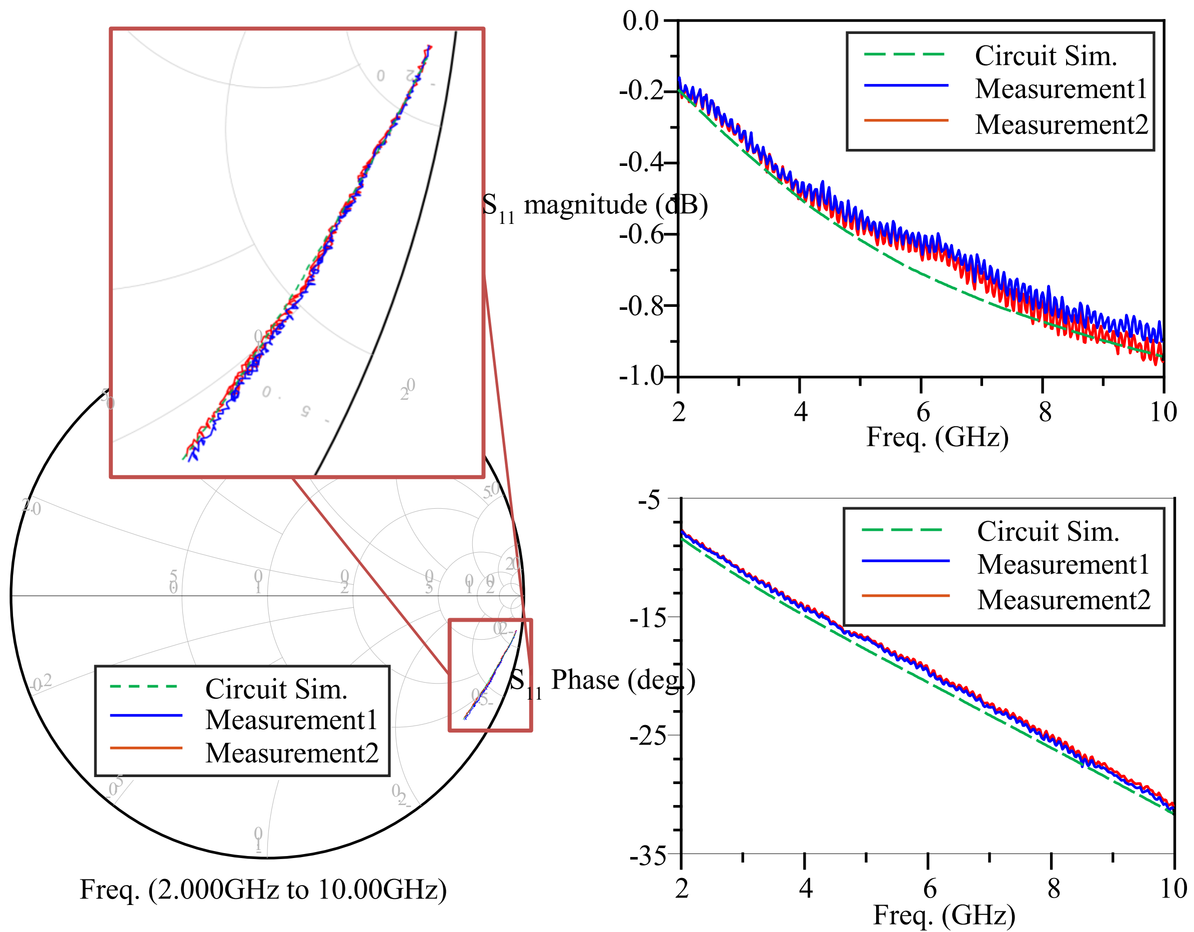

Fig. 4-32. Return loss measurement and circuit simulation comparison for a CMOS SMM. Smith chart, phase and magnitude of S_{11} is shown for two different measurements and corresponding circuit model.

4.5 Description of the Matching Network Circuit

By looking at the quality factor analysis in section 4.3 for lumped element matching and stub matching, we can see that lumped component matching improves sensitivity better than stub matching, if the same quality factor is achievable for both networks. However, one problem with lumped component matching is that it needs to be close to the tip (with an electrically short transmission line at the desired frequency), which requires the realization

of on-chip inductors at gigahertz frequencies. For the 0.35 μm CMOS technology from TSMC that we use, the best achievable Q factor is below 5 at the 5 GHz frequency range.

The second problem is that inductors occupy a relatively large footprint on the chip, which makes the mechanical design very challenging; they also use a lot of expensive space. In contrast, with careful design, achieving an overall quality factor of close to 100 is possible with single stub matching on Rogers PCB material such as RO4003. While there are lower loss PCB materials available, we selected RO4003 because of its higher stiffness, which is necessary for the vibration immunity of the board during imaging. With this higher Q, better sensitivity is achievable with stub matching. Therefore, we have chosen to use single stub matching over on-chip lumped matching.

Fig. 4-33 shows the impedance of a typical SMM device from the CPW bonding pads over a frequency range between 1-20 GHz on the Smith chart. This impedance is capacitive with some loss because the end of the tip is an open circuit and an electrically short lossy transmission line is connecting the tip to the CPW bond pads.

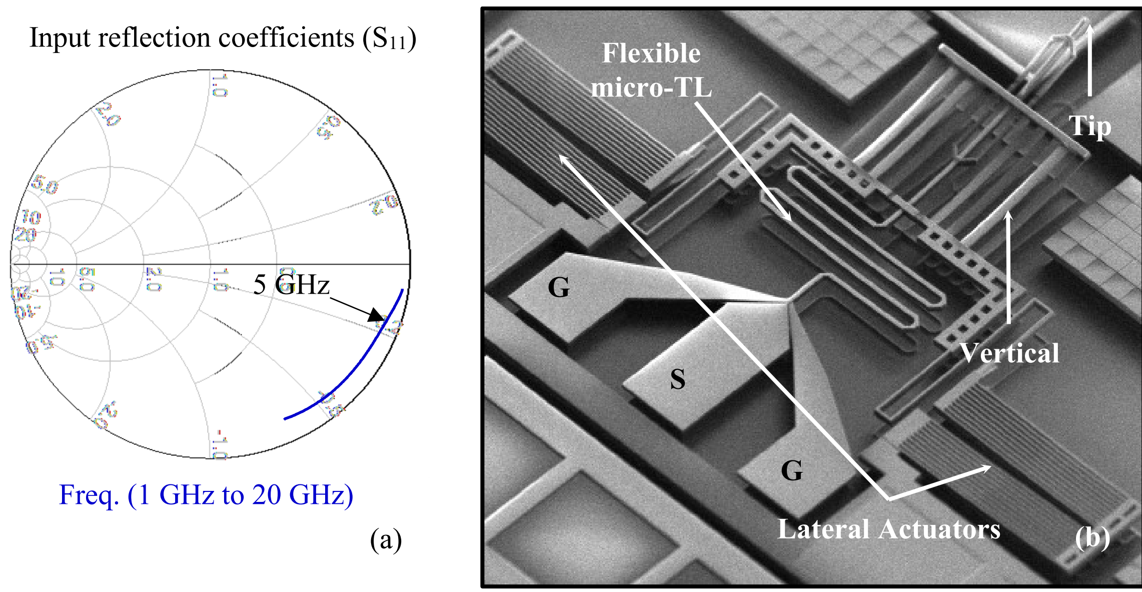

Fig. 4-33. (a) Typical impedance of an SMM device over frequency range of 1-20 GHz taken with PNA-X on an RF probe station. (b) SEM of the SMM device; impedance is measured from GSG pads.

In order to capture a small change in the impedance of the sample, a strong tip-sample field is required, so maximum power should be delivered to the tip. To deliver maximum power to the tip of the SMM, we need to match it to 50 ohms. Single stub matching is used to match the SMM at a single frequency to 50 ohm. CPW bond pads are connected through bond-wires to a short transmission line smaller than a quarter lambda on a PCB board. At a specific length, l_1 it will intersect with g=1 circle, and at this point (D shown in Fig. 4-34), the normalized admittance will be 1+jB. To cancel the jB part, a shunt stub with an admittance of -jB can be used. Since a -jB admittance is a small inductor, it can be realized with a very short short-circuited stub. This procedure for typical SMM impedance at 5 GHz is shown in Fig. 4-33. The resulting matching network with CPW line and fabricated PCBs are shown in Fig. 4-34 and Fig. 4-36.

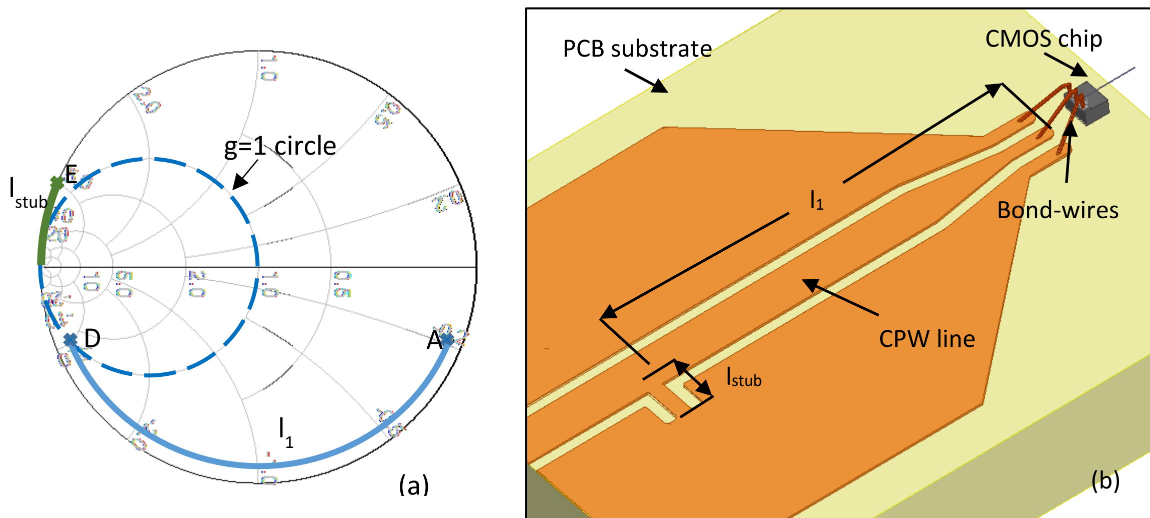

Fig. 4-34. Left: Stub matching of a typical SMM impedance at 5 GHz on a Smith chart. Right: HFSS simulation of the entire structure including matching network, bond-wires, CPW lines and micro-TL.

To ensure that the fabricated PCB results in a good match (-20 dB or lower), a series of HFSS simulations are run after the initial circuit simulations. In these simulations, the SMM device on the CMOS and bond-wires and the PCB are integrated in a single simulation and parametric simulation is run for the stub length. Some of the results are shown in Fig. 4-35. This method of simulating the entire structure in HFSS is the most accurate approach, but it

is also time-consuming. For most of the analysis and design, the circuit models presented in section 4.4 are used, and these considerably simplify the design and analysis.

The measurement result for this stub matching network is shown in Fig. 4-35-(a) indicating very good agreement with simulation results (the simulation is done with the circuit model). It is noteworthy that the quality factor estimated by the simulation is within 5% of what was measured, which is very important in the correct estimation of sensitivity.

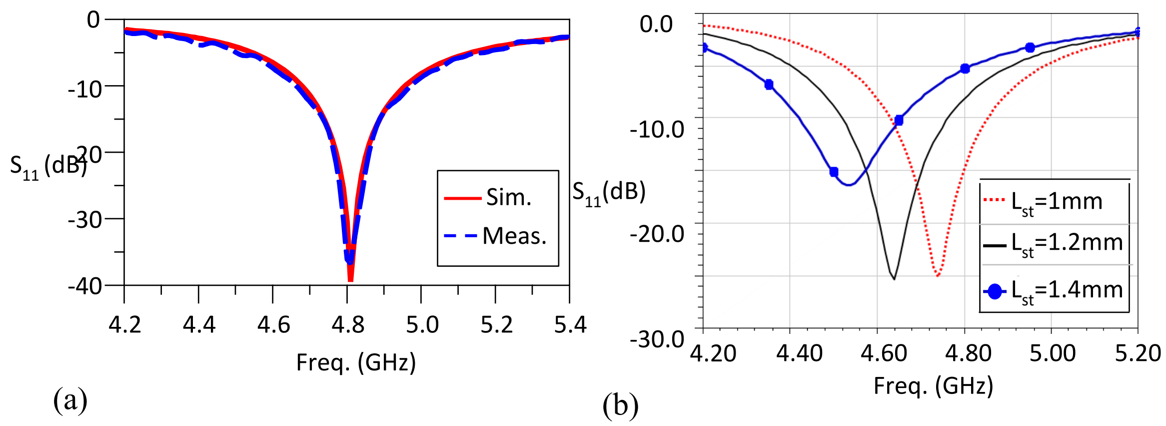

Fig. 4-35. Simulation and measurements results for the matching network, connected to the device. Simulation in HFSS.

Once the simulations and final design are completed, it is time to draw the PCB layout. The board on which the SMM chip is mounted is called the "daughter-board". The daughter-board is connected to another board, called the "motherboard", which is used for scanning the tip and AFM operation. On the daughter-board, apart from the RF path, there are up to 9 more signals routed to the chip: 6 for lateral and vertical actuators, and 3 for AFM operation (piezo-resistor signals).

Another method to realize the short inductance is to use the parasitic inductance of SMD capacitors above its series resonance frequency (SRF) frequency. This is shown in Fig. 4-37. The benefit of this method is that, with a single capacitor, DC and low-frequency ground noise are separated from the RF signal line, and a small inductor is seen at the desired

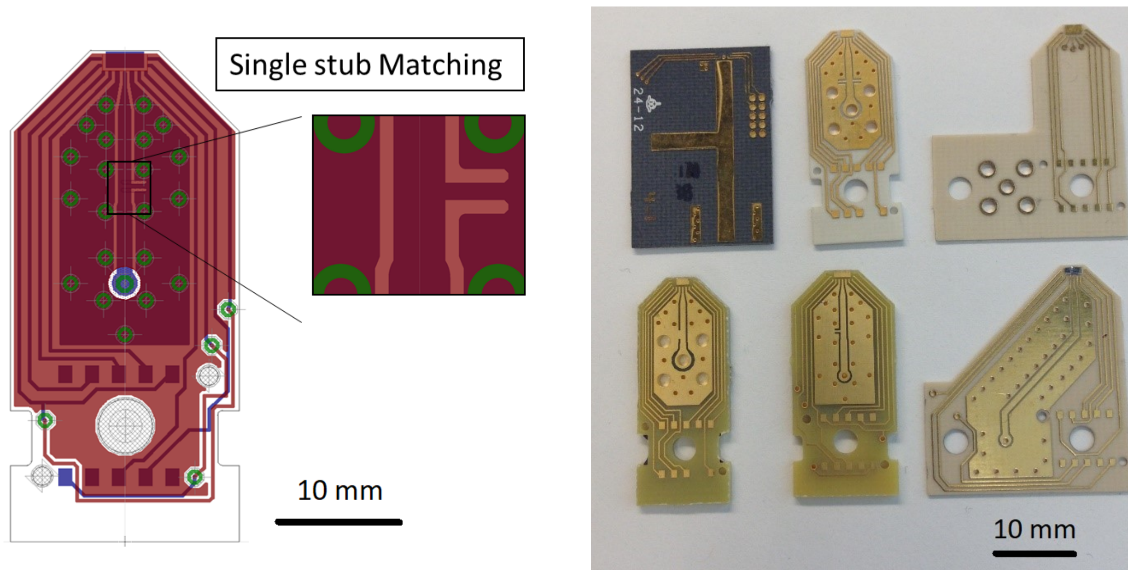

Fig. 4-36. PCB layout and picture of some of manufactured PCBs.

frequency. The problems with this approach are the limited quality factor of the capacitor at gigahertz frequencies and sensitivity of the inductance value with soldering and orientation of the SMD capacitor. Due to the lower Q of this method compared to stub-matching, the latter method is used for the measurements and is described in greater detail here.

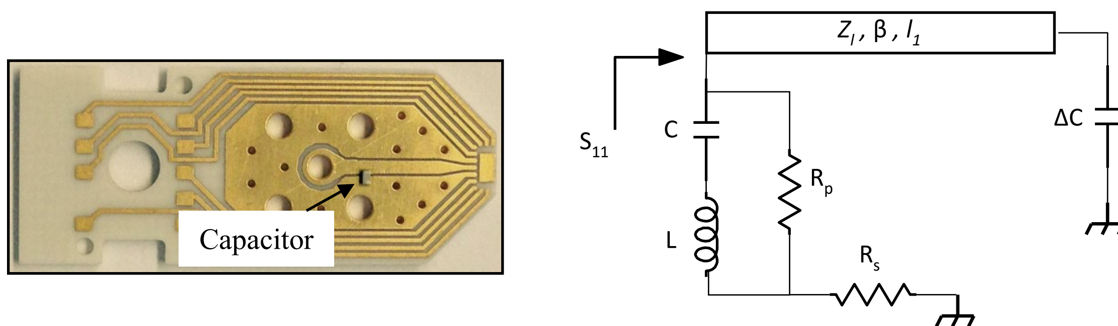

Fig. 4-37. Matching with transmission line on PCB and parasitic component of an SMD capacitor.

4.5.1 Discussion

Knowing the importance of quality factor to the sensitivity of the system, it is helpful and instructive to look at each section of the SMM in terms of the impact of individual quality

factors on the overall Q of the system. For a one-port resonator, the quality factor can be defined as [69]:

$$\mathrm{Q} = \frac{f_0}{2}\frac{\partial\varphi_{Z_{in}}}{\partial f} \tag{4-25}$$

where φ_{Zin} is the phase of the one port input impedance of the resonator. It is straightforward to show that the overall Q of the cascaded system if the stored energy remains constant is given by:

$$Q_t^{-1} = Q_1^{-1} + Q_2^{-1} + \cdots \tag{4-26}$$

where Q_1, Q_2, etc., are the quality factors due to the loss of different sections of the overall SMM system, such as micro-TL, bonding pads TL, bond wires, PCB, etc., while the loss of all other parts is set to zero. An ADS circuit simulation is carried out where circuit models for different sections of the SMM are used in cascade, and all of the losses are put to zero except for the section under study. The Q factor of the entire system is found by equation (B-1), while for PCB transmission lines, standard ADS physical transmission lines are used. To get the resonance at the desired frequency (5 GHz is used here), the matching network lengths are slightly tuned. Note that the stored energy of the entire system does not change (there is a slight change when tuning the matching network, but it is negligible) and only the loss of each section is altered. This means that for the circuit models series and parallel resistor, all but one section are set to zero, and for the standard physical ADS TLs, conductivity and loss tangent are changed. Table 4-5 shows the effect of each section (with some possible variations) on the overall quality factor of the SMM system.

Since the overall quality factor is dominated by the lower quality factors in the system, we will not get much improvement by increasing the higher Q-factors of the system. So, the focus of the design and improvement should be on the lower Q-factors. It is interesting to see that, when the shielding stripes are not used, even a very short length of the CPW bonding pads has a large effect on the overall quality factor and sensitivity of the system. When there is no shielding of the substrate, the 100-150 µm CPW pads dominate the Q factor, but when

it is shielded, the micro-TL and the matching network become dominant. Also worth mentioning is that a significant improvement (~10 times) is achieved with microstrip over stripline. For the matching network, obviously lower loss substrates such as RO4003 result in better Q-factor.

Table 4-5. Comparing the effect of each section of the CMOS-MEMS SMM on the overall sensitivity.

Section	Overall Q of individual sections	$\lvert\Delta S_{11}\rvert$ Circuit Sim. (*1e-6)
Micro-TL: microstrip (0.9mm)	224.6	267.5
Micro-TL: microstrip (1.1mm)	120.3	144.2
Micro-TL: stripline (0.9mm)	19.1	17.8
Micro-TL: stripline (1.1mm)	11.1	9.4
CPW: M1 (0.15mm)	7.5	9.7
CPW: M4 (0.15mm)	19.3	24.7
CPW: M4 with m1 stripes (0.15mm)	353	429
PCB MN: FR4 (~ 7.9mm)	57.6	71.5
PCB MN: RO4003 (~ 8.1mm)	161.7	191.2
MN: λ/2(ideal TL) + 50 ohm	1.48	1.01

4.5.2 Comparison with Keysight method

In section 4.3 the sensitivity of stub matching and "λ/2 + 50Ω" methods was analyzed. Comparing equations (4-8) and (4-15) , we can write:

$$\frac{|\Delta S_{11}|^{stub-MN}}{|\Delta S_{11}|^{\lambda/2+50\Omega}} = \left(\frac{Z_l}{25}\right)\frac{1}{\beta l}Q^{stub-MN} \qquad (4\text{-}27)$$

Which shows that for matching networks with Z_l = 50 ohms and with quarter-lambda matching ($\beta l=\pi/2$), better sensitivity can be achieved with the stub-matching method if the quality factor of the network is better than $\pi/4$. In this chapter, we have shown that it is

possible to achieve quality factors of 50 or more with the CMOS-MEMS process and PCB matching and achieve a more than 60-fold improvement in sensitivity compared to the $\lambda/2+50\Omega$ method. To confirm this, a circuit simulation in ADS is carried out, where either CMOS-MEMS SMM with quarter-lambda PCB matching or Keysight's $\lambda/2+50\Omega$ method is connected to a load that is changed from 1 to 1000 aF. The simulation results confirm equations (4-8), (4-15) and (4-27) as shown in Fig. 4-38.

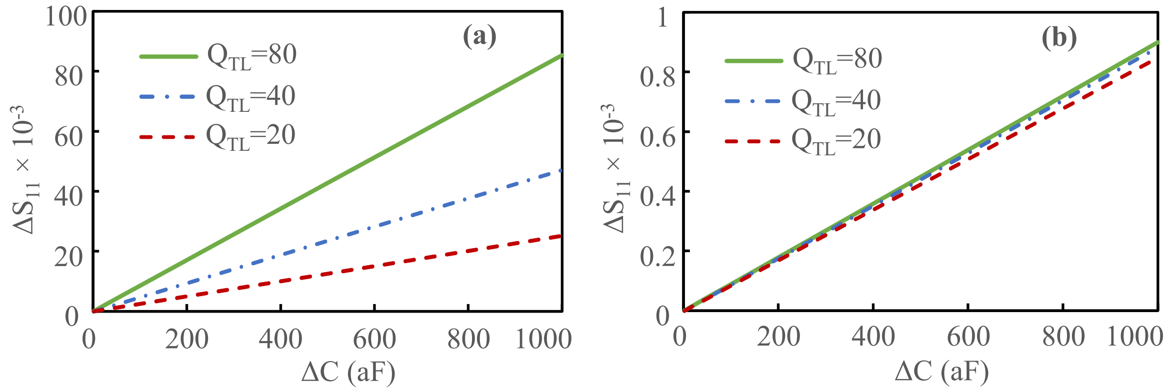

Fig. 4-38. Change in S_{11} vs. change in load when the CMOS-MEMS SMM device is matched with (a) a single-stub transmission-line and (b) with $\lambda/2+50\Omega$ method.

4.6 Measurement Circuit

When aiming to improve the sensitivity of SMM detection, one needs to increase the signal-to-noise ratio, similar to improving the sensitivity of receivers. This is possible by a combination of increasing the signal (without increasing the noise) and decreasing the noise (without decreasing the signal).

In SMM, the signal of interest is the reflected signal from the tip. All of the analyses and designs presented in this chapter, such as the Q improvement for the micro-TL and bonding pad TL, are aimed at increasing this reflected signal (increase $|\Delta S_{11}|$). Furthermore, the reflected signal is proportional to the transmitted signal to the tip. We can therefore assume that increasing the transmitted signal results in an increased reflected signal without any change in the thermal noise level, which means better SNR (but noise from phase noise also

increases with increasing input power, as described in section 4.6.1). A directional coupler can then be used to separate the reflected signal from the transmitted signal.

It should be noted that the transmitted signal cannot be arbitrarily increased because of power limitations of the SMM device, especially for micro-transmission line designs. This power is rather weak (assuming to have a minimum gap between the signal and the ground is 1 μm, which is the thickness of oxide layer; power should be less than 20 dBm to avoid air breakdown voltage). Also, since the electric field is strong at the tip, it might damage the sample. For these reasons, we usually apply less than 5 dBm of power to the SMM device for our measurements (typically around 0 dBm).

There are two main sources of noise in the SMM system: thermal noise and phase noise. Thermal noise depends on the operating temperature of the SMM device. Therefore, one way to reduce thermal noise is to decrease the device's temperature by placing the entire system in liquid nitrogen or helium [70]. However, this approach is cumbersome and expensive and goes against the idea of having a small and inexpensive SMM. Our CMOS-MEMS SMM device works at room temperature. The MEMS actuators used in our designs are electrothermal, so they increase the temperature of the microwave signal path. MEMS simulation shows that the temperature of the micro transmission line can go up to twice the room temperature ($2T_0 \simeq 600^o$ K), which means that the SNR at the tip is reduced by 3dB compared to the SNR at room temperature. It may seem that the output SNR would decrease by 3 dB as well, but more careful investigation of output SNR shows that this degradation depends on the total noise figure of the measurement circuit.

$$\frac{{SNR_{out}}^{T_{IN1}}}{{SNR_{out}}^{T_{IN2}}} = \frac{N_{out2}\ S_{out1}}{N_{out1}\ S_{out2}} = \frac{T_e + T_{IN2}}{T_e + T_{IN1}} \qquad (4\text{-}28)$$

If we assume a total noise figure of 3-dB (effective noise temp. of $T_e = T_0$) for the detection circuit, the total degradation of output SNR when the input temperature is $T_{IN2} = 2T_0$ compared to when it is at room temperature ($T_{IN1} = T_0$) is only10log ($3T_0/2T_0$) = 1.76 dB.

From equation (4-28) and Fig. 4-39 we can figure out that to improve output SNR and thus

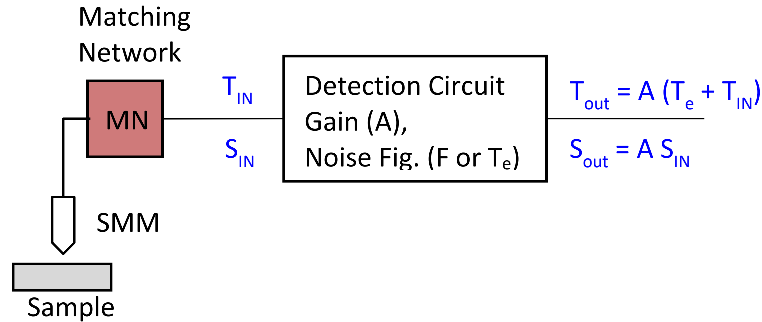

Fig. 4-39. Thermal noise effect of the device and detection circuit on the output noise.

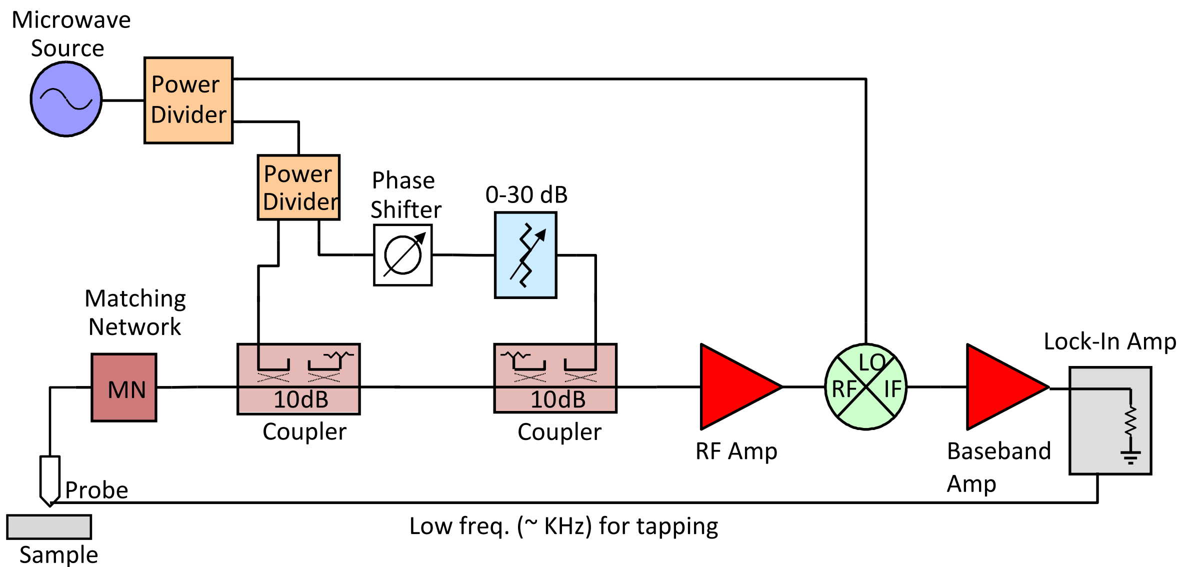

Fig. 4-40. High sensitivity measurement system. The modules of the system are shown in Appendix C.

improve system sensitivity, we need to reduce the noise figure of the detection system as much as possible. The noise figure of a standard PNA-X receiver is about 15-dB (with low noise option), and for a lock-in amplifier it is about the same (5nV/√Hz output noise). Better sensitivity can therefore be achieved if the reflected signal is amplified with a low noise amplifier. In order to detect the signal out of noise, the minimum gain of the detection circuit needs to be larger than the noise figure of the measurement device.

One challenge in selecting or designing an LNA is that the reflected signal from the SMM system is rather high ($P_{ref} = P_i$ - RL) and saturates the LNA. To overcome this problem, an interferometry technique can be used to cancel the common signal. A schematic of the

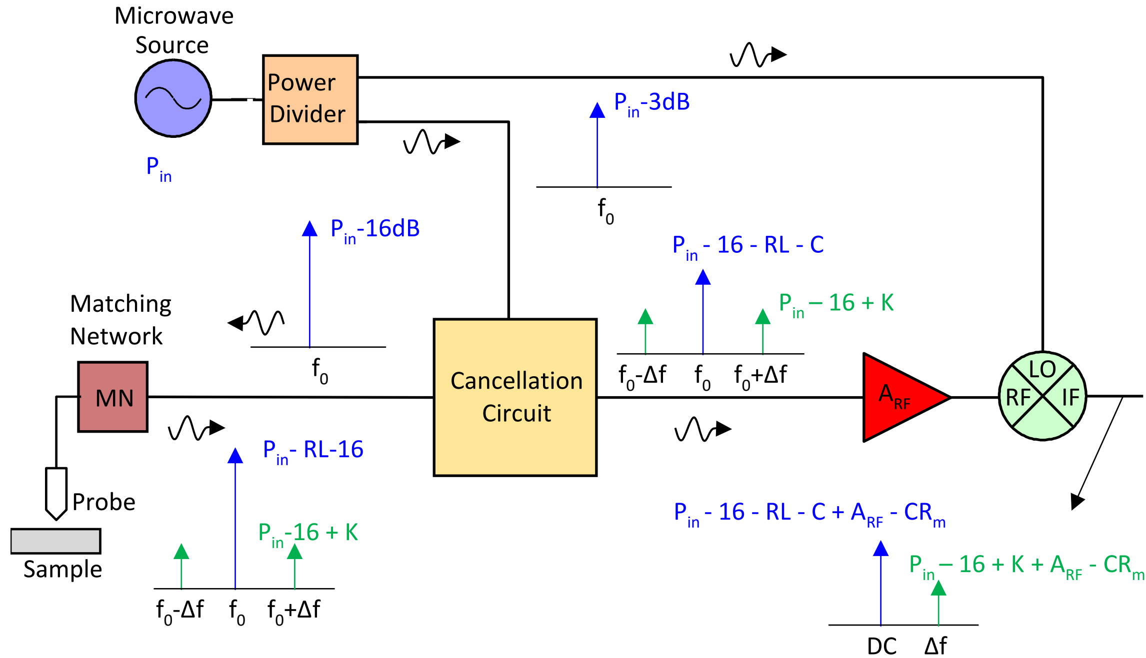

Fig. 4-41. Budget analysis for the SMM measurement system. P_{in}: Microwave Source power, RL: Return loss from the matching network, Δf: tapping frequency, K: constant depending on SMM design, A_{RF}: RF gain, CR_m: Mixer conversion loss, C: Cancellation of common signal.

microwave interferometry system is shown in Fig. 4-40. After RF amplification, the signal is mixed down to baseband with a mixer, where it is again amplified (optional: baseband amplifier design is explained in Appendix C) and detected with a lock-in amplifier. A lock-in amplifier can detect a small signal in a very small bandwidth and therefore reduces detection noise considerably.

A brief budget analysis of the SMM measurement system is shown in Fig. 4-41. When the SMM tip is actuated at the mechanical resonance frequency of the device (Δf), the microwave signal (at f_0) gets modulated and the reflected signal from the SMM device gets side signals at $f_0 \pm \Delta f$. We are interested in these modulated signals. The cancellation circuit cancels out the large common signal at f_0 without affecting the modulated signal. Eventually, the signal gets mixed down to the baseband after RF amplification and the amplitude and phase of the signal at Δf frequency is detected with the help of a lock-in amplifier.

Another source of noise in the SMM system is the phase noise that depends on the phase

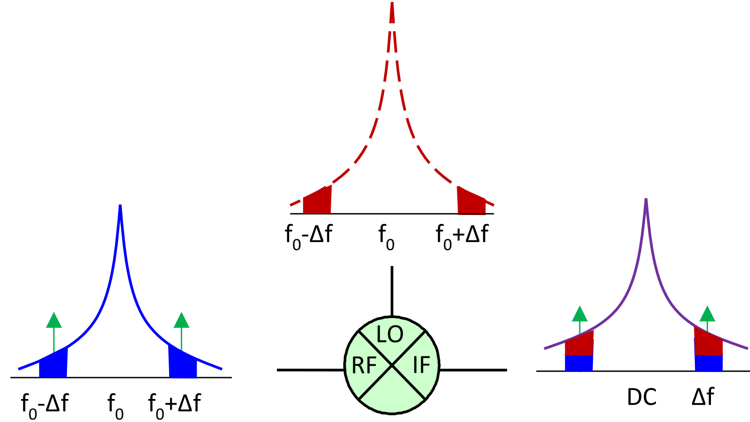

Fig. 4-42. Effect of phase noise at the output of the mixer.

noise of the microwave source. This noise gets added up in two ways; first, at the tip sample interaction, when the microwave signal gets modulated by the tip actuation, and second at the mixer, when the signal is mixed down to baseband. Fig. 4-42 graphically shows how these two mechanisms add noise.

4.6.1 Calculations for minimum detectable signal

With all the information about the SMM device, matching network, measurement circuit and noise calculations, we can then find the minimum detectable signal. For a stub matching SMM, we can use equation (4-8) to write:

$$\Delta V^{ref} = V^{in} Q_{TL} \frac{Z_0 \omega_0}{\beta l} \Delta C \tag{4-29}$$

where V^{in} and V^{ref} are the transmitted and reflected voltages from the matching network respectively. This reflected signal then passes two couplers, an RF amplifier, a mixer, and a baseband amplifier and it reaches the lock-in amplifier. We can define the total power gain of this chain (shown in Fig. 4-40) as:

$$G_t = A_{RF} + A_{BB} - 2IL_{coupler} - CL_{mixer} \tag{4-30}$$

Therefore, the voltage at the lock-in amplifier is:

$$\Delta V^{out} = \Delta V^{ref}\sqrt{G_t} \tag{4-31}$$

The thermal noise calculation was explained with the help of Fig. 4-39 and equation (4-28). We simply need to find total gain, from equation (4-30), and noise figure of the detection system, which depends on the modules used in the circuit and is straightforward to calculate. Here, with the use of a very high gain LNA immediately after the couplers we can find.

$$NF_t \cong 2IL_{coupler} + NF_{LNA} \tag{4-32}$$

where NF_t and NF_{LNA} are the total and the LNA's noise figures in dB. Therefore the total (linear) output thermal noise power will be:

$$N_{th}{}^{out} = KT_{in}[\,^oK]B[Hz]F_tG_t \tag{4-33}$$

where K is the Boltzmann constant, B is the receiver bandwidth, and F_t is the total noise factor of the circuit. To calculate the phase noise, we need to know the phase noise of the microwave source at the mechanical resonant frequency (Δf). Let us define it as L_{PN} [dBc/Hz]. Due to the interaction with the sample, the phase noise is going to be substantially higher than the phase noise from the mixer, since it is amplified by the high-gain RF amplifier. We can write the output noise contribution due to phase noise as:

$$N_{PN}{}^{out} = P_{in}10^{-RL/10}G_tB[Hz]10^{L_{PN}/10} \tag{4-34}$$

where RL is the return loss of the matching network at the desired frequency. Based on equations (4-29) to (4-33), and with the assumptions of input signal of +16 dBm at microwave source (0 dBm at the input of SMM) and a return loss of -20 dB from the matching network, overall Q = 50, Z_0 = 50 Ω, f_0 = 5 GHz, B = 100 Hz, L_{PN} = -100 dBc/Hz at 10 KHz, G_t = 50 dB and ΔC = 1aF, we will have:

$$N_{th}{}^{out} = -98\text{ dBm},\qquad N_{PN}{}^{out} = -50\text{ dBm},\qquad \Delta P^{out} = -36\text{ dBm} \tag{4-35}$$

These calculations for typical values in the SMM system shows that an output SNR of 14 dB is achievable with typical CMOS-MEMS SMM values if the change in tip-sample capacitance is 1 aF. The detector in the lock-in amplifier can easily detect signals with such an SNR, so

we can therefore claim that any sub-attofarad change in tip-sample impedance can be detected by the CMOS-MEMS SMM. It should be noted that noise arising from phase noise is considerably higher than thermal noise. It is also important to point out that both signals and noise from phase noise are proportional to the applied input power. Because of this, when a certain degree of input power exists (where noise from the phase noise becomes much higher than thermal noise), the output SNR will not improve by increasing the input the signal, since both the signal and the noise will increase together.

Chapter 5
Measurement Results

In this chapter, the measurement results obtained by our CMOS-MEMS SMM are presented. First, some of the preliminary results that were achieved without the use of the high sensitivity measurement circuit explained in Chapter 4 are presented. Then, the imaging results with the help of the measurement system are explained.

5.1 Preliminary Measurement Results

In this section, preliminary measurement results are reported. We used the PNA-X from Keysight for S_{11} measurements.

The relationship between S_{11} and tip-sample separation (approach curve) is measured using

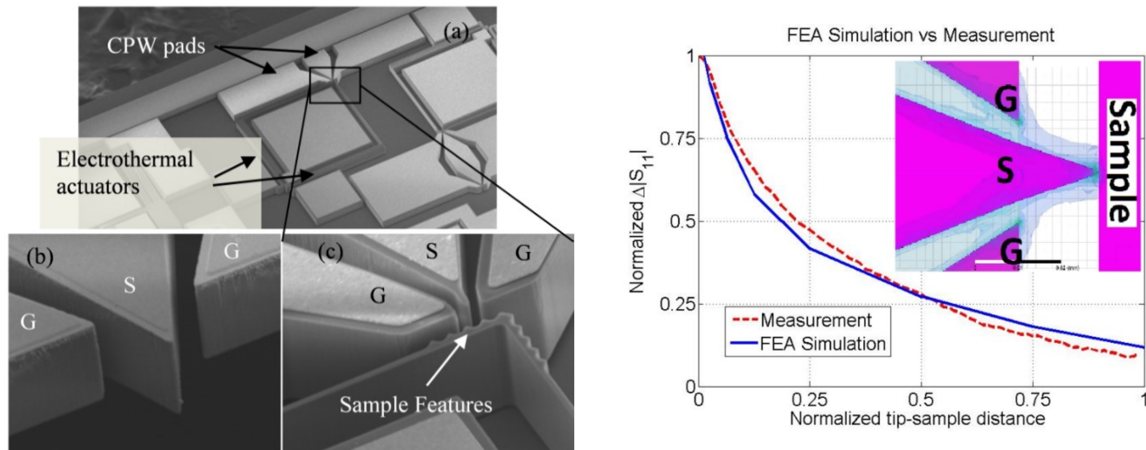

Fig. 5-1. (a) SMM probe with CPW pads and electrothermally actuated sample scanner. (b) Unshielded SPM probe design suspended over the edge of the die for scanning of off-chip samples. (c) Close-up of shielded SPM probe design with on-chip sample positioning. (right) The tip-sample approach curve for SMM. Inset figure shows FEA simulation of field distribution in tip-sample region for unshielded geometry.

our first device that was fabricated in the SOIMUMPs process (Fig. 5-1). This characteristic curve was obtained by actuating only the approach direction actuator. The results obtained are in agreement with the FEA simulations performed in HFSS.

The first step in obtaining measurements is to match the high tip-sample impedance to the 50 ohm input impedance of a PNA. This is achieved using the single-stub matching network shown in Fig. 5-2-(a). A single frequency measurement is used here. The measurement frequency should be close to the matched point to yield maximum sensitivity, as shown in Fig. 5-2-(b).

For the first fabricated CMOS-MEMS SMM, a control experiment was performed in order to quantify parasitic from thermal actuation. An FR4 PCB with copper traces was sectioned and planarized for use as a sample. The SMM probe was positioned near the copper surface using a coarse positioning micromanipulator. The z-actuator was then oscillated to place the SMM tip in intermittent contact with the copper surface. The comparison between measured S_{11} values in air and with copper contact is shown in Fig. 5-3. From this data, we can infer

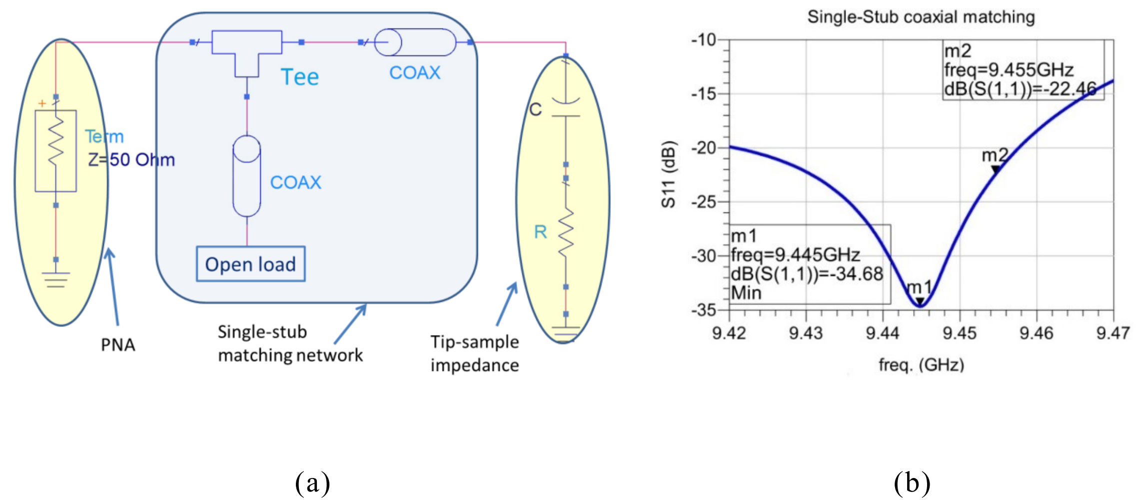

(a) (b)

Fig. 5-2. (a) System diagram for SMM measurements. From left to right: 50-ohm termination represents the PNA input impedance. Coax lines are a single-stub matching network. A simplified model of the tip sample interaction is on the right side. (b) Measurement frequency should be close to the matched point (m1).

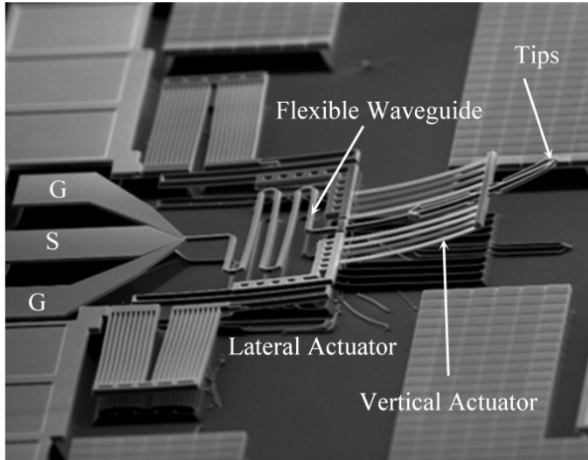

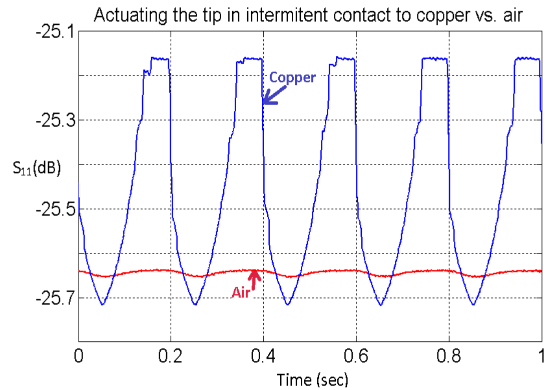

(a) (b)

Fig. 5-3. (a) CMOS-MEMS 3 DOF integrated AFM-SMM device. A CPW to flexible rectangular coaxial line transition connects the microwave signal to the tip. Actuators are used to bend the waveguide and scan the tips. (b) Data comparing intermittent contact with copper to parasitic signal from electrothermal actuation in air.

that the parasitic contribution from electrothermal actuation is ~30X lower than our signal levels. Similar curves were obtained over the FR4 regions of the PCB but with lower peak-to-peak amplitudes. With large tip-sample separations, calibration in air may be needed in order to compensate for thermal effects.

In order to mitigate the effects of *1/f* noise and other long-term drifts in the system, we modulated the tip-sample distance by applying a sinusoidal input at a frequency ω to the z-actuator. The thermal time constant of the z-actuator is approximately 2 kHz, after which its amplitude of oscillation decays at ~20dB per decade. The mechanical resonant frequency of the cantilevers is ~100 kHz. These values constrain the allowable range of frequencies for the oscillation of the z-actuator.

The amplitude of the S_{11} signal contains terms at the oscillation frequency ω as well as at higher harmonics due to the non-linearity of the tip-sample interaction. In Fig. 5-3-(b), the amplitude of the modulated signal as a function of time is plotted to capture only the ω component of the signal. This plot was obtained while the lateral scanners were repeatedly scanning a region that contained a transition between air and silicon. The demodulated signal

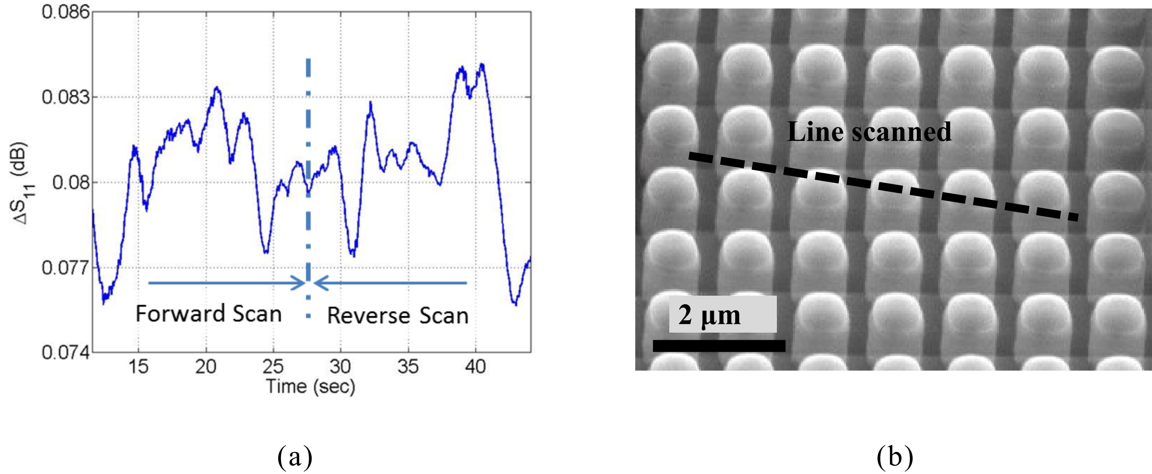

(a) (b)

Fig. 5-4. (a) Forward and reverse scans of a region of a CMOS chip. Arrays of aluminum vias on the sample were exposed with a SiO2 etch step. (b) Arrays of aluminum via holes on a CMOS chip that was exposed with a SiO_2 etch step and used as a sample for our device.

captures four lateral scans, revealing features within the silicon-air transition region.

The third sample that was tested reveals features on a CMOS chip. The scan region contains aluminum pillars that are partially exposed by etching the SiO_2 dielectric layer. The symmetry in the forward and reverse scans is clearly visible in this scan. These data were also obtained by modulating the tip-sample gap with a sinusoidal signal (Fig. 5-4-(a)).

5.2 Imaging Results

After wire-bonding the SMM device to the daughterboard and mounting it on the stage (shown in Fig. 5-5), a mechanical frequency sweep is done first to find the probe's resonance frequency (usually around 7-9 KHz). Then, the sample is brought close to the tip with a stepper motor and the voltage across the sensing piezo resistors on the SMM chip is monitored. As the sample gets closer, due to interaction forces between the tip and the sample, the voltage amplitude across the sensing piezo is dropped. When the tip makes intermittent contact with the sample, the voltage continues to decrease. A PID feedback loop is used to keep the voltage across the sensing piezo-resistors to a set constant value, which

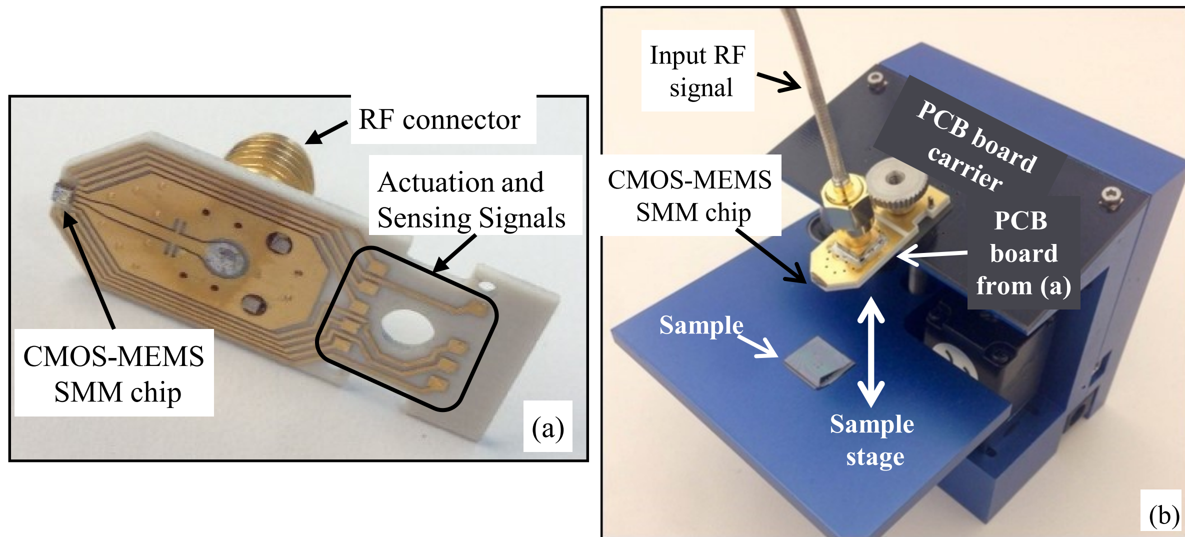

Fig. 5-5. (a) CMOS-MEMS SMM assembled on a daughter-board with stub matching and RF connector. (b) SMM with daughter-board mounted on a stage (stage from [28]). Sample stage moves up and down with a motor.

helps to keep the tip-sample distance constant. When the desired value from the sensing piezo is achieved, one can start lateral scanning and imaging the sample. The lock-in amplifier is synchronized with the resonant frequency of the cantilever and captures the amplitude and phase of the reflected signal in the baseband (described in section 4.6). Software is used to capture the amplitude and phase of the lock-in amplifier, creating a map to the scanned positions and finally generating an image based on the recorded amplitudes and phases.

The scan rate is about one second per line for a 256 points line, which means that a 128 by 128 pixel image can be obtained in ~1 minute. This numbers can be further improved by better software/hardware design.

The first sample imaged is a DVD, which has several pits and bumps to make zeros and ones; the pits have a height of 120 nm, 740 nm spacing between successive lines, and a minimum of 400 nm between the pits as shown in Fig. 5-6. Fig. 5-7 shows a simultaneous AFM and SMM image of DVD pits in a 7 µm x 7 µm scan area obtained by an older version of the CMOS-MEMS SMM and Fig. 5-8 shows the same image in a wider scan area of 13 µm x 13 µm obtained by the most recent chip that has wider scan area and less noise due to improvements in the mechanical design.

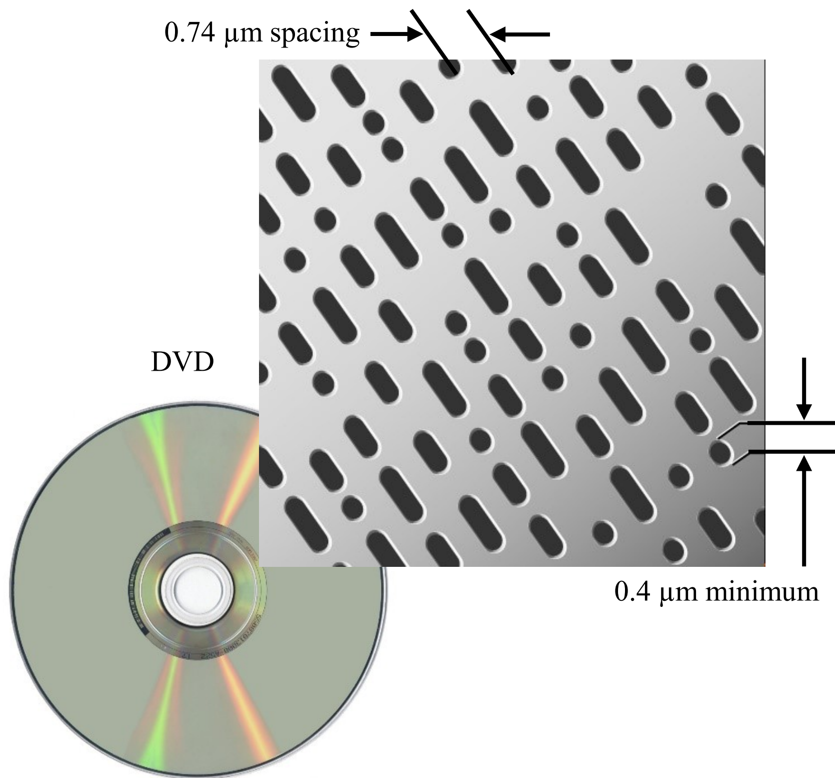

Fig. 5-6. DVD: 740 nm spacing between successive lines and minimum of 400 nm between the pits.

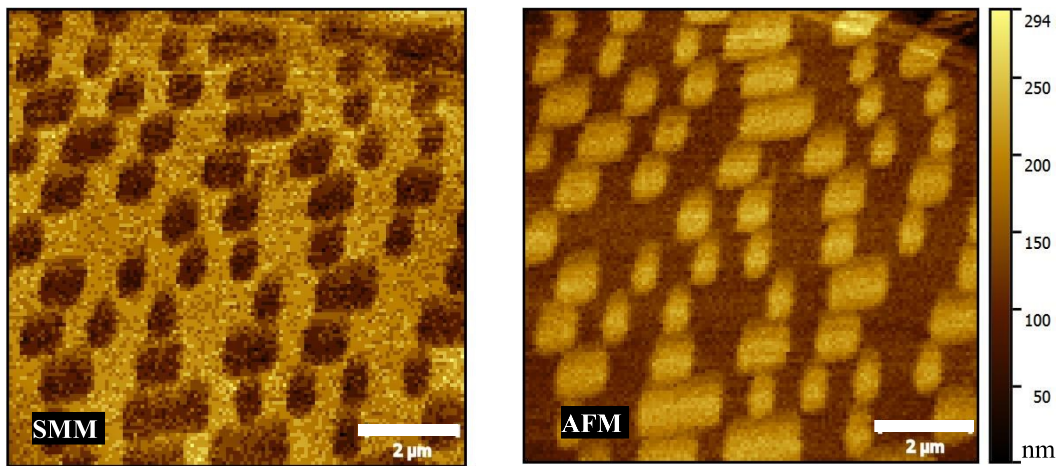

Fig. 5-7. Simultaneous AFM/SMM image of DVD pits imaged with an early version of SMM in a scan area of 7 µm x 7 µm taken with an early version of the SMM. (Right scale is for AFM image only.)

Another sample imaged is a 22 nm CMOS SRAM chip with exposed contact pads. Features are about 200 nm wide and 5 to 10 nm tall. Fig. 5-9 shows the simultaneous SMM and AFM

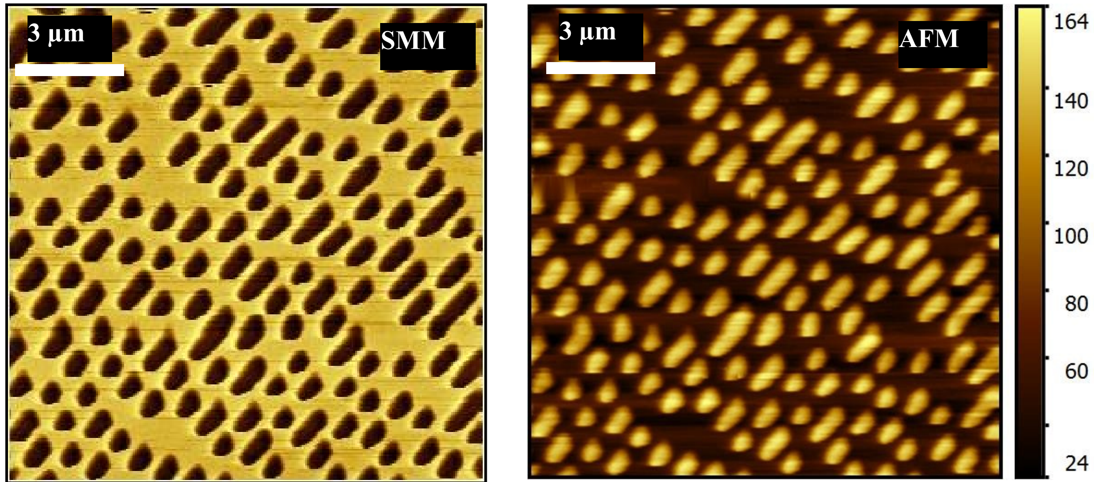

Fig. 5-8. Simultaneous AFM/SMM image of DVD pits with the latest SMM device with better sensitivity, less noise and more range of motion: 13µm x 13µm scan area. (scale is for AFM in nm)

image of this sample. We can see that there are some areas circled in the SMM image and shown with arrows with different electrical properties underneath (doping or dielectric constant), which is not detected by the AFM. This shows that SMM can potentially reveal features that are not detected by an AFM, such as buried structures and materials, and may also obtain better resolution due to the microwave field enhancement at the tip.

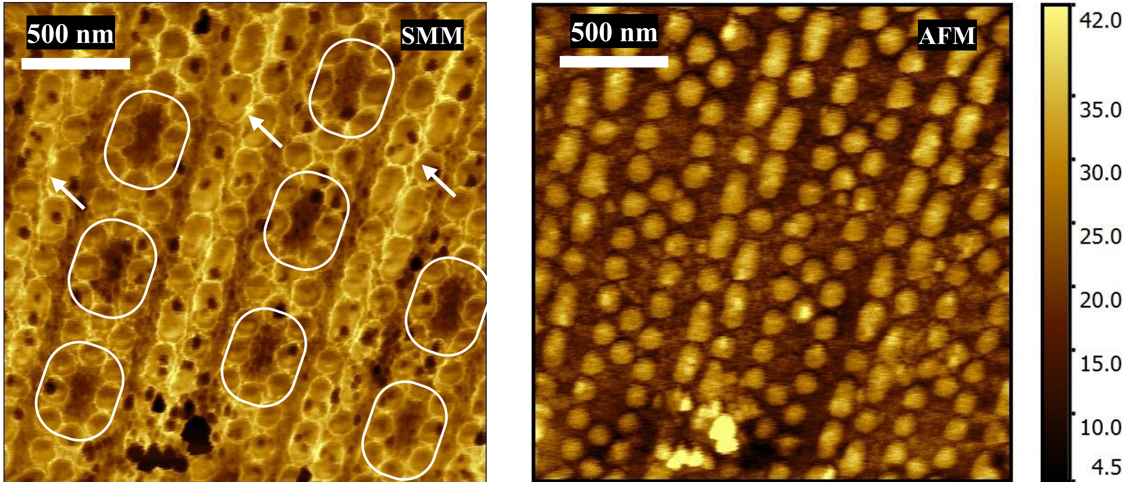

Fig. 5-9. Simultaneous AFM/SMM image of repeated 22nm Intel Ivy Bridge SRAM cells with exposed contact pads: some areas of doped silicon is visible in the SMM image but not in the AFM image. Features are less than 200 nm in width and approximately 5 to 10 nm tall. (scale is for AFM in nm)

Another area of the SRAM sample imaged by the integrated SMM/AFM device is shown

in Fig. 5-10. Again in these images, SMM reveals more features than AFM. Two different areas with different scan ranges are imaged and shown in Fig. 5-10.

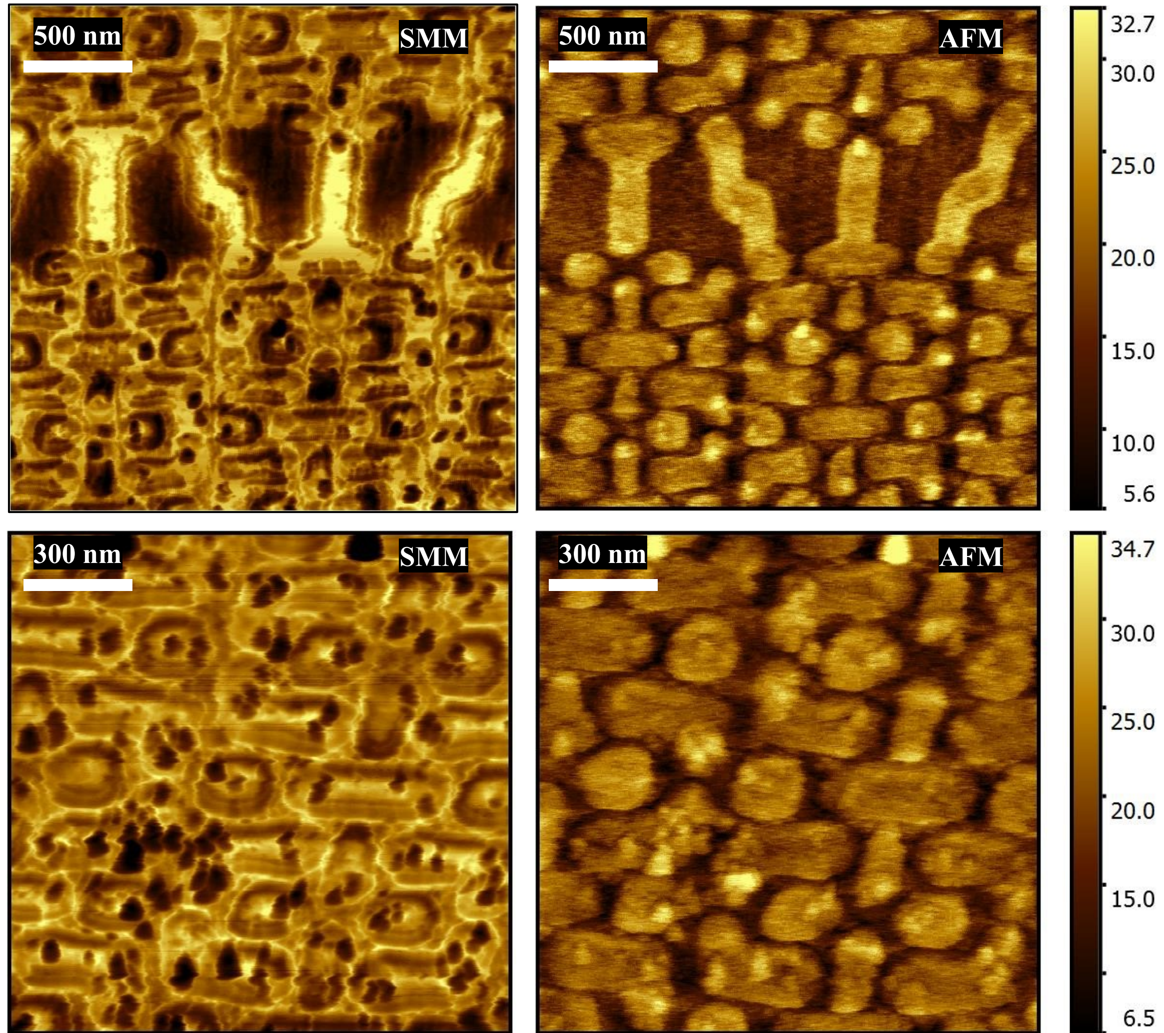

Fig. 5-10. Simultaneous AFM/SMM image of two different areas of repeating SRAM unit cells. SMM images show more detailed features of the sample compared to AFM. (scale is for AFM in nm)

Other samples imaged by our integrated SMM system are carbon nanotubes on a glass slide shown in Fig. 5-11. and graphene nano-flakes shown in Fig. 5-12. In this particular device, the integrated AFM amplitude channel could not detect the topography of these samples because the RMS noise of this integrated AFM is about 2 to 3 nanometers and the features on these sample are about or smaller than 2 nanometers. Nevertheless, the AFM phase

channel has picked up some signal. Both the carbon nanotubes and the graphene nano-flakes are detected by both the amplitude and the phase channels of the SMM.

Please note that in all the images reported in this thesis, there is no scale for the SMM image because different images are taken with different settings, and the overall system is not properly calibrated. Only AFM amplitude channel that shows topography is calibrated, and thus a vertical scale bar is included for the AFM images alone.

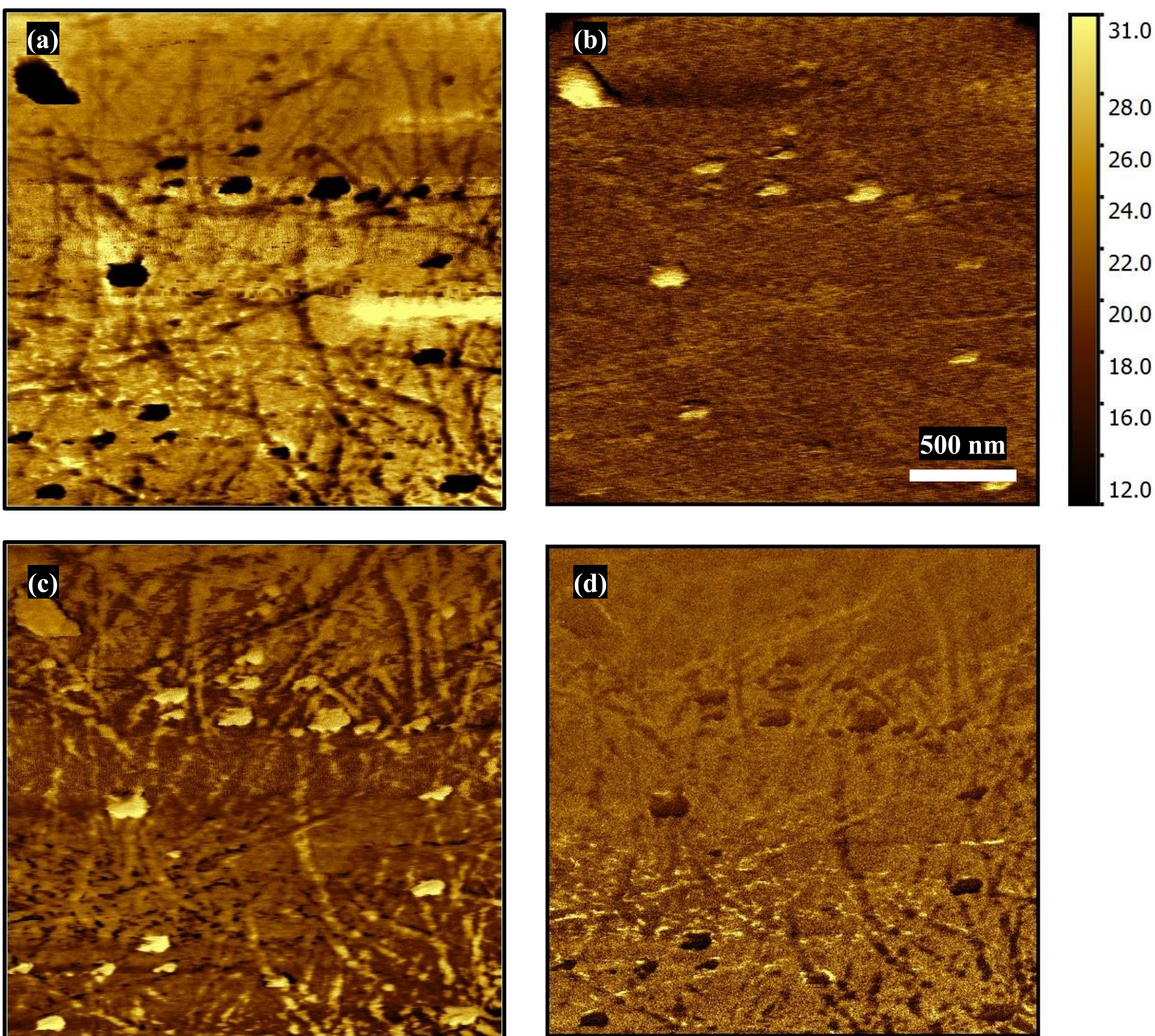

Fig. 5-11. Simultaneous AFM/SMM image of carbon nanotubes on a glass slide. (a) SMM amplitude, (b) AFM amplitude (scale in nm), (c) SMM phase and (d) AFM phase.

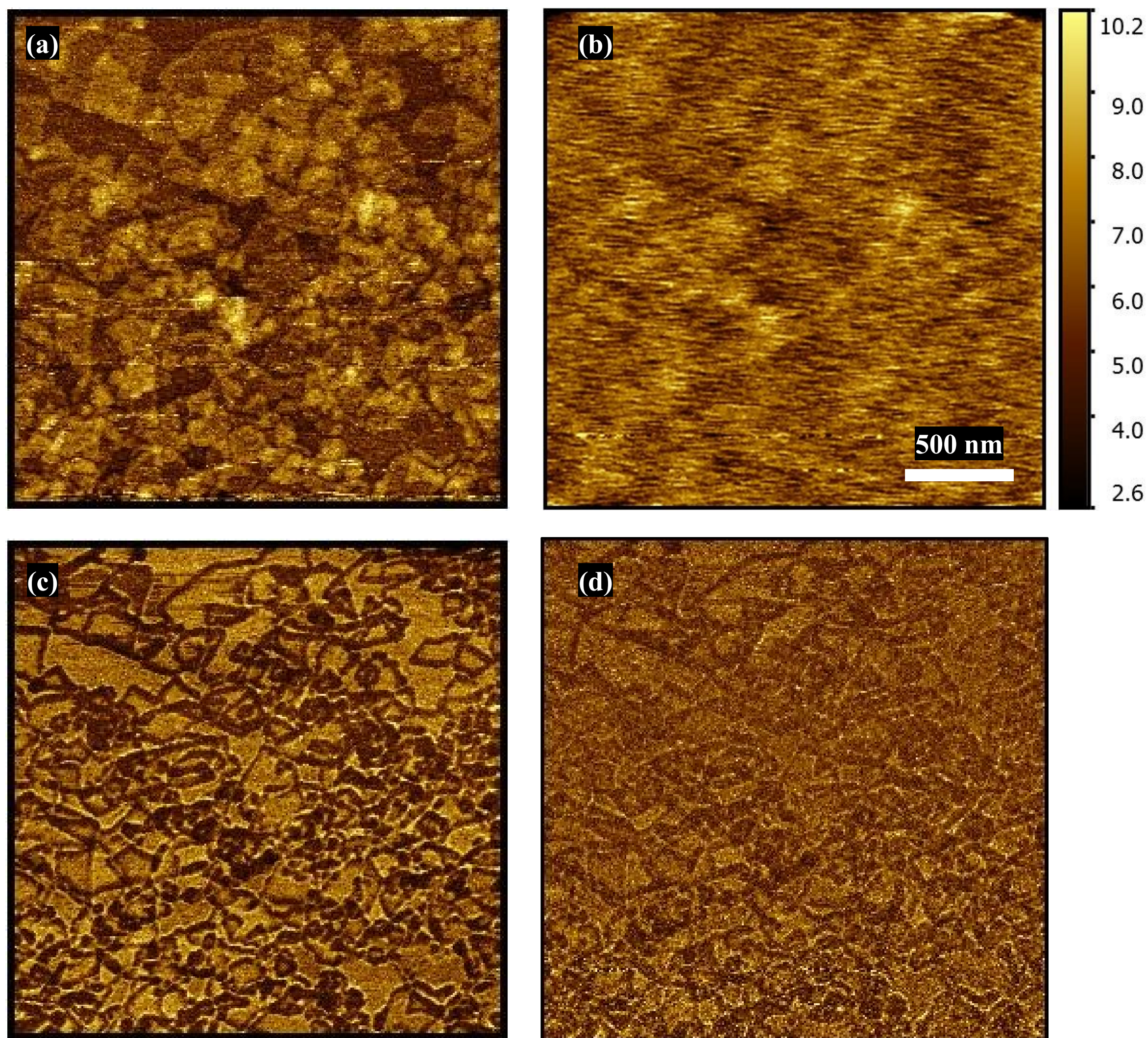

Fig. 5-12. Simultaneous AFM/SMM image of graphene nano-flakes. (a) SMM amplitude, (b) AFM amplitude (scale in nm), (c) SMM phase and (d) AFM phase.

5.2.1 Sample with Subsurface Features

One of the key benefits of microwave imaging is that it can penetrate into the sample and image underneath a dielectric [71]–[73]. To test this feature, we collaborated with the FORTH Group at the Institute of Computational Mathematics in Greece to fabricate an SMM test sample. The test sample is depicted in Fig. 5-13. A few different samples were fabricated. Grids and stripes of two different materials were repeated in 0.5 µm, 1 µm, 2 µm and 5 µm steps over an area of 500 µm x 500 µm as shown in Fig. 5-14. Two sets of samples were fabricated – one with a thin layer of HfO_2 and one without. The samples were designed to have no topology (i.e., a maximum of few nanometers), so that the AFM could not see the differences between the two areas but the SMM could. During the fabrication process, some of the samples with fine features (0.5 µm and 1 µm) did not survive the etching, so only the 2 µm and 5 µm samples were imaged.

The first sample imaged was the 5-micron grid sample without the oxide layer on top. The AFM image showed a few nanometers of topography, which means that the sample is not

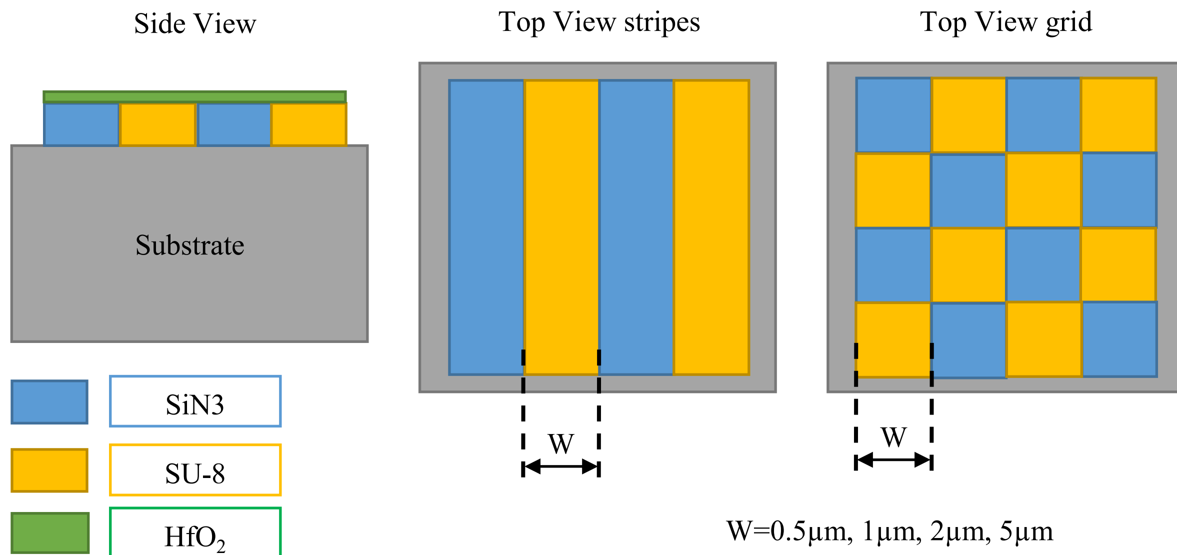

Fig. 5-13. SMM sample: Grids and stripes of silicon nitride and SU-8, repeated with different pitch in a total area of 500 µm x 500 µm. Two sets were fabricated: with and without a thin layer of HfO_2.

completely flat. However, the SMM shows a sharper image with more contrast between the regions, as can been seen in Fig. 5-16.

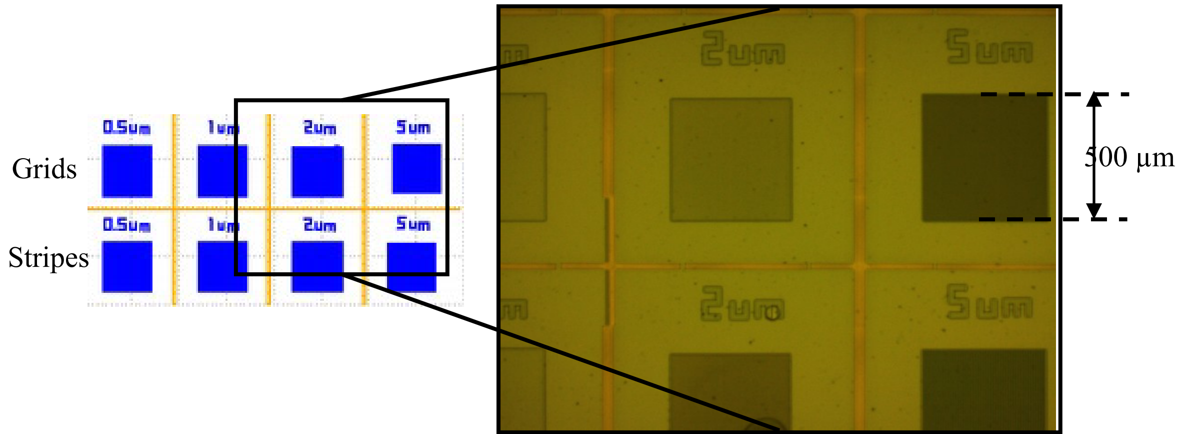

Fig. 5-14. Fabricated SMM samples: 0.5, 1, 2 and 5 μm grids and stripes in a 500 μm x 500 μm area.

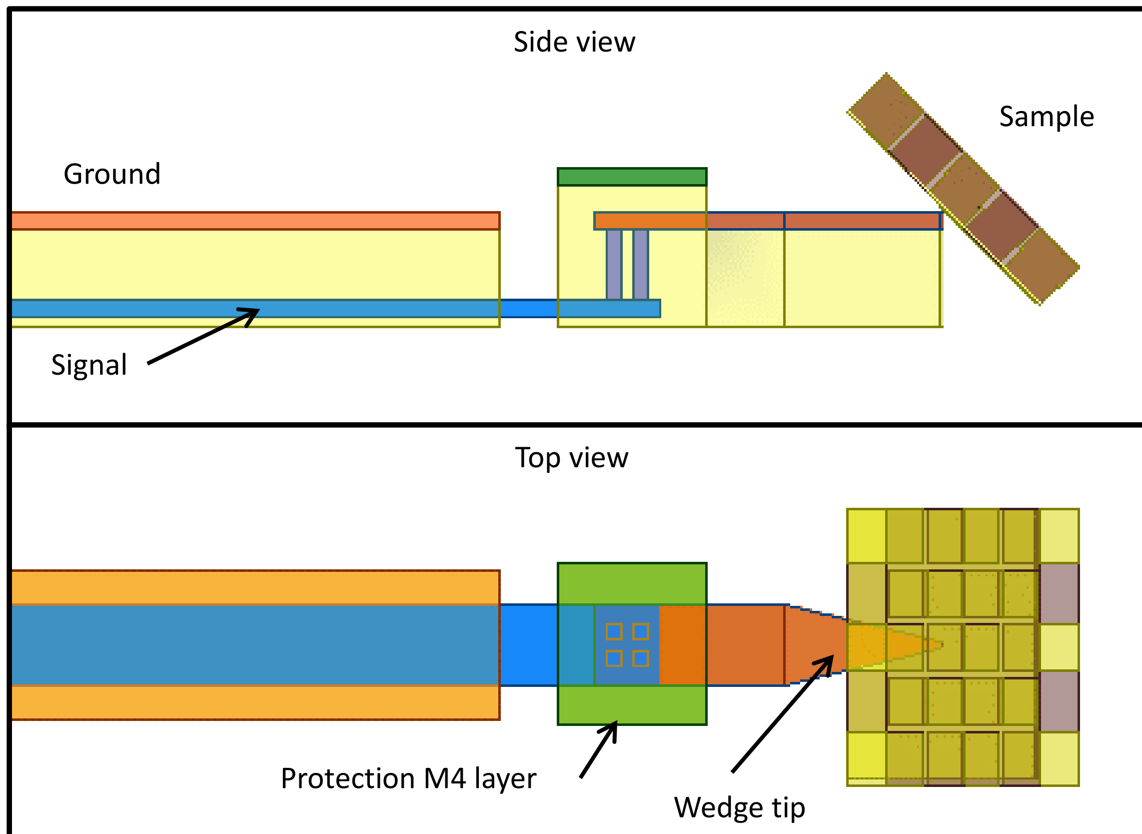

Fig. 5-15. HFSS simulation structure for the grid sample with a thin layer of oxide on top.

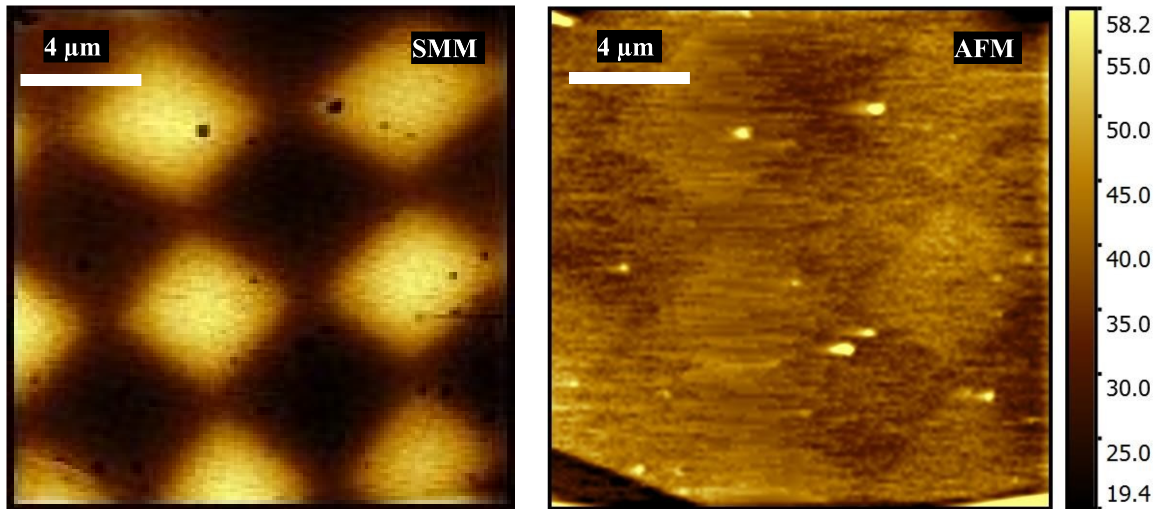

Fig. 5-16. Simultaneous SMM and AFM images of the 5 micron grid without HfO_2 on top. SMM reveals images with more contrast between the two regions. Scan area: 17 μm x17 μm.

After that, the 5 micron grid with HfO_2 on top is imaged. Fig. 5-17 shows that SMM can image buried samples. As one can see, there are many dirt and dust particles on these samples that may affect the sensitivity of the measurements.

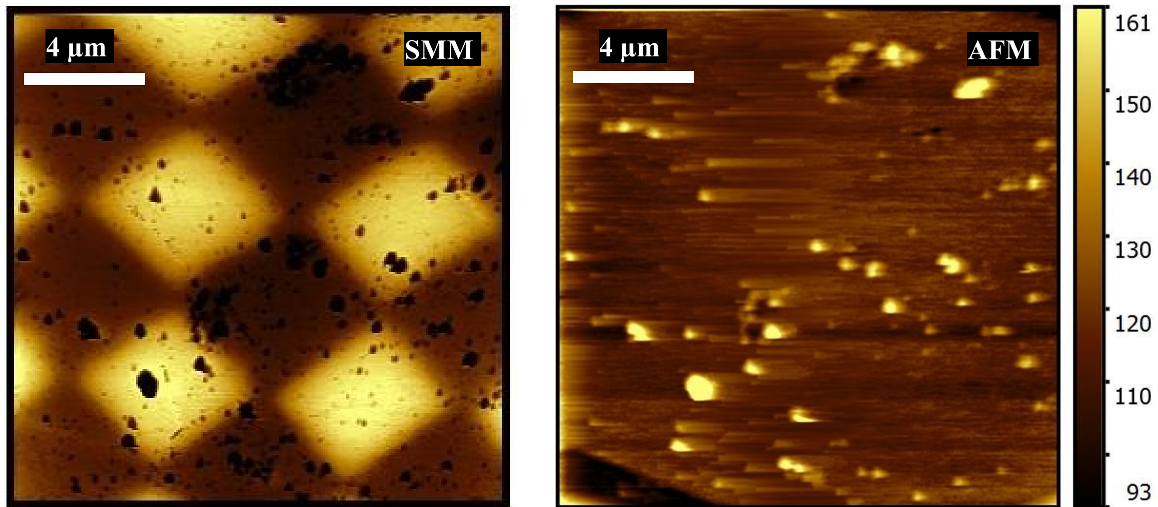

Fig. 5-17. Simultaneous SMM and AFM images of the 5 micron grid with HfO_2 on top. SMM can image buried samples. (right scale is for AFM in nm)

It should be noted that HfO_2 has a dielectric constant of more than 15 and therefore it confines the microwave signal and reduces the penetration depth of the microwave signal.

However, our SMM was able to pick up a clear signal.

Imaging results of the 2 μm grid sample without and with the HfO2 layer is shown in Fig. 5-18 and Fig. 5-19 respectively.

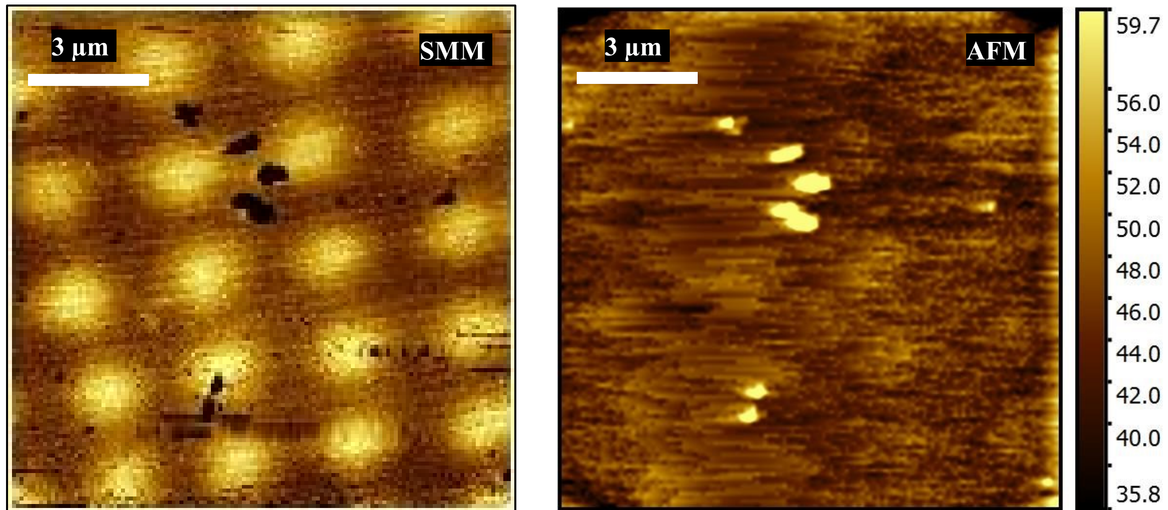

Fig. 5-18. Simultaneous SMM and AFM images of the 5 micron grid without HfO_2 on top.

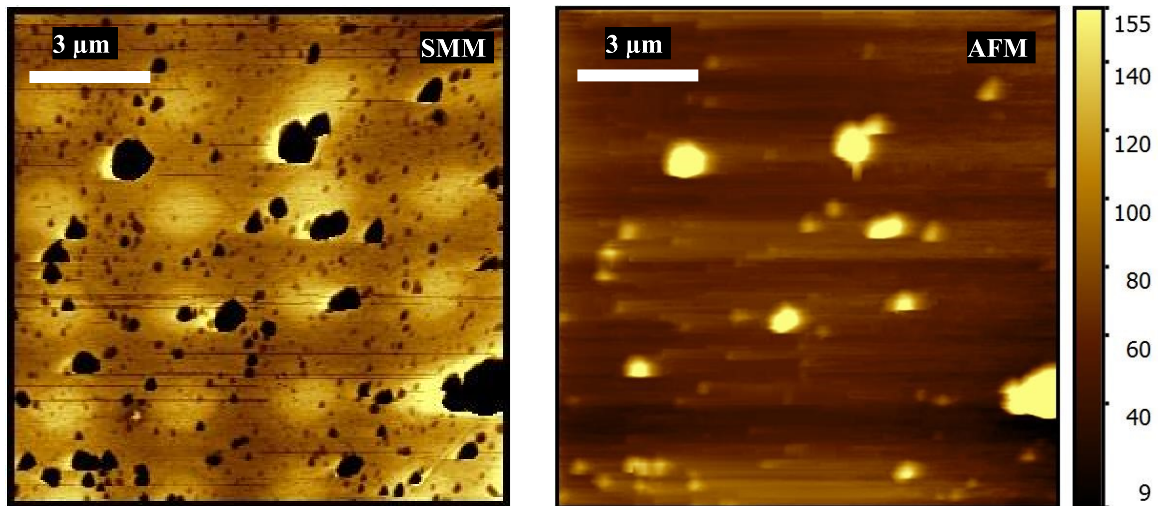

Fig. 5-19. Simultaneous SMM and AFM images of the 5 micron grid with HfO_2 on top.

Fig. 5-20 and Fig. 5-21 show the simultaneous SMM and AFM images of the 5 μm and the 2 μm stripes without the HfO_2 layer on top, respectively. Similar to the grid samples, one can see that the AFM shown a small height difference of less than 10 nm between the two areas but SMM signal shows a clear contrast between them.

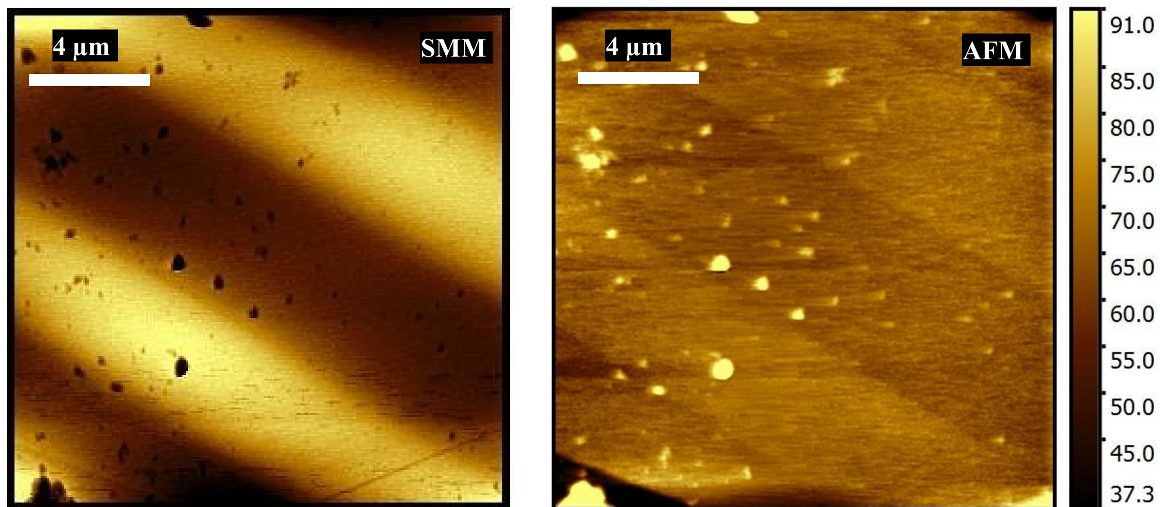

Fig. 5-20. Simultaneous SMM and AFM images of 5 μm stripes without the HfO_2 layer on top.

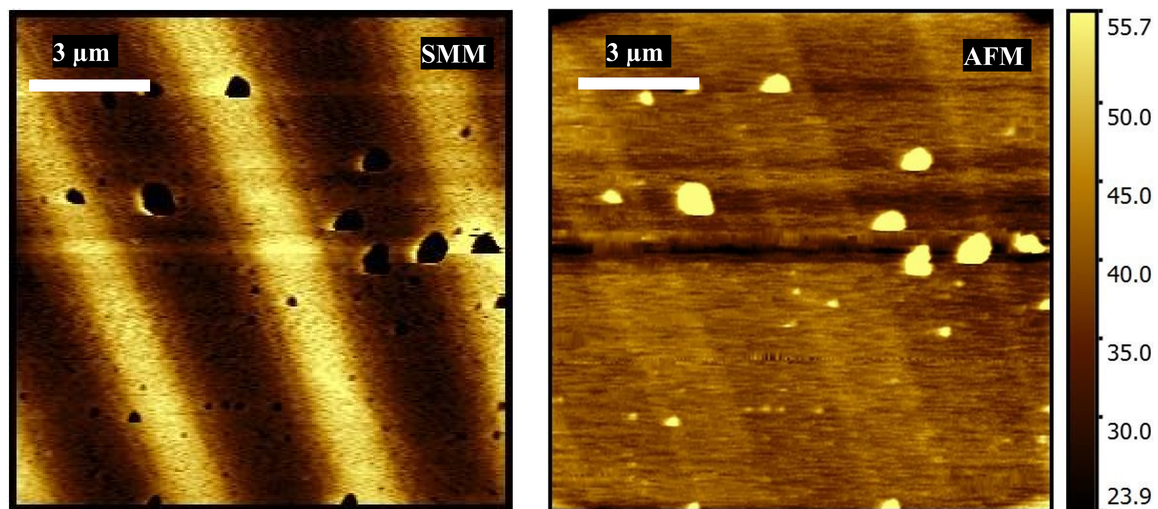

Fig. 5-21. Simultaneous SMM and AFM images of 2 μm stripes with 20 nm of HfO_2 on top. AFM does not show much topography, but SMM shows clear contrast between areas with different dielectric constant. (right scale is for AFM in nm)

Finally, the last image is the 2 μm the stripes with the HfO2 layer on top. Here, again the AFM was not able to pick up any signal (Fig. 5-22).

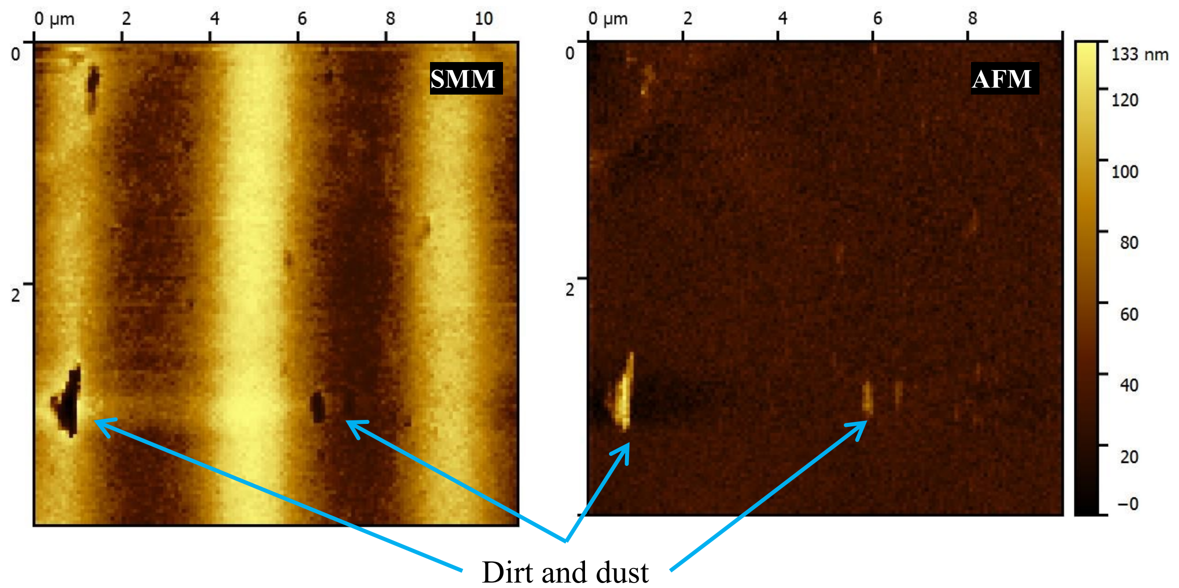

Fig. 5-22. Simultaneous SMM and AFM images of 2 µm stripes with 20 nm of HfO_2 on top. AFM does not show any topography, but SMM shows clear contrast between areas with different dielectric constant. (right scale is for AFM in nm)

Chapter 6
Conclusion and Future work

6.1 Conclusion

Scanning Microwave Microscopy is an emerging tool in sub-micron to nano-scale material characterization and imaging. In this research, we have investigated its advantageous characteristics and combined it with AFM using CMOS-MEMS technology to fabricate an inexpensive and compact SMM that also improves the sensitivity and resolution of quantitative imaging.

The motivations and objectives of this thesis were discussed in Chapter 1. Then a literature survey of research works reported in this area along with early theoretical analyses for SMMs were presented in Chapter 2. In Chapter 3, the CMOS-MEMS fabrication process was explained, showing how, with the help of electrothermal actuators, the tip can be scanned over the sample and thus negate the need for bulky and expensive external sample scanners. Piezo-resistive position sensing of AFM/SMM systems, which replaces the laser system for topography imaging and tip-sample interaction, is also explained.

In Chapter 4, the design and performance of a fully integrated CMOS-MEMS SMM was presented in detail. Comprehensive sensitivity analyses of the SMM system was carried out addressing the use of various matching networks and transmission lines realized in CMOS technology. These analyses, though intended here for the novel CMOS-MEMS SMM system described in this thesis, can still help designers improve the sensitivity of conventional SMM systems. A measurement system was developed, built, and implemented to improve the signal-to-noise ratio and maximize the sensitivity of the CMOS-MEMS SMM system.

In Chapter 5, simultaneous AFM/SMM imaging results for a DVD sample and a 22 nm

SRAM sample using our CMOS-MEMS SMM were presented. Additionally, a sample with no topography but with buried structures was designed and fabricated in collaboration with the FORTH Group in Greece; these samples were imaged to show the capability of SMMs in imaging subsurface structures.

6.2 Future Work

Scanning Microwave Microscopy is a recently developed tool for metrology and its full potential has not yet been unlocked due to its high price and difficulty of use. CMOS-MEMS SMM can unlock the full potential of microwave imaging and make it available and affordable for researchers. However, there is still significant room for improvement in CMOS-MEMS SMM. For example, it is always desirable to have scanners with a higher range of motion to image a larger area of the sample in a single scan.

In the sensitivity analysis in Chapter 4, we saw that a higher quality factor for the matching network translates into better sensitivity. Active compensation circuits can be utilized for both improved quality factor and improve sensitivity. This technique had been demonstrated and used for sensing in [74], [75]. Fig. 6-1 shows a block diagram of a feedback oscillator

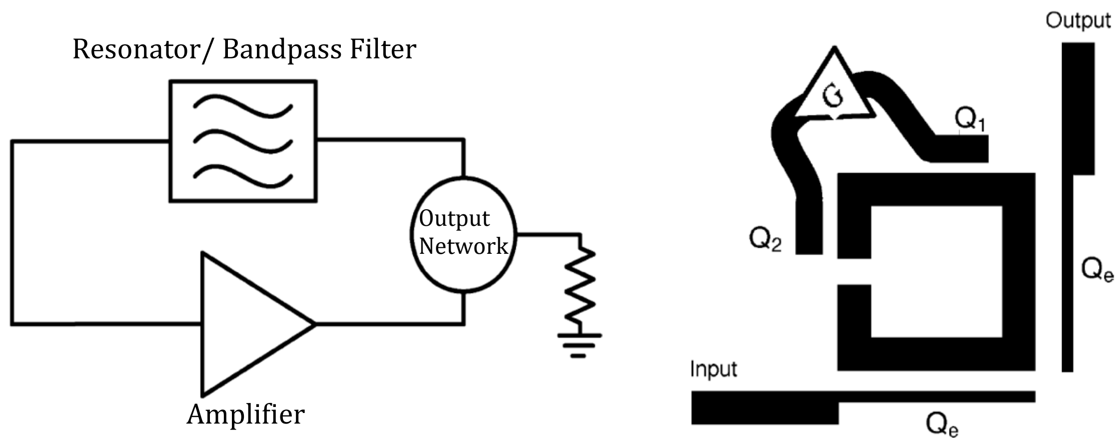

Fig. 6-1. Block diagram of a feedback oscillator employing a resonator for frequency stabilization. Square open-loop resonator with an active feedback loop for loss compensation [75].

employing a resonator or bandpass filter for frequency stabilization, and a square open-loop resonator with an active feedback loop for loss compensation [2]. A similar technique can be used for the loss compensation of the stub-matching used for SMM.

Another approach for improving the quality factor and sensitivity of the system is to use MEMS resonators. MEMS resonators are compact and have a very high quality factor. The Feng group has shown CMOS-MEMS resonators with a Q of more than 10,000 at around 50 MHz [76]–[78].

Bibliography

[1] C. Gao, B. Hu, I. Takeuchi, K.-S. Chang, X.-D. Xiang, and G. Wang, “Quantitative scanning evanescent microwave microscopy and its applications in characterization of functional materials libraries,” *Meas. Sci. Technol.*, vol. 16, no. 1, pp. 248–260, Jan. 2005.

[2] M. Tabib-Azar, D.-P. Su, A. Pohar, S. R. LeClair, and G. Ponchak, “0.4 μm spatial resolution with 1 GHz (λ=30 cm) evanescent microwave probe,” *Rev. Sci. Instrum.*, vol. 70, no. 3, p. 1725, 1999.

[3] S. M. Anlage, V. V. Talanov, and A. R. Schwartz, “Principles of near-field microwave microscopy,” in *Scanning Probe Microscopy: Electrical and Electromechanical Phenomena at the Nanoscale*, vol. 1, Berlin, Germany: Springer-Verlag, 2007, pp. 215–253.

[4] K. Lai, M. B. Ji, N. Leindecker, M. a. Kelly, and Z.-X. Shen, “Atomic-force-microscope-compatible near-field scanning microwave microscope with separated excitation and sensing probes.,” *Rev. Sci. Instrum.*, vol. 78, no. 6, p. 063702, Jun. 2007.

[5] H. P. Huber, I. Humer, M. Hochleitner, M. Fenner, M. Moertelmaier, C. Rankl, A. Imtiaz, T. M. Wallis, H. Tanbakuchi, P. Hinterdorfer, P. Kabos, J. Smoliner, J. J. Kopanski, and F. Kienberger, “Calibrated nanoscale dopant profiling using a scanning microwave microscope,” *J. Appl. Phys.*, vol. 111, no. 1, p. 014301, 2012.

[6] J. Smoliner, H. P. Huber, M. Hochleitner, M. Moertelmaier, and F. Kienberger, “Scanning microwave microscopy/spectroscopy on metal-oxide-semiconductor systems,” *J. Appl. Phys.*, vol. 108, no. 6, p. 064315, 2010.

[7] “Scanning Spreading Resistance Mi-imec.” [Online]. Available: http://www2.imec.be/be_en/collaboration/services/cams/scanning-spreading-resistance-mi.html.

[8] C. Plassard, E. Bourillot, J. Rossignol, Y. Lacroute, E. Lepleux, L. Pacheco, and E. Lesniewska, “Detection of defects buried in metallic samples by scanning microwave microscopy,” *Phys. Rev. B*, vol. 83, no. 12, pp. 2–5, Mar. 2011.

[9] Y. Xing, J. Myers, O. Obi, N. X. Sun, and Y. Zhuang, “Scanning Microwave Microscopy Characterization of Spin-Spray-Deposited Ferrite/Nonmagnetic Films,” *J. Electron. Mater.*, vol. 41, no. 3, pp. 530–534, Dec. 2011.

[10] N. Sarkar, R. R. Mansour, O. Patange, and K. Trainor, “CMOS-MEMS atomic force microscope,” in *2011 16th International Solid-State Sensors, Actuators and Microsystems Conference*, 2011, pp. 2610–2613.

[11] N. Sarkar, D. Strathearn, G. Lee, M. Olfat, and R. R. Mansour, “A 0.25mm^3 Atomic Force Microscope on-a-chip,” in *2015 28th IEEE International Conference on Micro Electro Mechanical Systems (MEMS)*, 2015, pp. 732–735.

[12] E. Synge, “A suggested method for extending microscopic resolution into the ultra-microscopic region,” *Philos. Mag. Ser. 7*, vol. 6, no. 35, pp. 356–362, 1928.

[13] L. Novotny, “The history of near-field optics,” *Prog. Opt.*, vol. 184, pp. 137–183, 2007.

[14] Z. Frait, “The use of High-Frequency Modulation in Studying Ferromagnetic Resonance,” *Czechosl. Journ. Phys.*, vol. 9, pp. 403–404, 1959.

[15] R. F. Soohoo, “A Microwave Magnetic Microscope,” *J. Appl. Phys.*, vol. 33, no. 3, p. 1276, 1962.

[16] E. Ash and G. Nicholls, “Super-resolution aperture scanning microscope,” *Nature*, vol. 237, pp. 510–512, 1972.

[17] M. Tabib-Azar and Y. Wang, “Design and Fabrication of Scanning Near-Field Microwave Probes Compatible With Atomic Force Microscopy to Image Embedded Nanostructures,” *IEEE Trans. Microw. Theory Tech.*, vol. 52, no. 3, pp. 971–979, Mar. 2004.

[18] M. Fee and S. Chu, “Scanning electromagnetic transmission line microscope with sub-wavelength resolution,” *Opt. Commun.*, vol. 69, no. 3, p. 219, 1989.

[19] D. E. Steinhauer, C. P. Vlahacos, S. K. Dutta, F. C. Wellstood, and S. M. Anlage, “Surface resistance imaging with a scanning near-field microwave microscope,” *Appl. Phys. Lett.*, vol. 71, no. 12, p. 1736, 1997.

[20] D. E. Steinhauer, C. P. Vlahacos, S. K. Dutta, B. J. Feenstra, F. C. Wellstood, and S. M. Anlage, “Quantitative imaging of sheet resistance with a scanning near-field microwave microscope,”

Appl. Phys. Lett., vol. 72, no. 7, p. 861, 1998.

[21] D. E. Steinhauer, C. P. Vlahacos, F. C. Wellstood, S. M. Anlage, C. Canedy, R. Ramesh, A. Stanishevsky, and J. Melngailis, “Imaging of microwave permittivity, tunability, and damage recovery in (Ba, Sr)TiO3 thin films,” *Appl. Phys. Lett.*, vol. 75, no. 20, p. 3180, 1999.

[22] C. P. Vlahacos, D. E. Steinhauer, S. K. Dutta, B. J. Feenstra, S. M. Anlage, and F. C. Wellstood, “Quantitative topographic imaging using a near-field scanning microwave microscope,” *Appl. Phys. Lett.*, vol. 72, no. 14, p. 1778, 1998.

[23] V. V. Talanov, A. Scherz, R. L. Moreland, and A. R. Schwartz, “A near-field scanned microwave probe for spatially localized electrical metrology,” *Appl. Phys. Lett.*, vol. 88, no. 13, p. 134106, 2006.

[24] T. Wei, X.-D. Xiang, W. G. Wallace-Freedman, and P. G. Schultz, “Scanning tip microwave near-field microscope,” *Appl. Phys. Lett.*, vol. 68, no. 24, p. 3506, 1996.

[25] C. Gao, T. Wei, F. Duewer, Y. Lu, and X.-D. Xiang, “High spatial resolution quantitative microwave impedance microscopy by a scanning tip microwave near-field microscope,” *Appl. Phys. Lett.*, vol. 71, no. 13, p. 1872, 1997.

[26] C. Gao and X.-D. Xiang, “Quantitative microwave near-field microscopy of dielectric properties,” *Rev. Sci. Instrum.*, vol. 69, no. 11, p. 3846, 1998.

[27] A. N. Reznik and V. V. Talanov, “Quantitative model for near-field scanning microwave microscopy: application to metrology of thin film dielectrics,” *Rev. Sci. Instrum.*, vol. 79, no. 11, p. 113708, Nov. 2008.

[28] X.-D. Xiang and C. Gao, “Quantitative complex electrical impedance microscopy by scanning evanescent microwave microscope,” *Mater. Charact.*, vol. 48, no. 2–3, pp. 117–125, Apr. 2002.

[29] M. Tabib-Azar, N. S. Shoemaker, and S. Harris, “Non-destructive characterization of materials by evanescent microwaves,” *Meas. Sci. Technol.*, vol. 4, no. 5, pp. 583–590, May 1993.

[30] K. Lai, W. Kundhikanjana, M. a. Kelly, and Z.-X. Shen, “Calibration of shielded microwave probes using bulk dielectrics,” *Appl. Phys. Lett.*, vol. 93, no. 12, p. 123105, 2008.

[31] K. Lai, W. Kundhikanjana, H. Peng, Y. Cui, M. a. Kelly, and Z.-X. Shen, “Tapping mode microwave

impedance microscopy.," *Rev. Sci. Instrum.*, vol. 80, no. 4, p. 043707, Apr. 2009.

[32] M. Tabib-Azar, D. Akinwande, G. E. Ponchak, and S. R. LeClair, "Novel physical sensors using evanescent microwave probes," *Rev. Sci. Instrum.*, vol. 70, no. 8, p. 3381, 1999.

[33] H. P. Huber, M. Moertelmaier, T. M. Wallis, C. J. Chiang, M. Hochleitner, A. Imtiaz, Y. J. Oh, K. Schilcher, M. Dieudonne, J. Smoliner, P. Hinterdorfer, S. J. Rosner, H. Tanbakuchi, P. Kabos, and F. Kienberger, "Calibrated nanoscale capacitance measurements using a scanning microwave microscope.," *Rev. Sci. Instrum.*, vol. 81, no. 11, p. 113701, Nov. 2010.

[34] M. Moertelmaier, H. P. Huber, C. Rankl, and F. Kienberger, "Continuous capacitance-voltage spectroscopy mapping for scanning microwave microscopy," *Ultramicroscopy*, vol. 136, pp. 67–72, 2014.

[35] F. Wang, N. Clément, D. Ducatteau, D. Troadec, H. Tanbakuchi, B. Legrand, G. Dambrine, and D. Théron, "Quantitative impedance characterization of sub-10 nm scale capacitors and tunnel junctions with an interferometric scanning microwave microscope.," *Nanotechnology*, vol. 25, no. 40, p. 405703, Oct. 2014.

[36] M. Farina, A. Di Donato, D. Mencarelli, G. Venanzoni, A. Morini, and T. Pietrangelo, "Time-Domain Reflectometry for Near-Field Scanning Microwave Microscopy," in *2015 IEEE MTT-S International Microwave Symposium*, 2015, pp. 1–4.

[37] A. Tselev, J. Velmurugan, A. V. Ievlev, S. V. Kalinin, and A. Kolmakov, "Seeing through Walls at the Nanoscale: Microwave Microscopy of Enclosed Objects and Processes in Liquids," *ACS Nano*, vol. 10, no. 3, pp. 3562–3570, Mar. 2016.

[38] A. Imtiaz and S. M. Anlage, "A novel STM-assisted microwave microscope with capacitance and loss imaging capability.," *Ultramicroscopy*, vol. 94, no. 3–4, pp. 209–16, Apr. 2003.

[39] A. Tselev, S. M. Anlage, H. M. Christen, R. L. Moreland, V. V. Talanov, and A. R. Schwartz, "Near-field microwave microscope with improved sensitivity and spatial resolution," *Rev. Sci. Instrum.*, vol. 74, no. 6, p. 3167, 2003.

[40] A. Karbassi, D. Ruf, a D. Bettermann, C. A. PAULSON, D. W. van der Weide, H. Tanbakuchi, and R. Stancliff, "Quantitative scanning near-field microwave microscopy for thin film dielectric

constant measurement.," *Rev. Sci. Instrum.*, vol. 79, no. 9, p. 094706, Sep. 2008.

[41] S. Akamine, T. R. Albrecht, M. J. Zdeblick, and C. F. Quate, "Microfabricated Scanning Tunneling Microscope," *IEEE ELECTRON DEVICE Lett.*, vol. 10, no. 11, pp. 490–492, 1989.

[42] Y. Xu, N. C. MacDonald, and S. A. Miller, "Integrated micro-scanning tunneling microscope," *Appl. Phys. Lett.*, vol. 67, no. 16, p. 2305, 1995.

[43] D. Barrettino, S. Hafizovic, T. Volden, J. Sedivy, K. Kirstein, a. Hierlemann, and H. Baltes, "CMOS monolithic atomic force microscope," *2004 Symp. VLSI Circuits. Dig. Tech. Pap. (IEEE Cat. No.04CH37525)*, pp. 306–309, 2004.

[44] "A-Probe." [Online]. Available: http://www.akiyamaprobe.com/.

[45] Y. B. Gianchandani and K. Najafi, "A silicon micromachined scanning thermal profiler with integrated elements for sensing and actuation," *IEEE Trans. Electron Devices*, vol. 44, no. 11, pp. 1857–1868, 1997.

[46] N. Sarkar and R. Mansour, "A CMOS-MEMS scanning probe microscope with integrated position sensors," in *1st Microsystems and Nanoelectronics Research Conference, MNRC 2008 - Enabling Synergy and Accelerating Excellence in Graduate Student Research*, 2008, pp. 77–80.

[47] N. Sarkar, R. R. Mansour, and K. Trainor, "Forced Oscillation and Higher Harmonic Detection in an Integrated CMOS-MEMS Scanning Probe Microscope," in *2012 Hilton Head Solid-State Sensors, Actuators, and Microsystems Workshop*, 2012, no. c, pp. 308–310.

[48] N. Sarkar, G. Lee, and R. R. Mansour, "CMOS-MEMS dynamic FM atomic force microscope," in *2013 Transducers & Eurosensors XXVII: The 17th International Conference on Solid-State Sensors, Actuators and Microsystems (TRANSDUCERS & EUROSENSORS XXVII)*, 2013, pp. 916–919.

[49] N. Sarkar, M. Azizi, S. Fouladi, and R. R. Mansour, "Self-actuating scanning microwave microscopy probes," in *2012 IEEE/MTT-S International Microwave Symposium Digest*, 2012, pp. 1–3.

[50] Baltes, Brand, Fedder, Hierold, Korvink, and Tabata, *CMOS—MEMS*. Weinheim, Germany:

Wiley-VCH Verlag GmbH, 2005.

[51] D. Lange, O. Brand, and H. Baltes, *CMOS Cantilever Sensor Systems*. Springer, 2002.

[52] S. F. Fouladi, “Reconfigurable Impedance Matching Networks Based on RF-MEMS and CMOS-MEMS Technologies,” University of Waterloo, Waterloo, ON, 2010.

[53] S. Fouladi, F. Domingue, N. Zahirovic, and R. R. Mansour, “Distributed MEMS Tunable Impedance-Matching Network Based on Suspended Slow-Wave Structure Fabricated in a Standard CMOS Technology,” *IEEE Trans. Microw. Theory Tech.*, vol. 58, no. 4, pp. 1056–1064, Apr. 2010.

[54] R. R. Mansour, “RF MEMS-CMOS Device Integration: An Overview of the Potential for RF Researchers,” *IEEE Microw. Mag.*, vol. 14, no. 1, pp. 39–56, Jan. 2013.

[55] P. J. Gilgunn, J. Liu, N. Sarkar, and G. K. Fedder, “CMOS–MEMS Lateral Electrothermal Actuators,” *J. Microelectromechanical Syst.*, vol. 17, no. 1, pp. 103–114, Feb. 2008.

[56] N. Sarkar, “Single-Chip Scanning Probe Microscopes,” University of Waterloo, Waterloo, ON, 2013.

[57] “AFM Standard Samples.” [Online]. Available: http://www.tedpella.com/.

[58] A. Imtiaz, S. M. Anlage, J. D. Barry, and J. Melngailis, “Nanometer-scale material contrast imaging with a near-field microwave microscope,” *Appl. Phys. Lett.*, vol. 90, no. 14, p. 143106, 2007.

[59] K. Lai, W. Kundhikanjana, M. a. Kelly, and Z.-X. Shen, “Modeling and characterization of a cantilever-based near-field scanning microwave impedance microscope.,” *Rev. Sci. Instrum.*, vol. 79, no. 6, p. 063703, Jun. 2008.

[60] O. C. Haenssler, “Integration of a Scanning Microwave Microscope and a Scanning Electron Microscope: Towards a new instrument to imaging, characterizing and manipulating at the nanoscale,” in *2014 International Conference on Manipulation, Manufacturing and Measurement on the Nanoscale, 3M-NANO 2014 - Conference Proceedings*, 2014, no. October, pp. 39–43.

[61] K. Lai, W. Kundhikanjana, M. a. Kelly, and Z.-X. Shen, “Nanoscale microwave microscopy using

shielded cantilever probes," *Appl. Nanosci.*, vol. 1, no. 1, pp. 13–18, Apr. 2011.

[62] C. H. Doan, S. Emami, A. M. Niknejad, and R. W. Brodersen, "Millimeter-wave CMOS design," *IEEE J. Solid-State Circuits*, vol. 40, no. 1, pp. 144–155, Jan. 2005.

[63] S. D. Santuria, *Microsystem Design*. Kluwer Academic publishers, 2001.

[64] J. J. Lee and C. S. Park, "A Slow-Wave Microstrip Line With a High-Q and a High Dielectric Constant for Millimeter-Wave CMOS Application," *IEEE Microw. Wirel. Components Lett.*, vol. 20, no. 7, pp. 381–383, Jul. 2010.

[65] D. Kaddour, H. Issa, A. L. Franc, N. Corrao, E. Pistono, F. Podevin, J. M. Fournier, J. M. Duchamp, and P. Ferrari, "High-Q Slow-Wave Coplanar Transmission Lines on 0.35 um CMOS Process," *IEEE Microw. Wirel. Components Lett.*, vol. 19, no. 9, pp. 542–544, Sep. 2009.

[66] F. Vecchi, M. Repossi, W. Eyssa, P. Arcioni, and F. Svelto, "Design of Low-Loss Transmission Lines in Scaled CMOS by Accurate Electromagnetic Simulations," *IEEE J. Solid-State Circuits*, vol. 44, no. 9, pp. 2605–2615, Sep. 2009.

[67] H.-Y. Cho, T.-J. Yeh, S. Liu, and C.-Y. Wu, "High-Performance Slow-Wave Transmission Lines With Optimized Slot-Type Floating Shields," *IEEE Trans. Electron Devices*, vol. 56, no. 8, pp. 1705–1711, Aug. 2009.

[68] A. Sutono, N. G. Cafaro, J. Laskar, and M. M. Tentzeris, "Experimental modeling, repeatability investigation and optimization of microwave bond wire interconnects," *IEEE Trans. Adv. Packag.*, vol. 24, no. 4, pp. 595–603, 2001.

[69] K. M. Lakin, G. R. Kline, and K. T. McCarron, "High-Q Microwave Acoustic Resonators and Filters," *IEEE Trans. Microw. Theory Tech.*, vol. 41, no. 12, pp. 2139–2146, 1993.

[70] W. Kundhikanjana, K. Lai, M. a Kelly, and Z.-X. Shen, "Cryogenic microwave imaging of metal-insulator transition in doped silicon.," *Rev. Sci. Instrum.*, vol. 82, no. 3, p. 033705, Mar. 2011.

[71] J. D. Chisum and Z. Popovic, "Performance Limitations and Measurement Analysis of a Near-Field Microwave Microscope for Nondestructive and Subsurface Detection," *IEEE Trans. Microw. Theory Tech.*, vol. 60, no. 8, pp. 2605–2615, Aug. 2012.

[72] M. Maazi, O. Benzaim, K. Haddadi, D. Glay, and T. Lasri, "Non-Contact Subsurface Defects

Characterization by Microwave and Millimeter Wave Techniques," *Sens. Imaging An Int. J.*, vol. 7, no. 4, pp. 125–154, Nov. 2006.

[73] K. Haddadi and T. Lasri, "60-GHz Near-Field Six-Port Microscope Using a Scanning Slit Probe for Subsurface Sensing," *IEEE Sens. J.*, vol. 12, no. 8, pp. 2575–2576, Aug. 2012.

[74] M. H. Zarifi, S. Farsinezhad, K. Shankar, and M. Daneshmand, "Liquid Sensing Using Active Feedback Assisted Planar Microwave Resonator," *IEEE Microw. Wirel. Components Lett.*, vol. 25, no. 9, pp. 621–623, Sep. 2015.

[75] M. Nick and A. Mortazawi, "Low phase-noise planar oscillators based on low-noise active resonators," *IEEE Trans. Microw. Theory Tech.*, vol. 58, no. 5 PART 1, pp. 1133–1139, 2010.

[76] W.-C. Chen, W. Fang, and S.-S. Li, "A generalized CMOS-MEMS platform for micromechanical resonators monolithically integrated with circuits," *J. Micromechanics Microengineering*, vol. 21, p. 065012, 2011.

[77] W. C. Chen, W. Fang, and S. S. Li, "VHF CMOS-MEMS oxide resonators with Q > 10,000," *2012 IEEE Int. Freq. Control Symp. IFCS 2012, Proc.*, no. c, pp. 576–579, 2012.

[78] W. Chen, W. Fang, and S. Li, "High-Integrated CMOS-MEMS Resonators With Deep-Submicrometer Gaps and Quasi-Linear Frequency Tuning," *J. Microelectromechanical Syst.*, vol. 21, no. 3, pp. 688–701, 2012.

[79] J. Audet, "Q Calculations of L-C Circuits and Transmission Lines : A Unified Approach," *Qex*, pp. 43–51, 2006.

[80] P. I. Somlo, "Some Aspects of the Measurement of the Q Factor of Transmission Lines," *IEEE Trans. Microw. Theory Tech.*, vol. 11, no. 6, pp. 472–478, 1963.

Appendix A
SiO_2 and Silicon etching recipes in the RIE

Before and after each process, RIE chamber should be cleaned using CIRFE Clean recipe

Oxide Etch Recipe

- Pressure: 20 (can usually be between 17-20)
- ICP: 200 (reflected is usually at around 1-3)
- RIE: 52 (reflected is usually around 5-8)
- CHF3: 50 (usually 50)
- Time: 5 minutes

(5 minutes of processing followed by 5 minutes of purge until 15 minutes of processing time total, vent the chamber and observe chips. Afterwards, 5 minutes of processing followed by 5 minutes of purge until another 15 minutes of processing time occurs. Vent the chamber and observe the chips. Run a clean cycle. Rinse and repeat until etched. May want to observe more often as the oxide layer gets closer to the silicon to prevent over etch); this usually takes approximately 2-2.5 hours of processing time

Silicon Etch Recipe

Pressure: 50 (usually 50)

ICP: 0

RIE: 50 (reflected can be 0)

SF6: 30 (usually 30)

Time: 1 minute

(1 min. processing, 1 min. cool down. Every 3 minutes of processing, one may remove the chips from the chamber and observe the etching); usually takes about 15-18 total minutes of processing time.

Appendix B
Quality factor of high loss transmission lines

There are several definitions to find quality factors of transmission lines. The most famous one is $Q=\beta/2\alpha$. But this definition of quality factor is only correct at multiple integers of quarter lambda [79], when the transmission line makes a resonator. Also, this equation is an approximation and it only gives accurate results if quality factor is big [80]:

$$\frac{\beta}{2\alpha} = Q(1 + \frac{1}{4Q^2} - \frac{1}{16Q^2} + \cdots) \qquad \text{(B-1)}$$

When, dealing with micro-TLs, usually the electric length of the transmission line is smaller than quarter lambda and the quality factor can be very small, therefore equation (B-1) does not give an accurate result but nevertheless it can be used for comparison between different micro-TLs.

If accurate quality factor needs to be calculated two methods can be use. The first method is based on finding the impedance of the transmission line as a function of frequency, determine whether the transmission line can be modeled as series or parallel RLC circuit and use quality factors of series or parallel RLC circuits [79]:

$$Q = \frac{|imag(Z)| + \omega \frac{d}{d\omega} imag(Z)}{2Re(Z)} \quad for\ series\ RLC \text{ circuits} \qquad \text{(B-2)}$$

$$Q = \frac{\left|imag\left(\frac{1}{Z}\right)\right| + \omega \frac{d}{d\omega} imag\left(\frac{1}{Z}\right)}{2Re\left(\frac{1}{Z}\right)} \quad for\ parallel\ RLC\ circuits \qquad \text{(B-3)}$$

And for finding Z in the above equations when the transmission line end is short or open, one can use:

$$Z_{short} = Z_0 \tanh(\gamma\ len) \quad \& \quad Z_{open} = Z_0 \,/ \tanh(\gamma\ len) \qquad \text{(B-4)}$$

The second method to find accurate quality factors is by decomposing total quality to conductive and dielectric quality factors as defined in equation (4-9):

$$Q_t = \omega \frac{W_m + W_e}{P_c + P_d} = \omega \frac{1}{\frac{P_c}{W_m \eta_L} + \frac{P_d}{W_e \eta_{cap}}}$$

$$where\ \eta_L = \frac{W_m + W_e}{W_m}\ and\ \eta_{cap} = \frac{W_m + W_e}{W_e} \tag{B-5}$$

where, W_m and W_e are the magnetic and electric stored energies and P_c and P_d are conductive and dielectric power losses respectively.

$$W_m = \int_0^l \frac{1}{2} L i^2(x) dx \quad \& \quad W_m = \int_0^l \frac{1}{2} C v^2(x) dx \tag{B-6}$$

where l is the physical length of the transmission line. From equations (B-5) and (B-6) we can write:

$$\frac{1}{Q_t} = \frac{1}{\eta_L Q_L} + \frac{1}{\eta_{cap} Q_{cap}} = \frac{1}{Q_c} + \frac{1}{Q_d} \tag{B-7}$$

Calculating Q with this method has the benefit of finding separate conductive and dielectric quality factors and can give more insight to the transmission line losses but it is more complicated because of the need to do integrations. These 3 definitions of Quality factor are compared for some typical micro-TLs below:

It should be mentioned here that for the quality factor in the right side of Fig. B-1, Q is only valid at resonance. Since in micro-TL s conductive quality factor is dominant, with increased frequency this type of Q increases. But, for the other two definitions of Q in the left side, the quality factor of a certain length of micro-TL is calculated. With increased frequency, electric length of the micro-TL increases and the losses will become more pronounced, that's why they decrease with frequency. If we used a longer transmission line at a certain frequency (at resonances) the left and right graphs will intersect.

It is useful to compare the actual quality factor of some of the micro-TLs we compared in section 4.4.2. One can see here that similar to the comparison of Fig. 4-18, here too, slotline and microstrip have higher q factors.

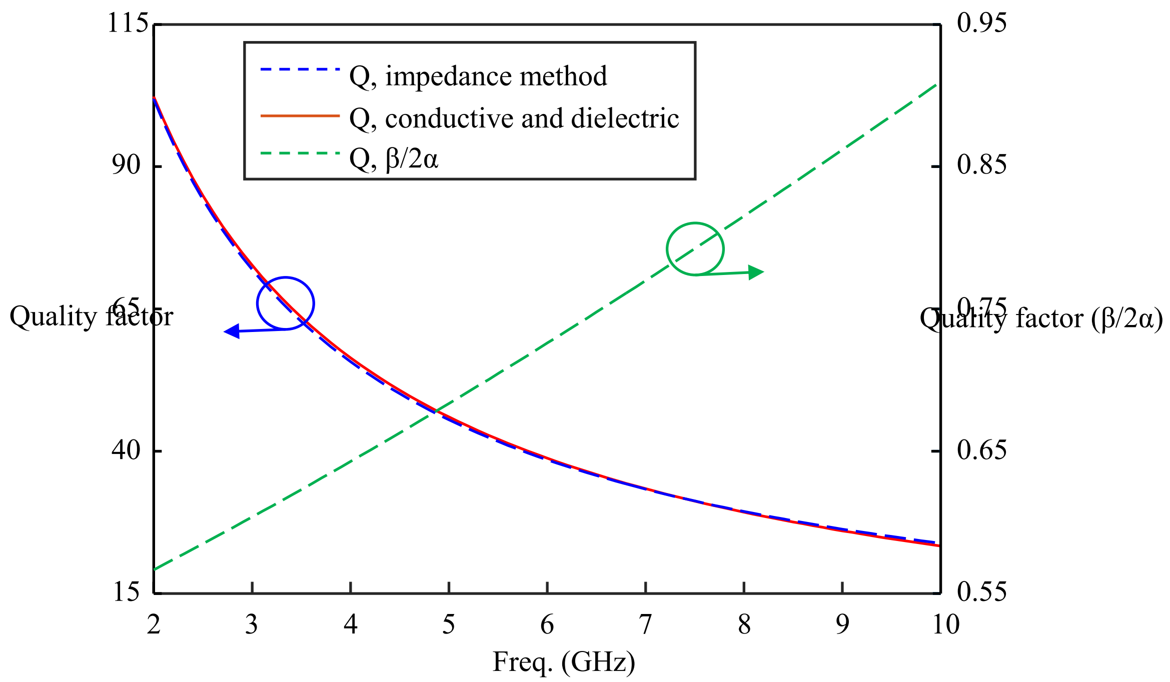

Fig. B-1. Comparing different quality factors for a microstrip micro-TL with 700 μm length.

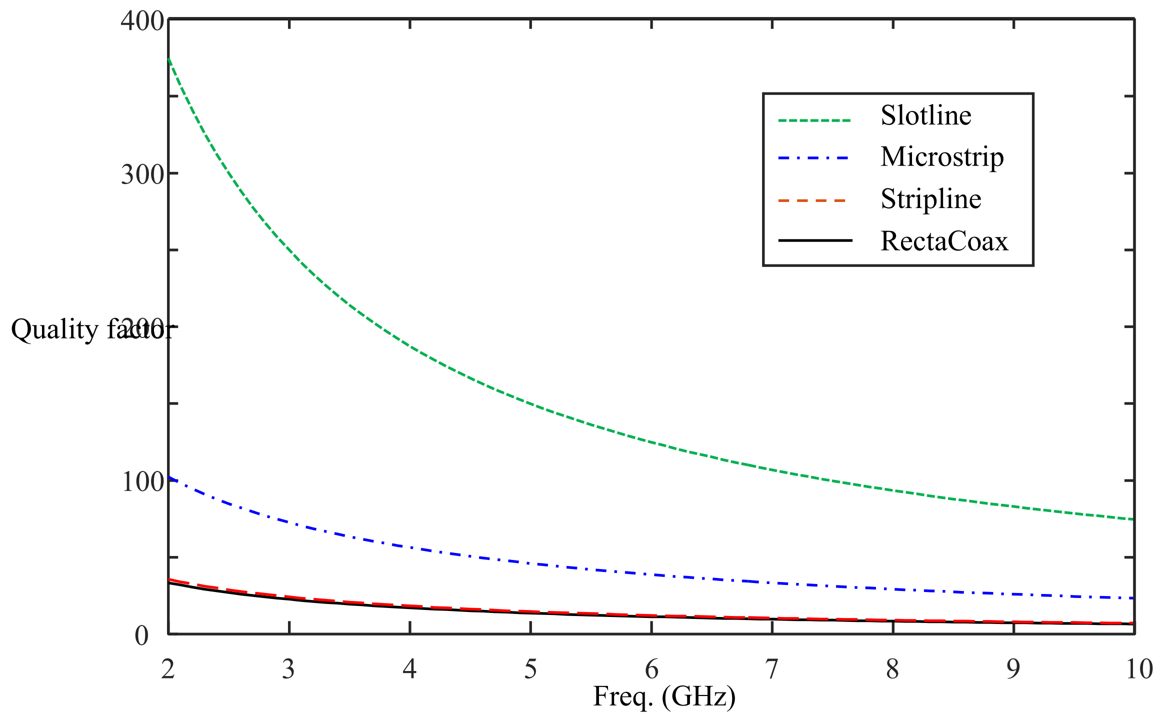

Fig. B-2. Actual Q factor for some of the micro-TLs.

Appendix C

Components used in the SMM measurement system

Below is a list of components that are used for the SMM measurement system:

1. Power divider, from RF lambda. Part Number: RFLT2W2G08G
2. Coupler, 10 dB, 2-8 GHz from RF Lambda. Part Number: RFDC2G8G10
3. LNA, from Pasternack. Part Number: PE15A1002
4. Mixer, from Mini-Circuits. Part Number: ZMX-7GR
5. Variable Phase shifter, from Pasternack. Part Number: PE8245
6. Variable attenuator, from Pasternack. Part Number: PE7065-4
7. Lock In Amplifier, from Zurich Instruments. Part Number: HF2LI
8. Baseband amplifier, from mini circuits: ZHL-6A+
9. In house baseband amplifier, explained in the following section

Baseband Amplifier Design

Baseband amplifier is designed to amplify the signal after the mixer in baseband from a few hundred hertz to around 100 KHz.

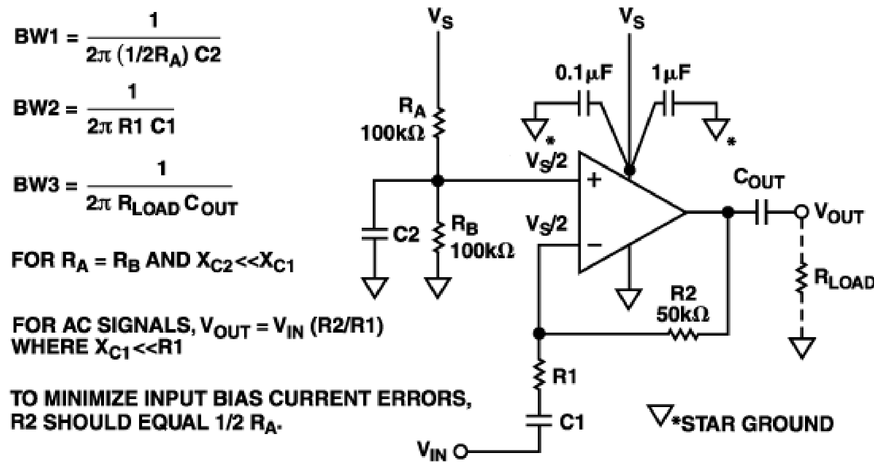

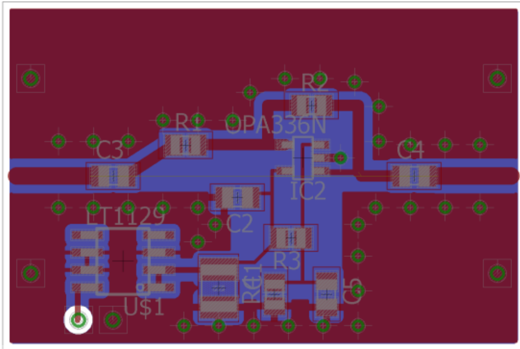

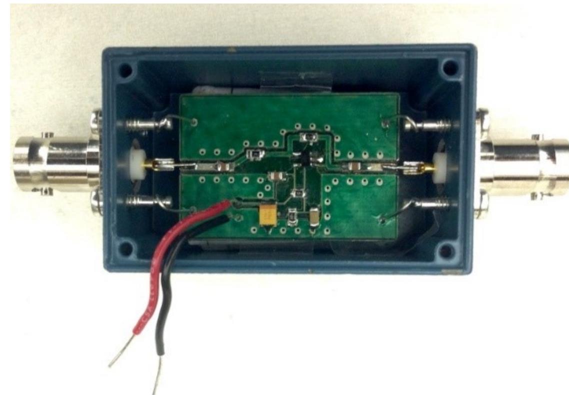

Fig. C-1. (top) Baseband Amplifier design, and Circuit. Bottom: Layout and fabricated BB amp.

Simulation and measurements results are shown in Fig. C-2. Simulation is done in ADS and the measurement is taken with the lock-in amplifier. The signal below 50 Hz is due to high phase noise at lower frequencies. Therefore it is best to have the mechanical resonance frequency well above 100 Hz to have less phase noise. The mechanical resonance frequencies of the CMOS-MEMS SMM is usually between 3 KHz to 10 KHz.

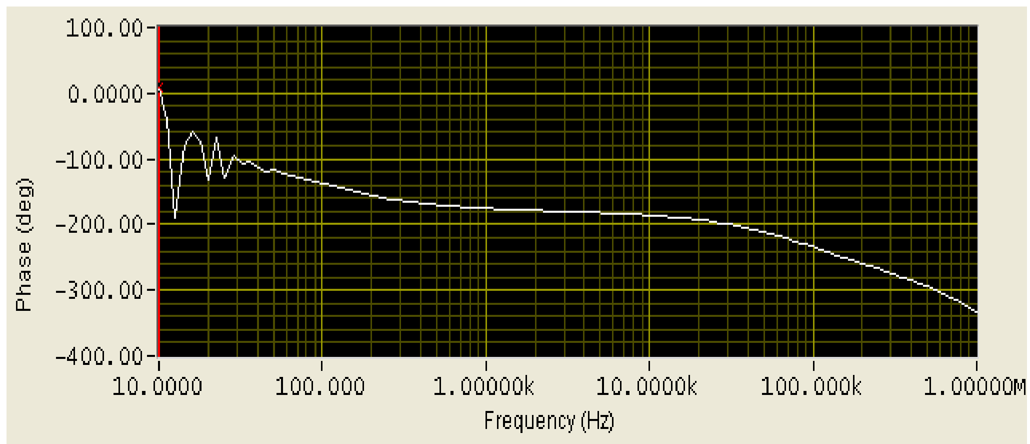

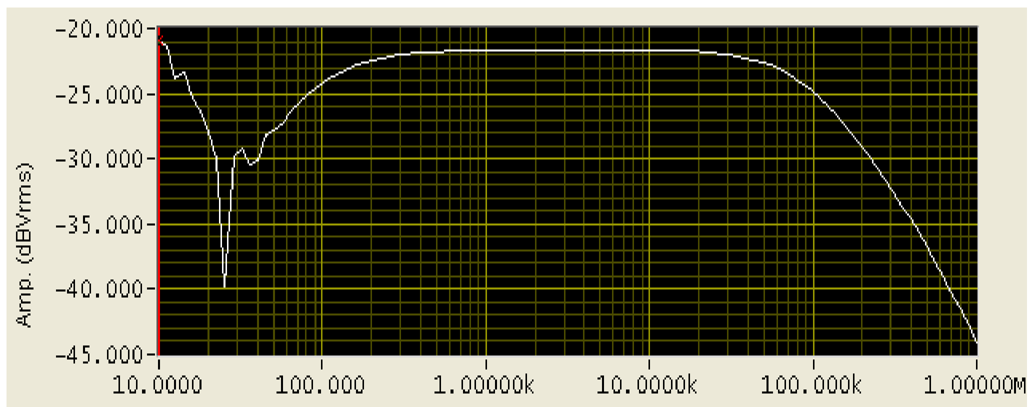

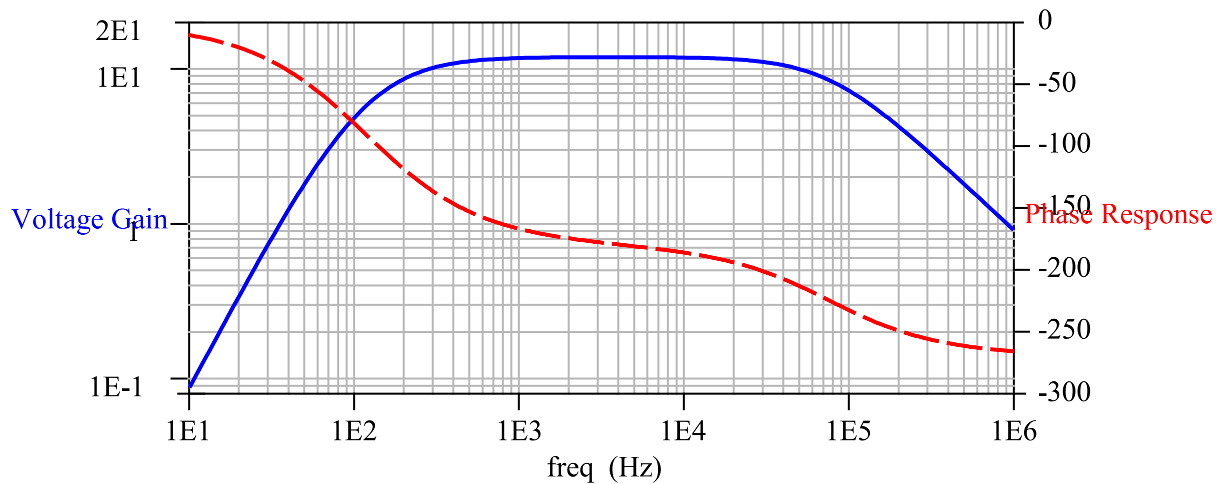

Fig. C-2. Baseband Amplifier measurements and simulation results.